Mechanics and calcium bursts in neutrophil chemotaxis and phagocytosis

By

EMMET A FRANCIS

DISSERTATION

Submitted in partial satisfaction of the requirements for the degree of

DOCTOR OF PHILOSOPHY

in

Biomedical Engineering

in the

OFFICE OF GRADUATE STUDIES

of the

UNIVERSITY OF CALIFORNIA

DAVIS

Approved:

Volkmar Heinrich, Chair

Soichiro Yamada

Scott Simon

Sean Collins

Committee in Charge

2022

Table of Contents

Acknowledgements

This dissertation is dedicated to my wife Katie and my cat Milo, who read over sections of this work in its early stages (Katie), helped me code by walking on my keyboard (Milo), and tolerated my sometimes manic behavior (both). They're simply the best.

This work was supported by a number of talented undergraduate researchers through the years, whom I had the privilege of training and working alongside. Hugh Xiao and Lay Heng Teng both contributed frustrated phagocytosis data for Chapters 2 and 5 of this dissertation, and Jonathan Brand gathered some of the micropipette experiment data shown in Chapter 5. Kay Hadrick and Yazan Haidar also helped gather data that will be key to future steps of this work in the Heinrich Lab. Additional work has gone into exploring phagocytosis and Ca^{2+} signaling in another type of immune cell, the eosinophil – Julie Zimmer, Yiting (Jenny) Chen, and Sahand Salari-Namin all made contributions to that project, which I am certain could fill out a dissertation of its own someday.

A big thank you to previous graduate students in the Heinrich lab, Lucas Murray and Wooten (Trey) Simpson, for providing great company and solid feedback on my research in the early years of my PhD. Also, I very much appreciate the input and collaboration with several other graduate students over the years – a particular thank you to Vasilios Morikis for many long discussions about neutrophils and calcium signaling. And, of course, many thanks to all my graduate student friends – between outreach events, intramural sports, book clubs, and even musical performances, they really helped round out my graduate school experience.

This work would not have been possible without the support of my advisor, Dr. Volkmar Heinrich. He has been an inspiration to me for many years of research now, from originally

teaching me to make and use our glass micropipettes to diving deep in many conversations on modeling neutrophil mechanics. My years in his lab have been an invaluable experience, and I will carry forward many lessons he has taught me about research and about life in general.

I would also like to sincerely thank the other members of my dissertation committee: Dr. Soichiro Yamada, Dr. Scott Simon, and Dr. Sean Collins. Dr. Yamada not only provided valuable input on actin imaging and immunofluorescence, but also trained me in cell culture. Dr. Simon gave valuable advice on techniques to probe integrin function and Ca^{2+} dynamics. My conversations with Dr. Collins led to many key insights about the main signaling networks involved in neutrophil motility and how they may overlap with Ca^{2+}. Thank you also to Dr. Bob Guy (practically an honorary committee member) for many helpful discussions on modeling fluids and for allowing me to attend his weekly group meetings to learn quite a bit about using numerical methods to solve fluid mechanics problems. I am grateful to many other professors and postdocs who have also helped me and/or collaborated with our lab along the way: Dr. Sanjeevi Sivasankar, Dr. Jamal Lewis, Dr. Tonya Kuhl, Dr. Eleanora Grandi, Dr. Stefano Morotti, Dr. Hari Manikantan, Dr. Becca Thomases, Dr. Tim Lewis, Dr. Kathryn Link, and Dr. Sam Walcott.

Finally, I want to thank my family. Thank you to my mom and dad for their strong support through all my years at UC Davis, from attending marching band performances to being there for my PhD graduation ceremony. And thanks to my brothers, Sam and Will, for being so supportive and encouraging through all my peculiar interests over the years, it means a lot.

Abstract

Human neutrophils play an essential role in the immune system, acting as first responders to infection by migrating through tissue along chemical gradients and consuming foreign objects such as pathogens. These processes, known as chemotaxis and phagocytosis respectively, require neutrophils to deform in a controlled manner, balancing adhesion to surfaces and protrusive forces exerted by the cell's own cytoskeleton. Bursts in the concentration of intracellular calcium ions (Ca^{2+}) are commonly observed during such deformations, but the link between neutrophil mechanics and Ca^{2+} bursts remains unclear. In this work, we first examine the mechanical underpinnings of neutrophil phagocytic spreading, and then study the causes and the effects of Ca^{2+} bursts during neutrophil chemotaxis and phagocytosis. Throughout, we use a combination of biophysical experiments and computational models to answer fundamental questions about neutrophil biology. In initial experiments, we deposit human neutrophils onto surfaces coated with different densities of IgG antibodies to probe the roles of adhesion and protrusion in phagocytic spreading. These experiments, in combination with computational models of cell deformation, demonstrate that frustrated phagocytic spreading is driven by cell protrusion, but the maximum contact area to which the cell can spread is limited by the availability of adhesion sites. We then turn our attention to the causes and effects of Ca^{2+} bursts in neutrophil chemotaxis and phagocytosis. Using single-cell biophysics experiments, we show that neutrophil chemotactic protrusion alone neither requires nor causes Ca^{2+} bursts. On the other hand, we find that phagocytic spreading is consistently accompanied by Ca^{2+} bursts, and the timing and magnitude of these bursts are determined in part by the density of ligands on a pathogenic surface. We develop a computational model of these Ca^{2+} bursts in phagocytosis and show that the model agrees with our experimental data. Finally, we determine the effects of altering

intracellular or extracellular Ca^{2+} on the dynamics of phagocytosis. Remarkably, we find that eliminating Ca^{2+} bursts by depleting intracellular Ca^{2+} stores does not prevent phagocytosis of IgG-coated targets but does result in slower cell spreading and lower maximum contact areas in frustrated phagocytosis experiments. Removing all extracellular divalent cations has only a small effect on Ca^{2+} bursts but does lead to altered cell morphology in phagocytosis; we attribute this to the general ability of divalent cations to modify the binding affinity of cell adhesion receptors such as integrins. Overall, our work shows that Ca^{2+} bursts, while not strictly required for neutrophil protrusion, do facilitate efficient spreading over pathogenic surfaces during phagocytosis.

Chapter 1: Introduction

Neutrophils are the most abundant type of white blood cells in the human body and are the first responders to infection. The initial steps of their recruitment involve rolling to arrest on the endothelium and exiting the vasculature via transmigration. They then navigate to the site of injury by migrating along chemical gradients, a process known as chemotaxis. At the site of interest, they bind to foreign objects such as pathogens and internalize them. This process of engulfment, known as phagocytosis, is central to neutrophil function and involves some of the same cytoskeletal machinery by which neutrophils and other cells migrate.

Although decades of research have been devoted to understanding chemotaxis and phagocytosis in neutrophils, there remain many gaps in knowledge, particularly with respect to the physical mechanisms underlying these processes. Furthermore, although diverse signaling pathways have been characterized during both chemotaxis and phagocytosis, it remains unclear how various signaling events are coupled with cell mechanics. In this introductory chapter, we give a brief overview of past studies on the biophysics of phagocytosis, followed by a summary of the research on large bursts in intracellular calcium concentration during neutrophil migration and phagocytosis. We then outline the content covered in this dissertation, which seeks to characterize the relationship between mechanics and calcium bursts in neutrophil chemotaxis and phagocytosis.

Much of the initial research on phagocytosis focused on identifying phagocytic receptors and their binding targets. Many of the strongest cues on the surfaces of pathogens come from molecules produced by a person's own body, including immunoglobulins such as IgG and complement fragments such as C3b or iC3b. These molecules bind to pathogen surfaces and are detected by receptors in the phagocyte's membrane, leading to phagocytosis. The best-known

cases of this include Fcγ receptors (FcγRs) binding to IgG molecules [1] and complement receptors binding to complement fragments [2]. Based on this knowledge of phagocytic receptors, early conceptual models of phagocytosis mostly agreed that immune cells spread over pathogen surfaces in a zipper-like fashion; that is, cells require circumferential adhesion to a pathogen to efficiently complete engulfment [3, 4]. This process was found to depend on the recruitment of certain signaling factors and the mobilization of the actin cytoskeleton to form protrusions known as pseudopods which extend around the target surface [5, 6].

The spreading of phagocytic immune cells over pathogenic surfaces is a mechanically intensive process. Accordingly, the biophysics of phagocytosis has been an area of great interest – in particular, how do neutrophils and other phagocytes generate the protrusive force and surface area required to engulf particles? Early work demonstrated that the success of phagocytosis depends on the size of the target particle [7, 8]. The consumption of larger particles is limited by the phagocyte's available surface area, dictated by the amount of membrane stored in plasma membrane folds (e.g., microvilli) and surface area recruited by exocytosis. The mechanics of phagocytosis were explored in detail through pioneering work that utilized single-cell biophysical experiments and computational modeling [9, 10]. These studies examined how tension in the cell cortex changes with the amount of cell deformation in phagocytosis and showed that cell morphology and dynamics in phagocytosis could be recapitulated remarkably well by a physical model in which repulsion between polymerizing actin and the cell membrane powers pseudopod extension.

Recently, it has been increasingly appreciated that linkages between the cell membrane and the actin cytoskeleton play a key role in the mechanics of phagocytosis. For instance, the difference in cell morphology during phagocytosis of serum-opsonized zymosan versus IgG-

coated microspheres was attributed to variations in the strength of cytoskeleton-membrane attachments [11, 12]. Specifically, it was suggested that the outward displacement of zymosan particles prior to consumption indicated weakened cytoskeleton-membrane attachments within the cell-target contact region; this idea was supported by computational modeling [11]. These linkages effectively steer the progress of pseudopod extension in phagocytosis by anchoring the membrane to the cytoskeletal network at adhesion sites such that the cell spreads around the particle rather than pushing it outwards [13]. The identity of these linkages is likely context-dependent, but the integrin $\alpha_M\beta_2$, also known as Mac-1 or complement receptor 3, can certainly provide connections to F-actin during complement-mediated phagocytosis [14]. The cytoplasmic tail of activated Mac-1 binds to talin, which in turn links to actin filaments [15]. Mac-1 may also provide anchoring connections to the cytoskeleton in IgG-mediated phagocytosis by cooperating with FcγRs [16, 17]. Other molecules such as myosins can also couple the membrane to the cytoskeleton [18]; myosin I in particular has been shown to play a key role in coordinating protrusion during phagocytosis [19].

Alongside this research on the mechanics of phagocytosis has come a large volume of work characterizing the biochemical signaling networks involved in phagocytosis [20]. One of the most dramatic signaling events that occurs consistently during neutrophil phagocytosis is a global burst in the cytosolic free calcium (Ca^{2+}) concentration. These Ca^{2+} bursts have been observed in both neutrophils and macrophages for several decades [21-25] and are similar to Ca^{2+} signals observed in lymphocytes [26]. However, basic questions about Ca^{2+} bursts in neutrophil biology remain unanswered. What chemical and mechanical inputs determine the onset of Ca^{2+} bursts? What are the relative contributions of Ca^{2+} influx versus intracellular store

release? Are Ca^{2+} bursts required for phagocytosis, or do they act in parallel to the main pathways involved in cell deformation?

Because Ca^{2+} plays many diverse roles in intracellular signaling and many different pathways are known to trigger Ca^{2+} elevations, answers to the above questions are often subtle and context dependent. For instance, although Ca^{2+} bursts often occur during neutrophil chemotaxis in response to G-protein-coupled receptor agonists, select studies have shown that these elevations are neither triggered by nor required for chemotactic protrusion itself [27, 28]. Rather, these signals appear to be mediated by a combination of cell-substrate adhesion and chemoattractant receptor engagement. Likewise, the reliance of phagocytosis on Ca^{2+} elevations differs depending on the type of receptor being engaged. One study showed that complement-mediated phagocytosis hardly depends on elevated intracellular Ca^{2+}, whereas IgG-mediated phagocytosis is significantly reduced when Ca^{2+} bursts are suppressed [24].

Ca^{2+} elevations are known to play a general role in neutrophil adhesion and spreading on surfaces. Inducing Ca^{2+} bursts by uncaging inositol triphosphate (IP_3) in the cytosol was sufficient to trigger neutrophil spreading on glass surfaces [29]. Ca^{2+} bursts were also found to be required for acceleration of β_2-integrin-mediated phagocytosis [30]. Both studies attributed these effects to calpain, a Ca^{2+}-sensitive enzyme which cleaves connections between the membrane and the cytoskeleton. Cleaving these connections allows for unfurling of membrane folds and permits more efficient receptor diffusion, both of which encourage faster cell spreading. Ca^{2+} bursts can also mediate the formation of cytoskeleton-membrane linkages within the cell-substrate contact region through inside-out integrin signaling [31]. As discussed above, cytoskeleton-membrane linkages at the site of contact play a key role in the mechanics of phagocytosis by anchoring the cytoskeletal network, allowing the cell to spread around a particle

rather than push it outwards. These known associations between Ca^{2+} dynamics and phagocytosis mechanics suggest that Ca^{2+} signaling and mechanics may be tightly coupled in phagocytosis.

This dissertation continues work on both the mechanics of phagocytosis (Chapters 2-3) and Ca^{2+} bursts in chemotaxis and phagocytosis (Chapters 4-6), with the overarching goal of understanding the complex interplay between Ca^{2+} bursts and neutrophil mechanics. Our central hypothesis is that human neutrophils integrate chemical and adhesive cues during chemotaxis and phagocytosis through global Ca^{2+} release, which leads to increased cytoskeletal protrusion and the controlled lock and release of cytoskeleton-membrane attachments.

Throughout, we use a combination of experiments and computational modeling to answer fundamental questions about neutrophil mechanics and Ca^{2+} signaling. Two primary experimental setups are utilized: single-cell micropipette experiments (Fig 1.1A) and frustrated phagocytosis assays (Fig 1.1B). In later chapters, both setups are used in combination with fluorescence imaging to examine Ca^{2+} dynamics simultaneously with changes in cell shape.

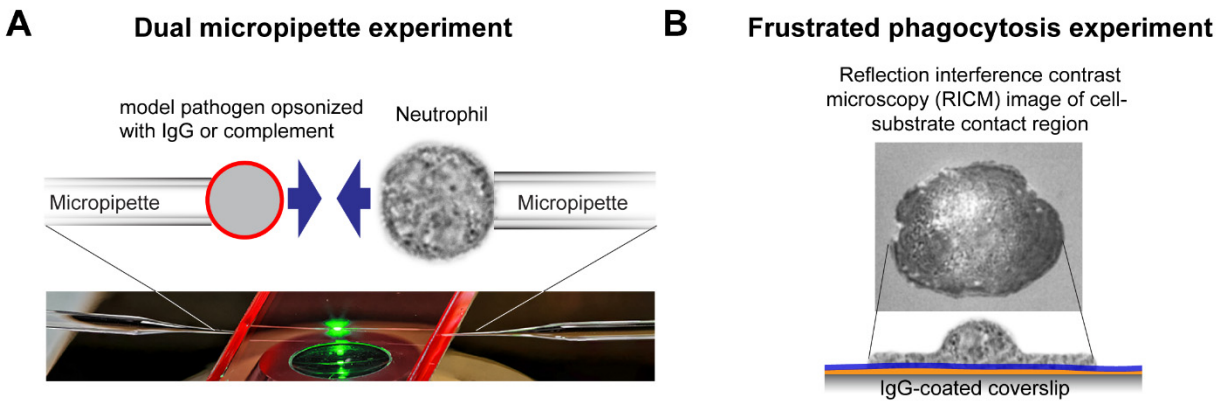

Fig 1.1: **Two experimental setups for phagocytosis. (A)** In dual-micropipette-manipulation experiments, opposing micropipettes hold a neutrophil (right) and a pathogen particle (left). The movement of these pipettes is precisely controlled using micromotors, allowing us to examine the response of a human neutrophil as the target particle is brought close to or in contact with the cell. **(B)** In frustrated phagocytosis experiments, neutrophils are deposited onto a coverslip coated with IgG and imaged during phagocytic spreading using reflection interference contrast microscopy (RICM).

Chapters 2 and 3 of this dissertation focus on the mechanics of phagocytic spreading over pathogenic surfaces, first from an experimental angle (Chapter 2) and then via computational modeling (Chapter 3). These studies show conclusively that phagocytic spreading is not well described by models of passive spreading in which ligand-receptor binding powers cell deformation. Rather, spreading is primarily driven by active forces exerted by the cell; actin polymerization powers membrane protrusion over opsonized pathogen surfaces.

In Chapter 4 of this dissertation, we show that extension of chemotactic pseudopods neither causes nor requires Ca^{2+} bursts in neutrophils. Although it is often observed that neutrophil chemotaxis is accompanied by large Ca^{2+} transients, such increases seem to require cell-substrate adhesion or supraphysiological concentrations of chemoattractant. Chapter 5 then turns to Ca^{2+} bursts in phagocytosis, examining global Ca^{2+} dynamics during phagocytosis of fungal model particles or surfaces coated with various densities of IgG. In addition to carefully quantifying global changes in intracellular Ca^{2+} concentration in our experiments, we develop a computational model of Ca^{2+} dynamics during phagocytosis using a system of ordinary differential equations, which reproduces key features of Ca^{2+} bursts observed experimentally.

Chapter 6 then characterizes the effects of perturbing intracellular or extracellular Ca^{2+} concentration on phagocytosis mechanics. Depleting extracellular Ca^{2+} and Mg^{2+} alters the mechanics of phagocytosis without eliminating Ca^{2+} bursts; this effect appears to primarily be due to inhibition of integrin binding rather than elimination of Ca^{2+} influx. On the other hand, we find that phagocytosis is surprisingly robust to treatments which either partially or fully inhibit Ca^{2+} bursts; for instance, pre-depleting intracellular Ca^{2+} stores essentially eliminates Ca^{2+} bursts, but only slightly decreases the speed of phagocytic spreading. Regardless, we conclude

that Ca^{2+} bursts help facilitate neutrophil protrusion; the nature of this relationship, as well as future directions for this work, are discussed in the conclusions to Chapter 6.

Chapter 2: Mechanisms of frustrated phagocytic spreading of human neutrophils on antibody-coated surfaces

Reproduced with permission from E.A. Francis, H. Xiao, L. Teng, and V. Heinrich. Manuscript currently in revision as of July 2022. Preprint available on BiorXiv [32].

Abstract

Complex motions of immune cells are an integral part of diapedesis, chemotaxis, phagocytosis, and other vital processes. To better understand how immune cells execute such motions, we present a detailed analysis of phagocytic spreading of human neutrophils on flat surfaces functionalized with different densities of immunoglobulin G (IgG) antibodies. We visualize the cell-substrate contact region at high resolution and without labels using reflection interference contrast microscopy (RICM) and quantify how the area, shape, and position of the contact region evolves over time. We find that the likelihood of the cell commitment to spreading strongly depends on the surface density of IgG, but the rate at which the substrate-contact area of spreading cells increases does not. Validated by a theoretical companion study, our results resolve controversial notions about the mechanisms controlling cell spreading, establishing that active forces generated by the cytoskeleton rather than cell-substrate adhesion primarily drive cellular protrusion. Adhesion, on the other hand, aids phagocytic spreading by regulating the cell commitment to spreading, the maximum cell-substrate contact area, and the directional movement of the contact region.

Introduction

Innate immune cells, in particular white blood cells, stand out among animal cells due to their deformability and extraordinary motility. Their mechanical flexibility enables them to carry out vital immune functions, such as chemotaxis toward sites of infection, and phagocytosis of foreign particles. These and other processes critically depend on the cells' ability to spread onto surfaces, for example, during firm arrest of white blood cells at the endothelium, or during the engulfment of target particles.

Phagocytic spreading is distinct from other forms of cell spreading in that it engages specific cell-surface receptors known to trigger phagocytosis [20, 33, 34]. In many physiological situations, phagocytosis is initiated by opsonic ligands such as immunoglobulin G (IgG) antibodies and complement fragments. When bound to a pathogen surface, these ligands are recognized by the immune cells' Fcγ receptors (FcγRs) and complement receptors, respectively [1, 2]. Ligation of these receptors activates receptor-specific intracellular signaling [20, 35-37] and ultimately leads to progressive spreading of the phagocyte over the target surface. In conventional phagocytosis, cell spreading concludes when the phagocytic cup closes to create a phagosome compartment. However, in some cases known as frustrated phagocytosis, the target is too large to be completely engulfed by a single phagocyte. During these encounters, immune cells strive to maximize the area of contact with the target surface, resulting in thinly spread, lamella-shaped cells that partially cover the target. Such frustrated phagocytic spreading has been observed, for instance, in interactions of human neutrophils with spherules of the fungal pathogen *Coccidioides posadasii* [38] as well as with large beads [9]. The extent of spreading in these cases seems to be limited by the maximum apparent cell-surface area that a phagocyte can generate. For example, the maximum surface area observed during phagocytosis by human

neutrophils amounts to about 300% of the surface area of the spherical resting shape of these cells [7, 9, 38, 39], while for macrophages this plateau value is as high as 600% of the respective resting area [8, 40].

The targets encountered by immune cells during frustrated phagocytosis are characterized by very low surface curvatures. Although curvature-dependent variations in phagocytic behavior have been reported [7, 8, 41-43], they do not appear to reflect qualitative changes in the cellular response but are likely due to the same response program coping with different "input" sizes and shapes of target particles [10, 44]. Thus, it is reasonable to assume that the same preprogrammed cellular response also controls phagocytic spreading of immune cells on surfaces with zero curvature, i.e., flat substrates. Considering the high resolution of imaging methods that inspect cell-substrate interactions directly at the bottom of an experiment chamber, the study of frustrated phagocytic spreading of immune cells on such planar surfaces is a powerful tool to examine fundamental mechanisms of phagocytosis [14, 19, 45, 46].

Here, we present an in-depth quantitative analysis of human neutrophil spreading on IgG-coated coverslips. Our main objective is to address the lacking consensus between two different hypotheses that have been put forward to explain the mechanistic origin of phagocytic spreading, denoted as "Brownian zipper" and "protrusive zipper" mechanisms [13]. Both hypotheses agree that fresh contact between the phagocyte membrane and target surface results in a zipper-like adhesive attachment that is essentially irreversible. However, they differ in their assumptions about the primary driving force of cellular protrusion that produces fresh cell-target contact in the first place. The Brownian zipper hypothesis views the phagocyte as a passive object and postulates that strong adhesion alone is responsible for pulling the cell membrane onto the target surface. In other words, this hypothesis treats phagocytic spreading as a wetting phenomenon,

akin to a water droplet spreading on a hydrophilic surface. In contrast, the protrusive zipper hypothesis assumes that the phagocyte's cytoskeleton actively generates protrusive force to push the front of the cell outwards.

We investigate which of these hypotheses captures the main driving force of phagocytic spreading using well-controlled frustrated phagocytosis experiments. Our strategy is based on the following reasoning. If the Brownian zipper hypothesis of adhesion-driven spreading holds true, then both the rate as well as the extent of spreading should strongly depend on the density of adhesive binding sites on the substrate. In contrast, because the protrusive zipper hypothesis assumes that the spreading speed is primarily set by the rate of cytoskeletal protrusion, this mechanism would predict a weaker dependence of the spreading speed on the ligand density. To expose which type of behavior human neutrophils exhibit, we allow the cells to settle onto coverslips pre-coated with different densities of rabbit IgG and analyze their subsequent spreading dynamics. Visualization of the cells with reflection interference contrast microscopy (RICM) allows us to image the cell-substrate contact region with exceptional contrast without the use of labels. In addition to the spreading speed and maximum contact area, this analysis enables us to further characterize the effects of IgG density on phagocytic spreading by quantifying parameters such as the spreading probability, contour roundness, and centroid motion. In an accompanying theoretical study in Chapter 3, we leverage these results against computational models of cell-spreading mechanics. Overall, we find that, although the strength of adhesion can modulate phagocytic spreading, it is the cellular protrusion that sets the rate of spreading, in support of the protrusive zipper hypothesis.

Materials and Methods

Surface preparation

After partial assembly of the 3D-printed chamber (Fig 2.3A), the surface of the glass coverslip serving as chamber bottom was incubated with 1% (10 mg/ml) bovine serum albumin (BSA; VWR, Radnor, PA) in phosphate buffered saline (PBS; Bio-Rad, Hercules, CA) for 1 hour at room temperature, then rinsed with PBS. The surface was then incubated with a mixture of polyclonal rabbit anti-BSA IgG (Cat# A11133; Invitrogen, Waltham, MA) and monoclonal mouse anti-BSA IgG-1 (Cat# MA1-82941, Invitrogen, Waltham, MA) for another hour at room temperature. All mixtures contained a total of 150 µg/ml IgG, which was sufficient to saturate the surface, but the ratio of rabbit to mouse IgG concentration was varied to produce solutions containing 0%, 0.1%, 1%, 10%, or 100% rabbit IgG. After a final rinse with Hanks' balanced salt solution (HBSS with Ca^{2+} and Mg^{2+}; Thermo Fisher Scientific, Waltham, MA), the chamber was loaded with HBSS containing 2% human serum albumin (HSA; MP Biomedicals, Irvine, CA) to block any uncoated regions.

To quantify the actual density of rabbit IgG on coated glass surfaces, coverslips of each batch were incubated with 30 µg/ml anti-human IgG Fc (cross-reacts with rabbit) conjugated to Alexa Fluor-488 (Cat# 409321; BioLegend, San Diego, CA) for 45 minutes at room temperature in the dark, then rinsed with PBS before imaging. Beads from the Quantum Simply Cellular Kit (QSC; Bangs Laboratories, Fishers, IN) were incubated with the same secondary antibody at 6.25 µg/ml, again for 45 minutes at room temperature in the dark, then washed 3 times in PBS with 0.01% Tween and deposited onto plain glass coverslips for imaging.

Quantification of IgG surface density from fluorescence microscopy

As outlined in the main text (Fig 2.2), we determined the density of deposited rabbit IgG by comparing the fluorescence intensities of labeled coverslips to a calibration curve created using a set of QSC beads with known numbers of antibody-binding sites. All fluorescence images were taken on a spinning disc confocal microscope (488 nm laser, 100x oil objective, NA = 1.4). Due to the large spread of fluorescence intensities of the inspected surfaces, we used two different exposure times $t_e = 1$ s and $t_e = 2$ s and adjusted the originally measured intensities I to a corrected value $\bar{I}$ using

$$\bar{I} = \frac{I - I_0}{t_e} \tag{2.1}$$

where I_0 is the background intensity, i.e., the intensity at the substrate surface in the absence of fluorophore. To minimize photobleaching, we first preadjusted the microscope focus at a suitable location, then moved the microscope stage to a neighboring field of view and acquired a *Z*-stack of images of this unbleached region.

In fluorescence measurements of coverslips, we chose a region of interest of at least 10,000 pixels and determined the most frequent pixel intensity in this region for each image using kernel density estimation. After plotting the most frequent intensity values of all images of a given stack as a function of *Z*-height and fitting a cubic polynomial to these data, we calculated the maximum of the polynomial fit and identified its function value as the fluorescence intensity of the plane containing the fluorophore.

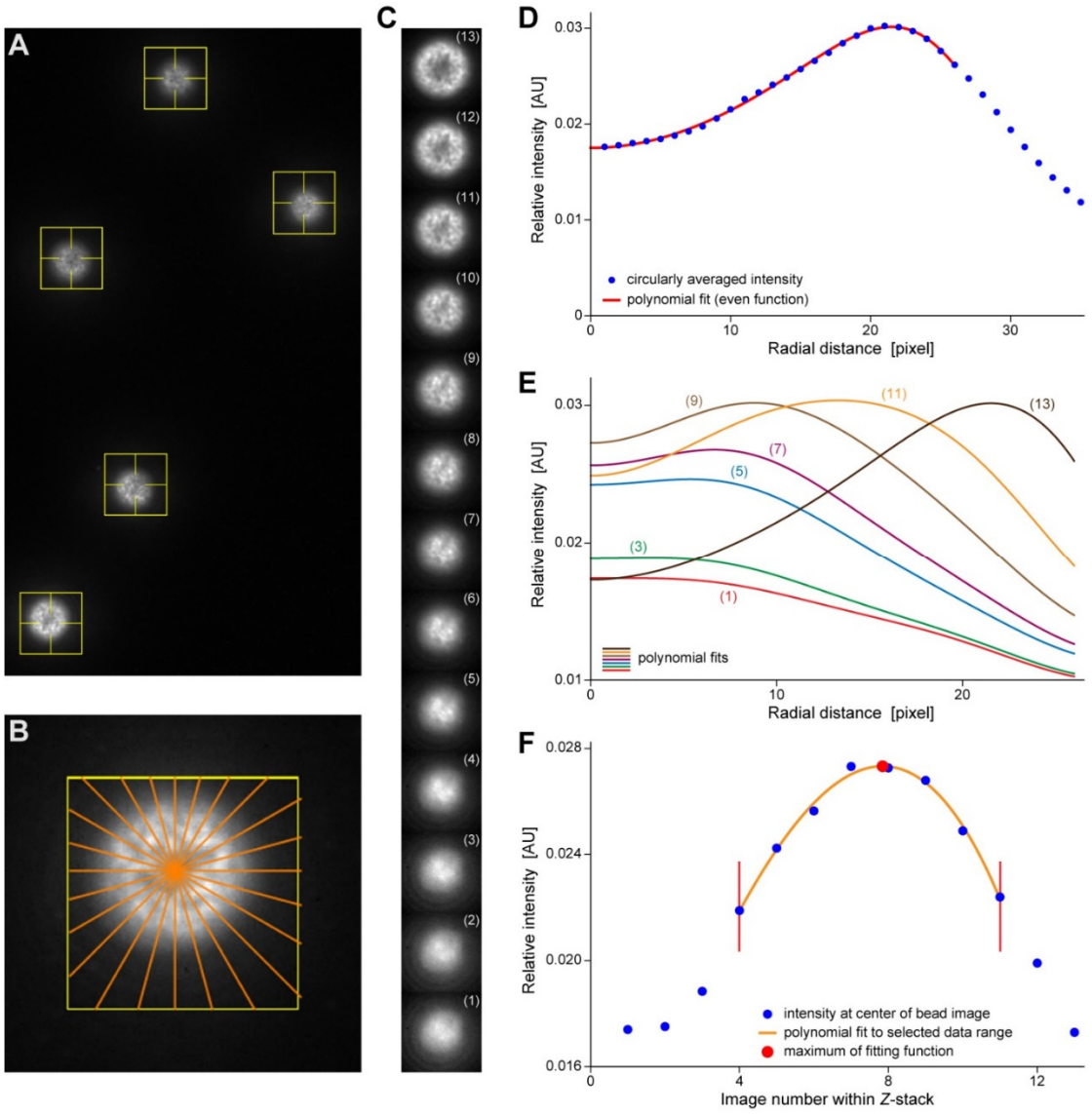

Fig 2.1. Procedure to quantify the fluorescence at the underside of labeled beads. (**A**) Confocal image of QSC beads labeled with secondary antibody resting at the bottom of a chamber. A search box (*yellow square*) was placed around each isolated bead. (**B**) Robust determination of the center of bead images. For each image, we first computed axes of mirror symmetry in a user-definable number of directions. We used 12 such axes in the present analysis (*orange lines*). For each direction, the symmetry axis was determined by shifting a straight line across the region of interest containing the bead image. For each position of this line, we calculated the cross-correlation of the bead image with its respective mirror image obtained by flipping the original image about this line. The line position corresponding to the interpolated maximum of cross-correlation values then defined the symmetry axis in the given direction. Finally, the bead center was calculated as the center of mass of the cross-sections of all pairs of symmetry axes. This procedure gave consistent results even for moderately noisy bead images and bead images with dark center regions. (**C**) Filmstrip representation of a *Z*-stack of confocal images of a QSC bead. The focal plane was moved from below the bead's underside (image (1)) to a height where it cut through the bead slightly above its lowest point (image (13)). The center of each bead image in the stack was determined as explained in (B). (**D**) Circularly averaged radial intensity profile of a confocal bead image. We calculated the mean intensities along circles centered about the center of the bead image, spaced out by one pixel (*blue symbols*). We then fit an even, low-order polynomial function to a subrange of the discrete intensity data (*red curve*). We identified the fluorescence intensity at the center of the bead image with the function value of the fitting function at radius zero.

(**E**) Plot of the polynomial fitting functions obtained for bead images of the stack of (C). For clarity, only the graphs for every other bead image are shown. (**F**) Determination of the fluorescence intensity at the lowest point of the bead surface. The intensity values at the center of all bead images of the stack of (C) (obtained as explained in (D)) are plotted as a function of their number within the stack (*blue symbols*). We fit a low-order polynomial function to a subrange of these data (*orange curve*) and identified the sought fluorescence intensity at the underside of the bead with the calculated maximum of the polynomial fitting function

A more elaborate procedure was needed to measure the pertinent fluorescence intensity of labeled QSC beads (Fig 2.1). We reasoned that the fluorescence at the underside of a bead resting at the chamber bottom is most closely relatable to the fluorescence at the top surface of labeled coverslips. Accordingly, we measured for each selected bead the fluorescence intensity at the center of all bead images in a given *Z*-stack and then again used polynomial fits to determine the interpolated maximum value of these intensities, which we identified as the fluorescence intensity corresponding to the known density of fluorophore coating the bead. Details of this procedure are illustrated in Fig 2.1. Having quantified the relationship between the surface density of rabbit IgG and the fluorescence intensity in this manner, we were able to establish the number of rabbit IgG molecules per μm^2 of the surface of functionalized coverslips for each of the used IgG incubation mixtures, i.e., for each nominal concentration of rabbit IgG (Fig 2.2).

Cell isolation

The protocol for this study was approved by the Institutional Review Board of the University of California, Davis and all donors provided written informed consent. Human neutrophils were isolated from whole blood of healthy donors by immunomagnetic negative selection using the EasySep Direct Human Neutrophil Isolation Kit (STEMCELL Technologies, Vancouver, Canada). Isolation began from an initial blood volume of 0.5-1 ml, and was carried out according to the protocol described by the manufacturer. Immediately following isolation, the

cells were resuspended at 5-10×10^6 cells per ml in HBSS without Ca^{2+} and Mg^{2+} (Thermo Fisher Scientific) to ensure their quiescence prior to stimulation by contact with IgG.

Contact area analysis

The cell-substrate contact area was quantified using customized MATLAB software based on code graciously provided by Daniel Kovari [45]. In brief, the RICM image was thresholded on both intensity and variance to construct an initial binary image by detecting regions where the local variance was greater than σ^2_{min} or the intensity was less than I_{max} (both thresholds could be adjusted on an image-by-image basis). The binary image was then convolved with a Gaussian kernel to smooth the outline of the cell footprint. Holes in the footprint were filled to define the total contact area. In cases where the automatic recognition algorithm performed poorly (especially during early spreading), the cell outlines were traced manually.

The spreading speed was quantified using sigmoidal fits to contact-area-versus-time graphs whenever possible. When necessary, a linear fit was used over a smaller range of the contact area data. The maximum contact area was determined as the average over the plateau region of the curve. To calculate the roundness of the cell-substrate contact region, we determined the largest inscribed and the smallest circumscribed circle of the cell footprint using open-source MATLAB functions [47, 48] (Fig 2.7A) and took the ratio the radii of these two circles.

Analysis of centroid directional persistence

We restricted our analysis of the directionality of the motion of the geometric centroid of the substrate contact region of each cell to the phase of fastest contact-area growth, where the spreading speed was greater than 0.4 $\mu m^2/s$. To assess for how long the centroid motion

typically maintained a preferred direction, we evaluated the directional autocorrelation function [49]. First, for each pair of successive video frames (recorded at times t_i and t_{i+1}, respectively), we determined the angle $\theta(t_i)$ between the x-axis and the line of centroid displacement using

$$\theta(t_i) = \arctan \frac{y_{i+1} - y_i}{x_{i+1} - x_i} \tag{2.2}$$

Then, after identifying all pairs of angles $\theta(t_i)$ and $\theta(t_j)$ along a given centroid trajectory for which the time gap $t_j - t_i$ equaled a given value Δt, we calculated the autocorrelation function $\mathrm{AC}(\Delta t)$ defined by

$$\mathrm{AC}(\Delta t) = \left\langle \cos\left[\theta(t_j) - \theta(t_i)\right]\right\rangle = \left\langle \cos\left[\theta(t_i + \Delta t) - \theta(t_i)\right]\right\rangle \tag{2.3}$$

where the angular brackets $\langle \ldots \rangle$ are used to denote the average over all such pairs. Persistence times are typically defined as the time constants of exponentially decaying autocorrelation functions; however, because of a limited number of data points in this analysis, the autocorrelation functions of the centroids of individual cells often did not lend themselves to exponential fits. Instead, recalling that the persistence time of an exponential decay equals the area under the autocorrelation curve, we here defined the directional persistence time by

$$\tau_{pers} = \int_{0\,\mathrm{s}}^{16\,\mathrm{s}} \mathrm{AC}(\Delta t)\,\mathrm{d}(\Delta t) \tag{2.4}$$

Computational modeling

Details of our computer model, including all equations and parameter values, are presented in Chapter 3 of this dissertation. In short, we represent the cell interior as a highly viscous Newtonian fluid and assume mechanical equilibrium. This allows us to solve a perturbed form of the Stokes equations at each time step using the finite element method, yielding the flow profile inside the cell. In order to complete this calculation, the relevant stresses are computed for a given shape of the cell, comprising *(i)* adhesion stress, assuming an attractive potential acting between the cell membrane and the IgG-coated surface, *(ii)* protrusion stress, assuming this stress acts normal to the cell membrane and decays exponentially along the membrane, and *(iii)* cortical stress, assuming a uniform cortical tension whose magnitude depends on the amount of surface area expansion as previously quantified for human neutrophils [9]. All calculations are carried out in MATLAB; our code is available at https://github.com/emmetfrancis/phagocyticSpreading.

Statistics

All tests for significance were conducted using one-way ANOVA followed by Tukey's post-hoc test in Origin software. Values more than 1.5 interquartile ranges above the upper quartile or below the lower quartile were excluded as outliers prior to ANOVA.

Results

Comparison with bead standards provides density of IgG on glass coverslips

We prepared surfaces displaying the Fc domains of IgG by saturating BSA-coated glass coverslips with anti-BSA antibodies (Fig 2.2). To adjust the surface density of human-reactive IgG, we used incubation buffers containing different ratios of polyclonal rabbit IgG and monoclonal mouse IgG-1. The total concentration of IgG was the same in all buffers. Because mouse IgG-1 is hardly recognized by human Fcγ receptors [50-52], it served to dilute the amount of human-reactive (rabbit) IgG decorating the coverslips. This approach appeared to produce consistently functionalized substrates for cell-spreading experiments. However, because the rabbit and mouse antibodies may have different affinities for BSA, the ratio of the two types of IgG deposited on the surface is not necessarily the same as in the incubation buffer.

To quantify the actual amount of deposited rabbit IgG, we labeled IgG-coated coverslips with fluorescent secondary antibody against rabbit IgG (Fig 2.2A) and compared the measured fluorescence intensity to a suitable standard. This standard consisted of batches of microspheres pre-functionalized with known numbers of antibody-binding sites (QSC Kit; Bangs Laboratories, Fishers, IN) that we saturated with the same secondary antibody as used to label the coverslips (Fig 2.2B). We analyzed *Z*-stacks of confocal images of these beads to determine the intensity of the fluorescent layer at the underside of each bead local to the center of the bead image (Materials and Methods; Fig 2.1). This analysis provided a calibration curve relating the fluorescence intensity of an essentially flat layer of secondary antibody to the known surface density of rabbit IgG (Fig 2.2B). The calibration curve then allowed us to convert measurements of the mean fluorescence intensity of confocal images of labeled coverslips (Fig 2.2A) to the density of rabbit IgG deposited on these coverslips. We note that the fluorescence intensity of

the most densely coated coverslips lay outside the intensity range of the bead standards; in this case, our analysis involved an extrapolation of the calibration curve.

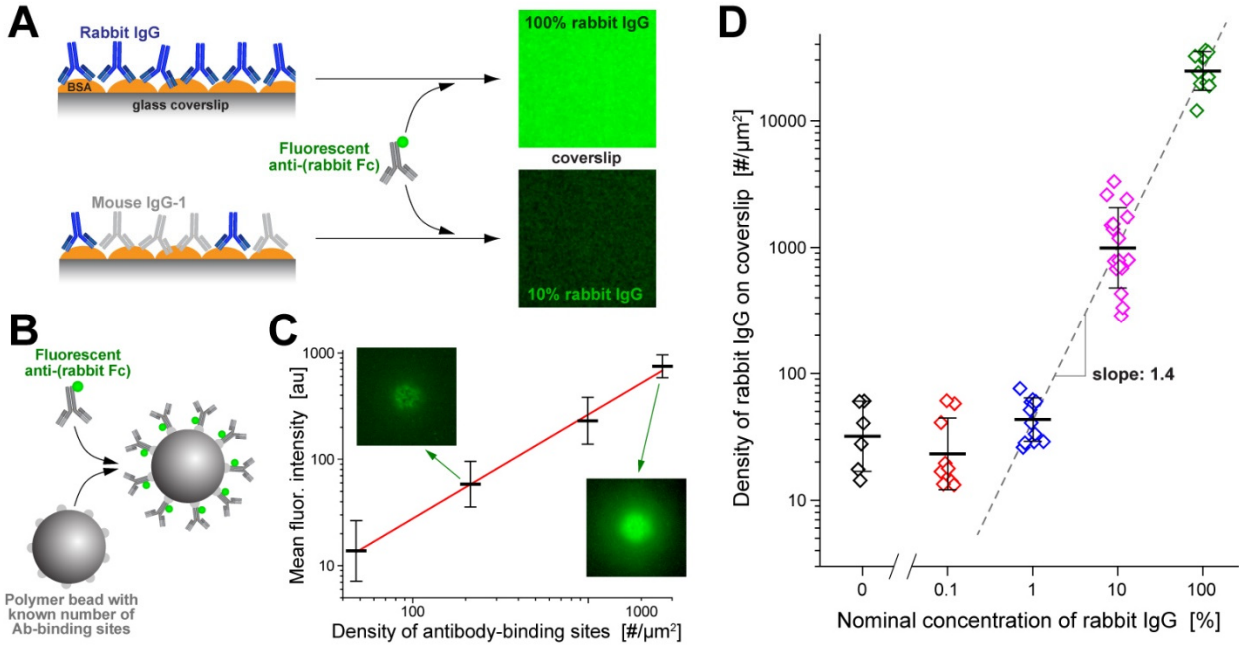

Fig 2.2. Preparation of substrates with controlled rabbit-IgG surface density. (**A**) BSA-coated glass coverslips that had been incubated with various ratios of rabbit and mouse anti-BSA antibodies were labeled with green-fluorescent secondary antibodies and then imaged on a confocal microscope. (**B**) Standard beads with known numbers of antibody-binding sites were saturated with the same fluorescent secondary antibody as used in (A). (**C**) The fluorescence intensity at the underside of the coated beads was measured with the same confocal-microscope settings as used in (A). (For a more detailed explanation see Fig 2.1.) The results, along with a straight-line fit (*red line*), are presented as a function of the known density of antibody-binding sites in a log-log plot. Error bars denote the geometric standard deviation. Examples of confocal bead images are included. (**D**) The calibration curve of (C) was used to convert the measured fluorescence intensities of labeled coverslips into the rabbit-IgG density. The geometric mean values (with error bars denoting geometric standard deviation) of the IgG density are plotted as a function of the concentration of rabbit IgG used in the incubation buffer. The result of a linear fit (*dashed line*) to the portion of the data obtained at IgG concentrations of 1% or higher is included.

These measurements confirmed that our method to functionalize coverslips resulted in a reproducible, broad spectrum of controlled rabbit-IgG densities. They also revealed that the relationship between the rabbit-IgG concentration in the incubation buffer—denoted as the "nominal" rabbit IgG concentration throughout this paper—and the actual surface density of rabbit IgG on coverslips was nonlinear (Fig 2.2C), indicating that the rabbit and mouse IgGs indeed had different affinities for BSA. Fitting a mathematical model of competitive binding to

these data allowed us to estimate that the effective affinity of the used polyclonal rabbit antibody was about 0.4 times that of the monoclonal mouse IgG. The measured surface densities of rabbit IgG ranged from below our detection limit (at 0.1% nominal rabbit-IgG concentration where the surface density was indistinguishable from our negative control) to a maximum density of ~25,000 rabbit-IgG molecules per μm^2 (at 100% nominal rabbit-IgG concentration). Assuming a uniform distribution of bound IgG molecules, the maximum surface density corresponded to an area of roughly 40 nm^2 occupied by each rabbit IgG, consistent with a dense, essentially contiguous layer of IgG coating the coverslips.

Cells are more likely to spread on higher densities of IgG

We used an IgG-coated coverslip as the bottom of our assembled experiment chamber (Fig 2.3A,B). A plastic insert with funnel-shaped vertical thru holes served as the chamber's top (Fig 2.3A). The chamber was filled with Hanks' balanced salt solution supplemented with 2% human serum albumin and placed on an inverted research microscope set up for epi-illumination. This design allowed us to introduce small volumes of a suspension of isolated human neutrophils at non-overlapping locations through the chamber ceiling. Each deposited cell population dispersed to some extent by diffusion while sinking to the chamber bottom. The cells settled onto the functionalized coverslip within ~5 minutes, usually without piling into clusters.

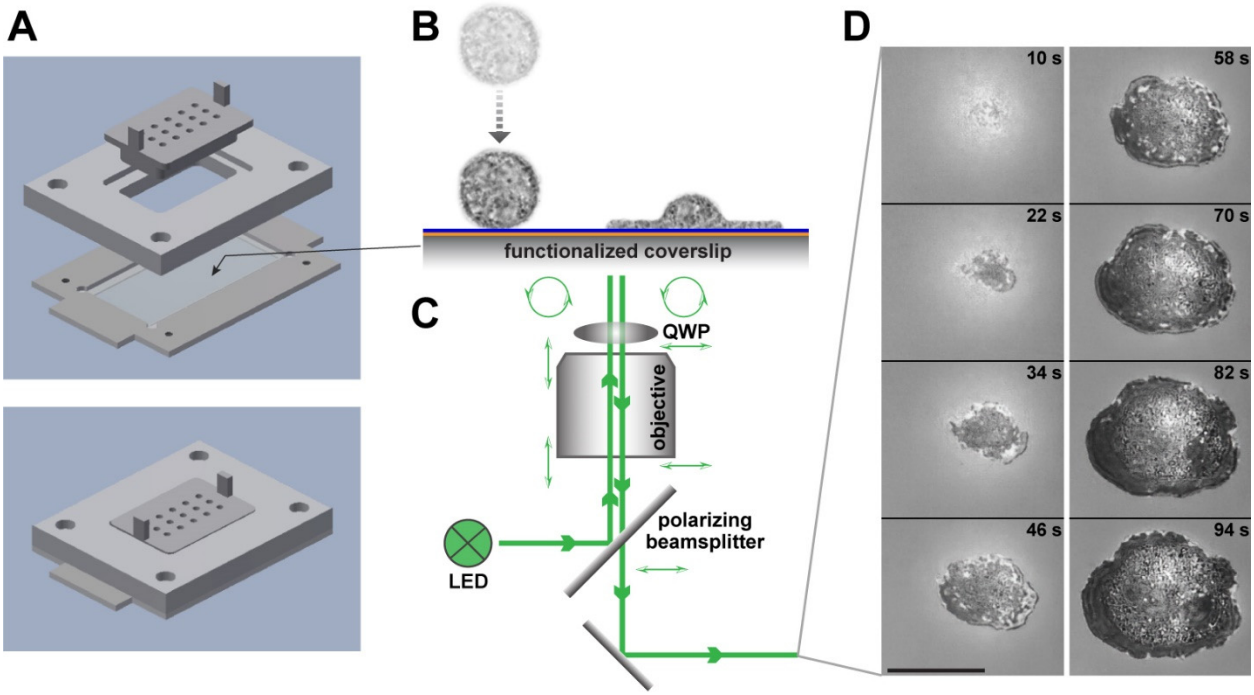

Fig 2.3. Illustration of a frustrated phagocytic spreading experiment. (**A**) Parts and assembly of the experiment chamber. (**B**) After settling onto the functionalized coverslip, initially passive, round cells recognize the deposited antibodies and spread along the surface. (**C**) Reflection interference contrast microscopy allows us to visualize the cell-substrate contact area label-free at high resolution. The combination of polarizing beamsplitter and quarter-wave plate (QWP) ensures that the light components reflected off the coverslip top surface and the cell are the dominant contributions to the recorded interference pattern. (**D**) Example snapshots from a series of recorded video images of the dark cell-substrate contact area. Timestamps are included. The scale bar denotes 10 μm.

We imaged the cells using reflection interference contrast microscopy (RICM, Fig 2.3C,D). The interference patterns produced by RICM markedly enhanced the visibility of contact regions between the primary light-reflecting interface—the top surface of the coverslip—and the underside of reflective objects resting on this surface. Regions of direct cell-substrate contact generally appeared as clearly outlined, distinctive dark patches. It is important to bear in mind though that light-reflecting structures inside a cell, such as granules, can produce brighter spots within the dark contact region that could be misinterpreted as areas where part of the cell has detached from the substrate. Close inspection of the interference patterns revealed that in our

experiments, contiguous contact regions did not appear to contain local areas of cell-substrate separation.

Contact with the substrate caused a fraction of the cells to start spreading either immediately or after some lag time. Despite the mixed response of the cells in a given population—reflecting cell-to-cell variation typical for the behavior of primary human immune cells—we found that the overall proportion of spreading to non-spreading cells strongly depended on the density of rabbit IgG coating the coverslip. We quantified the cells' commitment to spreading on a given surface in terms of the "spreading probability", i.e., the ratio between the number of spreading cells and the total number of observed cells. We consistently evaluated this ratio 30 minutes after depositing the cells, defining "spreading cells" as those cells whose cell-substrate contact area had reached at least 100 μm^2 at this time.

The measured spreading probabilities ranged from 0.16 on the lowest density of surface-bound rabbit IgG to about 0.85 on the highest density (Fig 2.4). The result for the lowest density was not significantly different from the spreading probability on substrates presenting pure mouse IgG-1 (negative control). While this result may be attributed in part to spurious recognition of mouse IgG-1 by human neutrophils, it also highlights that neutrophil populations almost always contain cells that can be activated by non-specific interactions with otherwise non-stimulatory target surfaces. On the other hand, almost all cells spread on substrates coated with high-density, 100% rabbit IgG, confirming that antibody-coated targets generally draw a vigorous response by human neutrophils.

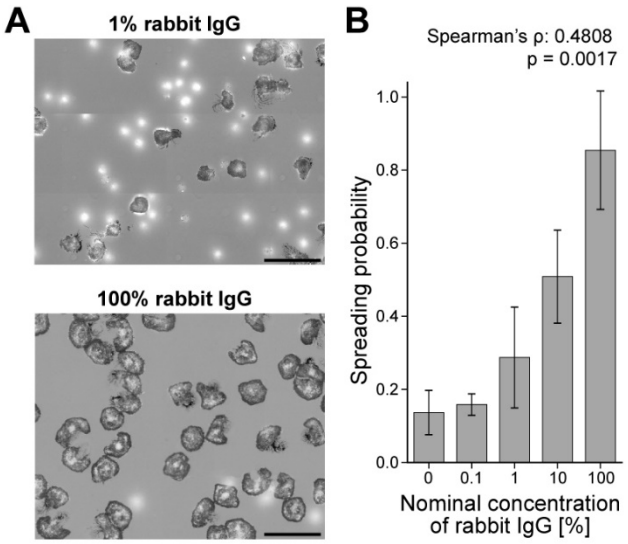

Fig 2.4. Dependence of the spreading probability on the surface density of IgG. (**A**) At low surface densities of rabbit IgG, the majority of deposited cells do not spread and appear as bright, out-of-focus spots in our RICM images (*top panel*). In contrast, almost all cells spread on surfaces coated with the highest density of rabbit IgG (*bottom panel*). Scale bars denote 50 μm. (**B**) The spreading probability depends strongly on the nominal concentration of rabbit IgG, confirming that the observed cell response is IgG-specific. Spearman's rank correlation coefficient ρ is reported with the associated *p*-value for the null hypothesis $\rho = 0$.

We limit our remaining analysis to spreading neutrophils. Thus, when interpreting the following results, it is important to bear in mind that they were obtained with selected subpopulations of cells, and that the fraction of cells making up each subpopulation depended on the cell response to a particular surface density of rabbit IgG.

The cell-substrate contact region of spreading cells is essentially radially symmetric

After settling on the bottom coverslip, individual neutrophils typically formed one or two initial attachment spots with the IgG-coated substrate. In cases were more than one spot was visible, the growing spots quickly merged into a single, contiguous region of cell-substrate contact. Subsequently, the contact region of spreading neutrophils generally had a roughly circular shape that expanded in a radially symmetric manner, as expected for phagocytic spreading (Fig 2.5). It typically took neutrophils only about 2 minutes from the start of spreading to form contact footprints with diameters as large as 20 μm.

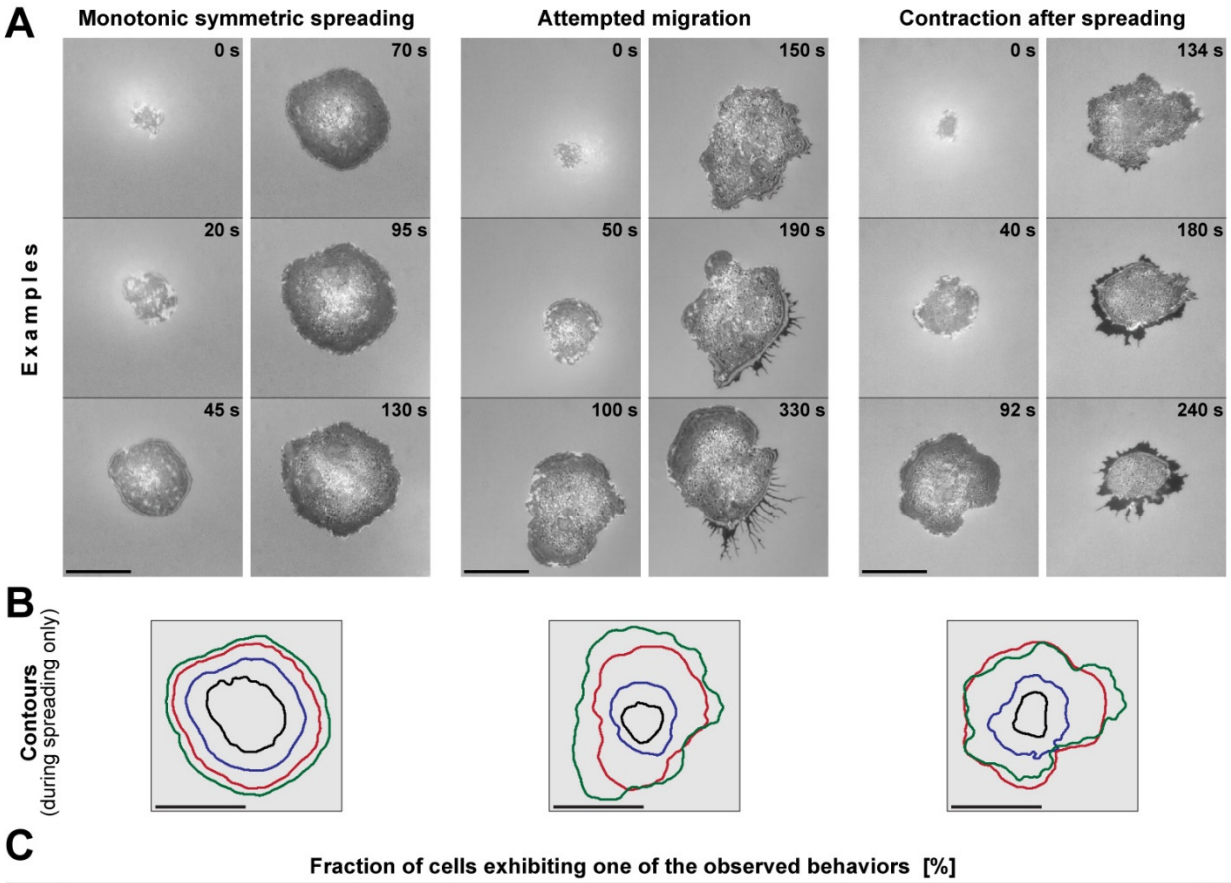

Fraction of cells exhibiting one of the observed behaviors [%]

% IgG	Monotonic symmetric spreading	Attempted migration	Contraction after spreading	*N*
0.1	5.9	76.5	17.6	17
1	0.0	100.0	0.0	7
10	24.0	68.0	8.0	25
100	66.7	33.3	0.0	21

Fig 2.5. Overview of the human neutrophil response to IgG-coated surfaces. (**A**) The first four snapshots of each video sequence illustrate the common morphology of the cell footprint observed during the outward-spreading phase of almost all cells. In contrast, three qualitatively distinct types of post-spreading cell behavior were observed, as illustrated in the last two snapshots of each video sequence. Time stamps are included. Scale bars denote 10 μm. (**B**) Contours of the cell footprint of the first four images of the respective video sequences of (A) demonstrate the roughly symmetric cell morphology during spreading. Scale bars denote 10 μm. (**C**) The table reports the fractions of cells that exhibit one of the three types of post-spreading behavior for each of the tested IgG concentrations. On low densities of IgG, the majority of cells attempted to migrate after reaching a maximum cell-substrate contact area. In contrast, on high IgG densities the majority of cells remained in place and exhibited little further shape changes.

After the contact area reached an apparent plateau, neutrophils exhibited a spectrum of different behaviors. Some remained in place but continued to modify the cell-substrate contact region, gradually expanding or contracting it, or altering its shape while leaving its net area essentially unchanged. Other cells appeared to adopt a more migratory phenotype, attempting to

crawl away from the original location of spreading. Common to most post-spreading behaviors was the formation of trailing membrane extrusions at retracting cell regions. These structures connected the main cell body to focal cell-substrate adhesion sites from which the moving cell often was unable to detach (Fig 2.5). We have not attempted to analyze this highly variable post-spreading behavior beyond a coarse empirical classification (Fig 2.5), demonstrating that cells spreading on higher densities of IgG were less likely to try to leave their original spot of spreading (Fig 2.5C).

Density of IgG does not affect spreading speed but weakly correlates with extent of spreading

Our quantitative comparison of neutrophils spreading on different densities of IgG is based on the analysis of image sequences recorded at intervals of 2 s. We semi-automatically traced the outline of the cell footprint in each image and stored the resulting polygons of cell peripheries (Fig 2.6A). Our primary quantity of interest was the area circumscribed by these polygons, i.e., the cell-substrate contact area. Plots of the contact area as a function of time revealed a comparatively slow, brief initial spreading phase, followed by a roughly linear expansion of the contact footprint, and eventually, a gradual approach to a plateau of maximum contact area (Fig 2.6A-C).

We define the speed of spreading as the value of the steepest slope of a given contact-area-versus-time graph. We used sigmoidal or linear fits to such curves to determine the spreading speeds in suitable experiments. Remarkably, the average spreading speeds, measured over a 1000-fold range of nominal IgG concentration, were all close to 3 $\mu m^2/s$, exhibiting no significant differences on different IgG densities (Fig 2.6D).

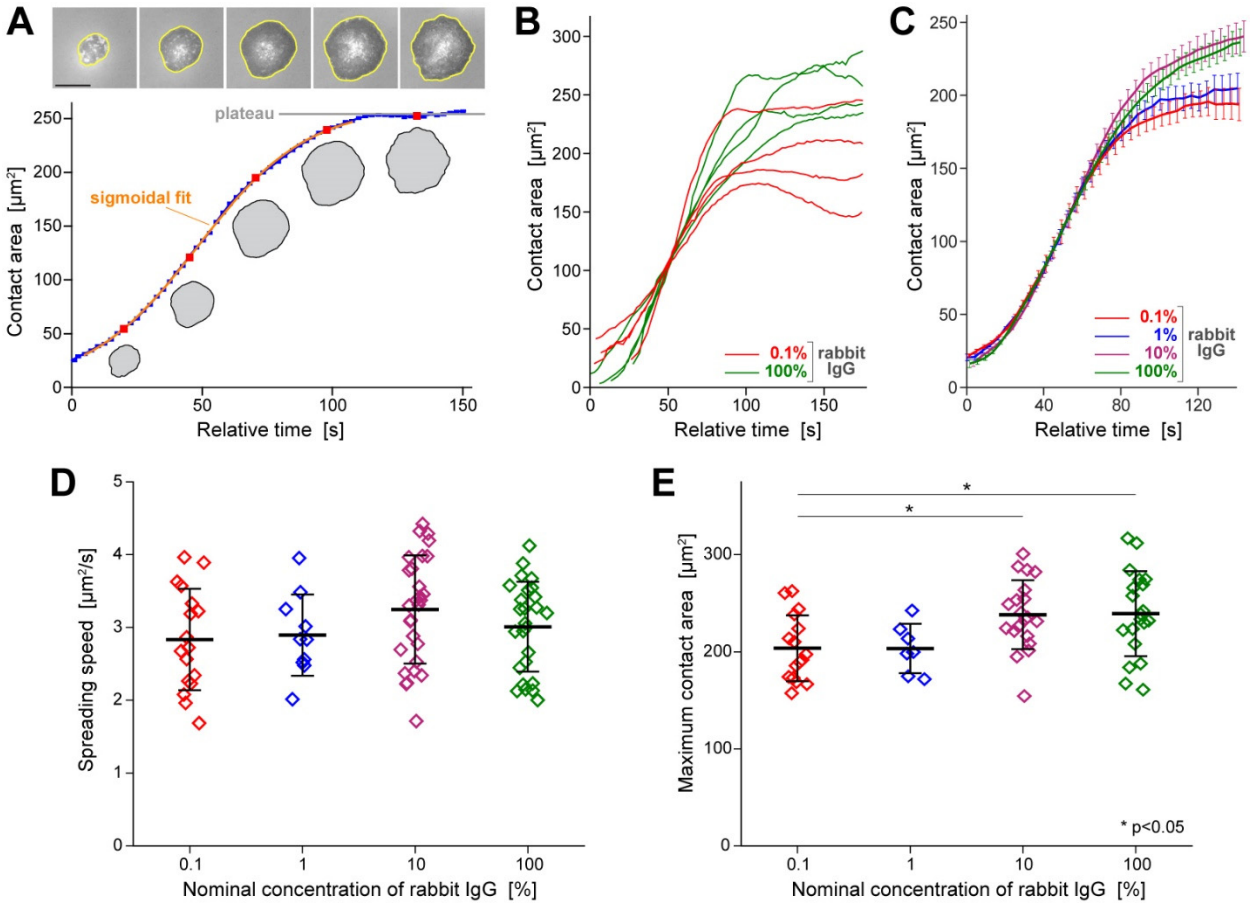

Fig 2.6. Quantitative analysis of the cell-substrate contact area of spreading cells. (**A**) The contact area is determined from a polygonal trace of the circumference of each cell footprint (*yellow polygons* in the examples included at the top; scale bar denotes 10 µm). A suitable fit to the time-dependent contact area yields the (maximum) spreading speed. The plateau value of the contact-area curves provides the maximum contact area. (**B**) Representative examples of contact-area-versus-time curves measured on the lowest (*red*) and highest (*green*) IgG densities illustrate the variability of the dynamical behavior of the cell footprint. (**C**) Average curves of all suitable area-versus-time measurements obtained for each tested rabbit-IgG density expose a largely conserved spreading speed. On the other hand, the maximum contact area appears to reach greater values on high IgG densities. Error bars denote standard errors. (**D**) The summary of all spreading speeds measured over three orders of magnitude of the IgG concentration confirms that the spreading speed is independent of the surface density of IgG. (**E**) The summary of maximum contact areas reveals a small but significant increase of the contact area at high densities of IgG. Error bars in (D) and (E) denote standard deviation.

The similarity in neutrophil behavior during the rapid-spreading phase also was evident in example curves measured for cells spreading on 0.1% versus 100% rabbit IgG (Fig 2.6B). On the other hand, the collection of graphs exposed an apparent difference between the maximum contact areas occupied by cells spreading on these two IgG densities. Most cells spreading on 100% IgG reached contact areas in the range of 200-300 µm^2, whereas on the substrates coated

with the lowest IgG density (0.1%), the maximum contact area tended to lie in the range of 150-250 μm^2. The statistical analysis of all measurements confirmed that the mean maximum contact areas on surfaces coated with 10% or 100% IgG were indeed significantly larger than those on 0.1% IgG (Fig 2.6E).

Recalling that originally spherical cells (with diameter D_0) must increase their apparent surface area when spreading on a substrate, it is instructive to convert the measured area of cell-substrate contact footprints into estimates of the overall cell-surface area (A) required to accommodate such deformations. Our conversion assumes that the cell volume remains constant during spreading, and that the cell-substrate contact region is circular, denoting its diameter by D_c. Furthermore, we approximate the shape of the upper, free surface of the spread cell as a spherical cap, which is the geometry with the smallest possible surface area for the given volume and a circular contact footprint. For this simplified geometry, one can calculate the ratio between the final area A and the initial cell-surface area $A_0=\pi D_0^2$ using the following prescription

$$\frac{A}{A_0}=\frac{1}{4}\left(\frac{{x_c}^4}{q}+q\right) \qquad \text{where} \qquad x_c \equiv \frac{D_c}{D_0} \quad \text{and} \quad q \equiv \left(\sqrt{{x_c}^6+16}-4\right)^{2/3} \tag{2.5}$$

The diameter of most non-adherent, resting human neutrophils lies in the range of 8.5-9 μm. With the choice of D_0 = 8.75 μm, Eq (2.5) predicts that a typical neutrophil will need to expand its surface area to ~210% of its initial area in order to form a contact footprint whose diameter is twice as large as the cell's resting diameter (where $x_c = 2$ and D_c = 17.5 μm).

The average of the 10 largest cell-substrate contact areas measured in our experiments is 359 μm^2, corresponding to a typical footprint diameter of D_c = 21.4 μm. Thus, we estimate that the

most-spread neutrophils have expanded their apparent surface area to about 303% of their resting area during our frustrated-phagocytosis experiments, in agreement with previous findings [7, 9, 38, 39].

Higher IgG density results in more uniform, concentric spreading

The results of the previous section provide compelling support for the protrusive-zipper hypothesis. A detailed analysis of additional features of the cell behavior is likely to produce further insight into the fundamental mechanisms of phagocytic spreading. We next examined how the IgG density affects the roundness and type of motion of the cell footprint during spreading.

We assessed the roundness of the cell-substrate contact region in terms of the ratio of the radii of two circles defined by the outline of this region, i.e., the largest inscribed circle and the smallest circumscribed circle (Fig 2.7A). The value of this roundness measure equals 1 for circular contours and is smaller otherwise, with lower values corresponding to less round contours. For each spreading cell, we measured the roundness of individual contours within the phase of fastest contact-area growth (where the spreading speed was greater than 0.4 $\mu m^2/s$), then applied a moving average filter with a window size of 8 s and finally determined the maximum of these averages. This approach yielded roundness values in the range of roughly 0.6-0.9 that exhibited no significant differences between surfaces coated with different densities of IgG (Fig 2.7B). Thus, the cell contours generally were characterized by a moderate roundness that was independent of the IgG density, indicating that phagocytic spreading proceeded in a more or less uniform fashion on all tested surfaces.

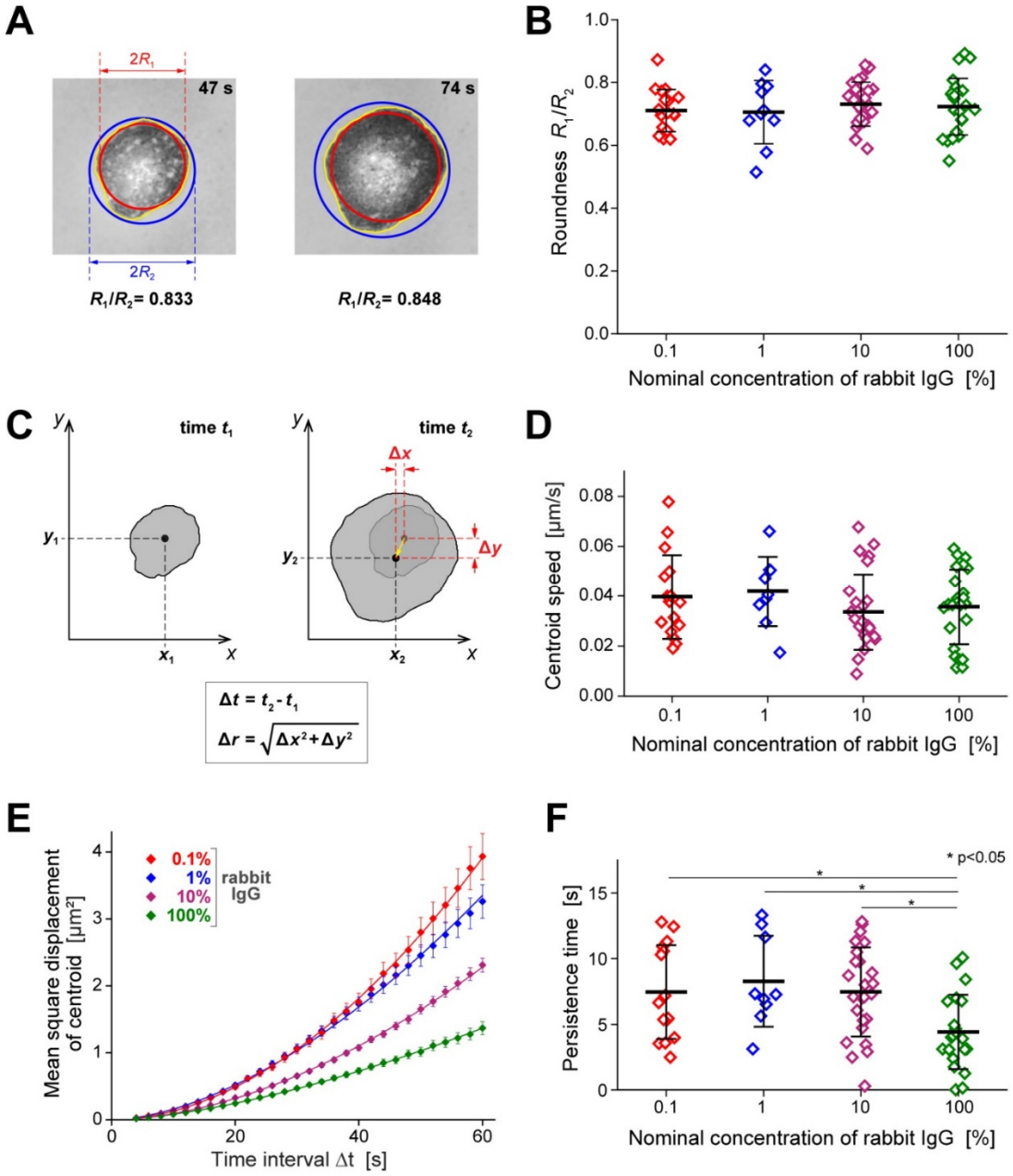

Fig 2.7. Roundness and type of motion of the footprints of spreading cells. (**A**) The roundness of the cell-substrate contact region was assessed in terms of the ratio between the radii of the largest inscribed (*red*) and the smallest circumscribed (*blue*) circles, as illustrated with two examples. (**B**) The summary of all roundness measurements reveals no significant differences on surfaces coated with different IgG densities. (**C**) Illustration of our measurement of the displacement Δr of the centroid of the cell footprint during the time interval Δt. (**D**) The summary of all centroid-speed measurements reveals no significant differences on surfaces coated with different IgG densities. (**E**) The mean square displacements of the centroid as a function of Δt (averaged over all suitable measurements obtained for each tested rabbit-IgG density; error bars denote standard errors) allow us to quantify the degree of randomness of the centroid motion. The included solid lines show power-law fits of the form $y^{\circ}=^{\circ}ax^{b}$ to the data. (**F**) The summary of all measured directional persistence times reveals that on the highest density of IgG, the cell footprint tended to move in roughly the same direction for significantly shorter times than on lower IgG densities. For more details see the text.

The roundness measure does not capture unambiguous information about possible lateral displacements of the cell footprint. To quantify the latter, we analyzed the positions of the centroid of the cell-substrate contact region of spreading cells in suitable video images. We defined the centroid displacement Δr as the Euclidean distance by which the centroid position moved during a given time interval Δt (Fig 2.7C). We used these measurements to estimate the instantaneous velocity of the centroid motion in terms of the ratio $\Delta r/\Delta t$ evaluated for successively recorded centroid positions. For each spreading cell, we then averaged the instantaneous values over the active spreading phase. Most of the resulting average centroid speeds were in the range of 0.01-0.06 μm/s and exhibited no significant differences between substrates coated with different IgG densities (Fig 2.7D).

In addition to evaluating the centroid speed, we also used the measured centroid positions to assess the type of motion of the cell footprint. Now choosing Δt-values in the range from 4 s to 60 s, we averaged the squared centroid displacements of a given cell over all pairs of video frames whose recording times differed by Δt. We then calculated the averages of these mean square displacements as a function of Δt for the whole population of cells spreading on a given substrate (Fig 2.7E). Power-law fits of the form $y°=°ax^b$ to plots of these mean square displacements as a function of Δt allow for a rough classification of the type of centroid motion. An exponent of $b°=°1$ of such a fit implies a random motion with Gaussian-distributed individual displacements, as is typical, for example, for diffusion. If the exponent approaches 2, the motion generally is interpreted as more migratory. The exponent of the power-law fit to the measured mean square centroid displacements was 1.57 on the highest density of IgG, whereas on the lowest IgG density it was 1.86, suggesting that lateral displacements of cells spreading on

the highest IgG density were more random, i.e., the cells were less likely to transiently explore the substrate in a preferred direction.

The lack of a clear correlation between IgG density and centroid speed (Fig 2.7D) contrasted with the observed differences in centroid displacement (Fig 2.7E), suggesting that on some substrates, moving cells changed direction more frequently than on others. We verified this assumption by assessing the directional persistence of centroid displacements in terms of the decay of the time-dependent autocorrelation function of the tangents of the centroid trajectory [49]. The resulting "directional persistence time" (Materials and Methods) exposes for how long a cell footprint continues to move in roughly the same direction. The measured persistence times generally were small and exhibited a large spread; however, they were significantly shorter (~4.4 s on average) on coverslips coated with the highest density of IgG than on lower IgG densities (~7.5-8.3 s) (Fig 2.7F). The averages of the closely related "directional persistence distances" (product of centroid speed and persistence time) traversed in a preferred direction were small, falling in the overall range of 0.16-0.36 μm, and exhibiting a significant difference between substrates coated with nominal IgG concentrations of 100% and 1% (data not shown). In summary, transient lateral polarization and directional movement of the cells, while generally unlikely, indeed met with stronger resistance on higher densities of IgG.

This analysis confirmed that the observed type of spreading motion was specific to the phagocytic ligand IgG. Overall, cells spreading on IgG tended to expand the contact region in a uniform, concentric manner without extending substantial exploratory protrusions in preferred directions. As shown earlier (Fig 2.5), this behavior may change once the area of the cell-substrate contact region has reached an apparent plateau.

Computer simulations reinforce mechanistic insights gained from experiments

The comparison of experimental results with theoretical predictions is an essential approach to test mechanistic hypotheses and decide whether observed correlations are coincidental or causative. In Chapter 3, we have translated different hypotheses about the driving force of phagocytic spreading into mathematical models and examined the mechanical ingredients that such models require to reproduce the cellular behavior. This section provides a broadly accessible summary of our comparison between the measured dynamics of the growth of the cell-substrate contact area and theoretical predictions based on the Brownian zipper and the protrusive zipper models, respectively.

Details of our mathematical models are provided in Chapter 3. In short, we consider an immune cell as an axisymmetric body with uniform surface tension that is filled with a highly viscous, incompressible fluid [53, 54]. The model incorporates adhesive interactions between the cell surface and a flat, rigid substrate in terms of a short-range attractive force that acts to pull the cell onto the substrate in an irreversible manner. This basic version of the model captures the essential assumptions of the Brownian zipper hypothesis.

To introduce active cellular protrusion into this framework, we postulate that fresh contact between the substrate and the cell surface results in a transient, outward-pushing force local to the leading edge of the cell-substrate contact region. We do not attempt to model the microscopic origin of this protrusive force, which would have to account for receptor-induced signaling, spatiotemporal redistribution of messenger molecules, translation of biochemical cues into mechanical stresses, etc. Instead, our semi-empirical approach lumps these highly complex processes into the rationale that receptor activation due to fresh cell-substrate contact ultimately causes the protrusive force. We also assume that the magnitude of protrusion decays as a

function of the time elapsed after the most recent receptor-ligand binding event. One objective of our theoretical study is to establish what distribution and magnitude of mechanical stresses can account for the experimental results, and whether the predicted stresses are physically realistic and biologically plausible. The model version that includes the protrusive force represents the protrusive zipper hypothesis.

As reasoned earlier, adhesion-driven, passive spreading, which forms the core of the Brownian zipper hypothesis, should result in a stronger correlation between the IgG density and the spreading speed than active, primarily protrusion-driven spreading. To verify this common-sense expectation and place it on sound quantitative grounds, we simulated the dependence of the spreading speed on the IgG density using both versions of our mathematical model (Fig 2.8). The simulations indeed revealed a dramatic difference in predicted cell-spreading behavior between these two models. For realistically chosen parameter values, the Brownian zipper model predicts a strong dependence of the cell spreading speed on the density of IgG binding sites, and the spreading speeds on low IgG densities are predicted to be much slower than observed experimentally. In contrast, the spreading speed predicted by the protrusive zipper model hardly changes over a 1000-fold range of nominal IgG concentrations and is similar to experimental results. Comparison of the predictions of Fig 2.8D,E with the measurements shown in Fig 2.6C,D clearly supports the conclusion that the protrusive zipper hypothesis successfully captures the basic mechanisms underlying phagocytic spreading, whereas the Brownian zipper hypothesis does not.

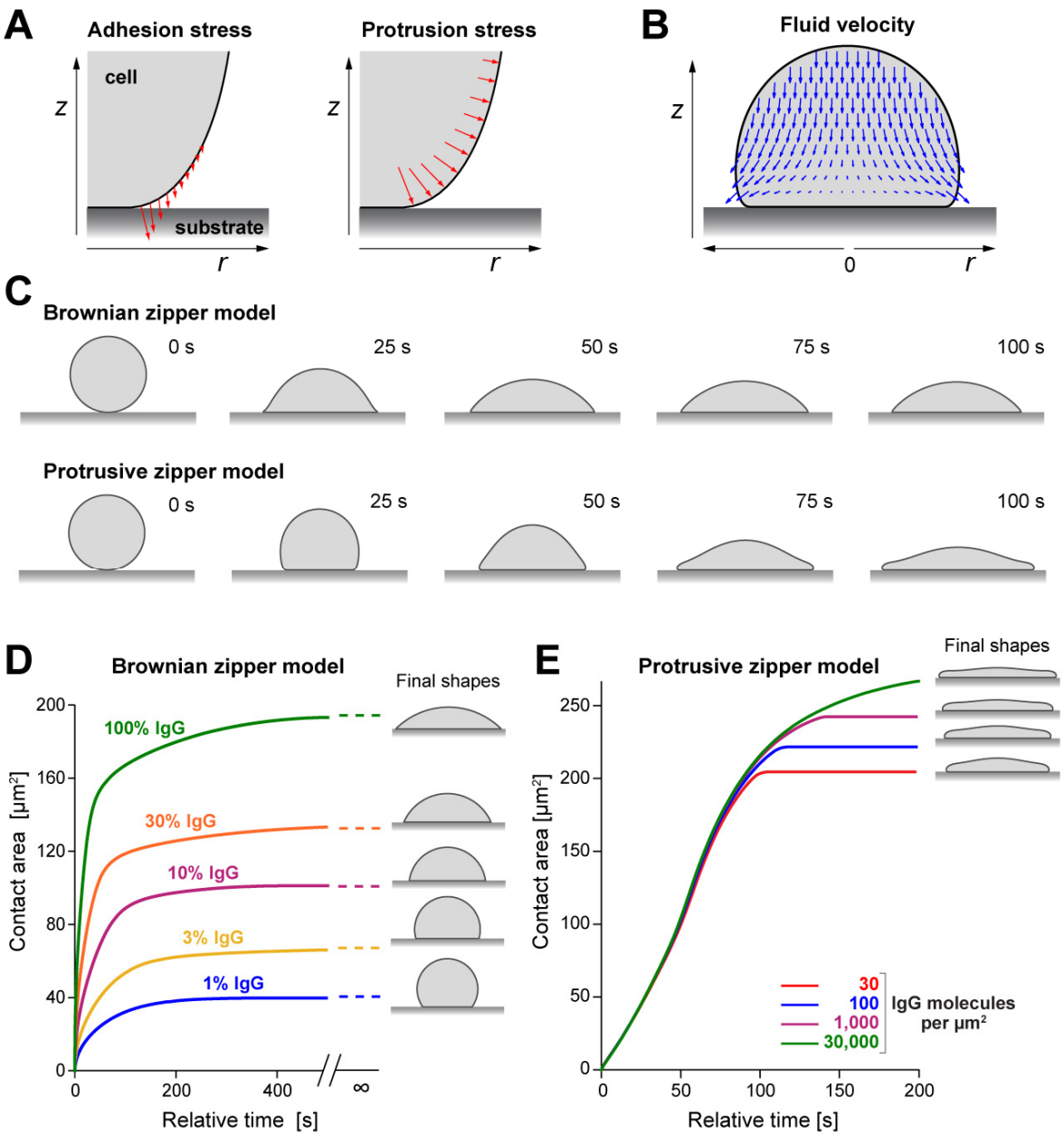

Fig 2.8. Summary of pertinent predictions by two different mechanistic models of cell spreading. (**A**) The models incorporate attractive interactions between the cell surface and the substrate via short-range adhesion stress (*left panel*). The protrusive-zipper model postulates that the cell interior generates protrusion stress local to the leading edge of the spreading cell in a manner that depends on fresh contact between the cell and substrate (*right panel*). (**B**) A snapshot of a computer simulation of a spreading model cell illustrates the motion of the viscous cell interior according to the Stokes equations for creeping flow. (**C**) Time series of cross-sectional shapes of spreading model cells illustrate morphological differences between the predictions of the two considered models. (**D**) The Brownian-zipper model predicts that both the cell-spreading speed as well as the maximum contact area exhibit a strong dependence on the surface density of IgG coating the substrate. The final shapes are predicted to be spherical caps in this case. These predictions fail to reproduce experimental observations such as those presented in Fig 5. (**E**) In agreement with our experimental results (Fig 5C,D), the spreading speeds predicted by the protrusive-zipper model are essentially independent of the IgG density, and the IgG dependence of the maximum contact area is much weaker than in (D).

The dependences of the maximum contact area on the IgG density (Fig 2.8D,E) reveal another difference between the two model versions. Recall that our experiments exposed a significant increase of the maximum contact area at higher IgG densities (Fig 2.6E). However, this increase is much smaller than the large differences between the plateau values of the graphs predicted by the Brownian zipper model (Fig 2.8D). On the other hand, the predictions of the protrusive zipper model again provide a notably better match with our experimental observations (Fig 2.8E).

Discussion and Conclusion

The rapid execution of complex cellular motions is one of the most amazing feats of immune cells, and critical to phagocytosis, cell migration, and other vital processes. However, precise descriptions of such motions and, more importantly, understanding of the underlying mechanisms, remain scarce. The quantitative analysis of frustrated phagocytosis presented in this paper is part of a larger research area that focuses on the biomechanics of cells spreading on surfaces, comprising both experimental work [55-61] as well as theoretical studies [62-69]. Our integrative experimental/theoretical approach expands most previous analyses by quantifying how the ligand density affects the cells' spreading behavior, and to what extent adhesive versus protrusive forces contribute to the cell motion. In conjunction with our theoretical companion paper, this approach has allowed us to resolve controversial mechanistic notions about the spreading behavior of immune cells.

Our experimental strategy has been to expose human neutrophils to target surfaces that presented a range spanning three orders of magnitude in density of deposited IgG. The strong dependence of the cells' spreading probability on the IgG density confirms that the ligation of

Fcγ receptors is the original cause of spreading. It also suggests that a threshold in cell stimulation needs to be reached to induce spreading. The most likely type of stimulating trigger appears to be a minimum number of engaged receptors. Alternatively, the primary stimulus could be the spacing between engaged receptors, in which case their total number might play a lesser role. Our current setup does not allow us to distinguish between these two alternatives. It also is important to bear in mind that the threshold level that triggers spreading can vary considerably from cell to cell, suggesting that it is affected by other factors such as the degree of quiescence of individual neutrophils.

The absence of a significant correlation between the IgG surface density and the spreading speed of the cells is perhaps the most consequential result of our experiments. It provides a counterexample to the notion that spreading might be driven by strong cell-substrate adhesion, thus discrediting the Brownian zipper hypothesis in the case of neutrophils and similar cells. In contrast, the protrusive zipper hypothesis intuitively provides a better explanation of our results. The strongest support for the validity of the latter hypothesis comes from the agreement between computer simulations based on the protrusive zipper model and our experiments performed on different substrates. Our finding agrees well with reports that during isotropic fibroblast spreading, the speed of spreading depended on protrusive stress generated by the actin cytoskeleton [57, 66, 67].

It is worth noting that the spreading speed of macrophage-like cells of the J774 murine cell line on IgG-coated surfaces also was found to be largely independent of the IgG density [45]. Thus, our conclusion that cell spreading is primarily driven by an active protrusive force likely holds for motile immune cells in general. It also agrees with a previously reported “all-or-nothing” signaling response during IgG-mediated phagocytosis by macrophages [70], as well as

with other studies in which macrophages readily consumed particles coated with low densities of IgG [42, 71]. On the other hand, it conflicts with computer simulations that neglected the role of cytoskeleton-driven protrusion and predicted that phagocytosis should proceed most quickly at an optimal ligand density [72].

Our finding that the spreading probability, but not the spreading speed, depends on the IgG density reveals that beyond the stimulus threshold that causes a cell to commit to spreading, further strengthening of the stimulus appears to have little effect on the mechanical cell response. In other words, the spreading speed becomes decoupled from the stimulus strength at some point. This raises the interesting question at which step in the sequence of processes leading from receptor ligation to cell movement the decoupling occurs. Does receptor-induced signaling reach a limiting level beyond which the activation of additional receptors is ignored? Is there a bottleneck built into the redistribution of messenger molecules? Or are the cell's resources to generate additional protrusive force exhausted? Answers to questions like these, although beyond the scope of this study, are an essential part of a comprehensive understanding of vital immune-cell functions.

Our analyses of the geometry and type of motion of the contact footprint, as well as the post-spreading behavior of neutrophils, round out this study, allowing us to paint a detailed picture of the events following cell contact with an IgG-coated surface. After reaching the surface, an initially quiescent cell may undergo detectable Brownian motion and/or be dragged along the surface by convection until cell-substrate adhesion causes its arrest. Cell arrest is usually faster—often immediate—on surfaces coated with higher densities of IgG, suggesting that it is mediated by specific bonds between immobilized Fc domains and Fcγ receptors of the cell. It is

worth bearing in mind though that neutrophils can arrest even on negative control surfaces through nonspecific interactions.

Ligation of Fcγ receptors ultimately leads to cell activation and spreading. Many intermediate mechanistic details of this response remain uncertain, but our results strongly suggest that an active protrusive force generated by the cell local to the periphery of the contact footprint is the main driver of spreading. There is ample qualitative evidence supporting the cytoskeleton's key role in the generation of this force through local actin polymerization and cross-linking, both generally [73-75] as well as in the specific context of phagocytosis [5, 14, 46, 76]. For example, F-actin accumulation at the front of the phagocytic cup has been shown to be correlated with force production during macrophage phagocytosis [77]. Novel techniques to measure phagocytic forces with high resolution hold great promise for illuminating the detailed mechanisms linking actin remodeling to force generation [78, 79]. It seems plausible to ascribe the local character of this cytoskeletal remodeling to localized signaling triggered by fresh cell-substrate contact.

Although cell-substrate adhesion is not the primary cause of spreading, it still plays a critical role by securing and stabilizing fresh contact regions, thus aiding further cell motion parallel to the surface. A subtle detail in the cell's control of its motion is the coordination of structural linkages between the actin cytoskeleton and the plasma membrane. Weakening of such linkages at the protruding front is likely to facilitate local forward displacements of the cell surface. A molecular example of such behavior is the calcium-dependent disruption of FERM-mediated linkages by calpain [30, 80, 81]. In contrast, in regions of established cell-substrate contact, strengthening of membrane-cytoskeleton linkages prevents the main cell body from being lifted away from the surface, while also providing bracing support to the protrusive motion along the

surface [11, 14, 19, 82]. Several molecular players that either link integrins to the cytoskeleton (e.g., talin, paxillin) or directly link the membrane to the cytoskeleton (e.g., myosin I, ezrin) have recently been shown to colocalize with the neutrophil or macrophage phagocytic cup and facilitate directional force generation [14, 19, 46, 83].

Once the cell commits to spreading, it generally expands its contact footprint in an isotropic, essentially concentric fashion, resulting in a more or less round contact region throughout the spreading phase. This behavior is fundamentally different from migratory cell motions like chemotaxis, which require sustained cell polarization not only in terms of morphology and mechanics, but also intracellular signaling. It seems logical to attribute this difference to the nature of the stimulus, which is uniform in one case and localized in the other. However, especially our substrates coated with low densities of IgG are unlikely to present perfectly uniform IgG layers. Yet even on these substrates, the cell roundness was unaffected by the IgG density, providing further support to the "all-or-nothing" notion of phagocytic spreading. This result also makes sense biologically, considering that a phagocyte should be able to engulf pathogens that are not uniformly coated with antibodies. Finally, our conclusion that phagocytic spreading tends to proceed in a symmetric fashion is particularly impactful for theoretical investigations, as it reinforces the validity of predictions made by mathematical models of phagocytosis that assume an axisymmetric cell-target configuration.

That said, we did observe larger centroid displacements and a significantly higher directional persistence of cells spreading on lower densities of IgG, in agreement with observations of neutrophils spreading on different densities of fibronectin or BSA [84] as well as other cell types, for instance, endothelial cells that spread more unevenly on lower densities of Arg-Gly-Asp

(RGD) [58]. This behavior appears to resemble haptokinesis, albeit on a very small scale considering that the overall cell displacements rarely exceeded 1 μm.

Our picture of phagocytic spreading would be incomplete without considering its limits. What determines the maximum extent of spreading? Key to answering this question is the mechanical resistance to expansion of the apparent cell surface area, i.e., the cortical tension. This ever-present tension maintains the spherical shape of quiescent immune cells, and it rises as the cell surface area increases during shape changes [9, 38, 85, 86]. Geometrical arguments similar to those leading to Eq (2.5) show that the apparent cell surface area grows monotonically as the cell-substrate contact region increases. Thus, the protrusive force generated by the cytoskeleton meets with increasing mechanical resistance during cell spreading. The magnitude of the outward pushing force is not unlimited, and neither is the amount of material that can be recruited to the cell surface to enable its further growth. Either one of these closely related constraints will stall spreading. Remarkably, our estimate of the maximum apparent cell surface area produced during frustrated phagocytic spreading agrees well with values measured previously in various types of experiments [7, 9, 38, 39].

Even before the cell-substrate contact region reaches its maximum extent, the rising resistance due to the cortical tension slows spreading. A higher substrate density of adhesive IgG ligands is expected to aid further spreading at this stage, because the distance over which the protruding cell membrane needs to be displaced before reaching the next adhesion site is smaller. The observed dependence of the maximum extent of spreading on the IgG density (Fig 5E) confirms that this is indeed the case. Yet, this dependence is much less pronounced than predicted by the Brownian zipper model. This finding underlines the role of adhesion as an important facilitator of spreading, regulating the cell's commitment to spreading, the maximum

contact area, and the directional movement of the contact region. However, the results of this and other studies leave little doubt that active cellular protrusion rather than adhesion is the primary driving force of phagocytic spreading.

Declaration of Interests

The authors declare no competing interests.

Acknowledgements

We thank Dr Soichiro Yamada for his help with confocal microscopy, Dr Daniel Kovari for providing MATLAB code for the analysis of the cell-substrate contact regions, and Dr Robert Guy for many helpful conversations regarding our computational model of cell spreading.

This work was supported by grant R01 GM098060 from the National Institutes of Health, USA, National Science Foundation Graduate Research Fellowship, award number 1650042, and a graduate student research award from the ARCS Foundation.

Chapter 3: Integrative experimental/computational approach establishes active cellular protrusion as the primary driving force of phagocytic spreading by immune cells

Reproduced with permission from E.A. Francis and V. Heinrich.

Manuscript currently in revision as of July 2022. Preprint available on BioRxiv [87].

Abstract

The dynamic interplay between cell adhesion and protrusion is a critical determinant of many forms of cell motility. When modeling cell spreading on adhesive surfaces, traditional mathematical treatments often consider passive cell adhesion as the primary, if not exclusive, mechanistic driving force of this cellular motion. To better assess the contribution of active cytoskeletal protrusion to immune-cell spreading during phagocytosis, we here develop a computational framework that allows us to optionally investigate both purely adhesive spreading ("Brownian zipper hypothesis") as well as protrusion-dominated spreading ("protrusive zipper hypothesis"). We model the cell as an axisymmetric body of highly viscous fluid surrounded by a cortex with uniform surface tension and incorporate as potential driving forces of cell spreading an attractive stress due to receptor-ligand binding and an outward normal stress representing cytoskeletal protrusion, both acting on the cell boundary. We leverage various model predictions against the results of a directly related experimental companion study of human neutrophil phagocytic spreading on substrates coated with different densities of antibodies. We find that the concept of adhesion-driven spreading is incompatible with experimental results such as the independence of the cell-spreading speed on the density of immobilized antibodies. In contrast, the protrusive zipper model agrees well with experimental findings and, when adapted to simulate cell spreading on discrete adhesion sites, it also reproduces the observed positive correlation between antibody density and maximum cell-

substrate contact area. Together, our integrative experimental/computational approach shows that phagocytic spreading is driven by cellular protrusion, and that the extent of spreading is limited by the density of adhesion sites.

Introduction

The ability of cells to spread on surfaces is critical to many biological processes, including cell migration, wound healing, and tissue formation. Immune cells are especially adept at rapid spreading; for instance, neutrophils commonly travel up to an order of magnitude faster in motility assays than fibroblasts or endothelial cells [84, 88-91]. Vital immune cell functions, such as firm arrest at the endothelium and phagocytosis of pathogens, rely on this ability. A deeper understanding of the physical mechanisms driving cell spreading is essential for informed pharmaceutical strategies and new therapies targeting immune cells, such as current efforts to enhance phagocytosis for more effective clearance of cancer cells [92, 93].

Many experimental and theoretical studies have sought to unravel the physical principles of cell spreading by analyzing the initial growth of cell contact regions on a flat, adhesive substrate [56, 58, 63, 67]. However, it often remains unclear whether any given type of cell spreading is primarily driven by passive forces due to adhesion or by active protrusive and/or contractile forces generated by the cell. In the simplest model, cell spreading is treated as a purely passive process, similar to a viscous droplet spreading on an adhesive substrate [62, 63, 94]. Alternative models assume that cytoskeleton-driven protrusion determines the rate of cell spreading, neglecting the effective attractive pre-contact force due to ligand-receptor interactions [66, 67, 95].

Here, we aim to illuminate fundamental cell-spreading mechanisms by focusing on the mechanistic driving force of phagocytic spreading. In conventional phagocytosis, an immune cell first adheres to the surface of a target particle such as a bacterium, often by binding to opsonic ligands such as immunoglobulin G (IgG) antibodies. The cell then spreads over the target surface until its membrane closes around the particle. On the other hand, when presented with an excessively large target, the cell is unable to fully engulf the particle and continues to spread until its target-contact area reaches a maximum [8, 45]. Such cases, including phagocytic spreading on flat substrates, are termed frustrated phagocytosis. The relatively simple geometry of a cell undergoing frustrated phagocytic spreading on a flat surface is particularly amenable to theoretical analysis, especially when the cell spreads in an axisymmetric manner. Moreover, it is reasonable to assume that insights generated by integrative experimental/theoretical analyses of cell spreading in this geometry also carry over to other target shapes. Although several recent experimental [41, 96, 97] and theoretical [98] studies have reported variations in the cell response to different target shapes, it seems doubtful that the fundamental mechanisms governing this response depend on the target curvature, except perhaps in extreme cases. The hitherto most successful integrative experimental/computational study of phagocytosis has shown that the same mechanical cell response can account for the observed differences in phagocytosis dynamics during encounters with beads in the size range of 3-11μm [10].

Reflecting the above-mentioned contrasting mechanistic notions about the driving force of generic cell spreading, two hypotheses have been put forward to explain phagocytic spreading, i.e., the “Brownian zipper” and “protrusive zipper” models [13]. Both models concur that fresh contact between the cell membrane and target surface results in a zipper-like adhesive attachment that is essentially irreversible, in agreement with experimental observations [32, 45,

99]. However, regarding the driving force of cellular advancement, the Brownian zipper model postulates that strong adhesion alone is responsible for pulling the cell membrane onto the target surface. In contrast, the protrusive zipper model assumes that an active protrusive force generated by the cytoskeleton is the predominant driver of outward motion of the cell surface, without excluding a possible contribution of adhesive cell-substrate interactions. It is important to bear in mind that our definition of these two models in terms of the driving force of spreading is not the same as the distinction between "passive" and "active zippers" used elsewhere [100]. In contrast, neither of the zipper models defined in [100] included active protrusion but instead implemented an effective adhesion stress as the sole driving force of spreading. Therefore, both zipper models defined in [100] fall into the category of a Brownian zipper as defined here.

We seek to establish which of these hypotheses is more realistic by developing mathematical models of the mechanics of isotropic cell spreading and comparing our theoretical predictions with experimental observations of human neutrophils spreading on flat, IgG-coated surfaces. As reported in detail in Chapter 2, our experimental design allowed us to examine the spreading behavior of neutrophils on surfaces coated with different densities of IgG. Because higher IgG densities correspond to stronger adhesive forces, we reasoned that the Brownian zipper model should predict a much stronger correlation between IgG density and rate of contact-area growth ("spreading speed") than the protrusive zipper model. Here, we use computer simulations of phagocytic spreading to verify this common-sense expectation and further investigate mechanisms governing immune-cell spreading. First, we present the predictions of a Brownian zipper model that realistically implements known insights about the mechanical behavior of human neutrophils. Then, we investigate the protrusive zipper model, including the contribution of adhesive pre-contact interactions to the driving force of spreading. Finally, we also present a

version of the Brownian zipper model that implements the discrete nature of receptor-ligand interactions more realistically than the continuum models introduced earlier. Together, our integrative experimental/theoretical approach establishes that the Brownian zipper model is inconsistent with experimental results, whereas the spreading dynamics predicted by the protrusive zipper model agree well with our experiments.

Results

Model implementation of key biophysical mechanisms of cell spreading

We consider a simple model cell that captures the basic geometrical and mechanical properties of human neutrophils, the most abundant type of white blood cell and one of the prototypes of professional phagocytes. This model cell consists of an axisymmetric, highly viscous fluid body of constant volume that is surrounded by an elastic cortex with uniform tension (Fig 3.1). Termed the "cortical shell, liquid core model", this theoretical concept has successfully reproduced the passive response of human neutrophils to imposed deformations [53, 54]. In the undeformed reference state, the persistent tension of the cortex maintains a spherical cell shape with a typical diameter of 8.5 μm. The nucleus of neutrophils is segmented into two to five lobes [101, 102] and appears to play only a minor role during deformations, lending support to the approximation of the cell interior as a homogeneous fluid. The effective viscosity (μ) of the cytoplasm has been found to be about 200,000 times the viscosity of water at room temperature in passive neutrophils [53, 54], and another ~3-times higher in active neutrophils [103]. It is well known to increase during phagocytosis [10, 11, 104]. We use a viscosity value of $\mu = 200$ Pa-s in our passive Brownian zipper model and a value of $\mu = 1660$ Pa-s in our active protrusive

zipper model. The original assumption of a constant cortical tension [54] was later found to be approximately true only for small deformations [105]. The revised relationship between tension (τ) and cell surface area (A_{cell}) was shown to be roughly biphasic [9]. Assuming an isotropic and uniform tension, our simulations incorporate a smoothed version of the following biphasic constitutive relationship, in overall agreement with a number of quantitative experimental studies [9, 10, 86] (plotted in Appendix C):

$$\tau(A_{cell}) = \begin{cases} 0.01 + 0.16\left(\frac{A_{cell}}{A_{cell,0}} - 1\right)\frac{\text{mN}}{\text{m}} & \text{if} \quad \frac{A_{cell}}{A_{cell,0}} \le 1.26 \\ 0.0516 + 0.545\left(\frac{A_{cell}}{A_{cell,0}} - 1.26\right)\frac{\text{mN}}{\text{m}} & \text{if} \quad \frac{A_{cell}}{A_{cell,0}} > 1.26 \end{cases} \tag{3.1}$$

where $A_{cell,0}$ is the surface area of the resting neutrophil before spreading. We also tested alternative versions of this constitutive relationship in Appendix C and found that they do not qualitatively alter the results of our simulations.

Movements of the viscous cytoplasm generally do not exceed velocities of 1 μm/s during phagocytic cell spreading and are characterized by low Reynolds numbers. Such movements are well described by the Stokes equations for creeping flow:

$$\mu\nabla^2\mathbf{v} = \nabla p \tag{3.2}$$

along with the continuity equation for incompressible fluids:

$$\nabla \cdot \mathbf{v} = 0 \tag{3.3}$$

Here, $\mathbf{v}$ denotes the fluid velocity vector, and p is fluid pressure. Together, these equations govern the flow behavior of our model cell.

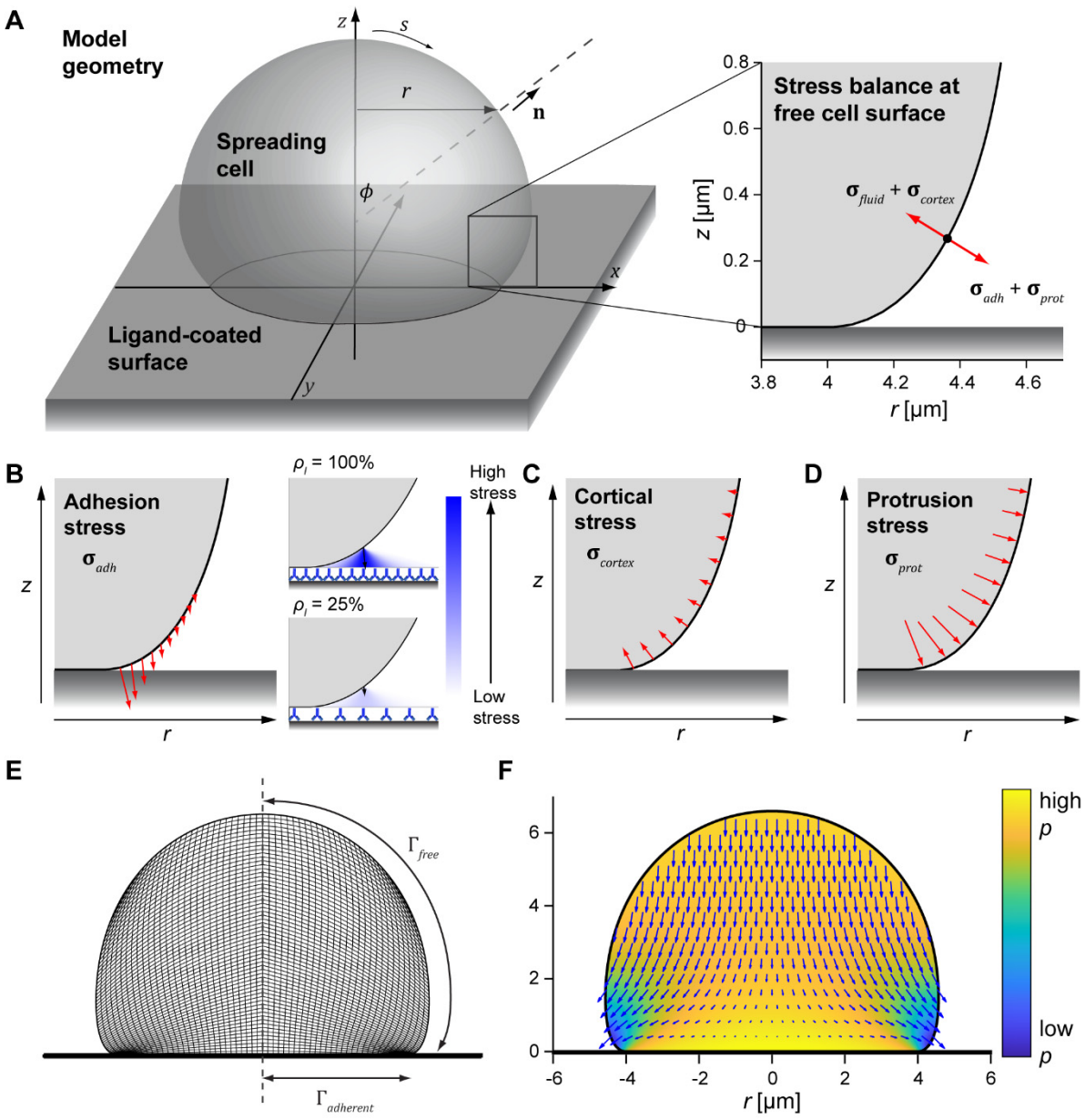

Fig 3.1. Illustration of our computational model of isotropic cell spreading.
(A) 3D rendering shows the geometry and defines coordinates for an axisymmetric spreading cell on a flat surface. The enlarged inset (right) illustrates the stress balance at the free cell boundary. (B) Pre-contact adhesion stress effectively pulls the membrane onto the flat surface. The enlarged insets conceptually depict how the adhesion stress is computed for different ligand densities ρ_l. (C) Cortical tension and membrane curvature give rise to an effective inward normal stress. (D) The protrusion stress acts normal to the cell membrane and is concentrated at the region of the membrane closest to the substrate. (E) The cross-sectional snapshot of a simulation illustrates the mesh composed of quadrilateral elements used in the calculations, with tighter element packing closer to the flat surface. The computational domain only includes half of this mesh due to axial symmetry. Boundary regions are labeled Γ, and the vertical dashed line is the symmetry axis ($r = 0$) (F) This snapshot of a simulation illustrates the fluid velocity (vector field) and relative pressure (heat map) computed for a given cell shape with known boundary stresses.

Interactions between the cell surface and the substrate can facilitate cell spreading directly via adhesion, and indirectly through receptor-induced signaling that leads to protrusion. Including the respective stresses, the moving boundary condition governing the free (i.e., nonadherent) part of the cell surface (Γ_{free}) balances up to four types of stress vectors: fluid stress ($\boldsymbol{\sigma}_{fluid}$), adhesion stress ($\boldsymbol{\sigma}_{adh}$), protrusion stress ($\boldsymbol{\sigma}_{prot}$), and cortical stress ($\boldsymbol{\sigma}_{cortex}$) (Fig 3.1A):

$$\boldsymbol{\sigma}_{fluid} + \boldsymbol{\sigma}_{adh} + \boldsymbol{\sigma}_{cortex} + \boldsymbol{\sigma}_{prot} = \mathbf{0} \quad \text{on } \Gamma_{free} \tag{3.4}$$

The fluid stress vector $\boldsymbol{\sigma}_{fluid}$ encompasses the pressure difference across the cell surface as well as the stress exerted on the surface by the moving cytoplasm. It is determined by the constitutive relation for a Newtonian fluid:

$$\boldsymbol{\sigma}_{fluid} = \boldsymbol{\sigma}_{fluid,out} - \boldsymbol{\sigma}_{fluid,in} = (p - p_{out})\mathbf{n} - \mu\left(\nabla\mathbf{v} + (\nabla\mathbf{v})^T\right)\cdot\mathbf{n} \tag{3.5}$$

where $\mathbf{n}$ is the unit surface normal, and the dot in the last term on the right-hand side denotes the inner product between a tensor and a vector. The extracellular medium has a much lower viscosity than the intracellular fluid; therefore, Eq (3.5) neglects the medium's viscous contribution and only accounts for its hydrostatic pressure denoted p_{out}.

Our implementation of the adhesion stress is based on the assumption that adhesion can effectively be represented by a short-range attractive potential between the cell surface and the ligand-coated substrate. We compute the effective adhesion stress at a given point on the cell surface by summing over all pairwise interactions with substrate molecules that lie outside the cell-substrate contact region at the time (Fig 3.1B). For a continuum of ligand molecules, the resulting expression takes the form (derived in Appendix A)

$$\boldsymbol{\sigma}_{adh} = \sigma_o \rho_l \iint_{\text{substrate}} \mathbf{f}_{unit}\left[\left(\frac{D_0}{D}\right)^7 - \left(\frac{D_0}{D}\right)^4\right] dA \tag{3.6}$$

where ρ_l is the ligand surface density and σ_0 is a scaling factor representing the strength of interaction per unit area of the cell surface. The unit vector $\mathbf{f}_{unit}$ specifies the direction of a given interaction, D denotes the distance between the interacting points, and D_0 is a constant setting the overall range of the adhesion potential (set to 50 nm in our simulations; Table 3.1).

The origin of the cortical stress is the cortical tension, which resists expansion of the cell surface area and acts along the curved surface of the cell (Fig 3.1D). The resulting stress acts normal to the surface and is given by the product of the tension τ (Eq (3.1)) and the mean curvature of the cell surface, as dictated by Laplace's law:

$$\boldsymbol{\sigma}_{cortex} = -\tau\left(\frac{\partial\phi}{\partial s} + \frac{\sin\phi}{r}\right)\mathbf{n} \tag{3.7}$$

Here, the term in parentheses is the mean curvature of the axisymmetric cell surface expressed in the coordinates defined in Fig 3.1A.

Table 3.1. Summary of modeling parameters, with supporting references.

Parameter	Description	Value	Notes
τ_0	Resting cortical tension	0.01 mN/m	Matches experimental value used by Herant et al. [11]
τ_{max}	Maximum cortical tension	~1 mN/m (see constitutive relation)	In a reasonable range for high tensions measured during neutrophil phagocytosis [38, 106]
μ	Effective cytoplasmic viscosity	200 Pa-s (passive) 1,660 Pa-s (active)	Matches experimentally measured values [53, 107]
κ_b	Effective membrane bending modulus	1×10^{-18} J	Matches experimentally measured values [108], much higher than values for RBCs or vesicles due to the neutrophil cortex
R_0	Initial cell radius	4.25 μm	Radius of a human neutrophil
σ_0	Adhesion stress constant	370 Pa	Together with the ligand density, this determines adhesion strength
$\rho_{IgG,max}$	Ligand density corresponding to 100% for Brownian Zipper model	10,000 IgG/μm^2	This density corresponds to about 600 μJ/m^2, which exceeds values derived from other cases of cell spreading [63]
D_0	Zero adhesion force distance	50 nm	Relatively large distance required for mesoscopic model, as standard in other continuum models [62, 109]
$\sigma_{prot,max}$	Max. protrusion stress	3,500 Pa	Actin filaments growing in parallel can achieve forces above 1 nN per μm^2 (> 1 kPa) [75, 110]
s_0	Protrusive force range	0.8 μm	Controls how the protrusion stress decays along the membrane (Eq 8)
t_0	Characteristic time for decay of protrusion stress	66 s	Used for discrete adhesion model (Eq 13)
k_BT	Energy scale factor	4.11×10^{-21} J	Boltzmann constant (k_B) times room temperature (298 K), sets scale for membrane fluctuations (Eq 12) and ligand-receptor binding energy.
$\rho_{Fc\gamma R}$	FcγR density in the neutrophil membrane	1,470 μm^{-2}	Receptor density used in discrete ligand + discrete receptor simulations shown in Fig 8B, explained in Appendix F
D_{eff}	Effective FcγR diffusion coefficient	1×10^{-4} μm^2/s	Chosen value explained in Appendix F

The protrusion stress comprises outward forces exerted on the cell surface by the actively remodeling cytoskeleton. Purposeful reorganization of intracellular structures requires tight coordination by biochemical signaling cues, which in turn are induced by receptor-ligand binding. Rather than attempting to implement these highly complex mechano-chemical mechanisms, we capture their localized character in a semiempirical manner. Our model postulates that the protrusive stress is greatest at the perimeter of the cell-substrate contact region and decays as a function of the distance from this leading edge measured along the arc length (s, Fig 3.1A) of the contour of the unbound cell surface. We assume that this stress acts normal to the cell boundary, and that its decay along the free cell surface is exponential (Fig 3.1C):

$$\boldsymbol{\sigma}_{prot} = \sigma_{prot} e^{-\frac{s_{contact} - s}{s_0}} \mathbf{n} \tag{3.8}$$

In this equation, $s_{contact}$ is the arc length value at which the cell-surface contour makes contact with the substrate, and s_0 is the characteristic length that sets the spatial range of the protrusion stress.

Bearing in mind that cytoskeletal remodeling also is responsible for the behavior of the cortical tension, and that the tension varies during cell spreading (Eq (3.1)), it is reasonable to assume that the overall strength of the protrusion stress (σ_{prot}) varies in a similar fashion. In addition to the spatial distribution of the cortical stress governed by Eq (3.8), we therefore also postulate a deformation-dependent strength of the protrusive stress. Our choice of this dependence, and its motivation, will be explained in a later section.

Finally, for the part of the cell surface that is in contact with the substrate, we enforce a no-slip boundary condition, requiring that

$$\mathbf{v} = \mathbf{0} \quad \text{on } \Gamma_{adherent} \tag{3.9}$$

Each simulation begins with a model cell that rests on the surface and has formed a very small initial contact footprint (area < 0.1 μm^2). The shape of the upper, free part of the cell at this time is a spherical cap. We determine the fluid velocities and pressure distribution at each time step by solving a perturbed form of the Stokes equations using the finite element method (FEM; Fig 3.1E,F) as described previously [111]. We then use the computed velocities to evolve the cell shape over a small time step. Details of our model implementation and solution method are given in Methods and Appendix D.

This generic modeling framework of cell spreading can easily be adopted to represent different mechanistic notions by adjusting the relative contributions of the adhesion and protrusion stresses. Disregarding the protrusion stress altogether results in a mathematical representation of the Brownian zipper model described in the Introduction. On the other hand, the protrusive zipper model generally includes both the protrusion stress as well as the adhesion stress. A purely protrusion-driven mode of spreading also can be tested by setting the pre-contact adhesion stress to zero, although one needs to bear in mind that irreversible adhesion still maintains the cell-substrate contact region in this case. In all model versions, the adhesion stress can be varied over several orders of magnitude to predict how the spreading behavior depends on the density of ligand displayed on the substrate.

Quantitative experimental results for the validation of model versions

The computational framework presented in the previous section can be adopted to simulate interactions by various cell types with targets of different axisymmetric geometries. Our present focus on human neutrophils spreading on flat substrates is motivated by a wealth of experimental results obtained for this particular scenario and presented in Chapter 2. In brief, we exposed cells

to glass coverslips coated with IgG antibodies at densities (ρ_{IgG}) spanning ~3 orders of magnitude. The analysis of these highly controlled experiments included measurements of the cell-substrate contact area of spreading cells over time (Fig 3.2). Regardless of IgG density, we found that the area-versus-time curves typically were sigmoidal in shape (Fig 3.2B,C). Defining a cell's "spreading speed" as the fastest rate of contact-area growth (i.e., the slope of a sigmoidal fit to the area-versus-time curve at the inflection point), we found that all spreading cells increased their substrate-contact area at speeds of around 3 $\mu m^2/s$ irrespective of the density of deposited IgG (Fig 3.2D). The measured values of the maximum contact area of spreading cells, on the other hand, exhibited a moderate but significant increase at higher IgG densities (Fig 3.2E). These experimental results provide useful quantitative benchmarks for comparison with computer simulations and will be used in the following sections to evaluate the validity of different mechanistic notions about cell spreading.

An additional measure of interest can be inferred from the actual surface densities of IgG used in the experiments. The most densely coated coverslips presented about 25,000 IgG molecules per μm^2 and induced ~85% of deposited cells to spread. Remarkably, even at a low IgG surface density of ~44 molecules per μm^2, about 30% of the deposited cells still spread in an IgG-dependent manner. Fcγ receptors bind IgG with an average equilibrium constant of about 10^{-6} M [112], corresponding to a binding energy per bond of $E_{bind} = -k_B T \ln\left(10^{-6}\right) \approx 14 k_B T$. Assuming that all IgG molecules in the cell-substrate contact region have formed bonds with the cell's Fcγ receptors, conservative (upper-limit) estimates of the adhesion energy density of cell-substrate interactions on substrates coated with the high and low numbers of IgG yield 1,500 $\mu J/m^2$ and 2.6 $\mu J/m^2$, respectively.

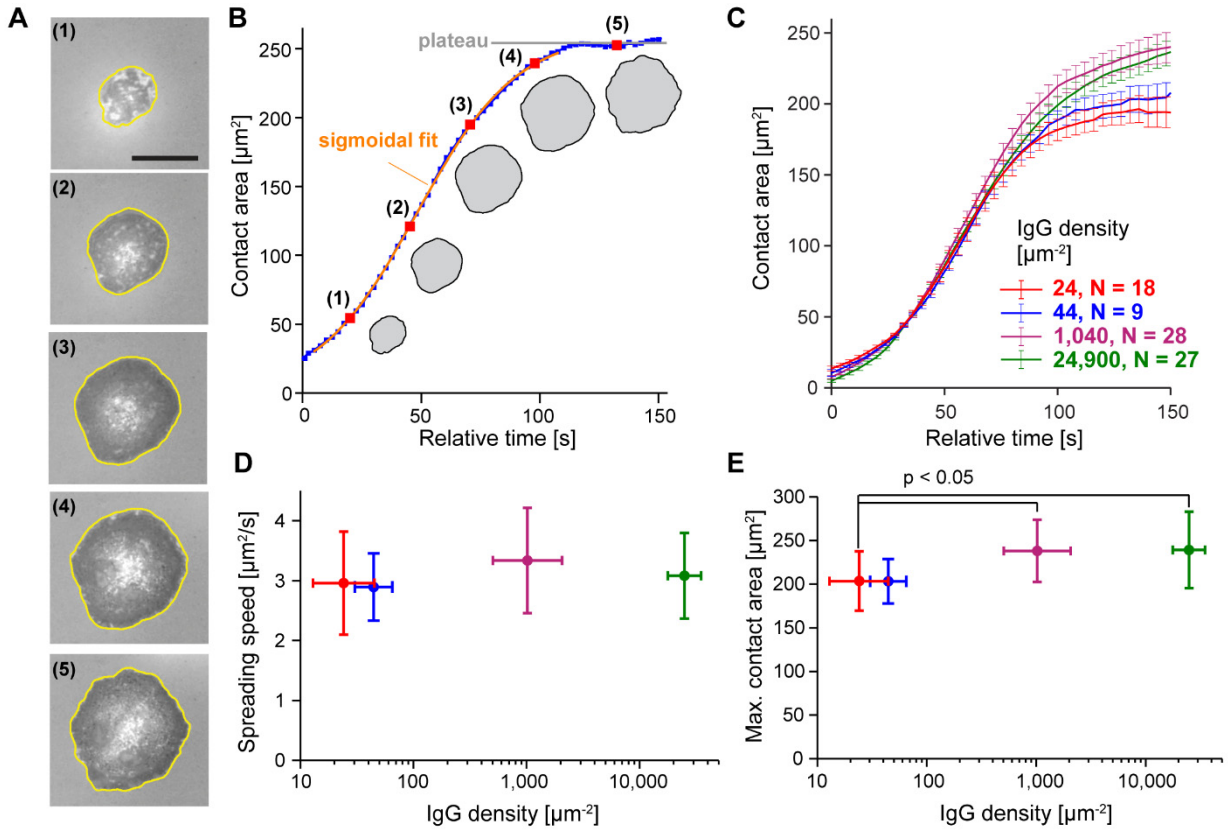

Fig 3.2. Summary of experimental results.
(A) The contact region of a spreading neutrophil was imaged using reflection interference contrast microscopy (RICM). Contact regions in this example are outlined in yellow. The scale bar in the first image denotes 10 μm. (B) Contact area is plotted as a function of time for the spreading cell shown in (A). The spreading speed is defined as the maximum slope extracted from a sigmoidal fit, and the maximum contact area is given by averaging the contact area at the plateau. (C) Mean contact area is computed at discrete time values for aligned curves of cells spreading on different densities of IgG. Mean quantified IgG densities are reported in the figure legend as IgG molecules per μm^2. Error bars represent standard error of the mean. (D) Average spreading speed was quantified for the different IgG densities. There is no significant difference between mean slope values. (E) Maximum contact area increases slightly as a function of IgG density. Statistically significant differences in maximum contact area values were verified using ANOVA followed by a Tukey post hoc test. Error bars in both (D) and (E) indicate standard deviation. The IgG density was quantified for each condition as described in Chapter 2.

Purely adhesion-driven spreading: predictions by the Brownian zipper model

We first tested the simplest version of our framework, the Brownian zipper model, by simulating purely adhesion-driven spreading in the absence of any protrusion stress (Fig 3.3, S1 Movie). In

this scenario, the model cell is passive and is pulled onto the substrate by short-range attraction. This case is conceptually equivalent to a viscous droplet spreading on an adhesive substrate.

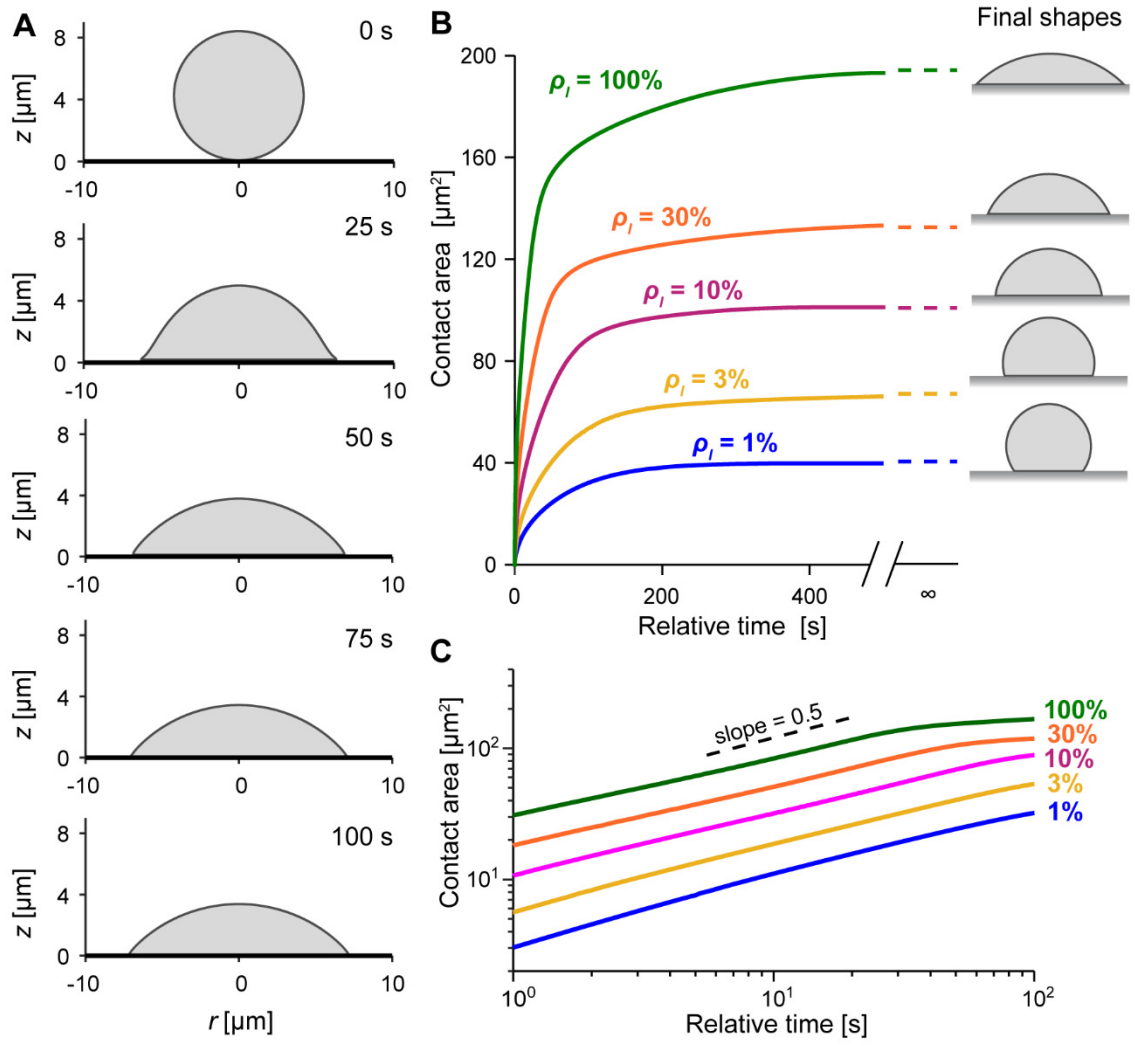

Fig 3.3. Predictions of the Brownian zipper model.
(A) A model cell spreading on the highest tested ligand density (100%) quickly approaches a spherical cap morphology. Time stamps are included for each snapshot. (B) Curves of contact area vs. time show that the spreading rate decreases monotonically. The contact area ultimately approaches steady-state values predicted by the Young-Dupre equation (dashed lines). Predicted equilibrium shapes are included on the right. (C) Log-log plot of contact area vs. time is nearly linear over the initial spreading phase. The slope of this line corresponds to the exponent of a power law describing contact area growth as a function of time. The dashed line shows a slope of 0.5 for reference.

Varying the ligand density ρ_l over two orders of magnitude, we found that the model cells generally spread fastest immediately after first contacting the substrate. Afterwards, the growth rate of the cell-substrate contact area decreased monotonically until the contact area reached a steady-state plateau marking equilibrium (Fig 3.3B). As expected, the equilibrium shapes were spherical caps. Log-log plots of the contact-area-versus-time predictions during the initial, fast spreading phase were approximately linear, with slopes close to 0.5 (Fig 3.3C). Hence, the contact-area growth initially obeys a power law, in agreement with various laws proposed to describe droplet wetting dynamics [113] or passive cell spreading [62, 63]. In fact, the exponent of 0.5 is an excellent match to results of a previous study that modeled cells as highly viscous droplets [62]. In Appendix B, we show how this exponent naturally arises during early spreading of a passive model cell driven by adhesion stresses concentrated at the contact perimeter.

Although the predictions of the Brownian zipper model agree well with the typical theoretical behavior expected for this kind of passive model cell, they clearly differ from the results of our phagocytic spreading experiments (Fig 3.2) in several important ways. First, the simulated contact-area-versus-time curves lack the characteristic sigmoidal shapes observed in experiments. Second, the predicted spreading curves exhibit a very strong dependence on the density of encountered ligands, in stark contrast to the observed spreading behavior. This dependence is evident in both the predicted spreading speeds, which increase dramatically with ligand density, as well as the predicted maximum contact areas, which increase several-fold as a function of the tested adhesive strengths.

Finally, the equilibrium shapes obtained for the adhesion energy densities used in the simulations are inconsistent with the cell deformations observed on the experimentally tested

IgG densities. At equilibrium, the adhesion energy density (γ) of the Brownian zipper model cell is related to the cortical tension τ and the contact angle θ_c via the Young-Dupre equation:

$$\gamma = \tau(1 - \cos\theta_c) \tag{3.10}$$

For a given value of the maximum cell-substrate contact area A_c, the equilibrium shape of the model cell—a spherical cap—is uniquely defined by A_c and the known, constant cell volume. Thus, basic geometry allows us to calculate the contact angle θ_c as well as the total cell surface area A_{cell}. Inserting the value of the latter into Eq (3.1) provides the cortical tension at equilibrium, which then can be used in Eq (3.10) to obtain the adhesion energy density as a function of A_c (Fig 3.4). As expected, the relationship between maximum contact area and adhesion strength predicted by our numerical simulations agrees well with the Young-Dupre equation (Appendix A). The quantitative comparison of this theoretical prediction to actual adhesion energy densities—estimated from the densities of deposited IgG molecules as explained earlier—exposes entirely different behaviors between the model and experiments, however (Fig 3.4). Especially in experiments performed at lower IgG densities, the conservatively estimated adhesion energy densities were much lower than what would be required to form the measured maximum contact areas solely by adhesion. In summary, the results of this section rule out adhesion as the primary driving force of frustrated phagocytic spreading.

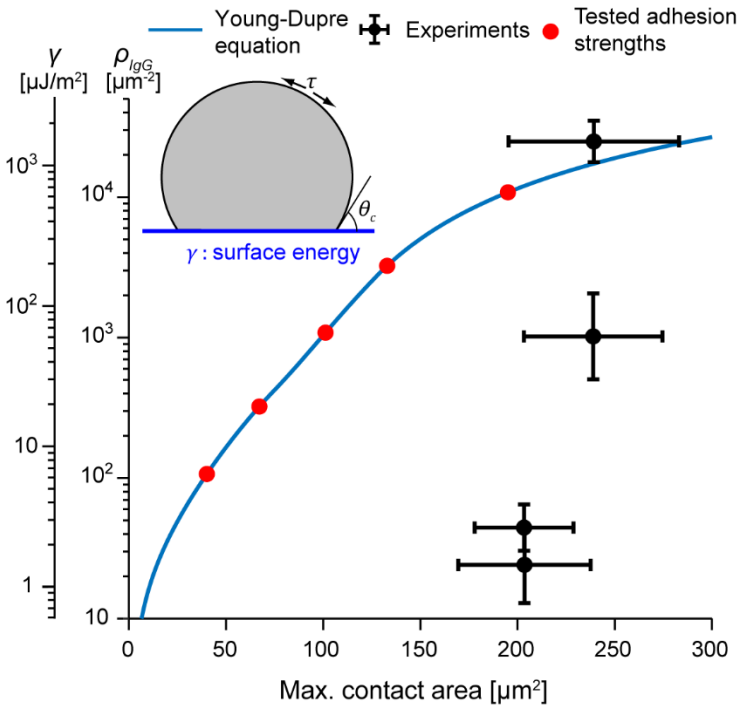

Fig 3.4. Relationship between ligand density and maximum contact area, as predicted by the Young-Dupre equation. The adhesion energy γ, and therefore the ligand density ρ_{IgG}, can be expressed as a function of the contact area of the final spherical cap formed by a viscous droplet. The tested adhesion strengths are marked as red dots. Actual experimental values are shown for comparison. Error bars indicate standard deviation.

Protrusion-dominated spreading: predictions of the protrusive zipper model

The protrusive zipper model incorporates the protrusion stress into the basic framework considered in the previous section, enabling us to account for active force generation by the model cell. Our semiempirical implementation is motivated by biological plausibility, and by the goal to reproduce experimental observations with a minimum set of rules for the spatial distribution (Eq (3.8)) and the deformation-dependent evolution of the protrusion stress during cell spreading. To capture the presumed correlation between receptor-induced signaling and protrusive force generation by the cytoskeleton, we express the strength of the protrusion stress as a function of the cell-substrate contact area A_c. We assume that in the initial low-tension regime, the protrusion stress grows linearly with A_c. Once the cortical tension increases more steeply, the protrusion stress is assumed to grow faster as well. Ultimately, the strength of the protrusion stress levels out at a maximum value of $\sigma_{prot,max} = 3.5$ kPa, within the range of

experimentally measured stresses exerted by parallel actin filaments [75, 110]. This behavior is implemented in our model through a smoothed version of the following rule (plotted in Appendix C):

$$\sigma_{prot} = \sigma_{prot,max} \times \begin{cases} \left[0.05 + 0.3\left(\dfrac{A_c}{A_{c,trans}}\right)\right] & \text{if} \quad \dfrac{A_{cell}}{A_{cell,0}} \le 1.26 \\ \left[0.35 + 0.65\left(\dfrac{A_c - A_{c,trans}}{120\ \mu m^2}\right)^{1/2}\right] & \text{if} \quad \dfrac{A_{cell}}{A_{cell,0}} > 1.26 \text{ and } A_c \le A_{c,trans} + 120\,\mu m^2 \\ 1 & \text{if} \quad A_c > A_{c,trans} + 120\,\mu m^2 \end{cases} \tag{3.11}$$

where $A_{c,trans}$ is the contact area when the total cell surface area A_{cell} is equal to $1.26A_{cell,0}$, the transitional moment when the cortical tension starts rising more rapidly (Eq (3.1)).

We started examining the behavior of this model by first disregarding the adhesion stress altogether. In this limiting scenario, cell spreading is driven by protrusion, whereas the only remaining role of adhesion is to render cell-substrate contacts irreversible, as in all our models. As mentioned above, cell-substrate contact is coupled to protrusion through biochemical signaling via Eq (3.11). We found that in this case, the model cell begins spreading slowly while a distinctive leading edge gradually develops (Fig 3.5A, S2 Movie), resulting in a morphology that clearly differs from the spherical caps predicted by the Brownian zipper model (Fig 3.3). Spreading slows noticeably at about 90 s, around the time the protrusion stress reaches its maximum value. The resulting contact-area-versus-time curve has a sigmoidal shape, in agreement with the mean spreading behavior observed in experiments on the highest density of IgG (Fig 3.5B). We also tested slightly different versions of Eq (3.11) and found that the overall curve remains sigmoidal even for these alternative relationships (Appendix C). On average, spreading appears to commence somewhat more gradually in experiments than in our model,

which may indicate an overestimate of the initial protrusion stress in Eq (3.11). Plots of the protrusion stress and the cortical tension as a function of time (Fig 3.5C) illustrate the qualitatively similar evolution of these two quantities, with the rise of the tension lagging due to the initial "slack" of the cell surface in the low-tension regime (Eq (3.1)).

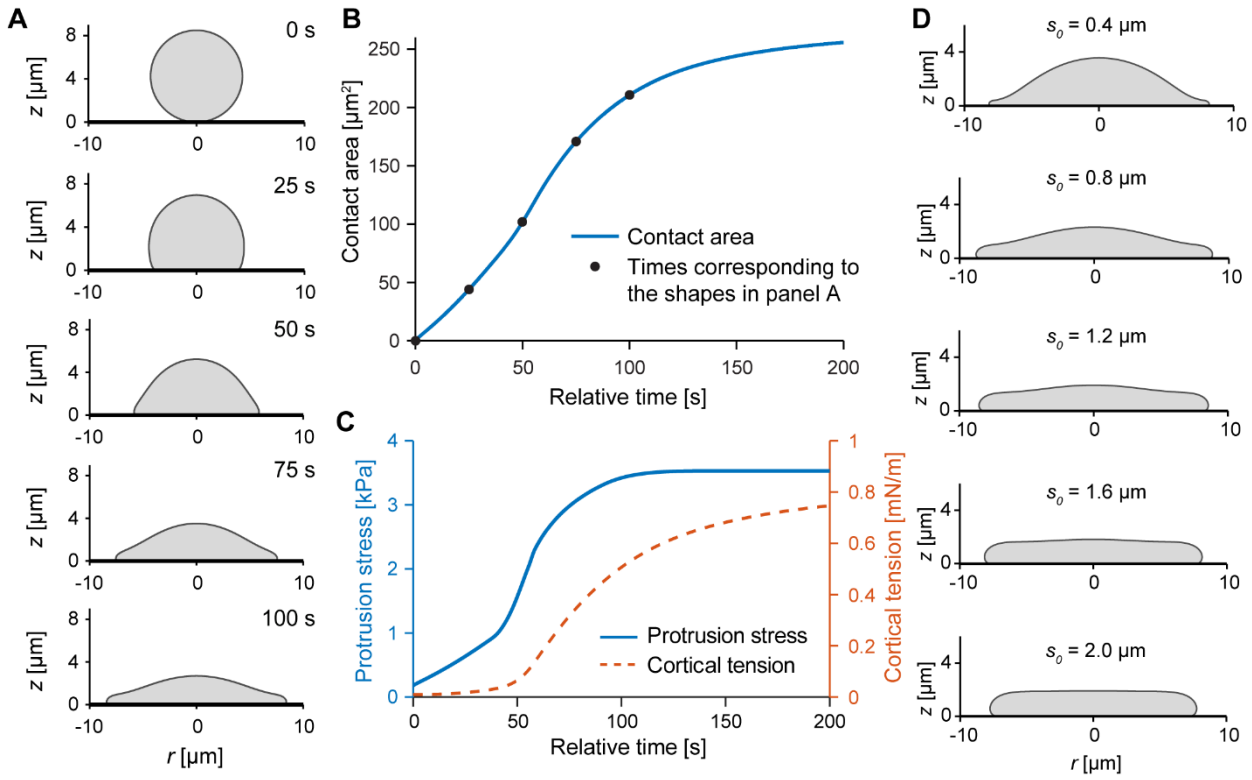

Fig 5. Predictions of the protrusive zipper model in the absence of adhesion stress.
(A) For purely protrusion-driven spreading, lamellar pseudopods form as the protrusion stress increases over time. Time stamps of the the shown sample shapes are included. (B) Contact area increases sigmoidally over time for the protrusive zipper model, in good agreement with our measurements of the time course of the mean contact area on the highest density of IgG. Filled circles indicate where the shapes shown in panel A were computed. (C) Protrusion stress (governed by Eq (3.11)) and cortical tension (governed by Eq (3.1)) increase during cell spreading. (D) Varying the parameter s_0 determines the thickness of the leading lamella, resulting in a thin pseudopod for s_0 = 0.4 μm (top) and coordinated global cell deformation for s_0 = 2.0 μm (bottom). The sample shapes are shown at t = 120 s. All other protrusive zipper simulations in this paper were carried out using s_0 = 0.8 μm.

We chose the value s_0 = 0.8 μm for the characteristic length that defines the spatial range of the protrusion stress (Eq (3.8)) in the simulations shown in Fig 3.5A-C. Because s_0 does not

appear to be a directly measurable quantity, it is instructive to inspect how its value affects the spreading model cell. Snapshots from simulations using different values of s_0 demonstrate how the cell morphology (here: at 120 s) depends on the spatial range over which the protrusion stress acts (Fig 3.5D, S3 Movie). The leading edge of the cell assumes the shape of a thin lamella for small values of s_0 and becomes increasingly thicker at larger s_0-values. Aside from this varying thickness of cellular protrusions, the overall spreading behavior is similar for different values of s_0.

Next, we inspected the behavior of the full protrusive zipper model by repeating the simulation with the same settings as used for Fig 3.5 but now also including the adhesion stress that captures the contribution of pre-contact attraction between cell and substrate to cell spreading. We again examined the same set of adhesion strengths as used in our tests of the Brownian zipper model (Fig 3.3). The simulations expose how, in this scenario, cell-substrate adhesion promotes spreading, affecting the overall spreading behavior in a quantitative manner but without altering it qualitatively. The model cells spread somewhat faster and farther on substrates coated with higher ligand densities (Fig 3.6A), with slightly larger contact angles between their leading edge and the substrate (Fig 3.6B, S4 Movie), but otherwise exhibited unchanged morphology. The sigmoidal character of the contact-area-versus-time curves is conserved through most of the tested adhesion strengths, and both the spreading speeds as well as the maximum contact areas vary much less than in the predictions of the Brownian zipper model (Fig 3.3).

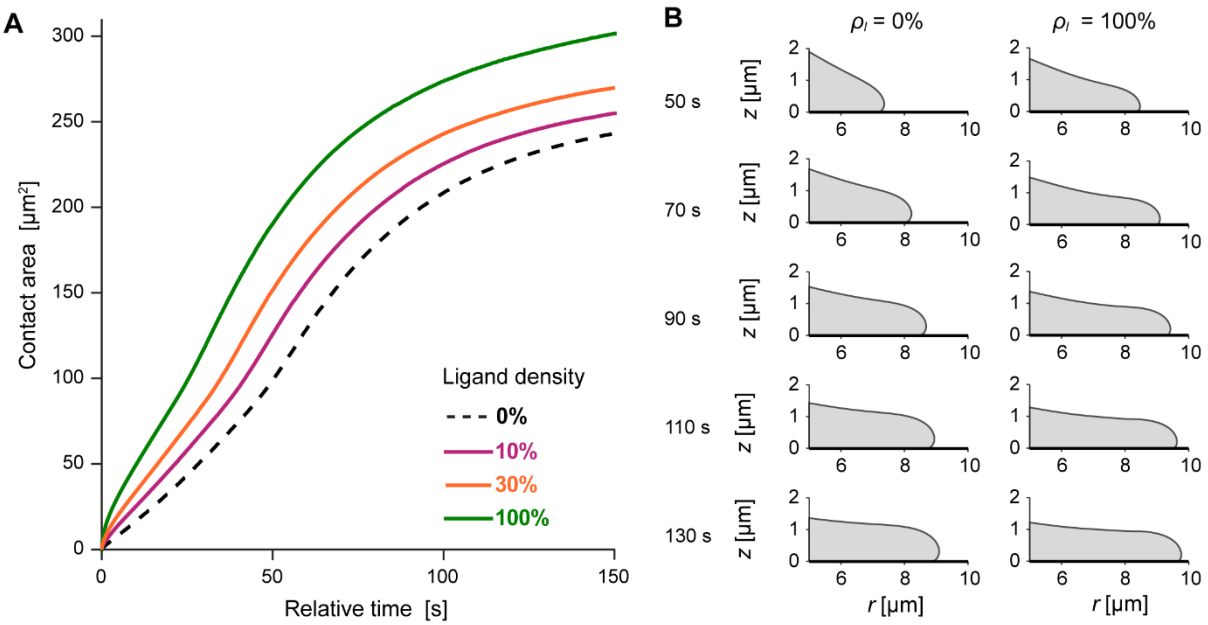

Fig 6. Predictions of the protrusive zipper model with varying adhesion stress.
(A) Contact area increases faster and reaches higher values for higher ligand densities. The protrusion-only curve is shown for reference as a dashed line. (B) Magnified views of the leading edge of the model cell highlight subtle, adhesion-dependent changes of the pseudopod morphology. The shapes of the leading cell edge are shown for ρ_l = 0% and ρ_l = 100% at times ranging from 50 s to 130 s. On higher ligand density, both the extent of spreading and the dynamic contact angle increase. Other than that, the cell shapes exhibit little dependence on adhesion strength within the full protrusive zipper model.

Clearly, the predictions of the protrusive zipper model are in much better agreement with experimental observations than those of the Brownian zipper. A spreading cell morphology that is characterized by a forward-bulging leading lamella (Figs. 3.5-3.6) matches the cross-sectional profile of phagocytes engulfing large particles well [10, 99], in contrast to model cell shapes whose leading edge coincides with the perimeter of contact between the cell and substrate (Fig 3.3). The timing of spreading and sigmoidal shapes of the contact-area-versus-time curves predicted by the protrusive zipper model (Fig 3.5-3.6) agree with experiments as well, and the time-dependent increase in protrusion stress is consistent with a biphasic signaling response measured during FcγR-mediated phagocytosis [70]. Furthermore, both the predicted spreading speeds as well as the maximum contact areas are comparable to the respective values measured

in experiments, and the slight increase of the maximum contact area at higher adhesion strengths is consistent with our measurements (Fig 3.6A). On the other hand, the predicted increase of the spreading speeds on higher ligand densities (Fig 3.6A) differs from our experimental data (Fig 3.2). Therefore, this model still somewhat overestimates the contribution of the adhesion stress to the dynamics of phagocytic spreading. Nevertheless, of the two considered models only the protrusive zipper model succeeds in capturing the essential dynamics of experimentally observed phagocytic spreading, establishing that active cellular protrusion rather than passive cell-substrate adhesion is the dominating driving force of this type of cellular motion.

Protrusive zipper model with discrete adhesion sites: best match between experiments and theory

The previous sections presented continuum models of cell spreading, resulting in predictions that overestimated the attractive force due to cell-substrate adhesion even in the case where short-range adhesion plays only a secondary role. In reality, however, adhesive ligands encountered by a spreading cell reside at discrete substrate locations rather than presenting a contiguous adhesive film. A pioneering study that considered discrete adhesion sites not only predicted dramatic qualitative differences compared to continuum models of adhesion but even concluded that, depending on the lateral spacing of discrete cell-substrate cross-bridges, “there is little or no tendency for the contact to spread unless the surfaces are forced together” [114]. These considerations prompted us to design and examine a version of the protrusive zipper model in which the model cell can only form new attachments to the substrate at prescribed locations (Fig 3.7, S5 Movie).

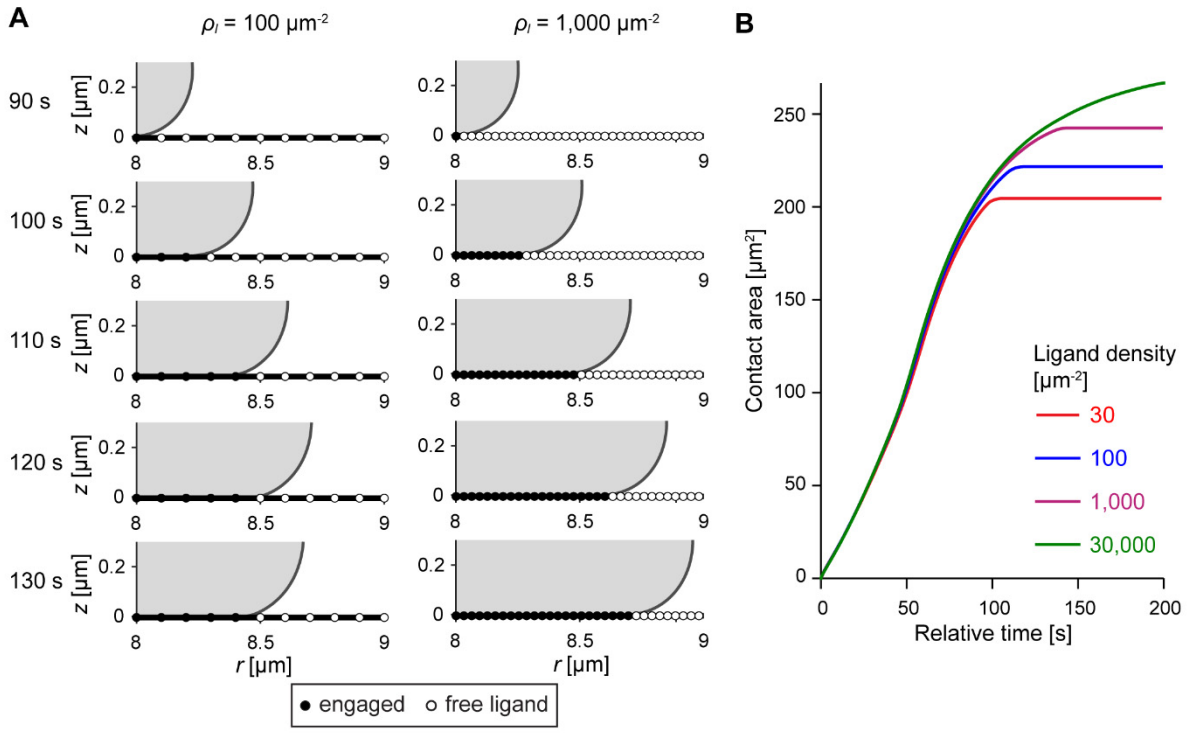

Fig 7. Predictions of the protrusive zipper model with discrete adhesion sites.
(A) Two time series (times shown at the left) of simulation snapshots illustrate how the progression of the model cell's leading edge is affected by the spacing of discrete adhesion sites. Unoccupied binding sites are depicted by empty circles, whereas filled circles indicate that the cell membrane is locally attached. (B) Contact-area-versus-time curves share similar slopes over three orders of magnitude of ligand density, but plateau at different maximum contact areas.

In this model version, the spacing of adhesion sites is determined by the ligand density ρ_l (the number of ligand molecules per μm^2), with the in-plane spacing given by $(\rho_l)^{-1/2}$. Furthermore, we introduce two additional rules to capture realistic aspects of cell spreading on discrete adhesion sites. First, we replace the continuous adhesion stress (Eq (3.6)) with the following concept of discrete bond formation. We consider a new bond as "formed" as soon as the distance between the next free ligand site and the closest point of the advancing cell membrane reaches a threshold distance d_{thresh}. As a consequence of such bonding, we place the cell surface into irreversible contact with this substrate site when carrying out computations at the next time step. The value of the threshold distance is determined by the magnitude of membrane fluctuations. Assuming that the time scale of membrane fluctuations is generally

smaller than our time step, we define d_{thresh} to be the root mean square height $<h^2>^{½}$ of membrane fluctuations at equilibrium through [115]:

$$d_{thresh} = \sqrt{\langle h^2 \rangle} = \sqrt{\frac{k_B T}{4\pi\tau} \ln\left(1 + \frac{\tau A_{cell}}{\pi^2 \kappa_b}\right)} \tag{3.12}$$

where k_B is Boltzmann's constant, T is temperature, A_{cell} is the cell surface area, and κ_b is the membrane bending modulus. According to this rule, increased cortical tension τ suppresses membrane fluctuations, making it more difficult for the cell to form new adhesive connections at later time points. The parameter values chosen in our simulations (Table 3.1) correspond to typical fluctuation amplitudes ranging from 18 nm at resting tension to about 2 nm for very high tension, in general agreement with measurements of membrane fluctuations in cells on surfaces [116, 117].

Second, because it seems unlikely that persistent receptor-ligand contacts induce signaling indefinitely, we also assume that the protrusion stress can diminish over time. This assumption is supported by experimental data showing that actin polymerization does not continue indefinitely during phagocytosis if the cell encounters an unopsonized region of the target particle [4, 13, 44]. We implement this behavior by postulating a transient protrusion stress that initially is triggered by fresh cell-substrate contact (occurring at time t_{bind}) and then decays exponentially according to the relation:

$$\tilde{\sigma}_{prot} = \sigma_{prot} e^{-\frac{t - t_{bind}}{t_0}} \tag{3.13}$$

In this version of the model, σ_{prot} in Eq (3.8) is replaced by $\tilde{\sigma}_{prot}$ defined in Eq (3.13). The effects of varying the rate of this decay are explored in Appendix F. We use a value of t_0 = 66 s in our simulations, which gave the best quantitative agreement with experimental data.

To avoid possible bias due to the exact placement of discrete binding sites, we performed each simulation multiple times, shifting all binding sites laterally by small increments without changing their spacing. We then averaged the results of these individual simulations to predict the cell-spreading behavior as a function of the chosen spacing—or density—of adhesion sites.

Overall, the predictions of this discrete protrusive zipper model (Fig 3.7) agree well with those of the continuum model version. For instance, maximum cell-substrate contact areas exhibit a similar dependence on the ligand density in both models. However, in this discrete model, the sigmoidal contact-area-versus-time curves obtained at different ligand densities are aligned much more closely during the spreading phase, reflecting spreading speeds that hardly depend on the ligand density anymore (Fig 3.7B).

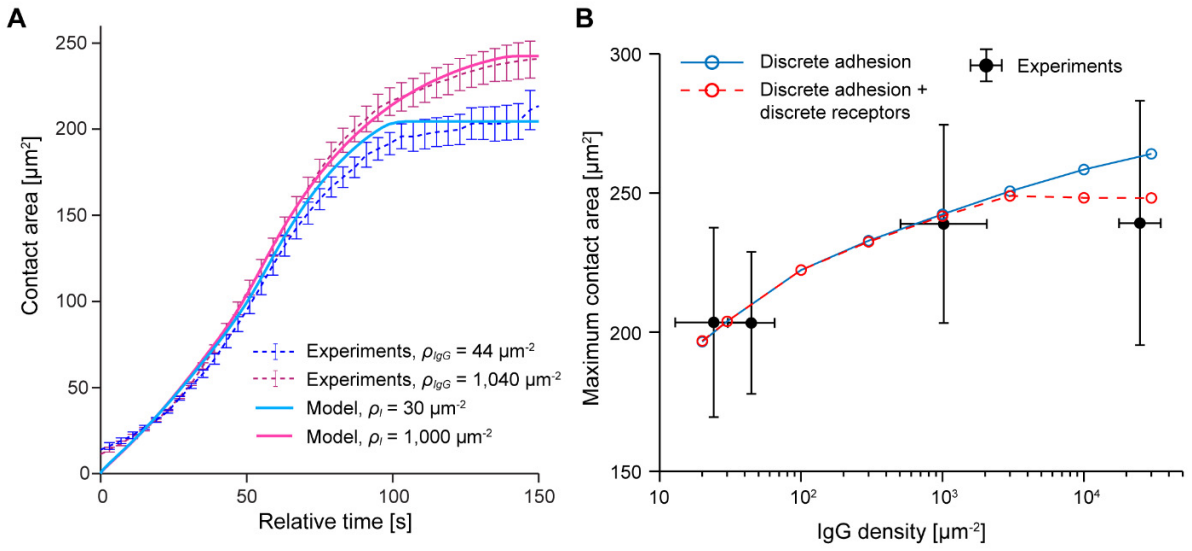

Fig 8. Direct comparison of experimental data with the predictions of the protrusive zipper model with discrete adhesion.
(A) Time courses of the cell-substrate contact area predicted by the protrusive zipper model with discrete adhesion are overlaid on experimental results for two different ligand densities. The model curves are not the result of nonlinear fits but simply the predictions based on reasonable choices of parameter values. (B) The predicted ligand-density-dependent increase in maximum contact area agrees well with experimental results obtained in frustrated phagocytosis experiments. Modeling only ligands as discrete entities results in an apparent overestimation of the maximum contact area at the highest IgG density (*solid blue curve*), indicating that the number of Fcγ receptors rather than the number of IgG ligands becomes the limiting factor of the maximum adhesion strength in this regime. A model version that accounts for the discrete nature of both ligands as well as receptors (Appendix F) improves the agreement with the data at the highest IgG density (*dashed red curve*). Error bars indicate standard deviation.

Together, the predictions by the model with discrete adhesion sites agree amazingly well with the behavior of real human neutrophils during frustrated phagocytosis (Fig 3.8). As in experiments, the spreading speed remains remarkably consistent over a range of ligand densities spanning 3 orders of magnitude (Figs 3.7B and 3.8A). Moreover, the predicted moderate increase of the maximum contact area at higher ligand densities matches experimental measurements quite well (Fig 3.8B). On the other hand, whereas the measured dependence of the maximum contact area on the IgG density appears to reach a plateau for IgG densities greater than 1,000 μm^{-2}, our model predicts a continuous increase of the maximum contact area over the whole range of ligand densities. A possible explanation for this discrepancy is the model assumption that the ligand density determines the maximum number of discrete adhesion bonds between the cell and the substrate, which implies that the receptors on the cell surface are always in excess. Human neutrophils indeed present a large number of Fcγ receptors on their surface, i.e., several thousand receptors per square micrometer. However, this receptor density is smaller than the highest ligand density of ~25,000 IgG molecules per square micrometer used in our experiments. Therefore, at the highest IgG densities, we expect the numbers of receptors to be the limiting factor determining the maximum number of adhesion sites, which is not accounted for in the above model. To verify this expectation, we conducted additional proof-of-principle simulations in which both the ligands as well as the receptors were treated as discrete, as explained in Appendix F. This approach indeed improved the agreement between experiments and theory further, as shown in Fig 3.8B.

Overall, these results reinforce the conclusion that active cytoskeletal protrusion drives phagocytic spreading. They also highlight that it can be important for realistic models of cell

spreading on substrates coated with specific adhesion molecules to account for the discrete distribution of these adhesion sites.

Discussion

Quantitative understanding of the behavior of motile mammalian cells—from immune cells to metastasizing cancer cells—is a prerequisite for transformative biomedical advances in diagnosis, treatment, and therapy of many current and future health threats [118]. Motile cells integrate a complex variety of physical and chemical cues to carry out specific functions. Genuine understanding of the underlying mechano-chemical processes not only requires an interdisciplinary strategy but also integrative experimental/theoretical approaches. Translation of mechanistic notions into mathematical models, and comparison of theoretical predictions with experimental observations, often provides the strongest arguments for or against the validity of biological hypotheses. Confidence in the predictive power of computer simulations requires that the model assumptions be realistic and biologically plausible. Guided by this perspective, we here examined fundamental biophysical mechanisms that potentially can facilitate spreading of biological cells on a substrate.

Unpolarized cells usually begin spreading in a symmetric fashion [63, 119]. This stage is often viewed as a passive process that is entirely driven by adhesion energy due to receptor-ligand binding [63, 120]. An alternative class of models considers such spreading as dependent on cytoskeletal activity [66, 67, 95]. In this study, we have developed a mechanical modeling framework that allows us to establish whether frustrated phagocytosis, a specific form of isotropic cell spreading, is primarily driven by adhesion (Brownian zipper model) or by

protrusive forces generated by the cell (protrusive zipper model). Our findings likely carry over to other types of cell spreading inasmuch as key characteristics of adhesion and protrusion are shared [34].

The incompatibility of our Brownian zipper simulations with experimental data invalidates models of phagocytosis that treat neutrophil spreading as an adhesion-driven wetting phenomenon [100]. Moreover, our findings invite a careful review of mathematical models of other types of cell spreading that consider pre-contact adhesive attraction between cell and substrate as the main driving force [62, 63]. A first important prerequisite for the validity of such models is the use of realistic values of basic mechanical parameters, such as the effective viscosity of the cell interior, the cortical tension, and the adhesion energy density. For example, if the equilibrium cell-substrate contact areas measured in our spreading experiments on low-to-moderate ligand densities were due to adhesion, then the involved adhesion energies would have to be several orders of magnitude higher than those estimated from our measurements of ligand density. Even receptor accumulation in the contact region could not make up for this difference, because the smaller number of available ligands limits the number of possible adhesion bonds. Furthermore, the ability to simulate not only equilibrium situations but also the dynamical cell behavior, and to leverage time-dependent experimental observations against the predictions of such models, considerably raises confidence in a model's evaluation. As demonstrated in this study, such comparison greatly benefits from the availability of experimental data obtained on substrates presenting a large range of known densities of adhesive ligands.

It appears that adhesion-driven spreading is largely limited to situations where adhesion is unusually strong, and where the cells—like red blood cells—or surrogate objects—like lipid vesicles—are characterized by a low-viscosity interior and very low tension of their cortex or

membrane. Indeed, a recent mechanical modeling study found that Brownian membrane fluctuations were only sufficient to drive very small amounts of cell spreading on a surface [69]. If there are cases in which motile mammalian cells spread predominantly due to adhesion, then such spreading will likely occur on much longer timescales than considered here. Finally, it may be possible that adhesion plays a more relevant role in the engulfment of very small particles, or very early during phagocytic spreading, where cell shape changes do not require a significant expansion of the cell surface area [72]. Irrespective of the relevance of Brownian-zipper-type models in a particular practical situation, we note that the excellent agreement of our theoretical treatment of purely adhesion-driven spreading with other studies focusing on this form of motion [62, 63] strengthens confidence in our modeling approach and its numerical implementation.

The only alternative mechanism by which cells can expand their region of contact with a suitable substrate appears to be active, protrusion-dominated spreading. Many imaging studies indeed have documented an increased density of F-actin at the protruding front of motile immune cells [45, 77, 121], supporting the biological plausibility of the protrusive zipper concept. Moreover, inhibition of actin polymerization with cytochalasin B or latrunculin A eliminates the rapid phase of fibroblast spreading [57, 66, 67]. Similarly, chemical disruption of the actin cytoskeleton generally inhibits phagocytosis by immune cells [44, 86]. We have previously shown that extremely small concentrations of actin inhibitors actually can increase the size of transient, chemotactic-like protrusions [86, 122]. However, the cortical tension was reduced in such cases, and phagocytic spreading was not enhanced, highlighting the multiplicity of—likely dichotomous—mechanical roles of F-actin during cell deformations.

Our simulations based on the protrusive zipper model not only reproduce the main features of neutrophil spreading on IgG-coated substrates but, in the case of discrete adhesion sites, they

also agree very well with experimental data. We note that this agreement neither is surprising, nor does it constitute solid proof of the validity of this model. The scarcity of quantitative insights into the underlying mechanisms simply does not place sufficient constraints on the design of computational models. Instead, our goal here was to explore what set of minimalistic rules would need to be postulated to achieve a good match between theory and experiment. The successful implementation of this approach allows us to propose likely mechanistic details that can then provide guidance for future studies. Still, we are confident that the protrusive zipper model paints a reasonably accurate picture of phagocytic spreading, not only because of the elimination of the only alternative hypothesis, but also because our semiempirical model is plausible, i.e., it does not contradict pertinent biophysical and biological insights. For example, our implementation of the relationship between receptor-induced signaling and the generation of protrusive force is consistent with the hitherto most successful model of phagocytosis [10], as well as with previous measurements of the biphasic signaling response from a macrophage-like cell line during Fcγ receptor-mediated phagocytosis [70]. Models based on the assumption that actin polymerization preferentially occurs in regions of higher membrane curvature [123] can result in a localization of protrusion stress that is similar to the form it takes in our model (Fig 3.1D), although the idea of curvature-induced actin polymerization seems problematic in view of the much higher membrane curvatures in ever-present surface wrinkles and microvilli of immune cells. Importantly, our implementation of the relationship between receptor-induced signaling and force generation is independent of the exact mechanism by which intracellular processes are translated into protrusive force; instead, it encompasses different mechanistic notions such as the Brownian ratchet [124] and end-tracking motors [125].

An important outcome of our simulations of the protrusive zipper model is the difference in predictions depending on whether we considered continuous or discrete cell-substrate adhesion, in agreement with a previous theoretical study [114]. We are unaware of physiological situations in which cell adhesion is not predominantly supported by specific receptor-ligand bonds. Thus, the model version that is based on discrete binding sites is the more realistic version of the protrusive zipper. Remarkably, it is also the version that yielded the best match between theory and experimental observations. To achieve this agreement, we postulated that the formation of new receptor-ligand bonds is coupled to the protrusion stress in a time-dependent manner (Eq (3.13)), based on the assumption that receptor-induced signaling and subsequential actin polymerization are not sustained indefinitely after a ligand activates the receptor. There are multiple factors that could lead to this effective decay, such as the depletion of precursor molecules needed for the production of signaling messengers (e.g. release of IP_3 will cease once PIP_2 has been locally depleted [20]).

Perhaps the most important insight from the comparison of model versions based on continuous versus discrete adhesion is that models based on continuous adhesion are likely to misrepresent key aspects of the cell behavior, especially on lower ligand densities. For example, such models cannot capture the possibility that too large ligand spacing may prevent the next unbound receptor-ligand pair from approaching one another to within the distance at which they are likely to form a bond. In our protrusive zipper model with discrete adhesion, variation of substrate adhesivity by changing the density of adhesion sites primarily affects the maximum cell-substrate contact area. This prediction agrees well with our experiments, unlike the predictions by model versions that treat the ligand layer as a continuum.

The mechanisms governing isotropic cell spreading studied here are likely to also play a crucial role in the directional motion of migrating cells. Many immune cells, for example, are capable of executing both types of motion, as required during phagocytic spreading versus chemotactic and other forms of migration. As revealed by our experiments and reproduced by our discrete adhesion model, the rate of isotropic cell spreading is largely conserved on substrates presenting a broad range of densities of adhesion sites. This finding exposes an interesting difference to the prediction by models of migrating cells, i.e., that the crawling speed of such cells has a maximum on substrates with intermediate adhesion strengths [126-128]. This difference is a reminder that directional migration generally is a more complex type of motion that involves, in addition to protrusion and adhesion, important mechanisms regulating contraction and detachment of the rear of the migrating cell from the substrate. The positive correlation between low-to-moderate ligand densities and the speed of motion predicted by models of migrating cells can be attributed to either a direct scaling of protrusion with the amount of adhesion [127], or a postulated increased actin retrograde flow at lower adhesion strengths [126]. The predicted slowing of migrating cells at higher ligand densities is caused by an effective frictional force due to the need to break stronger adhesive attachments at the cell's rear [129, 130]. A noteworthy recent model of cell migration that decoupled friction from adhesive attraction actually predicted faster movement for higher adhesion energies [120]. The excellent agreement between our experiments and the protrusive zipper model suggests that the above additional mechanisms included in models of migrating cells play at most a minor role in isotropic phagocytic spreading. On the other hand, we believe that the main insights exposed by our study provide important suggestions on how to treat the interplay between protrusion and adhesion in models of migrating cells.

Methods

The perturbed Stokes equations

Assuming the cell interior can be approximated by a single, highly viscous, slow-moving Newtonian fluid, its motion obeys the Stokes equations for creeping flow with no body force, as given by Eq (3.2). Furthermore, for an incompressible fluid, the equation of continuity simplifies to the incompressibility condition (Eq (3.3)). Due to axial symmetry, there are three unknowns: v_r, v_z, and p, where r and z are cylindrical polar coordinates.

To solve this system of partial differential equations, we use the finite element method (FEM). Because directly solving the Stokes equations using FEM leads to numerical instabilities [131], we follow the procedure outlined by Drury and Dembo [111] to solve a perturbed form of the Stokes equations, in which the incompressibility condition (Eq (3.3)) is approximated as

$$\nabla \cdot (\mathbf{v} - \epsilon \nabla p) = 0 \tag{3.14}$$

In this form, the fluid is nearly incompressible, which allows us to avoid the well-known problems with using FEM for incompressible problems [131]. To accurately solve the Stokes equations, the value for ϵ must be sufficiently small. Specifically, we use the condition given in [111]:

$$\epsilon \leq \frac{h_{mesh}^2}{\mu} \tag{3.15}$$

where h_{mesh} is the characteristic radius of a single quadrilateral element. We tested different values of ϵ in our models and found this condition to provide sufficient accuracy and convergence (Appendix E).

Over the unbound portion of the cell, we specify Neumann boundary conditions, corresponding to a stress balance (Eq (3.4)). For the adherent cell surface, we specify Dirichlet boundary conditions, simply a no-slip condition in this case (Eq (3.9)). The pressure boundary condition is given by assuming the normal component of the pressure gradient goes to zero at the cell surface:

$$\nabla p \cdot \mathbf{n} = 0 \tag{3.16}$$

Computational details

At each time step, we first compute values for the surface curvature of the cell. Local values of the angle of the normal ϕ are evaluated using cubic polynomial fits. We then calculate the boundary stresses using the relationships outlined in the main text. The integral for the effective adhesion stress (Eq (3.6)) is computed numerically as described in Appendix A. The values for tension and protrusion stress at each time step are evaluated using smoothed versions of the relationships given in Eq (3.1) and Eq (3.11) (see Appendix C for full forms).

To find the fluid velocity and pressure fields, we must simultaneously solve Eq (3.2) and Eq (3.14) for v_r, v_z, and p. We employ the strategy outlined in [111], which is an adaptation of the Uzawa method. Starting with an estimate for pressure p_{est} given either by the previous time step or as a uniform distribution prior to spreading, we solve for fluid velocities by treating the pressure as known in Eq (3.2):

$$\mu \nabla^2 \mathbf{v} = \nabla p_{est} \tag{3.17}$$

We then treat the fluid velocities as known ($\mathbf{v}_{est}$) and solve an altered version of equation (3.14):

$$\frac{1}{\mu}(p - p_{est}) = \nabla \cdot \mathbf{v}_{est} - \nabla \cdot (\epsilon \nabla p) \tag{3.18}$$

The updated pressure is then inserted back into Eq (3.17) and the procedure is repeated until the following condition is met:

$$\frac{\max\left(\left|p - p_{est}\right|\right)}{\max\left(\left|p - p_{out}\right|\right)} \leq 10^{-6} \tag{3.19}$$

This generally occurs in less than 50 iterations.

The new cell boundary is then given by

$$\begin{aligned} r(t+\Delta t) &= r(t) + v_r \Delta t \\ z(t+\Delta t) &= z(t) + v_z \Delta t \end{aligned} \tag{3.20}$$

The value for Δt was set relative to the Courant number for each iteration, such that fluid flow occurs over at most 10% of any individual element (Appendix E). In the continuum adhesion case (no discrete adhesion sites), the contact line is updated at each time step by computing the intersection between the cell boundary and the surface, then adding all points advected to $z \leq 0$ to the Dirichlet boundary condition (contact, no-slip) for the next time step. In the discrete adhesion model, contact is determined by the distance threshold computed from Eq (3.12). The contour is smoothed after each advection, and then small corrections are made to the cell contour to compensate for any deviations from constant volume due to smoothing and numerical error.

This model was implemented in MATLAB R2020b (MathWorks) and the full code is available at https://github.com/emmetfrancis/phagocyticSpreading. Individual simulations generally run within 1-3 hours on a personal computer.

Acknowledgements

We thank Dr. Robert Guy from UC Davis Mathematics for many helpful conversations on various iterations of our model and for assistance with the derivation found in Appendix B. We also thank Dr. Marc Herant for fruitful discussions on computational modeling of motile cells and Dr. Vasilios Morikis for his feedback on early versions of this manuscript.

Videos S1 to S6 are accessible at https://github.com/emmetfrancis/phagocyticSpreading.

Chapter 4: Extension of chemotactic pseudopods by nonadherent human neutrophils does not require or cause calcium bursts

Abstract

Global bursts in free intracellular calcium (Ca^{2+}) are among the most conspicuous signaling events in immune cells. To test the common view that Ca^{2+} bursts mediate rearrangement of the actin cytoskeleton in response to the activation of G protein–coupled receptors, we combined single-cell manipulation with fluorescence imaging and monitored the Ca^{2+} concentration in individual human neutrophils during complement-mediated chemotaxis. By decoupling purely chemotactic pseudopod formation from cell-substrate adhesion, we show that physiological concentrations of anaphylatoxins such as C5a induce nonadherent human neutrophils to form chemotactic pseudopods but do not elicit Ca^{2+} bursts. In contrast, pathological or supraphysiological concentrations of C5a often triggered Ca^{2+} bursts, but pseudopod protrusion stalled or reversed in such cases, effectively halting chemotaxis, similar to sepsis-associated neutrophil paralysis. Further inspection of the mechanoregulatory role of Ca^{2+} bursts revealed that the maximum increase in cell surface area during pure chemotaxis was much smaller—by a factor of 8—than the known capacity of adherent human neutrophils to expand their surface. Because this limited deformability could not be accounted for by the measured values of the resisting cortical tension, we attribute it to a reduced ability of the cytoskeleton to generate protrusive force. Thus, we hypothesize that Ca^{2+} bursts in neutrophils control a mechanistic switch between two distinct modes of cytoskeletal organization and dynamics. A key element of

this switch appears to be the expedient coordination of adhesion-dependent lock or release events of cytoskeletal membrane anchors.

Introduction

Calcium ions (Ca^{2+}) participate in many interactions between and within biomolecules. As a consequence, the cytoplasmic Ca^{2+} concentration in biological cells is an exceptionally potent effector of cellular behavior. Unlike the voltage-gated channels of electrically excitable cells, the Ca^{2+} channels of immune cells have long been thought to be actuated biochemically [133-138]. In addition, flow chamber experiments have demonstrated that Ca^{2+} channels can also respond to mechanical stimulation of immune cells by shear flow [139-142].

The majority of existing work on Ca^{2+} signaling in immune cells has focused on the identification of channels and adapter molecules that regulate Ca^{2+} dynamics, and some studies have begun to address the molecular mechanisms that govern Ca^{2+} fluxes [143-150]. The activation of G protein–coupled receptors (GPCRs) by chemoattractants [134-138, 148, 151-155] and the ligation of phagocytic [21, 25, 150, 156-160] or adhesive [139, 142, 143, 161] receptors have been implicated as primary causes of distinctive Ca^{2+} surges frequently observed in immune cells. But whereas the involvement of adhesive and phagocytic receptors in such transient signaling bursts seems well established, the notion of a causal relationship between chemotactic GPCR activation and Ca^{2+} bursts conflicts with a small number of studies that have reported GPCR-mediated immune cell chemotaxis without such bursts [27, 28].

We employed an interdisciplinary strategy to complement previous efforts by seeking to understand Ca^{2+} bursts in the context of their physiological role in critical immune processes.

Questions of interest include, for example: what are the original causes of Ca^{2+} bursts? When exactly do Ca^{2+} bursts occur, and why do they occur at those particular times? What are the major consequences of a Ca^{2+} burst, and which cellular functions depend on them? Such questions touch upon the core of our understanding of immune cell behavior, yet they are rarely addressed in the literature and generally lack definitive answers. Our knowledge gaps are especially wide when it comes to the most important study subjects of immunology—humans—whose immune cells cannot be cultured or genetically manipulated.

We applied a single-live-cell, single-target assay [13, 122, 162] to examine intracellular Ca^{2+} concentrations during controlled one-on-one encounters between neutrophils—the most abundant type of human white blood cell—and pathogenic surfaces. Our results invite a careful reevaluation of some common assumptions about Ca^{2+} signaling in immune cells. Therefore, it is crucial to bear in mind the definitions and experimental conditions that underlie our results. First, all our experiments use human neutrophils. To ensure that all experiments start from a common baseline, we always strive to maintain the neutrophils in a nonadherent, initially quiescent state. We use the term "pure chemotaxis" to denote an autonomous cell deformation induced by a gradient of chemoattractant in the absence of adhesion to a substrate. In other words, we examined purely chemotactic recognition and protrusion in a manner that rules out interference or bias caused by substrate adhesion, which also eliminated the possibility that adhesive bonds or the application of a pulling force to these bonds might induce Ca^{2+} bursts in our experiments.

We define a Ca^{2+} burst as a rapid, global, and large increase of the intracellular Ca^{2+} concentration. In all experiments reported here, occurrences of these bursts were distinctive all-or-nothing events, meaning that the mean fluorescence intensity (MFI) corresponding to the

intracellular Ca^{2+} concentration increased by at least a factor of 2.5 within a few seconds, in contrast to much smaller intensity changes that are slight in comparison. The present study focuses on Ca^{2+} bursts in the context of complement-mediated, pure chemotaxis. Although we frequently allowed neutrophils to phagocytose target particles at the end of single-live-cell experiments, the detailed analysis of this final stage is beyond the scope of this study. Relying on the well-established occurrence of Ca^{2+} bursts during phagocytosis [21, 25, 150, 155, 156, 159, 160], we simply use the phagocytic stage as a built-in, per-cell positive control.

Complement-directed chemotaxis is the predominant mechanism by which immune cells locate and home in on nearby pathogenic bacteria and fungi [163]. As part of the host's innate immune defense, fragments of serum-based complement proteins assemble into proteases on recognized pathogen surfaces. These convertases cleave other complement proteins to produce and release small chemoattractant peptides called anaphylatoxins which stimulate chemotactic receptors on immune cells [164]. Among the three anaphylatoxins C5a, C3a, and C4a, the most potent inflammatory peptide is C5a [165]. Its acute physiological relevance is underlined by its involvement in sepsis [166-170] and various other diseases [165]. Remarkably, the physiological concentration of C5a is uncertain because it is difficult to quantify C5a separately from its less active, desarginated form C5a(desArg). Reported C5a-concentrations in healthy donors ranging from 0.25 nM to 0.76 nM [171-173] usually represent the values of total concentrations of C5a and C5a(desArg) combined. Realistic estimates of the dynamics of C5a desargination reveal that C5a is rapidly metabolized by carboxypeptidases under physiological conditions and that appreciable amounts of C5a are expected to persist only within a thin anaphylatoxic cloud surrounding complement-recognized particles [163, 174]. This implies that systemic physiological concentrations of C5a are actually extremely low, perhaps even

negligible, as also supported by reports that picomolar C5a concentrations suffice to elicit a strong response by adherent neutrophils [175, 176]. In this study, we define "physiological concentration" in a simple empirical manner, based on the normal response of human neutrophils to nearby pathogenic targets under conditions where anaphylatoxins are produced and degraded naturally by the supplemented autologous donor serum.

Results

Absence of Ca^{2+} bursts during complement-mediated, pure chemotaxis

Our pure chemotaxis assay uses micropipette manipulation or optical tweezers to maneuver bacterial, fungal, or surrogate target particles into the proximity of nonadherent, initially quiescent human neutrophils [13]. If chemoattractants emanate from the target surface and stimulate a nearby neutrophil, the neutrophil extends a chemotactic process toward the target. This morphological change is readily observed microscopically and serves as a straightforward readout of the neutrophil's chemotactic activity, as demonstrated for a selection of previously studied bacterial and fungal target pathogens (Fig 4.1A-C) [38, 177]. Thus the neutrophils serve as ultrasensitive biodetectors of minuscule amounts of chemoattractant produced at the target surface (Fig 4.1D) [174].

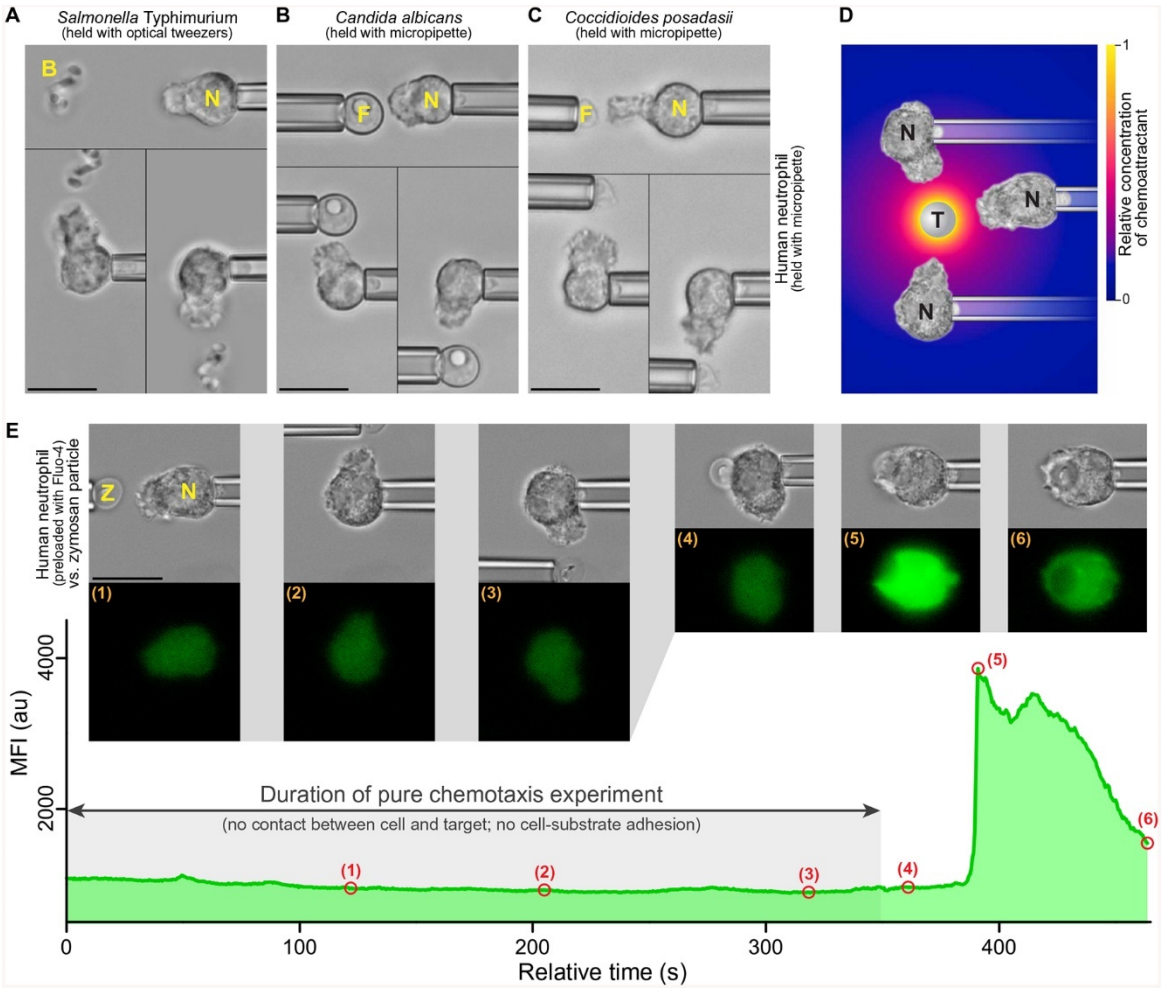

Fig 4.1. Complement-mediated, pure chemotaxis and Ca^{2+} bursts. (A-C) Examples of single-live-cell, pure-chemotaxis experiments [38, 177] in which human neutrophils (N) were placed near bacterial (B) or fungal (F) pathogens. The nonadherent neutrophils were held with gentle suction pressure at the tip of a micropipette and placed near a cluster of *Salmonella* Typhimurium bacteria trapped with optical tweezers (A), a single *Candida albicans* cell held with a micropipette (B), or a single *Coccidioides posadasii* endospore held with a micropipette (C). Each panel is a composite of 3 video images depicting the changes in neutrophil morphology in response to the placement of the pathogenic target at different sides of the cell. **(D)** The complement system in the serum of the host assembles complement complexes on the surface of foreign target particles (T). Some of these complexes, such as the C5 convertase, are enzymes that cleave other serum proteins and release anaphylatoxins, which are highly potent chemoattractants, such as C5a. The radial concentration profile of anaphylatoxins surrounding the target (color gradient) forms rapidly but has a limited spatial reach [163, 174]. Neutrophils (N) detect this anaphylatoxic cloud and respond by extending chemotactic pseudopods toward the target. **(E)** Example measurement of the time course of the mean fluorescence intensity (MFI) of the Ca^{2+} indicator Fluo-4 during pure chemotaxis of a human neutrophil (N) toward a pipette-held zymosan particle (Z) and eventual phagocytosis of the particle. Included are brightfield and fluorescence images taken at the time points numbered (1)-(6) in the MFI graph. The MFI remained low and essentially flat throughout the chemotaxis stage but exhibited a steep increase caused by a Ca^{2+} burst after the zymosan particle was brought into physical contact with the neutrophil. (See also Movies 4.1-4.3.) Scale bars, 10 μm.

In all cases where neutrophils extended chemotactic protrusions, this cell response required the presence of host serum in the medium, confirming that the chemoattractants inducing the neutrophil response did not originate from the targets themselves but were produced by the host's complement system. For bacterial targets such as *Salmonella* Typhimurium and *Escherichia coli*, the fungal targets *Coccidioides posadasii* and *Candida albicans*, and surrogate model particles made from cell walls of yeast (zymosan) or from microbial cell-wall polysaccharides (β-glucan), this type of microbe-directed chemotaxis was predominantly mediated by the anaphylatoxin C5a [38, 165, 177]. For example, blocking the C5a receptor CD88 or using C5-deficient serum diminished this chemotactic activity of neutrophils, and replacing the normal serum with heat-treated (at 52°C) autologous serum abolished it completely, even though the neutrophils still phagocytosed the targets after physical contact [38, 162, 177]. These findings confirm the broadly accepted view that C5a is the dominating chemoattractant in complement-mediated chemotaxis by neutrophils [165]; however, other anaphylatoxins are also expected to participate in this process to some extent. Bearing in mind that all complement pathways result in the production of anaphylatoxins, and assuming that the purely chemotactic neutrophil response examined in this study is common to all anaphylatoxins, we do not explicitly distinguish between different species of these chemoattractants here.

This study combines our pure-chemotaxis assay with fluorescent monitoring of the intracellular Ca^{2+} concentration of individual human neutrophils (Fig 4.1E). A dual-camera setup allowed us to simultaneously record brightfield and fluorescence images of single-live-cell experiments (Fig G.1, Materials and Methods). The neutrophils were preloaded with the fluorescent Ca^{2+} dye Fluo-4, following a protocol that reduced the dye's side effects in the current setting as much as possible (Materials and Methods). To mimic interactions between

complement proteins in the host serum and fungal pathogen surfaces, we used model particles made from yeast cell walls (zymosan) and from the microbial polysaccharide β-glucan as targets in buffer supplemented with normal, autologous serum. These model targets are known to activate the complement cascade, which results in the production of C5a and other chemoattractant peptides [122, 162, 163, 174]. Immunoglobulin G (IgG)-coated beads were used as a control. In each single-cell experiment we first placed the particle near the neutrophil and observed the purely chemotactic neutrophil response for ~5-10 minutes, and then placed the particle in contact with the cell.

In agreement with previous results [38], the neutrophils exhibited vigorous chemotactic activity in response to stimulation with zymosan or β-glucan particles but did not chemotax toward the IgG-coated beads (Fig 4.2A-C, Movies 4.1-4.3). All three target types readily adhered to the cells upon contact and triggered phagocytosis. We observed Ca^{2+} bursts in all experiments with targets of at least ~3μm in diameter, independent of the type of target particle. In all cases, however, the Ca^{2+} burst occurred only after the target had been brought into contact with a neutrophil (Fig 4.2A-C), usually when phagocytosis was already underway. Importantly, this final, phagocytic stage of our integrative recognition assay confirmed that each neutrophil was viable and that the cell's Ca^{2+} signaling machinery was intact.

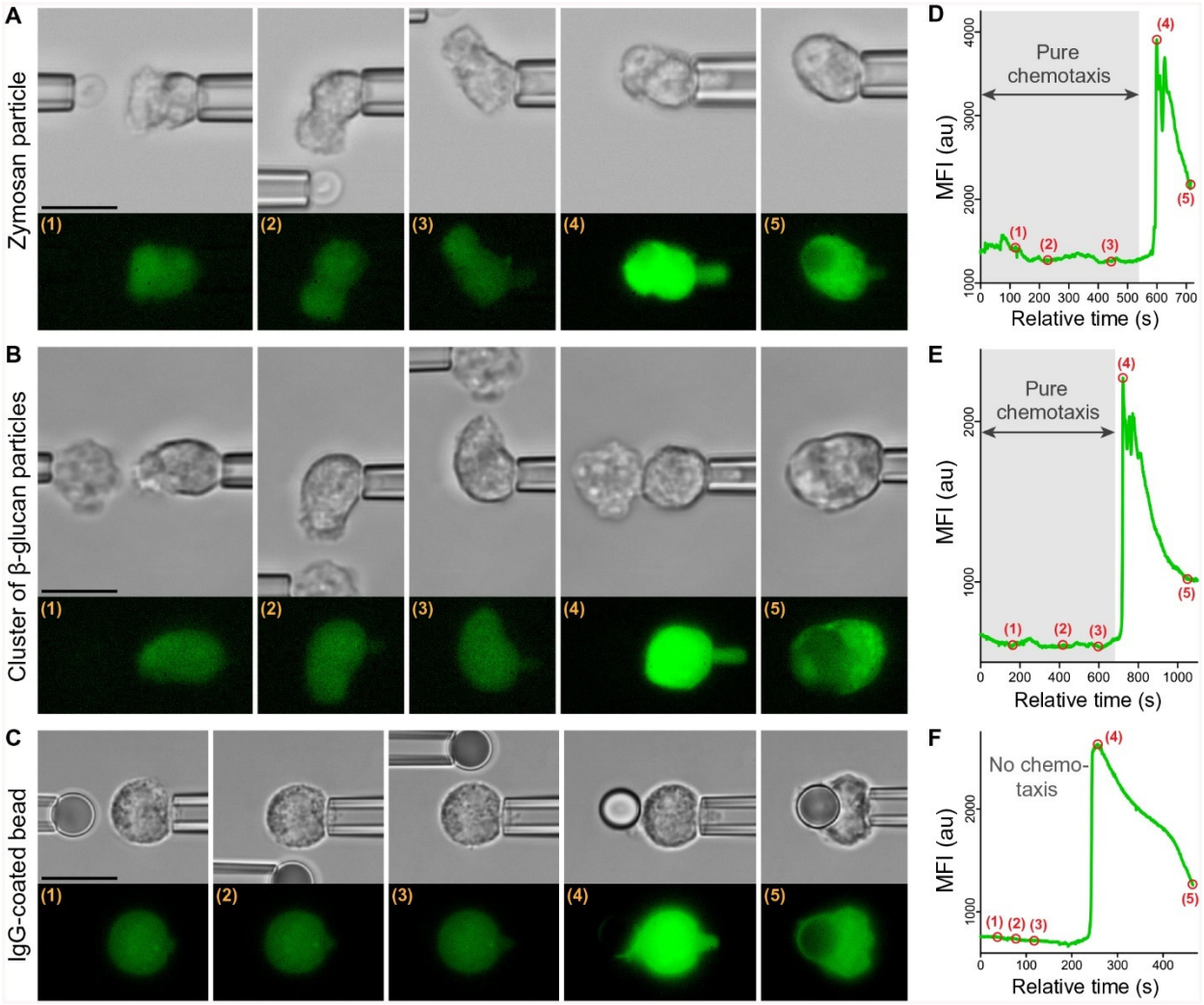

Fig 2. Absence of Ca^{2+} bursts during pure chemotaxis. Three representative examples show experiments that examined the response of individual pipette-held neutrophils to zymosan particles (A and D), β-glucan particles (B and E), and IgG-coated beads (C and F) using the dual-micropipette assay introduced in Fig 1E. **(A-C)** Filmstrips combine brightfield and fluorescence images of experiments in which a target (held in the left pipette in each image) was first placed near and eventually in contact with a neutrophil (held at the right in each image). The test with β-glucan (B) depicts an experiment using a cluster of β-glucan particles but is representative of experiments with both clusters as well as individual β-glucan particles. **(D-F)** The graphs show the time course of the MFI of Fluo-4 corresponding to the intracellular Ca^{2+} concentration during the experiment. The numbered points on the graphs mark the times at which the respective images in (A-C) were taken. During single-cell experiments with the fungal model particles, the shown neutrophil behavior—chemotaxis without a Ca^{2+} burst followed by phagocytosis with a Ca^{2+} burst—was observed in 34 (out of $N=36$) experiments with zymosan (A and D) and in 16 (out of $N=19$) experiments with β-glucan particles (B and E). The shown neutrophil response to an antibody-coated bead—no chemotaxis but phagocytosis that then triggered a Ca^{2+} burst (C and F)—was observed in all $N=43$ experiments with these beads. (See also Movies 4.1-4.3.) Scale bars,10 μm.

Each Ca^{2+} burst manifested as a rapid surge in fluorescence intensity that extended throughout the cell and exhibited similar features for all three target types (Fig 4.2D-F). Despite recording fluorescence images at 0.5 s intervals, using a camera exposure time of 100 ms or less, we never observed a gradual directional spreading of fluorescence across a cell. Instead, the fluorescence intensity increased throughout the neutrophil at about the same rate, reaching its peak within a few seconds. Surprisingly, Ca^{2+} bursts never occurred during the earlier, pure-chemotaxis stage of our experiments with zymosan or β-glucan particles, even when cells were stimulated with clusters of β-glucan particles. Although the cells formed pronounced protrusions during this stage, variations in the measured mean fluorescence intensity of Fluo-4 during pure chemotaxis were small and usually negligible compared to the surge of intensity observed later during phagocytosis (Figs. 4.1E and 2). Thus under the near-physiological conditions used in these experiments, complement-mediated chemotaxis does not trigger global intracellular Ca^{2+} bursts in nonadherent human neutrophils. In other words, stimulation of the GPCRs of anaphylatoxins by physiological concentrations of their ligands alone is insufficient to induce Ca^{2+} bursts in situations such as mimicked here. Moreover, the type of actin remodeling that accompanies the formation of purely chemotactic pseudopods neither requires nor causes Ca^{2+} bursts.

Anticorrelation of Ca^{2+} bursts and chemotactic protrusion

The observed absence of Ca^{2+} bursts during complement-mediated, pure chemotaxis of neutrophils agrees with a previous study that demonstrated neutrophil chemotaxis without Ca^{2+} bursts in a gradient of the chemotactic peptide formyl-Met-Leu-Phe (fMLP) [27]. But the same study also reported that Ca^{2+} bursts did eventually occur when the chemotaxing neutrophils encountered very high concentrations of fMLP [27]. Prompted by this observation, we tested

whether we could force the occurrence of Ca^{2+} bursts by exposing nonadherent neutrophils to concentrations of C5a higher than those generated by the presence of zymosan or β-glycan particles in serum. We modified our dual-micropipetting system by replacing the target-holding pipette (the left pipette in Figs. 4.1 and 4.2) with a micropipette filled with a buffer containing C5a [178, 179], which allowed us to apply jets of C5a solutions to individual, nonadherent neutrophils.

It is important to note that various issues handicap the unambiguous interpretation of this type of jet experiment. In short, the cells are not only stimulated by chemoattractant, but also by fluid shear flow. Moreover, neither the concentration gradient of chemoattractant nor the fluid flow profile experienced along the cell surface are generally well known, in contrast to the clear picture established for single-cell, single-target experiments (Figs. 4.1 and 4.2) [163].

To determine whether high concentrations of C5a triggered Ca^{2+} bursts, we first subjected human neutrophils resting on the chamber bottom to jets of a 0.1 μM solution of C5a. All tested cells indeed responded to these C5a jets with strong bursts of Ca^{2+} (Fig G.2). Remarkably though, the cells did not exhibit noticeable chemotactic deformations. Instead, cells that initially appeared smooth in microscopic images before the application of the C5a jet tended to develop visible surface ruffles without any directional preference after the Ca^{2+} burst elicited by the C5a jet.

Next, we used our modified setup to apply C5a jets to pipette-held neutrophils (Fig 4.3A-C, Movie 4.4), varying the C5a concentration, jet pressure, and distance between the C5a pipette and the neutrophil in order to stimulate Ca^{2+} bursts in chemotactically active cells. It is important to bear in mind that the C5a concentration at the cell surface is lower than in the jet pipette due to the fluid flow profile and the metabolization of C5a by carboxypeptidases that are

present in the autologous serum supplement in the chamber buffer. The observed neutrophil responses could be roughly categorized into three types (Fig 4.3A-C). In the first case (Fig 4.3A), the cells responded to ~0.1-10 nM C5a solutions by extending pseudopods toward the source of C5a without generating Ca^{2+} bursts, replicating the behavior of neutrophils encountering target particles under the near-physiological conditions imposed in the previous experiments (Figs. 4.1 and 4.2). In contrast, Ca^{2+} bursts did occur in the other two cases (Fig 4.3, B and C), usually after an increase of the C5a concentration or the jet pressure experienced at the cell surface. Almost all observed bursts exhibited similar features as described in the previous section, although in some instances (8 out of 26 jet experiments that induced Ca^{2+} bursts), the fluorescence intensity was somewhat stronger in the pseudopod than in the rest of the cell.

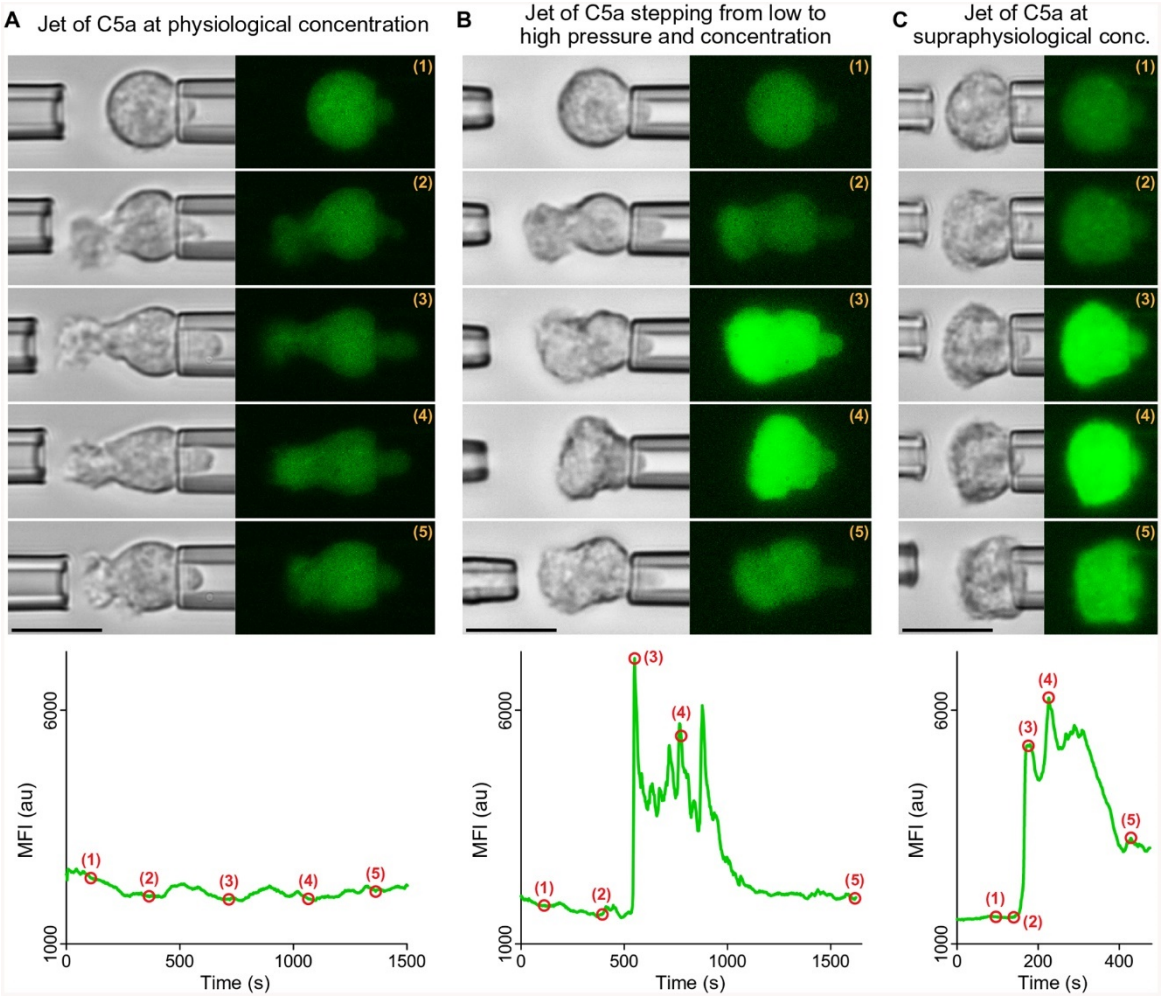

Fig 4.3. Supraphysiological concentrations of C5a or co-stimulation by shear flow can trigger Ca^{2+} bursts in nonadherent neutrophils. Three representative examples show experiments in which jets of C5a solutions were ejected from the left micropipette toward neutrophils held with the right pipette. Filmstrips of brightfield and fluorescence images show snapshots of the neutrophil response at the time points marked by numbers in the included graphs of the MFI of Fluo-4. **(A)** The neutrophil responded to a jet of a 0.1 nM C5a solution by extending a chemotactic pseudopod for more than 25 minutes. No Ca^{2+} burst occurred during this time. (This example is representative of $N = 19$ single-cell experiments.) **(B)** The neutrophil was subjected to a jet of a 10 nM C5a solution. The jet was initially applied with a low pressure over a distance of 7 µm, inducing the extension of a pseudopod. After ca. 9 minutes, a 5-fold increase of the pipette pressure triggered a Ca^{2+} burst, accompanied by a cell contraction in the horizontal direction. After temporary removal of the left pipette, a low-pressure jet was applied once more, causing the cell to resume the protrusion of a directed pseudopod. (This example is representative of $N = 16$ single-cell experiments in which C5a jets induced Ca^{2+} bursts in chemotaxing cells.) **(C)** Application of a low-pressure, 0.1 µM C5a jet from a short distance triggered a Ca^{2+} burst in a pipette-held neutrophil without prior pseudopod extension. In response, the cell appeared to flatten against the pipette. (This example is representative of $N = 10$ single-cell experiments. Movie 4.4 combines single-live-cell videos of the three example experiments included in this figure.) Scale bars, 10 µm.

The second type of neutrophil response was observed at C5a concentrations in the range of ~1-100 nM and comprised cases where pure chemotaxis was initiated before the Ca^{2+} burst occurred (Fig 4.3B). In the third type of response, jets with a C5a concentration of ~0.1 μM or higher that were applied from a short distance induced Ca^{2+} bursts in neutrophils that did not form pronounced chemotactic protrusions (Fig 4.3C). In both cases, the Ca^{2+} burst often appeared to coincide with a noticeable neutrophil contraction in the axial direction defined by the cell and its holding pipette. Further analysis revealed that this axial cell contraction was indeed a common occurrence, observed in 24 out of 26 cases of Ca^{2+} bursts (including cases of arrest of the axial cell extension; Fig 4.4, A and B, and Fig G.3). In a few experiments where we later retracted the C5a pipette or reduced the jet pressure, the cell recovered and resumed the protrusion of pseudopods (time point labeled (5) in Fig 4.3B, second example in Movie 4.4), demonstrating that the contractile change in cell morphology was reversible. Although the concurrence of Ca^{2+} bursts and cellular contraction was often striking (Fig G.3), these observations do not constitute definitive proof of a causal relationship between Ca^{2+} bursts and cell contraction. It is possible that a common original stimulus caused both the burst as well as the contraction in parallel. Yet given that cell contraction and protrusion are opposing types of deformation, we can conclude that Ca^{2+} bursts and purely chemotactic protrusion are anticorrelated.

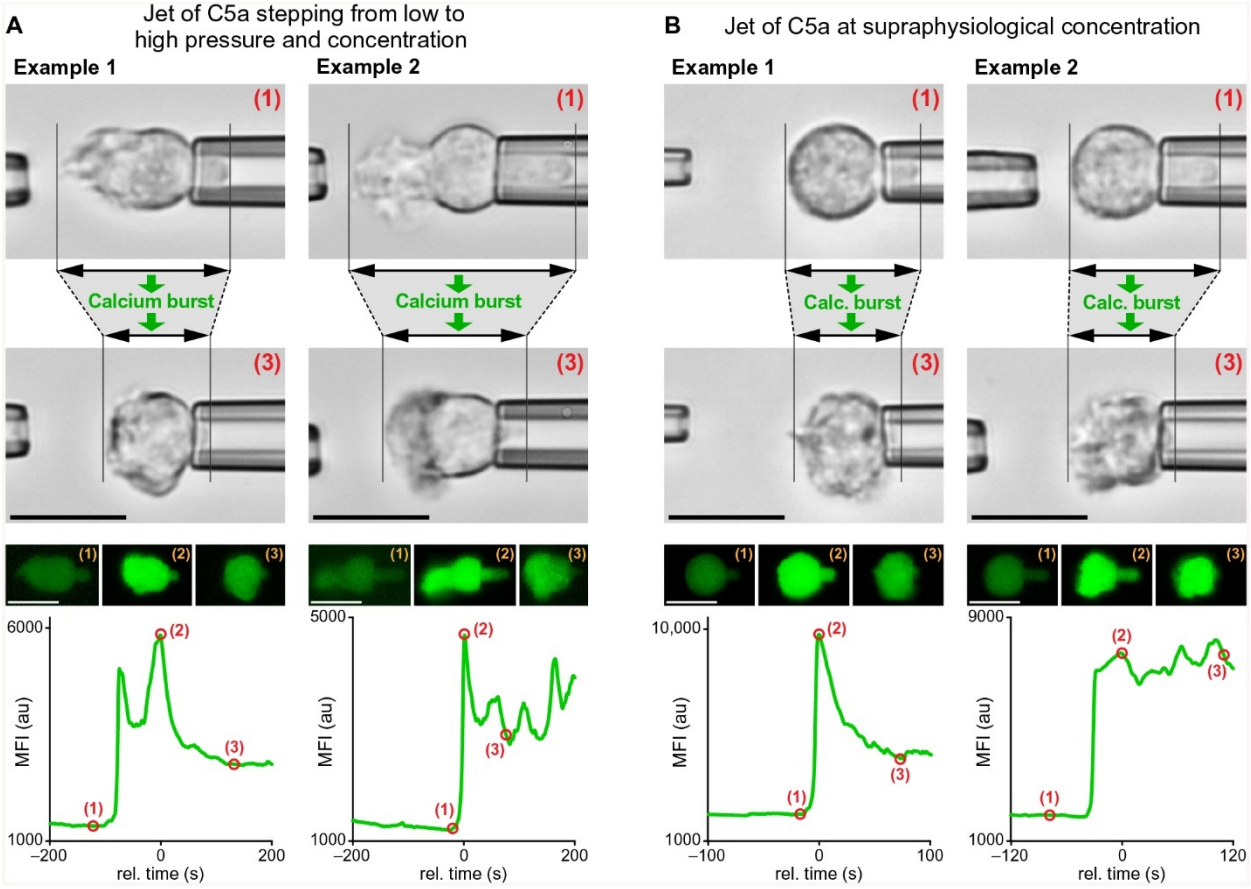

Fig 4.4. Coincidence of Ca^{2+} bursts and axial cell contraction. Representative examples of jet experiments in which C5a solutions were ejected from the left micropipette toward neutrophils held with the right pipette. The brightfield and fluorescence images show the changes of the neutrophil morphology that accompanied Ca^{2+} bursts during two different types of cell response, each illustrated with two examples. The images were taken at the time points marked by numbers in the included graphs of the MFI of Fluo-4. **(A)** Initially chemotaxing neutrophils were subjected to a sudden increase of the jet pressure, which also increased the C5a concentration at their surface. The resulting Ca^{2+} bursts coincided with a contractile morphology change of the cells in the horizontal direction. **(B)** Sudden exposure of neutrophils to jets of supraphysiological concentrations of C5a triggered Ca^{2+} bursts that coincided with a contractile morphology change of the cells. The cells did not extend chemotactic pseudopods in this case. We observed the shown behavior—Ca^{2+} bursts that were accompanied by a decrease or arrest of the total axial cell extension—in 24 (out of $N = 26$) single-cell experiments. (Detailed time courses of such cell contractions are shown in Fig S3.) Scale bars, 10 µm.

Two types of contractile force could govern the contractile change in cell morphology. One is the cortical tension, a force (per unit length) that acts tangential to the cell surface and opposes the expansion of the apparent surface area. The other is a normal force (per unit area) that acts to pull the cell surface inwards in a perpendicular direction. If cortical tension dominated the cell contraction, the resulting Laplace pressure would give rise to a smooth appearance of the cell

surface as well as a cell projection into the cell-holding pipette that fills this pipette and ends in a hemispherical cap. If an inward-pulling force, on the other hand, drove the cell contraction, this would result in a rougher cell surface, including a cell projection in the cell-holding pipette that might pull away from the pipette wall and partially collapse. Careful inspection of our videomicrographs revealed a mixture of these morphological features, indicating that both types of force contributed to the observed cell contraction.

Limited cell deformation during pure chemotaxis

Although the above experiments confirmed that high concentrations of C5a triggered Ca^{2+} bursts in nonadherent neutrophils in vitro, it is unlikely that neutrophils encounter similarly high C5a concentrations in healthy humans. Therefore, it is unclear to what extent the observed contractile morphology contributes to the natural repertoire of neutrophil behavior. It seems plausible that it represents an exaggerated version of some particular aspect of a preprogrammed neutrophil response to anaphylatoxins. The mechanical nature of the cell contraction prompted us to also take a closer look at the mechanical features of the purely chemotactic cell response under near-physiological conditions where Ca^{2+} bursts do not occur (Figs. 4.1, 4.2, and 4.3A).

An intriguing difference between the cell deformations accompanying pure chemotaxis and those accompanying phagocytosis or cell migration became evident when we quantified the increase in the apparent cell surface area during the formation of purely chemotactic pseudopods. For comparison, human neutrophils are able to increase their apparent surface area to up to 250-300% of their initial resting surface area during osmotic swelling [180] or phagocytosis [38, 181]. To establish how changes in surface area during pure chemotaxis compared to this value, we developed an image-analysis procedure that allowed us to estimate the cell surface area of

neutrophils in suitable video images. Our analysis is based on the assumption that the visible 2-dimensional (2D) outline of the cell represents a cross-section of a rotationally symmetric 3-dimensional (3D) object, and that this cross-section contains the symmetry axis (Fig G.4). This assumption seemed reasonable for many, but not all, video images. Images of cells that were too irregular to be approximated by a rotationally symmetric object were excluded from the analysis. We used this analysis to quantify the time course of the cell surface area during pure chemotaxis, as demonstrated for a neutrophil extending pseudopods toward a pipette-held zymosan particle (Fig 4.5A), and to determine the maximum cell surface area during this process. In addition to our current experiments with target particles and C5a jets, we also estimated the maximum surface area increase of neutrophils during the formation of particularly large pseudopods from images of previous pure-chemotaxis experiments that were performed with various bacterial, fungal, and model targets without Fluo-4 imaging (Fig 4.5B).

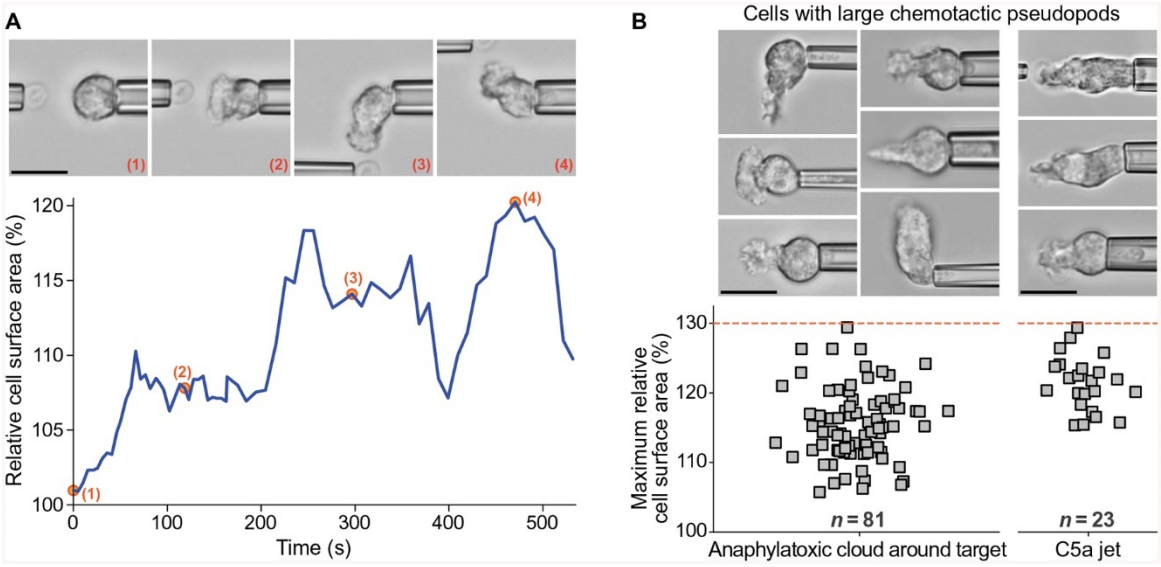

Fig 5. Limited surface-area expansion during pure chemotaxis. (A) The graph shows an example of the time-dependent surface area of a neutrophil during pure chemotaxis toward a pipette-held zymosan particle. Representative video snapshots that were taken at the time points marked by numbers are included. **(B)** The column-scatter plots show of the values of the maximum cell surface area measured during pure chemotaxis in previous and current experiments with target particles ($N = 81$) and during current jet experiments ($N = 23$), respectively. The upper limit of these values is indicated by a dashed red line. Example videomicrographs of cells extending large chemotactic pseudopods are included. (Our approach to measure the cell surface area is illustrated in Fig G.4.) Scale bars, 10 µm.

This analysis revealed that the cells rarely expanded their apparent surface area by more than ~25%, and never by more than 30%, during pure chemotaxis (Fig 4.5B). This limit is much smaller—by a factor of ~8—than the maximum capacity of human neutrophils to expand their surface area [38, 181]. However, this value coincides with the amount of mechanical slack exhibited by the cortex of these cells. Human neutrophils are known to accommodate surface-area expansions of up to ~30% without having to cope with a significantly increased mechanical resistance [182]. Larger changes of the surface area, however, require a much stronger outward push by the cytoskeleton in order to overcome the rising cortical tension and other contractile forces [13, 182].

The limited ability of nonadherent neutrophils to expand their surface area could thus be due to insufficient protrusive force generation or prohibitive resistance by contractile forces. In view of the peculiar cell contraction induced by high concentrations of C5a (Figs. 4.3, B and C, and 4.4, and Fig G.3), we next addressed whether physiological concentrations of anaphylatoxins might suffice to cause an abnormal rise of the cortical tension. Using a previously developed method (Fig 4.6A) [86, 182], we estimated the effective cortical tension during the formation of chemotactic pseudopods in the absence of Ca^{2+} bursts (Fig 4.6B). With very few exceptions, the measured tensions were within the expected range and consistent with the respective cell surface areas (Fig 4.6, B and C) [182]. We therefore conclude that it is not an excessive cortical tension, but a limited ability to generate protrusive force, that prevents nonadherent neutrophils from expanding their surface area by more than ~30% during pure chemotaxis. The decisive prerequisite for larger surface expansions therefore appears to be cell adhesion to a substrate or target particle. A possible explanation for this requirement is the hypothesis that adhesive bonds anchor adjacent cytoskeletal filaments to the substrate or particle and nucleate a local increase in

the rigidity of the cytoskeleton by promoting local actin crosslinking and polymerization. The resulting anchored and rigid cytoskeleton then provides the bracing support that is necessary for stronger protrusions of nonadherent patches of the cell surface.

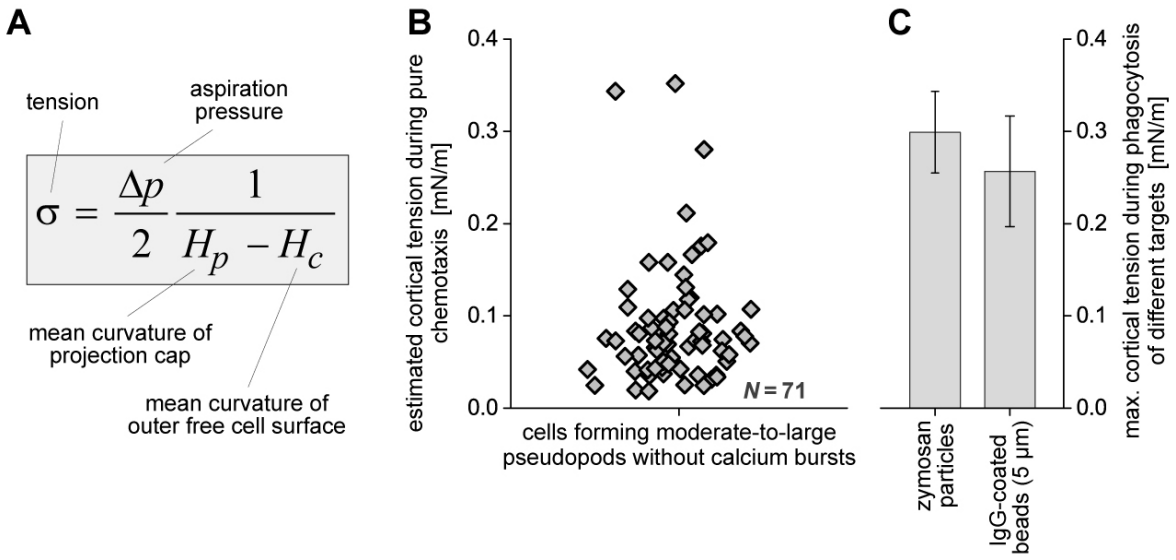

Fig 4.6. Effective cortical tension during pure chemotaxis. (A) The well-known equilibrium equation for converting the measured aspiration pressure Δp to the tension σ of a pipette-held fluid membrane capsule follows from Laplace's law. If the length of the cell projection into the pipette exceeds the pipette radius R_p, the mean curvature $H_p = 1/R_p$. For the mean curvature H_c, we here use the inverse radius of a sphere that approximates the outer part of the cell. **(B)** This column-scatter plot presents a total of $N = 71$ individual measurements of the cortical tension of nonadherent neutrophils extending chemotactic pseudopods (without calcium bursts). Because of the dynamic nature of the cell shape and other uncertainties in the current experiments, these values are crude estimates. **(C)** For direct comparison with our current data, we here include previously measured mean values (error bars denote standard deviations) of the maximum cortical tension of human neutrophils phagocytosing zymosan particles or antibody-coated beads (5 µm in diameter) [12].

Discussion

Ca^{2+} bursts in immune cells represent a highly distinctive signaling mechanism that conducts a signal throughout the entire cell extremely rapidly. The return of the released Ca^{2+} into storage compartments such as calciosomes or the endoplasmic reticulum requires ATP-dependent pumps and is energetically costly. Therefore, massive global Ca^{2+} bursts are unlikely to occur very frequently, in contrast to the common involvement of Ca^{2+} ions in local cell functions. Despite this distinctive nature, the question which physiological immune-cell functions cause or require

Ca^{2+} bursts remains unanswered and merits closer attention. It is reasonable to assume that the underlying physiological events occur only occasionally and tend to engage the whole cell. Given the prominence and easy detectability of Ca^{2+} bursts, a better understanding of the underlying events could provide a valuable foundation for new insights and tools in biomedical research and clinical diagnostics.

A closer look at the cause-and-effect sequences or mechanisms governing Ca^{2+} bursts in motile immune cells benefits greatly from a reductionist approach that separates recognition of chemotactic cues from other elements of chemotactic cell migration such as cell-substrate adhesion. Unlike other chemotaxis assays, our single-live-cell, pure-chemotaxis experiments were designed for this purpose. As a consequence, we were able to establish that complement-mediated, pure chemotaxis neither requires nor causes Ca^{2+} bursts, consistent with previous studies that used formyl peptides to stimulate chemotaxis of adherent neutrophils (32, 33). Inasmuch as chemoattractant gradient sensing and pseudopod formation can be viewed as local processes, our result agrees well with the assumption that Ca^{2+} bursts are linked to global cellular events.

Having ruled out that the ligation of GPCRs of anaphylatoxins acts as a direct biochemical cause of Ca^{2+} bursts under physiological conditions, we pursued two lines of further enquiry. First, we forced the occurrence of Ca^{2+} bursts in nonadherent neutrophils by subjecting the cells to jets of solutions containing supraphysiological concentrations of C5a. Second, we examined mechanical aspects of the cell behavior during pure chemotaxis. Although our jet experiments revealed important qualitative insights, their quantitative interpretation is difficult. Ever-present pressure drifts in the open experiment chamber make it impossible to completely stop flow through the C5a pipette over an appreciable amount of time. To avoid contamination of the

chamber, we therefore maintained a slightly negative pressure in the C5a pipette between actual single-cell tests. As a consequence, the exact moment when, after pressure reversal, the ejected jet starts delivering C5a is unknown. Furthermore, neither the concentration of C5a reaching the front of the cell, nor its gradient along the cell surface, are accurately known, for the following reasons. First, carboxypeptidases in the supplied donor serum rapidly metabolize C5a [163]. Second, the flow rate at which the C5a solution is expelled from the pipette tip is difficult to assess because it depends on the pipette geometry and possible additional flow bottlenecks in the pressure system. Third, the flow profile of the jet is affected by nearby walls and the changing cell shape. In addition to these uncertainties regarding the biochemical stimulation of the cells, it is also important to bear in mind that human neutrophils can sense and be activated by fluidic shear flow alone [139-142, 183-185].

Our jet experiments identified two causal stimuli of Ca^{2+} bursts in nonadherent neutrophils: *(i)* co-stimulation of the cells by a combination of fluid shear flow and moderate C5a concentrations (typically on the order of 1-10 nM), and *(ii)* high C5a concentrations alone (on the order of 0.1 μM or more). These observations are qualitatively consistent with the behavior of adherent neutrophils, which have been shown to be able to sense shear flow [183-185] and to exhibit Ca^{2+} bursts in response to a combination of shear flow and the chemoattractants interleukin 8 (IL-8) [139] or fMLP [140]. Moreover, adherent human neutrophils are able to chemotax without Ca^{2+} bursts when stimulated by low concentrations of fMLP, whereas high fMLP concentrations triggered Ca^{2+} bursts and stopped chemotaxis [27]. (In the latter study, the neutrophils might also have been co-stimulated by shear flow.) It is worth noting that the similarities between previously published studies and our findings exist despite the use of different chemoattractants. In general, one may not take for granted that different

chemoattractants elicit a common neutrophil response. In fact, different chemoattractants can activate distinct—and even mutually inhibitory—signaling processes in the same cell [175, 176]. Moreover, the quantitative interpretation of similarities between adherent and nonadherent cells is problematic because most types of adhesion to a substrate or phagocytic target cause activation of immune cells. For example, the release of reactive oxygen intermediates can vary up to 100-fold between adherent and nonadherent neutrophils under otherwise identical conditions [186].

As part of our second line of enquiry, we carefully examined the cell morphology during pure chemotaxis under near-physiological conditions where no Ca^{2+} bursts occurred. Quantifying the degree of cell deformation in terms of the increase of the apparent cell surface area, we discovered a large (~8-fold) difference between the increase in surface area due to purely chemotactic deformations and the enormous capacity of these cells to change their shape during adhesion-dependent processes such as phagocytosis or migration. Perhaps the most interesting outcome of this quantitative assessment was the coincidence between the maximum surface-area expansion measured during pure chemotaxis (30%) and the amount of cortical slack that neutrophils are known to possess [182]. This result implies that the largest protrusive forces that nonadherent neutrophils can generate are much lower than the forces that adherent neutrophils are able to produce [13].

Together, these experiments expose two seemingly contradictory mechanical correlates of Ca^{2+} bursts. The limited extent of protrusion in the absence of Ca^{2+} bursts (Fig 4.5) implies that such bursts might be a prerequisite for larger protrusive deformations. In contrast, when Ca^{2+} bursts did occur in our jet experiments, the accompanying cell deformation opposed protrusion (Figs. 4.3, B and C, and 4.4, and Fig G.3). It is important to bear in mind though that the high concentrations of C5a required to trigger Ca^{2+} bursts in nonadherent neutrophils are unlikely to

be encountered in vivo. A quantitative analysis of C5a production under near-physiological conditions showed that the highest concentrations of C5a are found in the immediate vicinity of pathogenic particles [163]. On the other hand, this analysis also showed that the C5a concentration correlates positively with the particle size. Therefore, the concentrations of both C5a as well as the derived C5a(desArg) are expected to rise during infections. C5a(desArg) binds to the C5a receptor with a lower affinity than C5a, but high concentrations of C5a(desArg) still significantly contribute to immune-cell activation [187]. It is therefore possible that in pathological situations, the total concentration of C5a and C5a(desArg) reaches values high enough to stall chemotaxis by the same mechanism that causes the contractile cell deformation reported here. Indeed, high C5a concentrations are an important factor in the neutrophil paralysis that is observed in sepsis [166-170]. Thus, the type of single-cell experiments presented here could provide an instructive window into the behavior of immune cells during sepsis and other pathological conditions.

Both tangential as well as normal (perpendicular) surface forces are responsible for the peculiar cell deformation that accompanies Ca^{2+} bursts in nonadherent neutrophils. If we conceptually translate these forces to neutrophils that adhere to a substrate or phagocytic target under physiological conditions, their actual role becomes clearer. As part of a "push-and-lock" mechanism [13], the normal force stabilizes adhesion by flattening the cell against the substrate or particle [155], thus locally counteracting protrusive forces that would otherwise lift the cell off the substrate or push phagocytic targets away. The tangential force, or cortical tension, acts globally to pull phagocytic particles into the cell [13] or to reel in the trailing end of a cell crawling on a substrate. Our results (Figs. 3, B and C, and 4) suggest that exposure of

neutrophils to excess C5a causes a mechanical imbalance that boosts the contractile forces beyond the ability of protrusive forces to keep pace.

Central to the balance between contraction and protrusion are cytoskeletal membrane anchors, which are structural linkages that connect the cytoplasmic domains of transmembrane receptors to the actin cytoskeleton either directly or through adapter proteins [11, 13, 122]. The function of many of these linkages involves Ca^{2+}. Examples include the cleavage of anchor components by proteases like calpain [29, 188-190], the interaction of β2-integrins with Ca^{2+} channels [139-141, 143, 157, 158], and the involvement of moesin in P-selectin glycoprotein ligand-1 (PSGL-1)-mediated Ca^{2+} signaling [142]. Complement receptor 3 (CR3, also known as Mac-1, CD11b/CD18, and $\alpha_M\beta_2$ integrin) seems particularly suited to function as a mechanistic switchboard in the regulation of Ca^{2+}-related neutrophil deformations [143, 157, 158]. CR3 is one of the most promiscuous immune cell receptors [191, 192], capable of funneling a multitude of stimuli into one or a few common response pipelines. Not only does the affinity of CR3 depend on divalent cations, it can also be adjusted by conformational changes induced by extracellular as well as intracellular stimuli, including the exposure to C5a and the ligation of other phagocytic receptors [193]. The number of CR3 molecules on the surface of neutrophils can be increased up to three-fold through exposure to chemokines like fMLP [194] and C5a [195]. Lastly, neutrophils are able to regulate the mobility of CR3 [159, 193, 196], implying that the cells can control the state of the receptor's cytoskeletal anchor. The sum of these features tentatively assigns to structural linkages involving CR3, its sibling lymphocyte function-associated antigen 1 (LFA-1), or similar receptors, along with their cytoskeletal anchors, a pivotal mechanistic role in the governance of Ca^{2+} bursts in immune cells.

In summary, pure chemotactic protrusion under physiological conditions is characterized by

the absences of Ca^{2+} bursts, cell adhesion, and surface area increases beyond the extent permitted by the inherent slack of the neutrophil surface. It is possible that the release of cytoskeletal membrane anchors locally eases the formation of protrusive pseudopods, but this type of assist does not require Ca^{2+} bursts during pure chemotaxis. A qualitatively different mode of cytoskeletal organization and dynamics governs the balance of protrusion and contraction during larger deformations of adherent neutrophils. Maintenance of this balance across various immune cell functions requires the expedient coordination of locking or release of cytoskeletal membrane anchors. We hypothesize that the mechanistic switch between the two modes of cytoskeletal behavior is an adhesion-dependent, global event that is mediated by a Ca^{2+} burst. This hypothesis is consistent with previous interdisciplinary studies of Ca^{2+} bursts in neutrophils [27, 139-142, 155, 159], and agrees well with the established behavior of the cortical tension of these cells [182]. It assigns to Ca^{2+} bursts a primarily mechanotransductory function. Although further dissection of the nature of this mechanistic switch is beyond this study's focus on pure chemotaxis, our findings have taken us closer to a sound understanding of the physiological role of Ca^{2+} bursts in immune cells.

Materials and Methods

Human neutrophil isolation

Written informed consent was obtained from all subjects. The Institutional Review Board of the University of California Davis approved the protocol for this study. Neutrophils were isolated from whole blood of healthy donors by immunomagnetic negative selection using the EasySep Direct Human Neutrophil Isolation Kit (STEMCELL Technologies). First, 25 μL each of the isolation cocktail and the magnetic bead solution were added to a small volume of blood (~0.5

mL) to facilitate cross-linking of cells other than neutrophils to magnetic beads using tetrameric antibody complexes. After 5 minutes, the sample was diluted with phosphate-buffered saline containing 2% fetal bovine serum and 1mM EDTA (EasySep Buffer, STEMCELL Technologies) at a minimum 2:1 ratio, and placed adjacent to a magnet. After 10 minutes, 0.5-1.0 mL of the enriched, lighter-colored neutrophil fraction was carefully transferred into a new test tube, and another 25 µL of the magnetic bead solution was added. After two more 5-minute magnetic separation cycles, the cells were re-suspended in Hank's balanced salt solution containing 1.26 mM Ca^{2+} and 0.9 mM Mg^{2+} (HBSS with Ca^{2+} and Mg^{2+}; Thermo Fisher Scientific) and treated with Fluo-4 as described below.

Fluo-4 labeling of live human neutrophils and reduction of side effects

Fluo-4 (Fluo-4, AM; Thermo Fisher Scientific) was reconstituted in anhydrous dimethyl sulfoxide (DMSO; Thermo Fisher Scientific) at a concentration of 1 µM and stored at 4°C protected from light. For each experiment, 1 mL of isolated neutrophil suspension was incubated with 0.5 µL of Fluo-4 solution at 37°C for 25 minutes, and then re-suspended in HBSS. The labeled cells were gently rotated in a dark container at room temperature until use.

We encountered the following side effects of the fluorescent Ca^{2+} dye Fluo-4. When examining neutrophils preloaded with Fluo-4 under the high-power excitation light provided by a mercury arc lamp, we occasionally observed spontaneous increases of the intensity of the emitted fluorescence without any other sign of neutrophil activation, presumably due to photo or heat activation of the dye. Such false positives were overcome by using, as our standard excitation source, the cyan LED of the SpectraX light engine (Lumencor), strobed at 0.5-second intervals at 10% of its maximum intensity and filtered through an ET480/40x bandpass excitation filter

(Chroma Technology). Despite this low-power excitation, we still frequently observed cell death toward the end of an experiment, usually after a Ca^{2+} burst. This cytotoxic effect of Fluo-4 was noticeably reduced after we decreased the concentration of the dye in the neutrophil-preincubation buffer to half the recommended value. Even then, we found that the cortical tension of the neutrophils was often slightly increased, causing the cells to appear stiffer than in the absence of Fluo-4. Therefore, we cannot exclude that the presence of Fluo-4 affected the values of our quantitative measurements somewhat. However, throughout the relevant stages of our experiments (pure chemotaxis, adhesion, phagocytosis), the time-dependent behavior of neutrophils preloaded with Fluo-4 was the same as in numerous previous experiments without the dye. Therefore, it seems reasonable to assume that Fluo-4 did not qualitatively affect the main results reported here.

Preparation of target particles

Zymosan particles (Sigma-Aldrich) were suspended in phosphate-buffered saline (PBS; IBI Scientific) at 3-10 mg/mL, boiled in a water bath for 30 minutes, washed twice in PBS, and stored at 4°C. On each day of experimentation, the solution was sonicated for 30-60 minutes before use. Whole 1,3/1,6-β-glucan particles (WGP Dispersible; InvivoGen) were suspended in PBS at 2-10 mg/mL. After three washes in PBS, the solution was sonicated for 30-60 minutes. The solution was stored at 4°C. Sonication was repeated on each day of experimentation. Polystyrene microspheres were opsonized with antibody as described previously [182]. In short, beads with 5.0 or 9.7 μm nominal diameter (Duke Standards Microspheres; Thermo Fisher Scientific) were incubated overnight at 4°C in PBS containing 10 mg/mL BSA. After 3 washes in PBS with 0.01% Tween 20 (Calbiochem/MilliporeSigma), the beads were incubated with rabbit polyclonal anti-bovine albumin antibody (Thermo Fisher Scientific) at room temperature

for one hour. The beads were then washed three more times in the PBS/Tween solution, and re-suspended in PBS for storage at 4°C.

Single-live-cell, single-target experiments

An inverted microscope (Zeiss) was equipped with a dual micropipette manipulation system as described previously [86, 197]. The experiment chamber was filled with HBSS with Ca^{2+} and Mg^{2+}. For experiments with zymosan or β-glucan particles, the buffer was supplemented with 20% autologous donor serum. When using opsonized microspheres, the buffer was supplemented with serum or 20 mg/mL bovine serum albumin (BSA; AMRESCO). All experiments using human neutrophils were performed at room temperature.

Jet experiments

Native (not recombinant) human C5a (Complement Technology, Inc.) was diluted in serum-free buffer to the desired concentration and preloaded into the pipette facing the cells. To minimize contamination of the experiment chamber, the C5a pipette was kept under a slight suction (negative) pressure until the start of each single-cell test. Once the cell-holding pipette and the C5a pipette had been positioned at the desired distance from one another, the pressure in the C5a pipette was reversed to the desired positive value, causing its solution to be expelled in a jet directed toward the cell.

Dual-camera setup for simultaneous recording of fluorescence and brightfield images

Micropipette manipulation requires a low-noise environment. To prevent vibrations caused by mechanical shutters or filter wheels, we used a dual-camera setup that allowed us to record fluorescence and brightfield images without such devices (Fig G.1). The microscope was

coupled to two video cameras using a Zeiss dual-camera adapter. A uEye USB-3 camera (UI-3240; IDS/1stVision) was used to record brightfield images, and a sensitive EMCCD camera (Andor Ixon Ultra; Technical Instruments) was synchronized with an electronically strobed LED (SpectraX light engine) and used to record fluorescence images under low-intensity excitation. White LED light (Thorlabs) was filtered to produce red light for brightfield illumination. Epi-illumination by the cyan LED of the SpectraX light engine provided optimum excitation of Fluo-4. The emitted green light was passed through suitable dichroic mirrors and an emission filter (Fig G.1) to be imaged by the EMCCD camera.

Measurement of the cell surface area

The principal workflow of our measurement of the cell surface area involved the following steps (Fig G.4). First, we manually traced the boundary of the cell body outside the pipette in a suitable video image (Fig G.4). We then found the mathematical expression of a Fourier-smoothed, continuous representation of the resulting polygon (Fig G.4). The 2D region enclosed by this curve was assumed to be the cross-section of a rotationally symmetric 3D body containing the symmetry axis. We also assumed that the axis of rotation ran through the 2D center of mass of the cross-sectional region. We next determined those two straight lines containing the mass center for which the contour parts on either side exhibited maximal mirror symmetry. From these two candidates, we chose the most likely axis of rotation based on the experimental context, usually defined by the position of the nearby target particle. The two parts of the contour on either side of this axis were not usually exact mirror-symmetric replicas of each other, so we approximated the actual contour with a mirror symmetric version, which here is the average of the two parts. Finally, we used this symmetric contour to generate a 3D image of the resulting axisymmetric shape (Fig G.4). We used a slightly different approach in our surface

area calculation. Rather than averaging the two contour parts, we generated separate axisymmetric 3D bodies for each of them and then calculated the average of the surface areas of these two bodies.

As long as the osmotic conditions do not change, the cell volume remains constant during the deformations considered here. We calculated the total volume of the deformed cell as the sum of the volume of the axisymmetric approximation of the cell body outside the pipette and the volume of the cell projection in the pipette, which was assumed to consist of cylindrical and hemispherical parts. If this total volume was different from the volume of the same cell measured in its initially relaxed, spherical state, we enforced the volume constraint by rescaling the outer cell body. Only then did we calculate the total surface of the deformed cell. Our calculation accounted for the hole in the surface of the outer cell body at the pipette entrance by subtracting the area of a disc that had the same radius as the pipette.

Funding: This work was supported by National Institutes of Health, USA, grant R01 GM098060. **Author contributions**: E.A.F. developed, performed, and analyzed experiments and prepared the manuscript. V.H. developed, performed, and analyzed experiments, prepared figures and movies, and wrote the paper. **Competing interests**: The authors declare no competing interests.

Movies 4.1 to 4.4 are accessible at https://www.ncbi.nlm.nih.gov/pmc/articles/PMC7053518/

Chapter 5: Experimental characterization and computational modeling of calcium bursts during neutrophil phagocytosis

Abstract

Rapid, global bursts in free cytosolic calcium (Ca^{2+}) are well-known to occur during a variety of immune cell processes including migration and phagocytosis. However, the key factors determining the onset, magnitude, and duration of Ca^{2+} bursts have not been fully characterized. Here, we examine Ca^{2+} bursts in human neutrophils during phagocytosis of serum-opsonized fungal model particles or IgG-coated targets using a combination of biophysical experiments and computational modeling. In one experimental setup, we used two opposing micropipettes to hold a human neutrophil and a pathogenic particle; by gently handing over the target particle, we could closely observe single phagocytosis events. In an alternative setup, we deposited human neutrophils onto an IgG-coated coverslip and imaged them during frustrated phagocytic spreading. Ca^{2+} bursts occurred consistently during phagocytosis of the particles tested in our micropipette experiments, but the timing and magnitude of these bursts depended on the type of target particle. Additionally, we found that Ca^{2+} burst duration, but not magnitude, correlated with particle size. In frustrated phagocytosis experiments, IgG density determined the timing of Ca^{2+} burst onset and correlated with the magnitude and duration of Ca^{2+} bursts. Ca^{2+} bursts still occurred in the absence of extracellular Ca^{2} but were eliminated by pre-treating cells with thapsigargin in Ca^{2+}-free media. Therefore, the predominant source of Ca^{2+} for these bursts was a pool of thapsigargin-sensitive intracellular stores. Extracellular Ca^{2+}, on the other hand, was mainly important for refilling Ca^{2+} stores on longer timescales. Our experimental findings matched well with predictions from our computational model of Ca^{2+} bursts during phagocytic

spreading. This model predicted that the timing and magnitude of Ca^{2+} bursts would both be altered by changes in IgG density and that the majority of Ca^{2+} in the initial burst comes from the endoplasmic reticulum. Together, our experiments and computational model illuminate key quantitative features of Ca^{2+} bursts in human neutrophil phagocytosis.

Introduction

Rapid, global bursts in free intracellular calcium (Ca^{2+}) concentration are a hallmark of immune cell activation, observed in diverse processes including arrest and spreading on the endothelium, immunological synapse formation, and phagocytosis [26, 139, 140, 160]. Unlike other localized Ca^{2+} signaling events, these Ca^{2+} bursts occur uniformly throughout the cell body, with the cytosolic Ca^{2+} increasing several-fold in a matter of seconds. Although Ca^{2+} bursts are commonly used as a readout of immune cell activity, many fundamental questions about these bursts remain unanswered. What determines the onset of a Ca^{2+} burst? Does the overall magnitude of a Ca^{2+} burst depend on the types of receptors being engaged? Are Ca^{2+} bursts primarily a result of release from intracellular stores such as the endoplasmic reticulum (ER) or influx through the plasma membrane (PM)?

In neutrophils, the resting Ca^{2+} concentration is typically 100 nM [198], whereas the Ca^{2+} concentration in intracellular stores such as the ER or in the extracellular space is typically several orders of magnitude higher (about 200 μM in the ER lumen [155] and 1-2 mM in the extracellular medium). The steep electrochemical gradients across the ER membrane and the PM can be exploited to drive rapid elevations in cytosolic Ca^{2+} levels. Following biochemical stimulus, the opening of channels such as the IP_3 receptor in the ER membrane can quickly

increase cytosolic Ca^{2+} levels, accelerated by positive feedback loops that drive the opening of Ca^{2+} channels in both the ER membrane and the PM. Some experiments have indicated that these signals can also be modulated by tension acting on integrins in the presence of shear flow [139-141, 199].

Ca^{2+} bursts have been observed in phagocytosis for several decades (reviewed in [160]). One key study in human neutrophils indicated that, compared to complement-mediated phagocytosis, IgG-mediated phagocytosis is much more sensitive to intracellular Ca^{2+} chelation [24]. Additionally, it is known that the biochemical pathway leading to Ca^{2+} bursts differs depending on the receptors being engaged. Release of Ca^{2+} from intracellular stores occurs via a phospholipase C gamma (PLCγ)-mediated pathway in Fcγ receptor (FcγR)-mediated phagocytosis [200], but depends on phospholipase D (PLD) activation in complement receptor 3 (CR3)-mediated phagocytosis [201]. In either case, store emptying leads to a Ca^{2+} influx through the process of store-operated calcium entry (SOCE) [147]. However, the contribution of store-release vs. influx through SOCE remains unclear in the literature. Some studies attribute most of the global Ca^{2+} elevation to influx through store-operated channels [141, 148, 157, 202], but others find that eliminating influx has only small effects on Ca^{2+} bursts [203, 204].

In this study, we examine global Ca^{2+} dynamics during neutrophil phagocytosis using experiments and computational modeling. We test two complementary experimental setups: dual-micropipette-manipulation experiments to examine single events of phagocytosis and frustrated phagocytosis experiments to image cells in bulk during phagocytic spreading on IgG-coated coverslips. In either case, we label neutrophils with a Ca^{2+}-sensitive fluorophore and examine changes in cell shape and intracellular Ca^{2+} over the time course of phagocytosis. We measure differences in global Ca^{2+} dynamics depending on the type of target particle (serum-

opsonized fungal model particles vs. IgG-coated particles), the size of target particle, and opsonin density on the target surface. In the case of IgG-mediated phagocytosis, we also assess how the removal of extracellular Ca^{2+} or the pre-depletion of intracellular Ca^{2+} stores influences the magnitude of Ca^{2+} bursts during phagocytosis. We then relate our experimental findings to the predictions of a computational model of global Ca^{2+} dynamics during phagocytosis of an IgG-coated target. The model consists of a system of ordinary differential equations that account for Ca^{2+} fluxes passing through the ER membrane and the PM, allowing us to predict changes in global Ca^{2+} concentration over time. We examine the predicted effects of varying IgG density, eliminating extracellular Ca^{2+}, and depleting intracellular stores, and compare these predictions to our experimental observations.

Materials and Methods

Cell isolation and treatment conditions

The protocol for this study was approved by the Institutional Review Board of the University of California, Davis and all donors provided written informed consent. Human neutrophils were isolated from the whole blood of healthy donors using the EasySep Human Neutrophil Isolation Kit (Cat#17957; STEMCELL Technologies). Prior to use of the kit, blood was mixed at a 1:5 ratio with HetaSep (STEMCELL Technologies) and centrifuged for 5 minutes at 110g, then the leukocyte-rich fraction was collected. Cells were washed twice more (once at 500g to remove platelets, then once more at 120g), and then resuspended at about 5×10^7 cells per mL. The isolation protocol was then completed according to the manufacturer's protocol.

For Fluo-4 or Fura Red loading, cells were resuspended at about 1×10^6 cells per mL in Hanks' balanced salt solution with Ca^{2+} and Mg^{2+} (HBSS+; Thermo Fisher Scientific) with 0.1% human serum albumin (HSA; MP Biomedicals) and either 0.5 μM Fluo-4 AM (Thermo Fisher Scientific) or 1 μM Fura Red AM (AAT Bioquest). The suspension was placed on a rotator in the dark at 37°C for 15 minutes. For pipette experiments, cells were resuspended in HBSS without Ca^{2+} or Mg^{2+} (HBSS-; Thermo Fisher Scientific) with 2% HSA following this incubation step. A small volume of cells was then added to the experimental chamber which contained HBSS+ with 2% HSA (in experiments with IgG-coated beads) or 20% autologous donor human serum (in experiments with fungal model particles).

In frustrated phagocytosis experiments, cells were resuspended according to their treatment condition. Because the 1 mM stock solution of thapsigargin (Thermo Fisher Scientific) was prepared in anhydrous dimethyl sulfoxide (DMSO; Sigma-Aldrich), DMSO was present in thapsigargin experiments at a final concentration of 0.01%. To ensure this small amount of DMSO did not contribute to any differences observed in our experiments, we included 0.01% DMSO in all other solutions used during the frustrated phagocytosis experiments. Accordingly, under standard conditions, we resuspended cells in HBSS+ with 2% HSA and 0.01% DMSO. In the Ca^{2+}-free media condition, we resuspended cells in HBSS- with 0.1 mM ethylenediamine tetraacetic acid (EDTA; Affymetrix), 2% HSA, and 0.01% DMSO. In the thapsigargin condition, cells were resuspended in HBSS- with 0.1 mM ethylene glycol tetraacetic acid (EGTA; Research Products International), 0.9 mM $MgCl_2$, 100 nM thapsigargin, and 2% HSA. Thapsigargin was added 40 min prior to starting the experiment and cells were rotated at room temperature for the duration of treatment.

Surface preparation

Zymosan (Sigma-Aldrich) and β-glucan particles (WGP Dispersible; InvivoGen) were dissolved at ~10 mg/ml in 1X phosphate buffered saline (PBS; Bio-Rad) by boiling in a water bath for 1 hour. They were then washed two times in PBS and stored at 4°C. Prior to use, either solution was sonicated for 30 minutes to break apart large clusters of particles. Experiments using these particles were conducted in the presence of 20% autologous donor serum in HBSS+.

IgG beads were prepared using the same approach described in Chapter 4. 5 or 10 μm polystyrene microspheres (Duke Standards) were incubated in 1% (10 mg/ml) bovine serum albumin (BSA; VWR) in PBS for 1 hour at room temperature or overnight at 4°C, then washed 3 times in PBS with .01% Tween-20 (PBST; Tween-20 from Calbiochem). Beads were then incubated in 150 μg/ml polyclonal rabbit anti-BSA IgG (Cat# A11133; Invitrogen) in PBS for 1 hour at RT or overnight at 4°C. We ensured that at least 10 μg of IgG was present per 1 cm^2 of bead surface area for consistency with our coverslip coating protocol. Finally, beads were washed twice more in PBST, resuspended in PBS, and stored for up to 1 month at 4°C.

IgG-coated coverslips were prepared as described in Chapter 2. However, for these experiments, we used a new experimental chamber with individual wells sealed to the glass coverslip, allowing us to easily test different conditions in parallel. Each well had 0.3 cm^2 of exposed glass and was incubated with 30 μL of 150 μg/mL anti-BSA IgG to ensure at least 10 μg of IgG was present per cm^2 of glass. Effective IgG density was altered by preparing mixtures of polyclonal rabbit anti-BSA IgG and monoclonal mouse anti-BSA IgG-1 (Cat# MA1-82941; Invitrogen, Waltham, MA), as described in Chapter 2. The coating densities are reported as percentages present in the incubation solutions (100 × moles of rabbit IgG / moles of total IgG), or, in some cases, as the absolute surface densities measured for these surfaces in Chapter 2.

Fura Red imaging and dye calibration

To image cells loaded with Fura Red, we alternated between excitation with two LEDs; their excitation filters were centered at 436 nm (blue) and 470 nm (cyan). Emission light passed through a 585 nm long-pass filter and was then collected with an emission filter centered at 640 nm. The two fluorescence images were collected in quick succession, with a 100 ms exposure time each. Brightfield images were collected simultaneously using green light (centered at 546 nm).

Given the intensity upon excitation with blue light (I_{blue}) and upon excitation with cyan light (I_{cyan}), the Fura Red ratio r was calculated by subtracting the background noise for each channel ($I_{blue,BG}$ and $I_{cyan,BG}$) and taking the overall ratio:

$$r = \frac{I_{blue} - I_{blue,BG}}{I_{cyan} - I_{cyan,BG}} \tag{5.1}$$

Background images were collected each day to correct for any day-to-day experimental variability in ambient light. From this ratio, the Ca^{2+} concentration was calculated using the following well-known relationship:

$$c_i = K_{d,FR} \frac{I_{cyan,zero}}{I_{cyan,high}} \left(\frac{r - r_{zero}}{r_{high} - r} \right) \tag{5.2}$$

To complete this calculation, one must first determine the Fura Red ratio at zero Ca^{2+} (r_{zero}) and the Fura Red ratio at very high Ca^{2+} (r_{high}) [205, 206]. The ratio between $I_{cyan,zero}$ and $I_{cyan,high}$ was approximated by r_{high} / r_{zero}, because I_{blue} did not change for different Ca^{2+} concentrations in our setup. $K_{d,FR}$ is the Fura Red:Ca^{2+} dissociation constant (400 nM, according to supplier).

We calibrated Fura Red ratios in the neutrophil-like cell line PLB-985, which allowed us to measure r_{zero} and r_{high} in cells without drawing extra blood samples. We followed protocols

previously developed for Fura-2 calibration in T cells [207]. Cells were incubated with 1 μM Fura Red in RPMI Medium 1640 (Thermo Fisher Scientific) with 10% fetal bovine serum (FBS; Atlanta Biologicals) for 15 minutes at 37°C and then resuspended at a very high concentration (>1×10^7 / mL) in intracellular buffer [208] (140 mM KCl, 1 mM $MgCl_2$, 2 mM EGTA, 20 mM HEPES, 0.2% HSA, all chemicals but HSA and EGTA from Sigma-Aldrich) or intracellular buffer supplemented with 20 mM $CaCl_2$ (Sigma-Aldrich). Cells were deposited into wells, and after imaging was initiated, a bolus of diluted Triton-X 100 (Sigma-Aldrich) in intracellular buffer was added to a final concentration of 1% to achieve rapid cell permeabilization, and the Fura Red ratio was measured over time (Fig 6.1). We performed this test on 9 different days, and averaged the ratios reached after permeabilization in high-Ca^{2+} media (intracellular buffer with $CaCl_2$) and zero-Ca^{2+} media (intracellular buffer) to approximate r_{high} and r_{zero}, respectively (Fig 6.1A). This then allowed us to compute Ca^{2+} concentration using Eq (5.2) (Fig 6.1B).

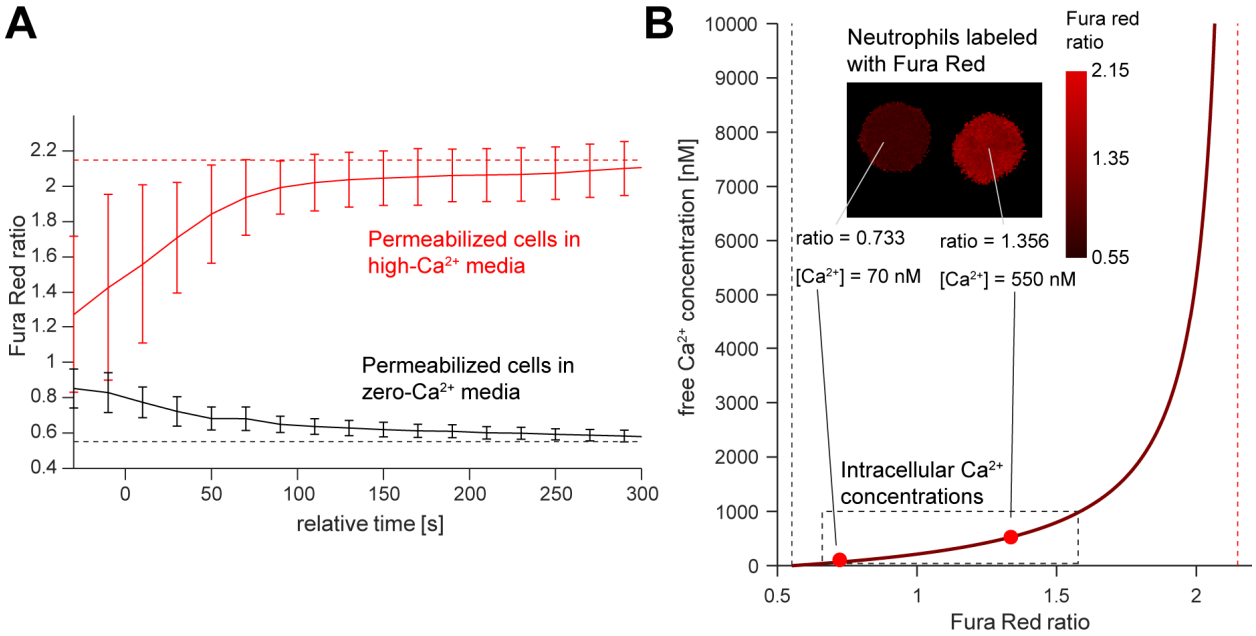

Fig 6.1: Calibration of Fura Red in PLB-985 cells. (A) The Fura Red ratio over time averaged over 9 different trials is shown in high-Ca^{2+} (red curve) and in zero-Ca^{2+} (black curve) media, with error bars denoting the standard deviation across trials at each time point. Dashed lines indicate the chosen values for r_{high} (red) and r_{zero} (black). **(B)** This plot shows the relationship between free Ca^{2+} concentration and Fura Red ratio, as given by Eq (5.2) for our calibrated values of r_{high} and r_{zero}. The image shows Fura Red ratios for two human neutrophils on an IgG-coated surface; their average Fura Red ratios correspond to the points labeled in the plot.

Image analysis

All image analysis was conducted using custom-written software in MATLAB. Our code is available at https://github.com/emmetfrancis/MFICalc and https://github.com/emmetfrancis/ratiometric. Fluo-4 images were analyzed by first thresholding on intensity and filling holes to identify a contiguous cell body (or multiple bodies in frustrated phagocytosis assays) and then averaging over the brightest pixel values in each cell region. For consistency, in all cases, we averaged over a number of pixels which corresponded to 40 μm^2 (about 2/3 of the cross-sectional area of a resting neutrophil) and we excluded the brightest 5 pixel values to avoid any effects due to outlier hot pixels.

Fura Red analysis was similar, although in this case, we initially segmented on the blue channel intensity to identify cell bodies and then assessed the ratio (Eq (5.1)) within each of these regions, averaging over the ratio values within a 5 μm radius of the identified cell centroid. The average ratio was then used to compute the Ca^{2+} concentration through Eq (5.2).

RICM images were analyzed as described in Chapter 2; contact areas were segmented by thresholding on both local variance and intensity. The resulting contours were smoothed through convolution with a Gaussian kernel. When necessary, cell outlines were manually traced. The code used to complete this analysis was written in MATLAB, developed from code originally written by Daniel Kovari [45]. Our version of this code is available at https://github.com/emmetfrancis/RICMAnalysis.

Statistics

All comparisons were made using ANOVA followed by Tukey's post-hoc test, with $p = 0.05$ set as the threshold for significance. Some outliers were excluded from plots but were included in

the statistical analysis. For ease of viewing, statistical significance is indicated using compact letter display in some graphs, where groups that share a letter are not significantly different from one another. These analyses were completed in Origin graphing software. Correlations were assessed in MATLAB, with reported *p*-values corresponding to the null hypothesis that the correlation coefficient equals zero.

Computational modeling

Our computational model is described in full in Appendix H, with a full table of parameter values, all model equations, and documentation of our sensitivity analysis. The model was implemented in MATLAB, using ode15s to solve our system of differential equations; the code is available at https://github.com/emmetfrancis/neutrophilCalcium. We approximated the Sobol indices for our sensitivity analysis using SALib in Python [209, 210].

Results

Ca^{2+} bursts occur consistently during neutrophil phagocytosis

We first measured changes in cytosolic Ca^{2+} during phagocytosis in dual-micropipette experiments, in which we used two opposing micropipettes to hold a neutrophil and a target particle (Fig 5.2A, Fig 5.3A). This allowed us to gently hand over the target particle and observe the subsequent phagocytic response by the neutrophil. We pre-loaded neutrophils with the Ca^{2+}-sensitive fluorescent label, Fluo-4, allowing us to measure relative changes in cytosolic Ca^{2+} concentration during phagocytosis. Each target particle consisted of either a serum-opsonized fungal model particle (zymosan or β-glucan particle, Fig 5.2) or an IgG-coated polystyrene microsphere (Fig 5.3). Serum-opsonized fungal model particles generally presented a mixture of

stimuli on their surface, including serum immunoglobulins (e.g. IgG), complement fragments (C3b, iC3b, C3d, C3dg), and fungal sugars (e.g. β-glucan).

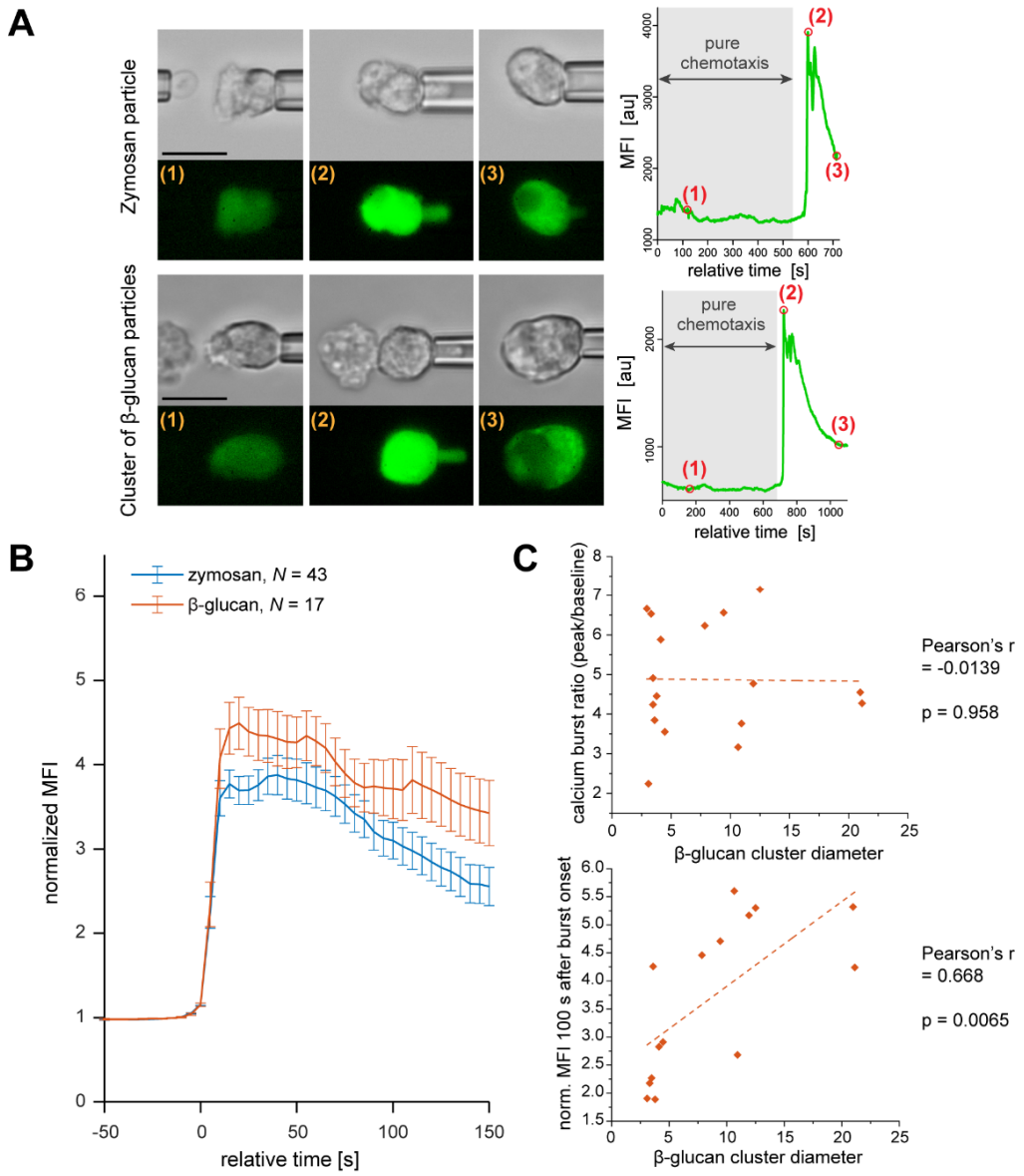

Fig 5.2: Ca^{2+} dynamics during phagocytosis of fungal model particles. (A) Time lapse images of Fluo-4-labeled neutrophils show initial chemotaxis without a Ca^{2+} burst, followed a Ca^{2+} burst after the cell adheres and starts to phagocytose zymosan or a cluster of beta glucan. Mean fluorescence intensity (MFI) is plotted over time for both cells pictured. Scale bars in images denote 10 µm. **(B)** Plot shows the averaged MFI-versus-time curves during phagocytosis of zymosan (43 cells) and phagocytosis of β-glucan particles (17 cells). Curves from individual cells were aligned by the start of the Ca^{2+} burst, defined as $t = 0$. Error bars denote standard error of the mean. **(C)** The duration of Ca^{2+} burst (as indicated by the MFI 100 s after the Ca^{2+} burst, bottom plot), but not its magnitude (as indicated by the ratio between the first Ca^{2+} peak and the initial level, upper plot) correlates with the size of β-glucan cluster being phagocytosed.

In nearly all cases of phagocytosis, the mean fluorescence intensity increased several-fold above baseline within about 5-10 s. Assuming equal baseline Ca^{2+} concentrations, Ca^{2+} increased more during phagocytosis of IgG-coated beads than during phagocytosis of serum-opsonized zymosan and β-glucan particles (Fig 5.2B, Fig 5.3B).

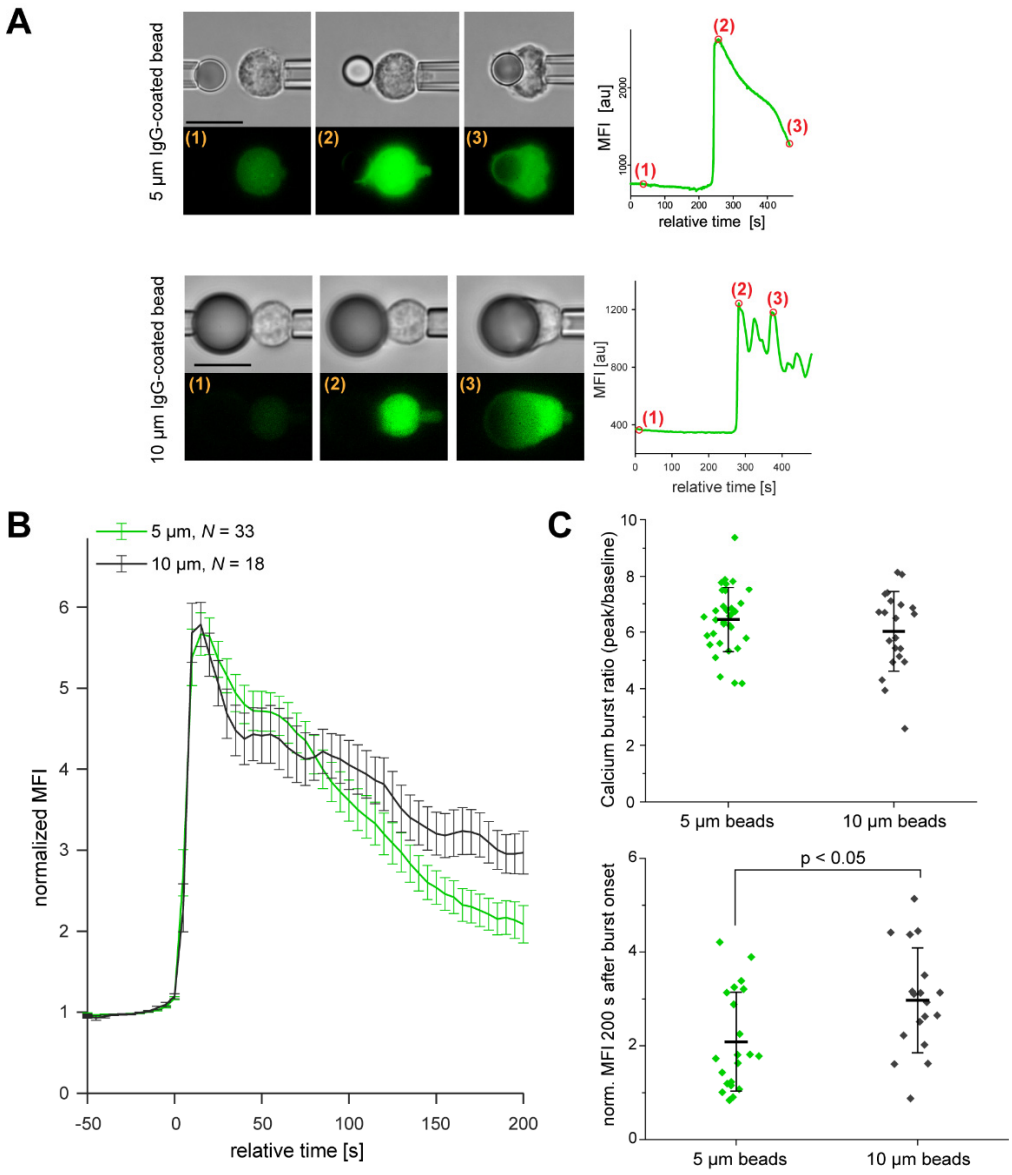

Figure 5.3: Ca^{2+} dynamics during phagocytosis of 5 or 10 µm diameter IgG-coated microspheres. **(A)** Time-lapse images of Fluo-4 labeled neutrophils show Ca^{2+} burst onset soon after cells contacted IgG-coated beads. Mean fluorescence intensity (MFI) is plotted over time for both cells pictured. Scale bars in images denote 10 µm. **(B)** Plot shows the averaged MFI vs. time curves during phagocytosis of 5 µm (33 cells) and 10 µm (18 cells) IgG-coated beads. Curves from individual cells were aligned by the start of the Ca^{2+} burst, defined as $t = 0$. Error bars denote standard error of the mean. **(C)** Ca^{2+} remains elevated longer during phagocytosis of 10µm beads, but the initial Ca^{2+} burst has the same magnitude for both bead sizes. Error bars in these graphs denote standard deviation.

Our target particles spanned a range of sizes; β-glucan particles alone formed aggregates from diameters of about 3 μm (single particles) to 20 μm (larger clusters). We exploited this feature of β-glucan to test for correlations between particle/cluster size and Ca^{2+} burst magnitude or duration. We observed a significant positive correlation between the duration of Ca^{2+} bursts and target size, but no dependence of the initial burst magnitude on target size (Fig 5.2C). The same trend held for IgG-coated beads; Ca^{2+} generally stayed elevated longer during phagocytosis of 10 μm beads, but the initial bursts were essentially identical in magnitude to those observed during phagocytosis of 5 μm beads (Fig 5.3B-C).

Finally, we compared the timing of Ca^{2+} bursts in experiments with each of these different targets (Fig 5.4). For each target, the time delay between the apparent start of phagocytosis and the onset of the Ca^{2+} burst was highly variable, reflecting the inherent heterogeneity in neutrophil behavior. However, Ca^{2+} bursts were significantly more delayed during phagocytosis of zymosan particles compared to IgG-coated beads. On average, Ca^{2+} bursts occurred about one minute after the start of cell deformation during phagocytosis of fungal model particles, but almost always occurred within a minute of the apparent start of phagocytosis of IgG-coated beads.

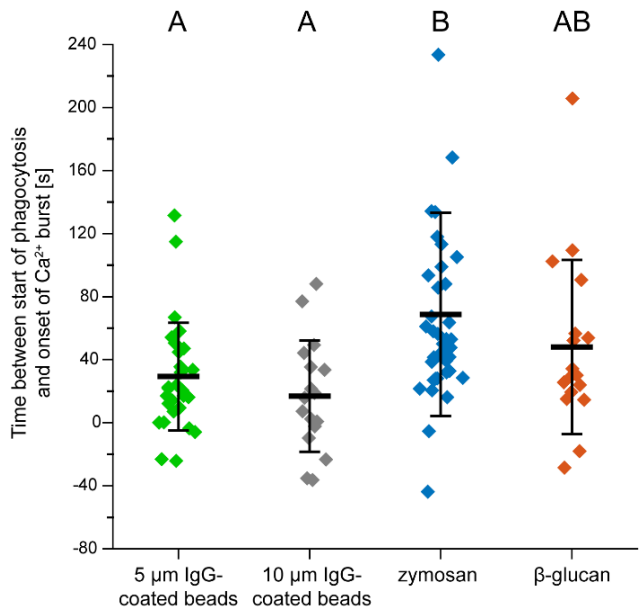

Fig 5.4: Timing of Ca^{2+} bursts during phagocytosis of different model pathogens. For each instance of phagocytosis in micropipette experiments, we assessed the apparent start of phagocytosis by close examination of video sequences, then determined the time gap between the start of phagocytosis and the onset of the Ca^{2+} burst. Error bars denote standard deviation. Letters above each group are used to denote statistically significant differences.

Ca^{2+} burst timing and magnitude correlate with IgG density

We next considered the limiting case in which the cell is confronted with a very large target particle that it cannot fully engulf, known as frustrated phagocytosis. For this, we used our previously developed frustrated phagocytosis assay (Chapter 2); in this case, reflection interference contrast microscopy (RICM) was used to image the cell-substrate contact region with high resolution and fluorescence images were collected simultaneously to track intracellular Ca^{2+} dynamics (Fig 5.5A). As described in Chapter 2, we modulated the effective IgG density on our surfaces by changing the ratio of polyclonal rabbit IgG (strongly recognized by human neutrophils) to mouse IgG-1 (weakly recognized).

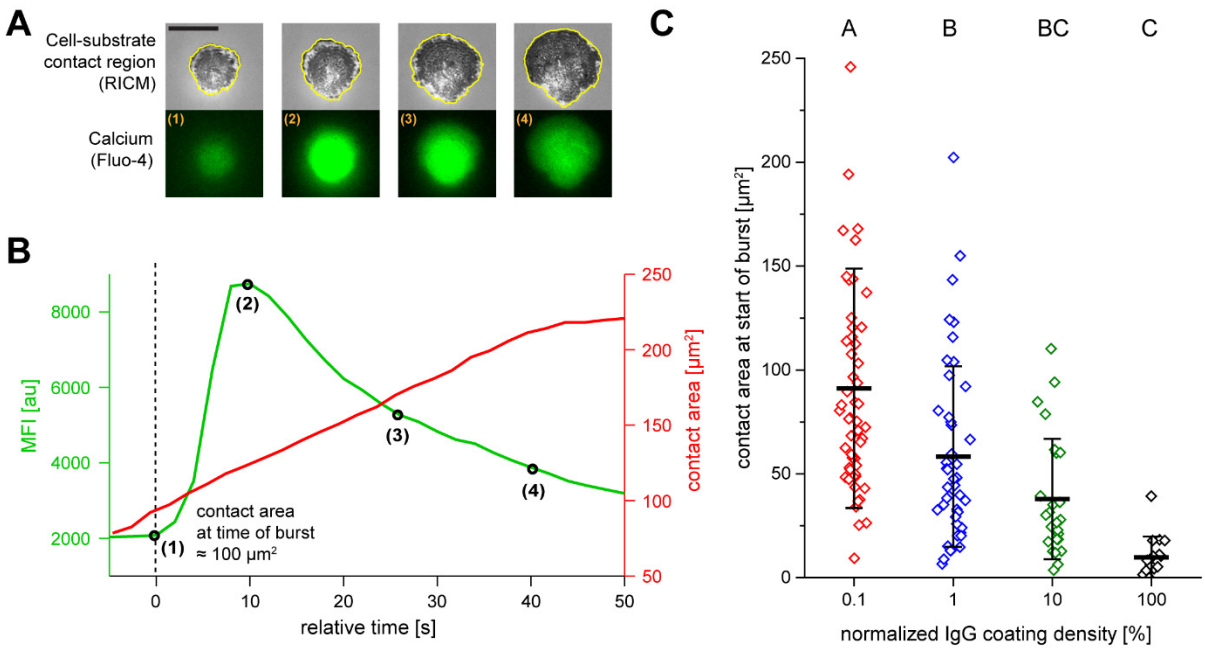

Fig 5.5: Measurement of contact area at the onset of Ca^{2+} bursts. (A) RICM images and fluorescence images (Fluo-4) were collected simultaneously to track both intracellular Ca^{2+} and cell-substrate contact area (outlined in yellow in RICM images). Scale bar denotes 10 µm. **(B)** Fluo-4 mean fluorescence intensity (MFI; green) and contact area (red) are both plotted over time for the cell pictured in (A). Contact area at the onset of the Ca^{2+} burst can be readily determined as shown. **(C)** Contact area at the start of Ca^{2+} bursts correlates with IgG surface density. Letters are used to denote significantly different groups. Error bars denote standard deviation.

We observed Ca^{2+} bursts during frustrated phagocytosis on a range of different IgG densities. Even when lowering IgG density 1000-fold from the saturating concentration, we found that Ca^{2+} bursts occurred consistently during spreading. We quantified the cell-substrate contact area at the onset of Ca^{2+} bursts to measure the dependence of Ca^{2+} burst induction on FcγR-IgG binding. On the lowest density of IgG (0.1%), cells sometimes spread to a contact area of 100 μm^2 or more before the Ca^{2+} burst onset, whereas in nearly all cases of spreading on the highest density, the Ca^{2+} burst began almost immediately upon cell-substrate contact (Fig 3C). This indicates that the density and number of engaged FcγRs dictate the timing of Ca^{2+} bursts during phagocytic spreading.

Although the combination of RICM and fluorescence imaging in these experiments was a powerful tool, we could only quantify relative changes in Ca^{2+} concentration rather than absolute concentrations. Furthermore, using only a single wavelength Ca^{2+} indicator (Fluo-4), the absolute values of fluorescence intensity depend not only on Ca^{2+}, but also on cell-loading efficiency, uneven fluorophore distribution in the cell body, and slight shifts in focal plane. Therefore, we ran additional experiments in which we loaded cells with the ratiometric Ca^{2+} dye, Fura Red, and imaged the midplane of cell bodies during spreading. In this manner, we could acquire bulk measurements of Ca^{2+} dynamics during frustrated phagocytic spreading (Fig 5.6A).

We tested spreading of Fura Red-labeled cells on different densities of IgG, observing Ca^{2+} dynamics that agreed well with our Fluo-4 measurements. On the highest density of IgG, Ca^{2+} levels increased 4-5-fold in less than 10 seconds, and we generally observed at least two peaks in Ca^{2+} concentration during spreading. This multi-peak pattern appears in both the overall average Ca^{2+} dynamics (Fig 5.6B) and the Ca^{2+} dynamics in individual cells (Fig 5.6C). We measured an average resting Ca^{2+} level of about 100 nM (in agreement with previous measurements in neutrophils [198]) and an average initial peak of about 370 nM on 100% polyclonal rabbit IgG (Fig 5.6B). On lower densities of IgG, we observed lower overall Ca^{2+} elevations, as indicated by area under the curve over the first 100 s after the onset of the Ca^{2+} burst (Fig 5.6D). However, the overall pattern of Ca^{2+} dynamics was remarkably consistent, with two primary peaks before the Ca^{2+} levels gradually started to decay.

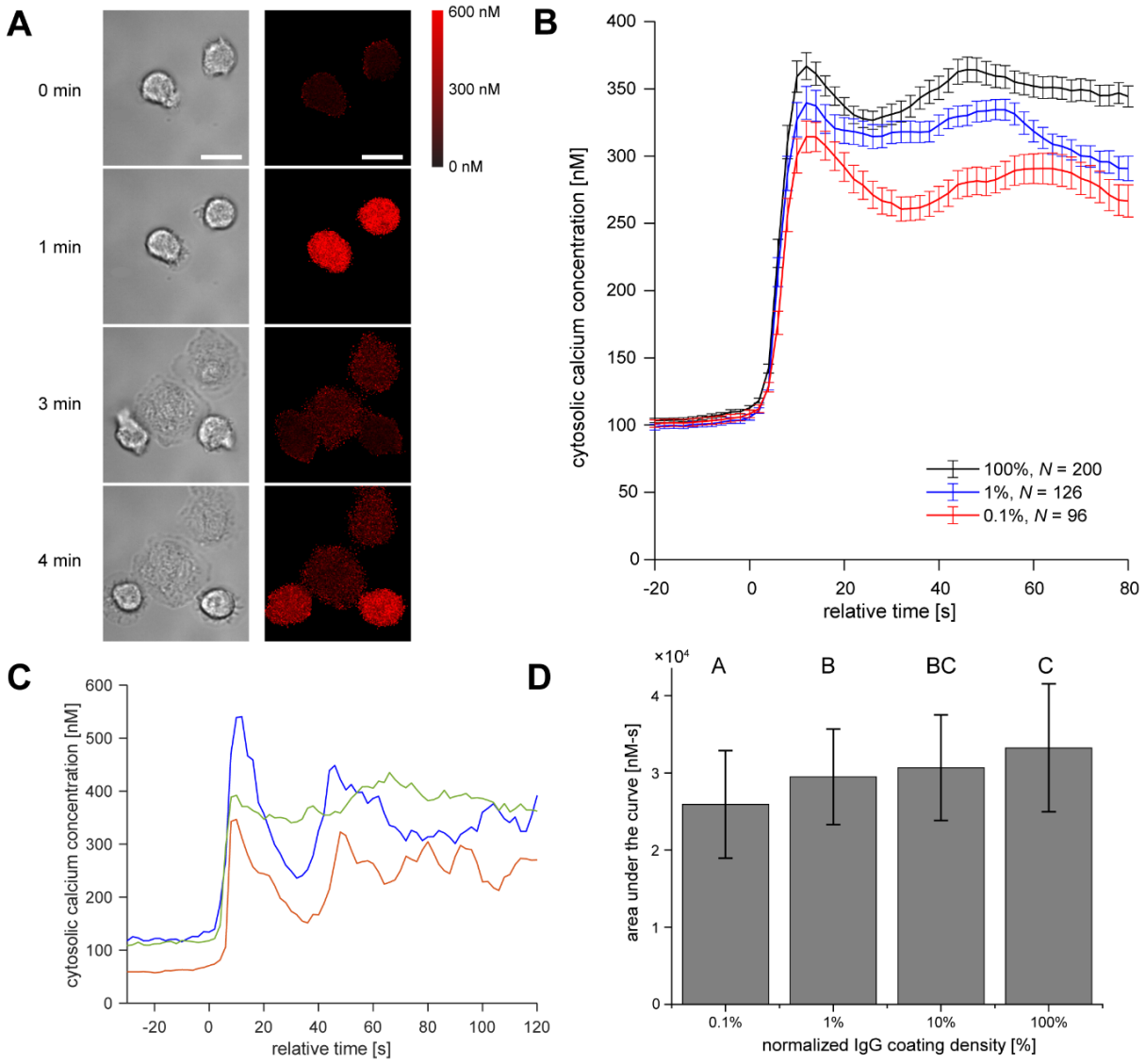

Fig 5.6: Fura Red measurements of Ca^{2+} dynamics during spreading on different IgG densities. (A) Sample brightfield (left) and Fura Red (right, converted to Ca^{2+} concentration) images of neutrophils spreading on the highest density of IgG are shown for several different time points. Scale bars denote 10 µm. **(B)** Average Ca^{2+} is plotted over time for neutrophils spreading on different densities of IgG, aligned by the start of the Ca^{2+} burst. Error bars denote standard error of the mean. **(C)** Sample Ca^{2+}-versus-time curves are displayed for three neutrophils spreading on the highest density of IgG. **(D)** Area under the curve from $t = 0$ s (start of the burst) to $t = 100$ s is significantly greater on higher densities of IgG. Error bars denote standard deviation.

Intracellular stores are the predominant Ca^{2+} source in Ca^{2+} bursts

We then tested whether Ca^{2+} bursts were primarily driven by extracellular Ca^{2+} influx or intracellular release from Ca^{2+} stores such as the ER. We either conducted experiments in Ca^{2+}-free media supplemented with EDTA or pre-treated cells with thapsigargin, which blocks Ca^{2+}

reuptake into the ER, leading to store depletion over time (Fig 5.7A). In this latter condition, Ca^{2+} was also absent from the extracellular medium.

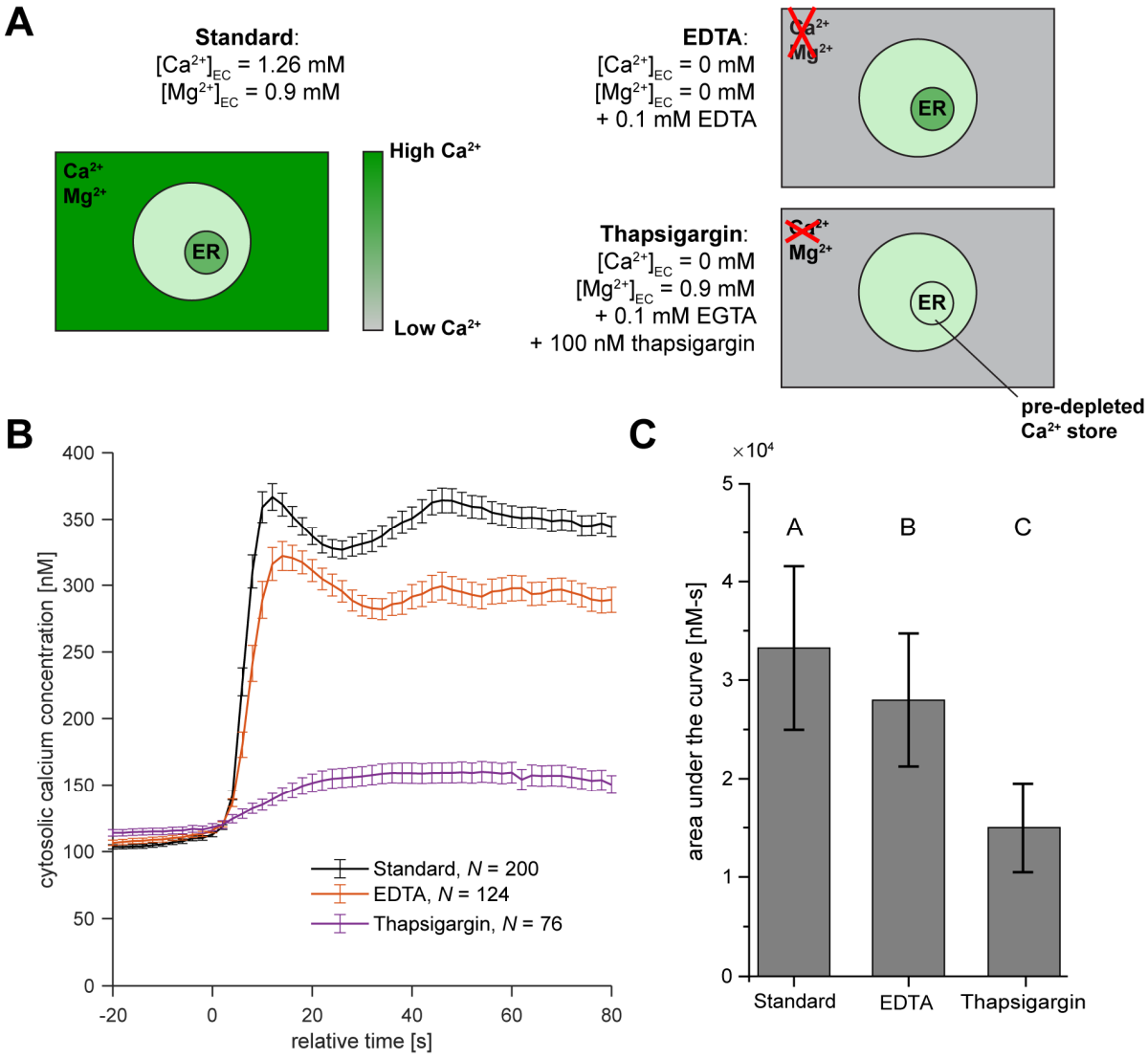

Fig 5.7: Changes in Ca^{2+} bursts after altering intracellular or extracellular Ca^{2+}. (A) These drawings depict treatments to eliminate extracellular Ca^{2+} (EDTA) or deplete intracellular stores (thapsigargin). $[Ca^{2+}]_{EC}$ and $[Mg^{2+}]_{EC}$ denote the extracellular concentrations of Ca^{2+} and Mg^{2+}. **(B)** This plot shows the average Ca^{2+} over time under standard conditions compared to EDTA and thapsigargin treatment conditions, aligned by the start of the Ca^{2+} burst. Error bars denote standard error of the mean. In the case of thapsigargin-treated cells with no detectable burst, $t = 0$ was defined by the start of cell spreading. **(C)** Area under the curve computed over the first 100 s of Ca^{2+}-versus-time reveals significant differences in the magnitude and duration of Ca^{2+} bursts between conditions. Error bars show standard deviation and different letters denote statistically different groups.

For either treatment (EDTA or thapsigargin), we found that cells were still capable of frustrated phagocytic spreading despite altered Ca^{2+} dynamics. Removing extracellular Ca^{2+} (EDTA treatment) only slightly reduced the magnitude of Ca^{2+} bursts, whereas additionally treating cells with thapsigargin essentially eliminated Ca^{2+} bursts (Fig 5.7B-C). Together, these measurements clearly demonstrate that the primary source of Ca^{2+} in Ca^{2+} bursts is a pool of thapsigargin-sensitive intracellular stores, the largest of which is the ER.

Computational modeling recapitulates global Ca^{2+} dynamics during phagocytic spreading

The above experiments demonstrated how Ca^{2+} bursts change with factors such as IgG density and elimination of extracellular Ca^{2+}. However, to build a better quantitative understanding of the events underlying Ca^{2+} bursts, we developed a compartment model of Ca^{2+} dynamics during phagocytosis. This allowed us to confirm that our experimental data aligned with our understanding of known Ca^{2+} signaling pathways, and to also make quantitative predictions about information not directly available in our experiments, such as the concentration of Ca^{2+} in the ER. The model consists of a system of ordinary differential equations (ODEs), which is detailed in full in Appendix H. In summary, our model involves the following sequence of events (Fig 5.8):

1. *Ligand-receptor binding*: Given the cell-target contact area as a function of time (chosen to match experimental measurements in Chapter 2), we solve for the number of FcγRs bound to IgG at each time step. In this calculation, we account for both the rate at which receptors diffuse in the membrane [211] and the estimated binding affinity of low-affinity FcγRs for IgG [112].

2. *Phosphorylation events*: Binding and clustering of FcγRs leads to Src-family-kinase (SFK)-mediated phosphorylation of immunoreceptor tyrosine activation motifs (ITAMs), which are cytosolic domains present on some subtypes of FcγRs expressed by neutrophils (predominantly FcγRIIa here). This triggers phosphorylation of spleen tyrosine kinase (Syk), which phosphorylates many other enzymes downstream. FcγRIIa-mediated Ca^{2+} signals are primarily mediated by phospholipase C gamma (PLCγ) [22, 200], which cleaves phosphatidylinositol 4,5-bisphosphate (PIP_2) in the membrane, producing diacylglycerol (DAG) and inositol triphosphate (IP_3).
3. *IP_3 receptor (IP_3R)-mediated Ca^{2+} release*: IP_3 binds to its receptor in the ER membrane, which also acts as a Ca^{2+} channel. Ca^{2+} flux through the IP_3R is highly nonlinear; it is enhanced by elevated intracellular Ca^{2+} on a fast time scale but is also deactivated by Ca^{2+} on a slower time scale, which introduces two opposing feedback loops [212, 213]. Additionally, Ca^{2+} is pumped back into the ER by sarcoendoplasmic reticulum Ca^{2+} ATPase (SERCA) pumps and leaks out of the ER. At steady state, the leak and SERCA fluxes must perfectly balance each other assuming no baseline activation of the IP_3R. However, upon production of IP_3, the system departs from equilibrium, and is known to exhibit Ca^{2+} oscillations for certain parameter choices [212-214].
4. *Store-operated calcium entry*: Following Ca^{2+} release from the ER, stromal interaction molecules (STIMs) oligomerize in the ER membrane and associate with Orai channels in the plasma membrane, leading to a Ca^{2+} influx through a process known as store-operated calcium entry (SOCE) [147, 150]. In conjunction with this influx, Ca^{2+} is also pumped out of the cytosol by plasma membrane Ca^{2+} ATPase (PMCA) pumps.

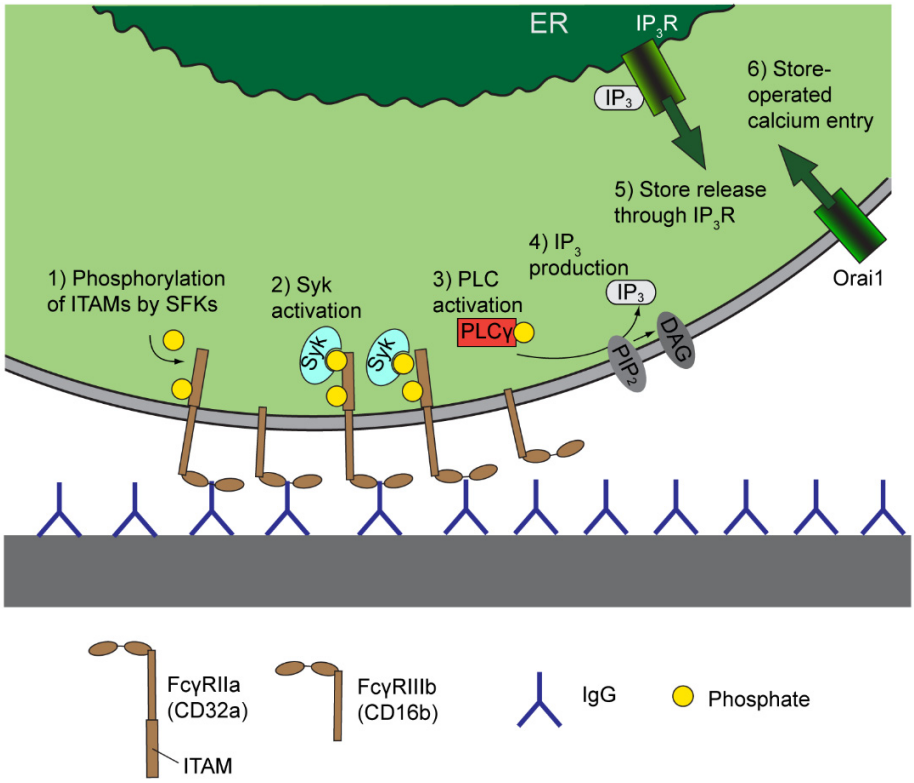

Fig 5.8: Depiction of the sequence of events in a neutrophil Ca^{2+} burst. Following FcγR clustering, Src family kinases (SFKs) phosphorylate the ITAM domains of FcγRIIa (step 1), leading to the recruitment and phosphorylation of Syk (step 2). Syk phosphorylates other enzymes downstream, including PLCγ (step 3), which cleaves PIP_2 molecules in the membrane, producing DAG (membrane lipid) and the diffusible second messenger IP_3 (step 4). Finally, IP_3 binds to its receptor in the ER (step 5), leading to release of Ca^{2+} from the ER and subsequent Ca^{2+} influx through PM channels such as Orai1 via store-operated calcium entry (step 6).

Together, this sequence of events specifies the overall flux balance relationships for free Ca^{2+} in the cytosol (c_i) and free Ca^{2+} in the ER (c_{ER}):

$$\frac{dc_i}{dt} = B_i\left(j_{IP_3R} + j_{ER,leak} - j_{SERCA} + j_{SOCE} - j_{PMCA}\right) \tag{5.3}$$

$$\frac{dc_{ER}}{dt} = B_{ER}\frac{vol_i}{vol_{ER}}\left(j_{SERCA} - j_{IP_3R} - j_{ER,leak}\right) \tag{5.4}$$

All fluxes (j terms) are given in terms of concentration per unit time (μM/s). They are presumed positive, and their directionality is indicated by their associated sign in the flux balance equations

(see also Fig 5.9C). The prefactors B_i and B_{ER} are a consequence of the rapid-buffering approximation [214], including contributions from common intracellular and intraluminal buffers such as calmodulin and calsequestrin. vol_i and vol_{ER} denote the cytosolic volume and the ER volume, respectively.

These two ODEs are coupled with five other ODEs controlling the evolution of five additional state variables: the number of bound receptors, the number of phosphorylated ITAM domains, the number of PIP_2 molecules in the membrane, the cytosolic concentration of IP_3, and the fraction of IP_3Rs that have not been deactivated by Ca^{2+}.

This system of ODEs contains many parameters that are either unknown or have only been measured in other cell types. Whenever possible, we estimated values based on our own experiments or measurements and models in neutrophils or other types of immune cells (Table H.1). However, there is a high degree of uncertainty in the actual values of these parameters, and they likely vary from cell-to-cell and/or donor-to-donor. We therefore conducted a sensitivity analysis, which is documented in Appendix H. Our approach was to estimate the Sobol indices as indicators of the sensitivity of a given model output (area under the curve, contact area at the onset of the Ca^{2+} burst, etc.) to changes in parameter values [215, 216]. This approach also allowed us to differentiate between first-order effects and higher-order effects due to interactions between parameters.

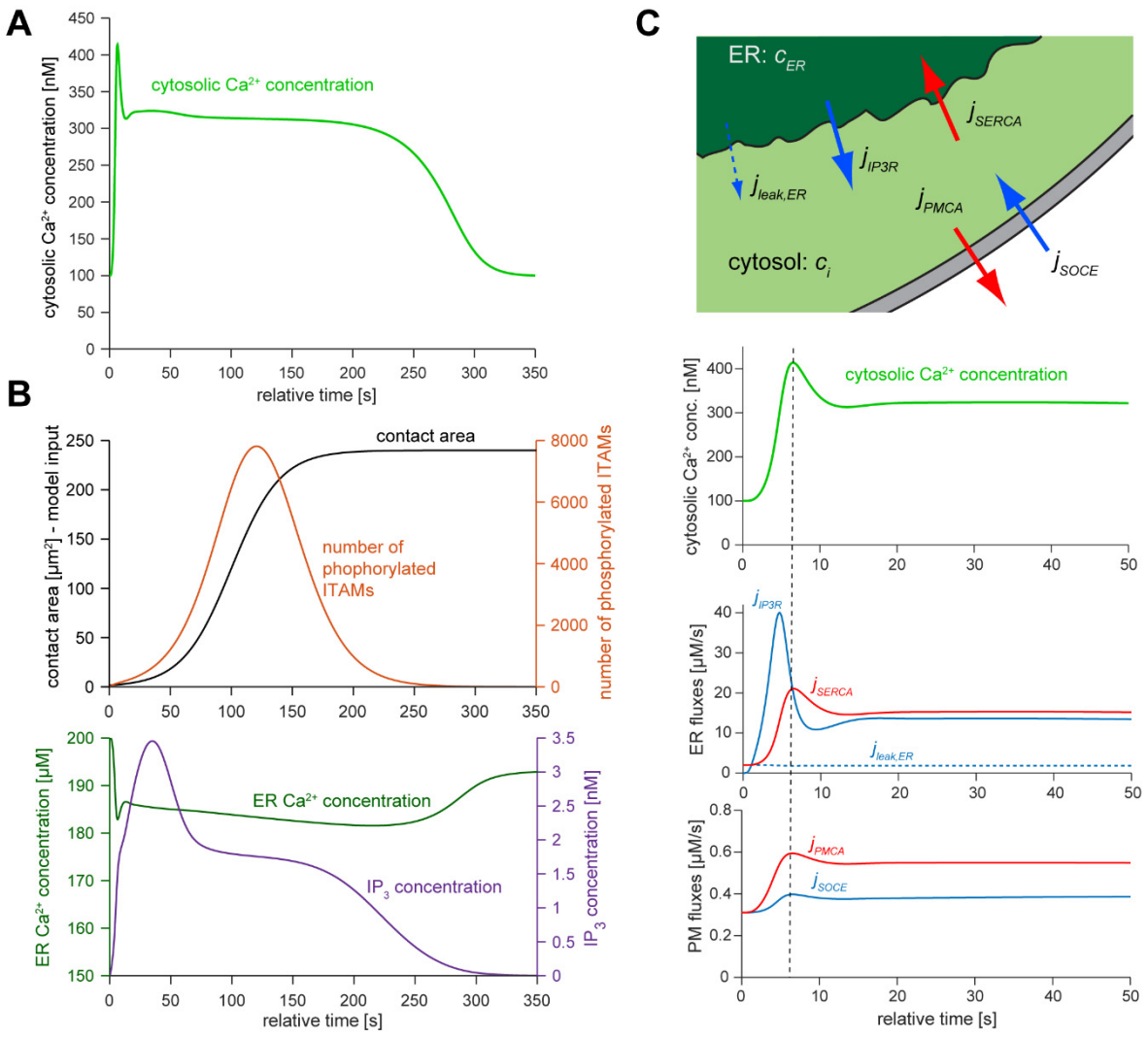

Figure 5.9: Simulations of neutrophil Ca^{2+} bursts. (A) Predicted Ca^{2+}-versus-time curve for spreading on the highest density of IgG using the baseline parameter set specified in Table H.1. **(B)** Contact area (input function, black curve) and other select other state variables are plotted over time (number of phosphorylated ITAM domains in orange, IP_3 concentration in purple, and ER Ca^{2+} concentration in green). **(C)** The five Ca^{2+} fluxes considered in this model are depicted in the upper drawing and their behavior is plotted over time in the lower graphs. Note that ER fluxes are almost two orders of magnitude higher than PM fluxes. Red curves make a negative contribution to intracellular Ca^{2+} and blue curves make a positive contribution. The vertical dashed line going across plots marks the peak of the Ca^{2+} burst for reference.

The Ca^{2+} dynamics predicted by our model agree well with our experimental data of Ca^{2+} bursts during frustrated phagocytosis on the highest density of IgG tested (Fig 5.9A). In simulations, Ca^{2+} concentration increases several-fold in less than 10 s; there is one initial

compact peak in Ca^{2+} followed by a broader extended elevation, as frequently observed in experiments (Fig 5.6C). Our model also predicts underlying events which were not measured directly in our experiments: as the contact area increases over time, ITAM domains are transiently phosphorylated, leading to a rapid burst in IP_3 production, accompanied by Ca^{2+} release from the ER (Fig 5.9B). Our model indicates that the presence of multiple peaks in the Ca^{2+}-versus-time curve is primarily due to the dynamics of the flux through the IP_3R (Fig 5.9C). The predominant source of Ca^{2+} in these elevations was the ER, in agreement with our experiments in Ca^{2+}-free media. Fluxes through the PM were almost two orders of magnitude lower than the ER Ca^{2+} fluxes; however, we still found that Ca^{2+} influx via SOCE was crucial for store refilling over longer time scales, in agreement with the literature [217].

Comparison of model predictions with experimental data

We tested the effects of varying IgG density in our model and compared this to our experimental outcomes (Fig 5.10). In agreement with our experiments, the density of IgG governed the timing of Ca^{2+} bursts (Fig 5.10A-B). The predicted relationship between IgG density and contact area at the onset of the Ca^{2+} burst agrees qualitatively with our experimental data (Fig 5.10B), but the model generally underestimates the contact area at the time of the Ca^{2+} burst. This may be partially remedied by conducting a formal parameter fitting; sensitivity analysis reveals that the burst timing is quite sensitive to the fraction of FcγRs that contain ITAM domains and the Ca^{2+} concentration at which the IP_3R is activated (Figs H.2, H.3, H.4). Our model also predicts that Ca^{2+} burst duration and magnitude both increase with IgG density (Fig 5.10A,C), which agrees qualitatively with our experiments. However, the relationship predicted by the model underestimates the magnitude of Ca^{2+} bursts at lower IgG densities (Fig 5.10C). This discrepancy may indicate a need to include other mechanical and biochemical features in future

versions of our model. For instance, Ca^{2+} bursts may be at least weakly dependent on increases in cortical tension, as suggested in Chapter 4.

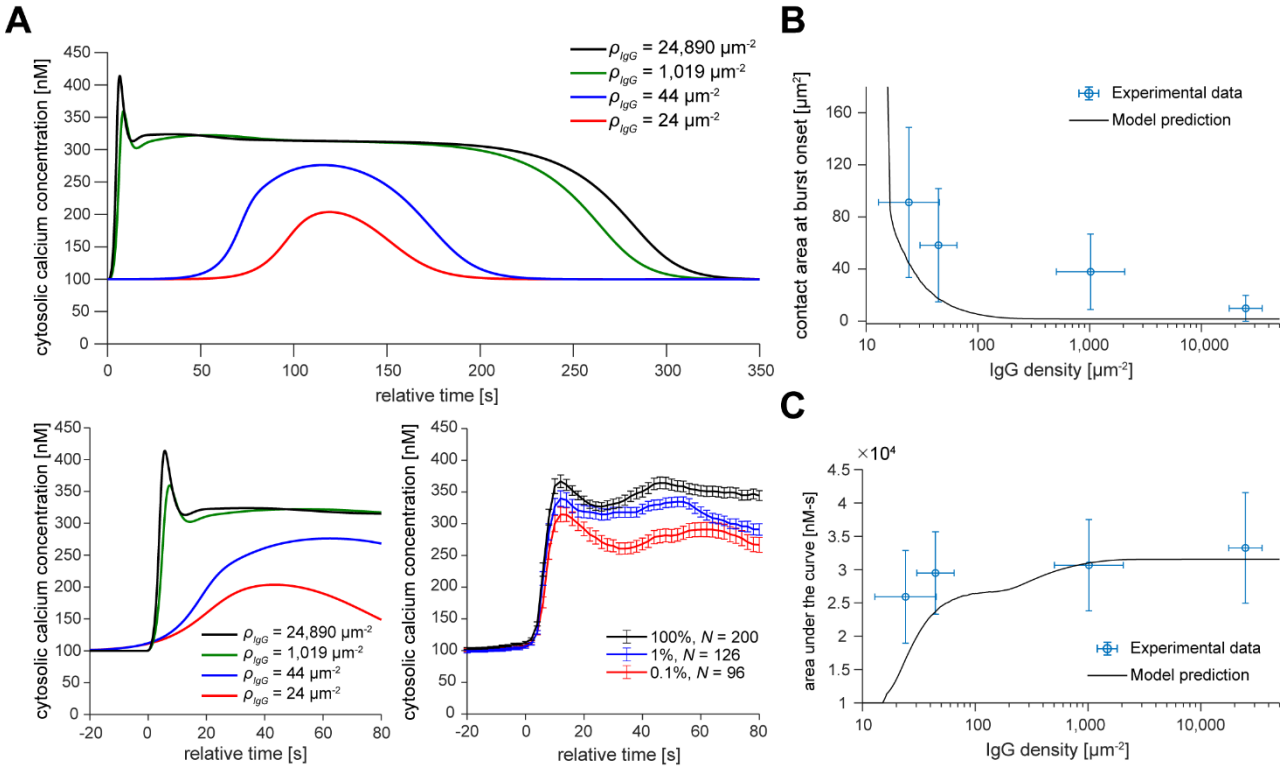

Figure 5.10: Comparison of simulated vs. experimental Ca^{2+} bursts on different IgG densities. (A) These curves show the model's predictions of Ca^{2+} dynamics for the IgG densities tested experimentally. Ca^{2+} bursts are similar on high densities of IgG, but for densities lower than 100 μm^{-2}, the onset of the signal is delayed and the overall magnitude and duration of Ca^{2+} bursts decrease significantly. A smaller region of the curves aligned by the start of the Ca^{2+} burst is shown below the first plot side-by-side with experimental measurements for comparison. **(B)** The predicted dependence of contact area at the time of the Ca^{2+} burst onset on IgG density agrees qualitatively, but not quantitatively, with experimental data. **(C)** Magnitude and duration of Ca^{2+} bursts, as indicated by the area under the Ca^{2+} curve from t = 0 s (start of burst) to t = 100 s, increase as a function of IgG density in both experiments and simulations, but the magnitude of Ca^{2+} bursts is underestimated at low IgG densities. Error bars in **(C)** and **(D)** indicate either standard deviation (y axis error bars) or geometric standard deviation (x axis error bars).

Finally, we tested how well our model matched experimental data upon perturbations of extracellular or intracellular Ca^{2+} levels via EDTA or thapsigargin treatment, respectively. We mimicked EDTA treatment by setting extracellular Ca^{2+} concentration to zero in our model, which eliminates the SOCE influx. Because Ca^{2+} stores are partially depleted over time without SOCE [217], we also set the initial ER Ca^{2+} concentration to 160 μM. In this case, the small

decrease in Ca^{2+} burst magnitude exhibited by our model (Fig 5.11A) agrees well with experimental observations (Fig 5.11B). Thapsigargin treatment was modeled by setting the SERCA pumping rate to 10% of its baseline value and assuming the ER Ca^{2+} is lowered to approximately 10 μM after our 40-minute treatment. In this case, Ca^{2+} bursts were strongly inhibited in our model (Fig 5.11A), matching well to experimental measurements (Fig 5.11B).

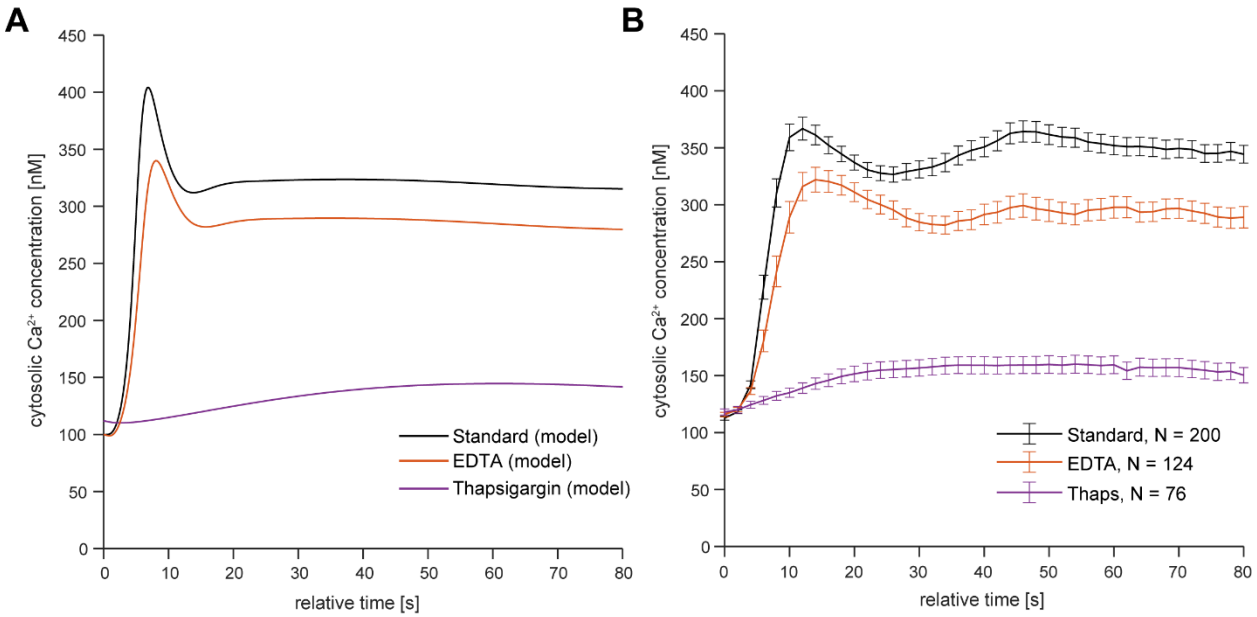

Figure 5.11: Comparison of simulated vs. experimental Ca^{2+} dynamics after altering intracellular or extracellular Ca^{2+}. (A) Predicted Ca^{2+} concentration is plotted over time for standard conditions, EDTA treatment and thapsigargin treatment, given the assumptions laid out in the main text. **(B)** Experimental curves are shown for ease of comparison. Error bars here denote standard error of the mean.

Discussion

Ca^{2+} bursts are consistently observed during neutrophil phagocytosis, but their causes and downstream effects remain poorly characterized. In this work, we examined Ca^{2+} dynamics in human neutrophils during phagocytosis of serum-opsonized fungal model particles, IgG-coated microspheres, and IgG-coated coverslips. Our data yield several key insights about the causes of Ca^{2+} bursts in phagocytosis.

Experiments with serum-opsonized zymosan or β-glucan particles represented a physiologically relevant case, in which fungal model particles were encountered in the presence of autologous donor serum. In these conditions, target surfaces presented multiple stimuli, including serum immunoglobulins, complement fragments (both surface-bound and soluble), and fungal sugars. Our finding that Ca^{2+} bursts during phagocytosis of these particles are smaller in magnitude compared to those elicited by IgG-coated beads may be explained by the distinct signaling pathways triggered during complement-mediated versus IgG-mediated phagocytosis [24]. Additionally, there is likely a lower opsonin density on these fungal surfaces compared to beads saturated with IgG, contributing to a lower Ca^{2+} burst magnitude. This would also be consistent with the finding that Ca^{2+} bursts occurred relatively later during phagocytosis of zymosan than they did during phagocytosis of IgG-coated particles (Fig 5.4).

Between our experiments with IgG-coated beads and IgG-coated coverslips, we uncovered several key aspects of Ca^{2+} bursts in IgG-mediated phagocytosis. First, we found that Ca^{2+} bursts in response to IgG were essentially all-or-nothing events; while the onset of these bursts was strongly influenced by IgG density, their magnitude depended only weakly on the amount of stimulus. We also saw that the duration of Ca^{2+} bursts correlated with the size of the target particle, likely because phagocytosis persists over longer time periods for larger particles. Finally, in our experiments, Ca^{2+} bursts occurred even in the absence of extracellular Ca^{2+}. This agrees with some studies of IgG-mediated Ca^{2+} bursts [203, 204], but many studies attribute Ca^{2+} bursts to influx through the plasma membrane [141, 148, 157, 202]. It is possible that the predominant mechanism for Ca^{2+} elevations depends on the type of receptor being engaged; that is, engagement of Mac-1 may lead to global elevations via Ca^{2+} influx, whereas engagement of FcγRs may lead to elevations via store release.

Few computational models of Ca^{2+} dynamics in neutrophils or other phagocytes have been developed [155, 218]; to our knowledge, this is the first computational model of Ca^{2+} dynamics during IgG-mediated phagocytosis. For simplicity, we include one main pathway leading to store release (PLC-mediated IP_3 production), although it is possible that other pathways contribute simultaneously. For instance, a previous study showed that Ca^{2+} elevations induced by stimulation of neutrophils with insoluble immune complexes did not require elevations in IP_3 [203]. However, most of the literature concurs that FcγRIIa engagement leads to downstream activation of PLCγ, in support of our model's assumptions [200, 219-221]. Future iterations of this model should include contributions of other pathways, such as PLD-mediated Ca^{2+} release, which may also play an important role in FcγR signaling in neutrophils [222, 223].

Our computational model not only agrees with Ca^{2+} bursts observed on high densities of IgG, but also matches trends observed in our other experiments, in which we either altered IgG density or perturbed intracellular or extracellular Ca^{2+}. However, our model predictions do not quantitatively match the experimentally measured dependence of Ca^{2+} burst timing and magnitude on IgG density (Fig 5.10). The match may be improved by conducting formal parameter fitting and by adding additional components to our model, such as fluxes of other ions or involvement of other Ca^{2+} channels. We may also need to consider the effects of forces and mechanical deformation on Ca^{2+} signaling. In neutrophils, force on the β_2 integrin LFA-1 is a known regulator of local Ca^{2+} release from the ER and Ca^{2+} influx through the channel Orai-1 [199, 224]. Force on LFA-1 has also been recently shown to enhance T-cell activation on surfaces that engage both LFA-1 and the T cell receptor [225]. Therefore, it seems likely that forces on Mac-1 (also a β_2 integrin) during phagocytosis may also contribute to Ca^{2+} dynamics. Mac-1 is known to play a cooperative role in IgG-mediated phagocytosis [16, 17], but because it

does not directly bind to IgG, it remains to be determined whether forces are exerted on Mac-1 in the absence of other ligands.

We have largely left aside the question of the downstream roles for Ca^{2+} during phagocytosis. As shown here, we see that IgG-mediated phagocytic spreading proceeds when Ca^{2+} bursts are inhibited by thapsigargin treatment. It is clear from the literature that such treatments will inhibit later stages of phagocytosis such as phagosomal maturation [156, 226]. The degree to which cell morphology and mechanics may be altered under these conditions is investigated in the final chapter of this dissertation.

Acknowledgements

The data for Figs 5.3, 5.4, and 5.5 were gathered in part by undergraduate students in our lab, Jonathan Brand and Hugh Xiao.

The development of our computational model was done in collaboration with Dr. Eleonora Grandi and Dr. Stefano Morotti in the UC Davis Department of Pharmacology. Additionally, we received key advice on approaches to sensitivity analysis from Dr. Kathryn Link, a postdoctoral scholar in UC Davis Mathematics.

Chapter 6: Roles of intracellular and extracellular calcium in the mechanics of neutrophil deformation during antibody-mediated phagocytosis

Abstract

Although Ca^{2+} bursts are well-known to occur during phagocytosis, it remains unclear if or when they are required for efficient target consumption. In this final chapter, we examine IgG-mediated phagocytosis after chelating extracellular or intracellular Ca^{2+} or pre-depleting intracellular Ca^{2+} stores. We restrict our focus to phagocytosis of IgG-coated microspheres in dual-micropipette experiments and frustrated phagocytic spreading on IgG-coated coverslips. In both experimental setups, we tested for any effects of the above treatments on cell morphology and phagocytic spreading dynamics. We also fixed and stained cells during frustrated phagocytic spreading to examine the organization of F-actin. In micropipette experiments, we found that neutrophils were capable of phagocytosing IgG-coated particles in all the conditions tested. However, frustrated phagocytic spreading was significantly slower when Ca^{2+} bursts were eliminated by pre-depletion of intracellular stores. In the absence of all extracellular divalent cations, cell morphology was significantly altered – neutrophils pushed IgG-coated beads outward prior to internalization. This push-out was not observed in Ca^{2+}-free solutions containing Mg^{2+}, indicating that the observed effect was not due to lack of Ca^{2+} influx. Rather, we attributed the push-out to the general inhibition of integrin binding in the absence of divalent cations. Finally, we found there were significant changes in F-actin distribution during frustrated phagocytosis after fully eliminating Ca^{2+} bursts or removing all extracellular divalent cations. Overall, this study shows that Ca^{2+} bursts regulate phagocytic spreading dynamics and also provides evidence that integrins play a key role in the mechanics of IgG-mediated phagocytosis.

Introduction

Phagocytosis, the process by which neutrophils engulf pathogens, is a mechanically intensive process, requiring precise spatiotemporal regulation of the cytoskeleton. Upon encountering pathogens such as bacteria or fungi, neutrophils must first adhere to the pathogen surface and then form pseudopod extensions around the particle via actin polymerization.

Cytoskeletal reorganization during phagocytosis is supported by different biochemical signaling pathways, many of which are associated with rapid, global bursts in intracellular Ca^{2+} concentration. Ca^{2+} is a known regulator of the cytoskeleton in a variety of cell types; the best-known example comes from muscle fibers, in which Ca^{2+} elevations are the key cell-wide events leading to muscle contraction [227]. However, in the context of neutrophil phagocytosis, it remains unclear if or how Ca^{2+} elevations may be coupled to the actomyosin machinery of the cell.

In Chapter 4, we showed that Ca^{2+} bursts are not required for actin polymerization during chemotactic protrusion. On the other hand, we also found that stimulating cells with higher concentrations of chemoattractant led to Ca^{2+} bursts in conjunction with cell contraction, suggesting that elevated intracellular Ca^{2+} is in fact coupled to the contractile machinery of neutrophils. Past studies have found that phagocytosis did not strictly require Ca^{2+} bursts, but upon chelation of intracellular Ca^{2+}, phagocytosis of IgG-coated particles was significantly reduced [24] or, after phagocytosis of yeast particles, actin disassembly was inhibited [228]. The elimination of Ca^{2+} bursts also significantly slowed or stalled β_2-integrin mediated phagocytosis [30] and was shown to inhibit neutrophil spreading more generally [29].

The effects of Ca^{2+} on phagocytosis and cell spreading have been partially attributed to the Ca^{2+}-sensitivity of the enzyme calpain, which cleaves FERM (4.1/ezrin/radixin/moesin)-domain-mediated connections between the membrane and the cytoskeleton [80, 81]. These cleavage events increase the mobile fraction of receptors and facilitate rapid unfurling of membrane folds. Ca^{2+} elevations can also mediate the formation of cytoskeleton-membrane attachments; for example, elevated cytosolic Ca^{2+} levels can lead to inside-out activation of integrins such as Mac-1 ($\alpha_M\beta_2$, complement receptor 3) [31, 229], which then form connections to the cytoskeleton through the molecule talin [15]. Based on these known functions of Ca^{2+}, we hypothesize that Ca^{2+} bursts regulate phagocytic spreading by controlling the lock and release of cytoskeleton-membrane attachments.

In this chapter, we address the role of Ca^{2+} in phagocytosis by systematically altering intracellular or extracellular Ca^{2+} in single-cell phagocytosis experiments and in frustrated phagocytosis assays. We also image the F-actin distribution in cells fixed during frustrated phagocytic spreading, to examine whether altering Ca^{2+} bursts leads to any changes in the underlying actin architecture. Overall, our findings strongly support the importance of cytoskeleton-membrane attachments to the mechanics of phagocytosis and suggest that Ca^{2+} bursts play a role in regulating the formation and cleavage of these structures.

Materials and Methods

Cell isolation and treatment conditions

Cells were isolated from the whole blood of healthy donors as described in Chapter 5, using the EasySep Human Neutrophil Isolation Kit (Cat#17957; STEMCELL Technologies). In all cases

except phalloidin staining, cells were resuspended in 0.5 μM Fluo-4 (Thermo Fisher Scientific) in HBSS+ (Hanks' Balanced Salt Solution with Ca^{2+} and Mg^{2+}; Thermo Fisher Scientific) with 0.1% human serum albumin (HSA; MP Biomedicals) following isolation and incubated at 37°C for 15 minutes.

Prior to experiments, cells were resuspended according to their treatment condition. All solution compositions and treatment protocols are summarized in Table 6.1 below. In frustrated phagocytosis experiments, thapsigargin-treated cells were deposited 40 minutes after the start of treatment. All experimental solutions included 0.01% anhydrous dimethyl sulfoxide (DMSO; Sigma-Aldrich) to account for the fact that the 1 mM thapsigargin stock solution was dissolved in DMSO.

Treatment	**Treatment conditions**	**Experimental conditions***
Control	Same as experimental conditions	HBSS+ with 2% HSA
Thapsigargin (TG)	40 min pre-treatment at room temperature in HBSS- with 0.1 mM EGTA, 0.9 mM $MgCl_2$, 100 nM thapsigargin, and 2% HSA	HBSS- with 0.1 mM EGTA, 0.9 mM $MgCl_2$, 100 nM thapsigargin, and 2% HSA
BAPTA	20 min pre-treatment at room temperature in HBSS- with 0.1 mM EGTA, 0.9 mM $MgCl_2$, 2 μM BAPTA-AM, and 2% HSA, then re-suspended in HBSS+ with 2% HSA	HBSS+ with 2% HSA *(no BAPTA present during experiment)*
EDTA	Same as experimental conditions	HBSS- with 0.1 mM EDTA and 2% HSA
EGTA	Same as experimental conditions	HBSS- with 0.1 mM EGTA, 0.9 mM $MgCl_2$, and 2% HSA

Table 6.1: Summary of treatment conditions for Chapter 6.
Abbreviations and suppliers: HBSS-: Hanks' Balanced Salt Solution without Ca^{2+} or Mg^{2+} (Thermo Fisher Scientific); EDTA: ethylenediamine tetraacetic acid (Affymetrix); EGTA: ethylene glycol tetraacetic acid (Research Products International); BAPTA-AM: (Abcam); thapsigargin (Thermo Fisher Scientific)

*see notes in text about presence of DMSO for certain experiments

Treatments were similar in micropipette experiments, although thapsigargin treatment continued for the entire duration of each experiment because all trials were conducted in a single chamber. DMSO was not present for pipette experiments in EDTA, EGTA, BAPTA, or control conditions. However, careful measurements of phagocytic spreading in frustrated phagocytosis experiments in 0% DMSO vs. 0.01% DMSO revealed no significant differences in spreading dynamics (data not shown).

Surface preparation

Preparation of IgG-coated surfaces and IgG-coated polystyrene microspheres is described in Chapter 5. For each surface, a dense monolayer of bovine serum albumin (BSA; VWR) was initially deposited, followed by a layer of rabbit polyclonal anti-BSA IgG (Cat# A11133; Invitrogen). All surfaces for these experiments were prepared using 150 μg/mL rabbit IgG, resulting in surfaces saturated with a monolayer of IgG (see Chapter 2).

Fixation and phalloidin staining

Fixation of human neutrophils after frustrated phagocytic spreading required careful considerations to effectively preserve their cytoskeletal structure. 15 minutes after depositing neutrophils onto the IgG-coated surface, the fluid volume was doubled in each well by adding 2X extraction buffer (0.5% glutaraldehyde, 0.4% Triton X-100, and 640 mM sucrose in 2X intracellular buffer, constituents of intracellular buffer listed below) for a 2-minute treatment. Cells were then gently washed with 1X intracellular buffer (as specified in [208]: 140 mM KCl, 1 mM $MgCl_2$, 2 mM EGTA, 20 mM HEPES, and 1% BSA) and incubated in the main fixation buffer (4% formaldehyde and 320 mM sucrose in 1X intracellular buffer; formaldehyde from Thermo Fisher Scientific) for 10 minutes. Due to presence of glutaraldehyde in the initial

extraction step, an extra step was required to quench glutaraldehyde autofluorescence. Therefore, after another gentle wash, cells were incubated in 0.2% (2 mg/ml) sodium borohydride dissolved in 1X intracellular buffer with 10% fetal bovine serum (FBS; Atlanta Biologicals) for an additional 10 minutes. Cells were gently washed twice more, then incubated in a solution of Alexa-Fluor-488-conjugated phalloidin (Abcam, 1000X diluted from stock) with 0.2% Triton X-100 and 10% FBS (to block non-specific binding) in 1X intracellular buffer for 30-45 minutes in the dark at room temperature. After two final washes, the cells were imaged on a spinning disc confocal microscope. All chemicals except EGTA, BSA, FBS, formaldehyde, and phalloidin were purchased from Sigma-Aldrich.

Image analysis

Particle trajectories in micropipette experiments were analyzed manually using in-house software. Mean intensity in Fluo-4 images was measured using MATLAB code as described in Chapter 5 (accessible at https://github.com/emmetfrancis/MFICalc). For each cell, we averaged the pixel intensity over a number of pixels corresponding to 40 μm^2 at each time point.

Phalloidin images were analyzed using a machine-learning-based approach in ImageJ. We used the Weka plugin [230] to train a classifier to distinguish between pixels belonging to punctate actin structures, pixels corresponding to the main cell body, and background pixels (see Fig 6.5). Our overall analysis workflow consisted of 1) cropping out single cells from each image and choosing the focal plane corresponding to the cell-substrate interface from the *Z*-stack for that given cell; 2) applying the classifier to a stack of single-cell images in Weka; and 3) post-processing segmented images to quantify the number and density of puncta within the cell-substrate contact region. Puncta were required to have a circularity greater than 0.9 and an area between 0.04 μm^2 and 0.4 μm^2.

Statistics

For each output, ANOVA was conducted for the five groups (standard, BAPTA, TG, EDTA, EGTA), followed by Tukey's post-hoc test in Origin graphing software. Correlation coefficients for Fig 6.2 were computed in MATLAB, with the reported *p* values corresponding to the null hypothesis that the correlation coefficient equals zero.

Results

Inhibition of Ca^{2+} bursts slows phagocytic spreading, but does not eliminate phagocytosis

As shown in Chapter 5, Ca^{2+} bursts in IgG-mediated phagocytosis involve release of Ca^{2+} from the endoplasmic reticulum (ER), with a secondary role of influx through the plasma membrane. We first tested for phagocytosis after treating with 100 nM thapsigargin (TG) to pre-deplete intracellular Ca^{2+} stores or after loading cells with BAPTA-AM to chelate free intracellular Ca^{2+} (Table 6.1). TG treatment effectively eliminated Ca^{2+} bursts in most cases, whereas BAPTA-loading dampened Ca^{2+} increases (Fig 6.1A).

In both conditions (TG and BAPTA), we still observed phagocytosis of 5 μm IgG-coated beads in single-cell micropipette experiments (Fig 6.1B). We quantified the dynamics of phagocytosis in these experiments by monitoring the relative position of the bead over time (Fig 6.1C). For each phagocytosing cell, we measured the distance by which the cell displaced the bead outwards at the start of phagocytosis (push-out distance, Fig 6.1C) and the maximum speed at which the bead moved inward during mid-to-late phagocytosis (pull-in speed, Fig 6.1C). By either metric, phagocytosis remained unchanged for either full (TG) or partial (BAPTA)

inhibition of Ca^{2+} bursts. We also examined the efficiency of phagocytosis by measuring the total time required for phagocytosis, from initial cell deformation to closure of the phagocytic cup. Under control conditions, phagocytosis of a single bead from the time of initial deformation to phagosome closure was 125 s on average, but phagocytosis took slightly longer (145 s on average) for TG-treated cells. This difference was not statistically significant, but still invited further investigation.

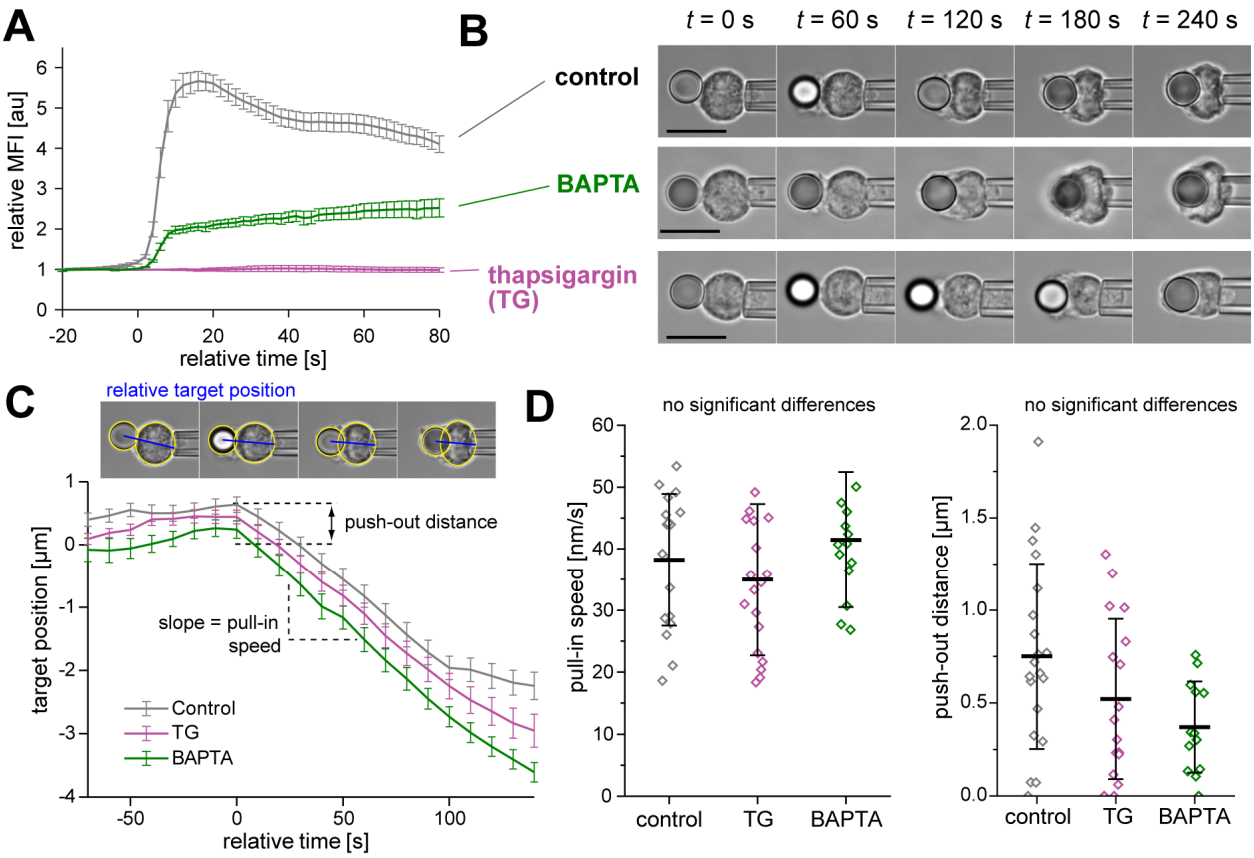

Fig 6.1: Thapsigargin-treated and BAPTA-loaded neutrophils in dual-micropipette phagocytosis experiments. (A) Averaged Fluo-4 mean fluorescent intensity (MFI) is plotted over time for cells under each condition, aligned by defining the start of the Ca^{2+} burst as $t = 0$. In the case of TG-treated cells that showed no detectable increase in fluorescence, $t = 0$ was defined by the start of the pull-in. **(B)** Sample images of neutrophils phagocytosing 5µm beads are shown for all three conditions. Cells are representative of data from several experiments with different donors (21 cells for TG, 14 cells for BAPTA, and 21 control cells). Scale bars denote 10 µm. **(C)** Mean target trajectories over time were similar for these three conditions. Target position was defined as shown by the blue lines in the sample images – the distance from the center of the bead to the back of the cell body (passing through the center of the cell). Trajectory curves from individual cells were aligned by defining $t = 0$ as the start of the pull-in. **(D)** There were no significant differences in either pull-in speed or push-out distance for these tests. Error bars in (A) and (C) denote standard error of the mean, and those in panel (D) denote standard deviation.

We postulated that phagocytosis by TG-treated cells took longer on average because they spread more slowly over pathogen surfaces. To test this, we utilized our frustrated phagocytosis assay, as described in Chapters 2 and 5. In these experiments, Fluo-4-labeled neutrophils were deposited onto an IgG-coated coverslip and imaged during spreading using a combination of reflection interference contrast microscopy (RICM) and fluorescence imaging. For each spreading cell, we measured the spreading speed (maximum slope of the contact-area-versus-time curve) and the maximum contact area (contact area value at the first post-spreading plateau of the contact-area-versus-time curve) while also monitoring Fluo-4 fluorescence. We aligned these contact area curves and plotted the overall average growth for ease of comparison (Fig 6.2A). We found that both the spreading speed and the maximum contact area were significantly lower for TG-treated cells as compared to control cells (Fig 6.2B-C). BAPTA-loaded cells were similar to control cells with respect to both metrics.

Due to cell-to-cell variability, there was inevitably a range of Ca^{2+} burst magnitudes within any of the three conditions. We accounted for this variability by examining the overall correlation between our spreading metrics (spreading speed and maximum contact area) and Ca^{2+} burst magnitude (peak MFI divided by baseline MFI) for cells from all three conditions (Fig 6.2D-E). Both metrics correlated significantly with Ca^{2+} burst magnitude, providing strong evidence for a mechanoregulatory role of Ca^{2+} bursts during phagocytic spreading.

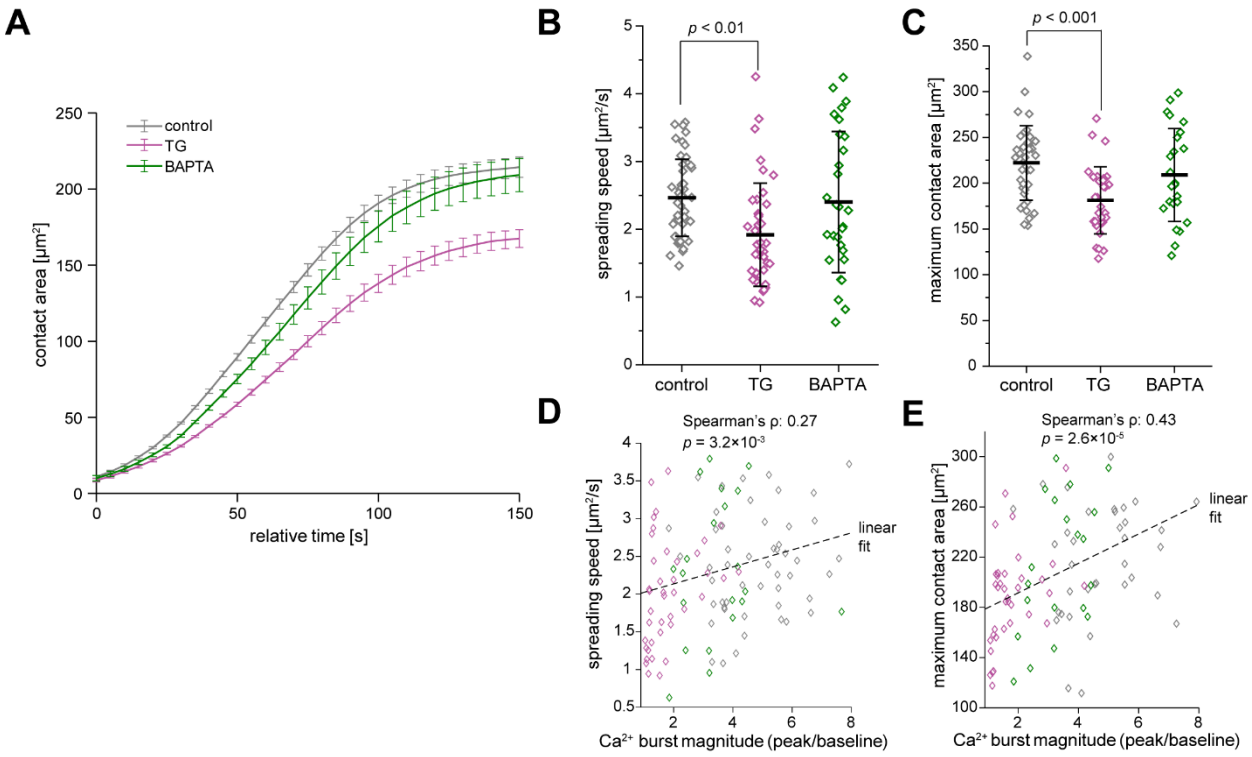

Fig 6.2: Thapsigargin-treated and BAPTA-loaded neutrophils in frustrated phagocytosis assays. (A) Mean spreading dynamics show that TG-treated cells spread more slowly and reached smaller maximum contact areas on average, but BAPTA-loaded cells spread similarly to control cells. Error bars denote standard error of the mean. **(B)** TG-treated cells spread more slowly than control or BAPTA-loaded neutrophils. **(C)** TG-treated cells reached much lower maximum contact areas than control cells on average. **(D)** This scatter plot shows a significant correlation between spreading speed and Ca^{2+} burst ratio (MFI value at the first peak divided the baseline value prior to phagocytosis), including cells from all three conditions. **(E)** This scatter plot shows a significant correlation between maximum contact area and Ca^{2+} burst ratio, including cells from all three conditions. Correlations in (D) and (E) were tested using Spearman's rank correlation coefficient (ρ). Error bars in (B) and (C) denote standard deviation.

Removal of extracellular divalent cations alters the dynamics of phagocytosis

Although extracellular Ca^{2+} is not the primary source of Ca^{2+} in initial bursts (shown in Chapter 5), it is required for prolonged oscillations and refilling of Ca^{2+} stores over time [22, 147, 217]. We tested the effects of removing extracellular Ca^{2+} in two conditions, one in which both Ca^{2+} and Mg^{2+} were absent from the medium (supplemented with the divalent cation chelator EDTA) and another in which Ca^{2+} was absent, but Mg^{2+} was present in normal amounts (supplemented with EGTA, which has a much higher affinity for Ca^{2+} than Mg^{2+}) (Table 6.1). These two conditions are referred to as "EDTA" and "EGTA" below.

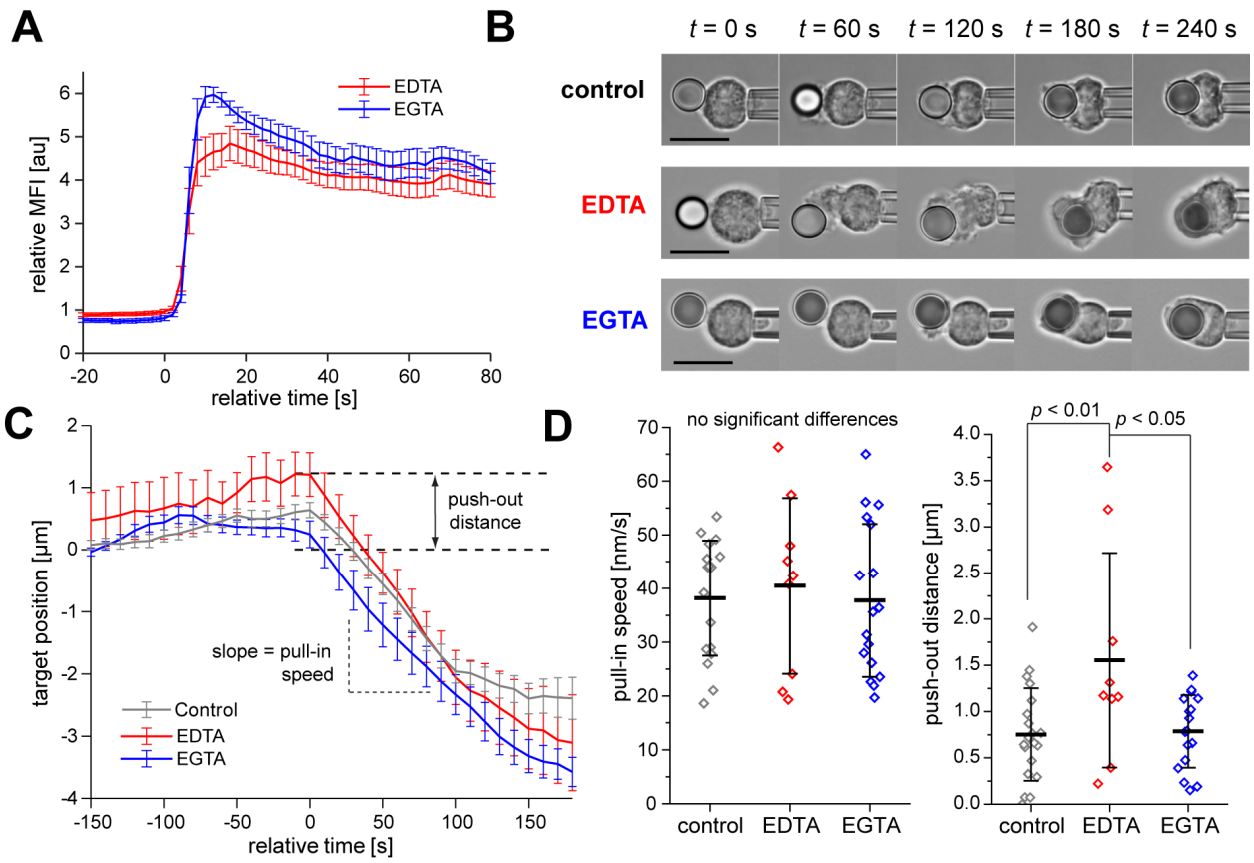

Fig 6.3: Micropipette experiments in the absence of extracellular Ca^{2+}. (A) Averaged MFI over time for EDTA (extracellular Ca^{2+} and Mg^{2+} both absent) and EGTA (extracellular Ca^{2+} absent, Mg^{2+} present) conditions both show Ca^{2+} bursts. Curves from individual cells were aligned by the start of the Ca^{2+} burst before averaging. A lower baseline was assumed for cases in which the Ca^{2+} burst ratio (first peak divided by baseline) was greater than 10. **(B)** Sample time-lapse images are shown for neutrophil phagocytosis under control conditions, compared with the two treatment conditions. In the EDTA condition, the cell displaces the IgG coated bead outwards prior to consumption, but in the EGTA condition, the cell phagocytoses normally. Cells are representative of data from several experiments with different donors (10 cells for EDTA, 18 cells for EGTA, and 21 control cells). Scale bars denote 10 µm. **(C)** Mean target trajectory is plotted over time, showing similar pull-in speeds for all three conditions, but a significantly larger push-out distance for the EDTA condition. Target position was defined as shown in Fig 6.1C. Individual trajectory curves were aligned by defining $t = 0$ as the start of the target pull-in. **(D)** The pull-in speed remained similar across conditions, but in the absence of all divalent cations (EDTA condition), there was significantly greater outward displacement of the target particle compared to control. Error bars in (A) and (C) denote standard error of the mean, and error bars in (D) indicate standard deviation.

In micropipette experiments conducted in the absence of extracellular Ca^{2+}, cells exhibited Ca^{2+} bursts, in line with our results in Chapter 5 (Fig 6.3A). Ca^{2+} bursts appeared to be higher in magnitude on average for the EGTA condition, but this difference was not consistent across days and was likely dependent on how long the cells were in Ca^{2+}-free media prior to phagocytosis, which was not controlled for in our experiments.

Neutrophils successfully completed phagocytosis under both conditions (Fig 6.3B). However, we found that cell morphology was significantly altered when no divalent cations were present. Rather than immediately spread around the IgG-coated bead, cells tended to push the bead outwards initially (Fig 6.3B). This push-out distance was significantly greater in the EDTA condition than it was for the EGTA condition or for control cells. Furthermore, there was no significant push-out observed for cells in the EGTA condition compared to control cells. Therefore, we concluded that the push-out observed in the EDTA condition was not due the lack of Ca^{2+} influx through the plasma membrane.

We then assessed phagocytic spreading for each of these conditions in our frustrated phagocytosis assay. In the absence of all divalent cations (EDTA condition), cells spread faster when compared to control conditions (Fig 6.4B). This effect was not observed for cells in the EGTA condition. We observed no significant differences in the maximum contact area achieved during spreading between these three conditions (Fig 6.4C). Given these data, we conclude that Ca^{2+} influx itself plays a minimal role in the progression of phagocytic spreading on IgG, but extracellular divalent cations are generally required for normal morphology and spreading in phagocytosis.

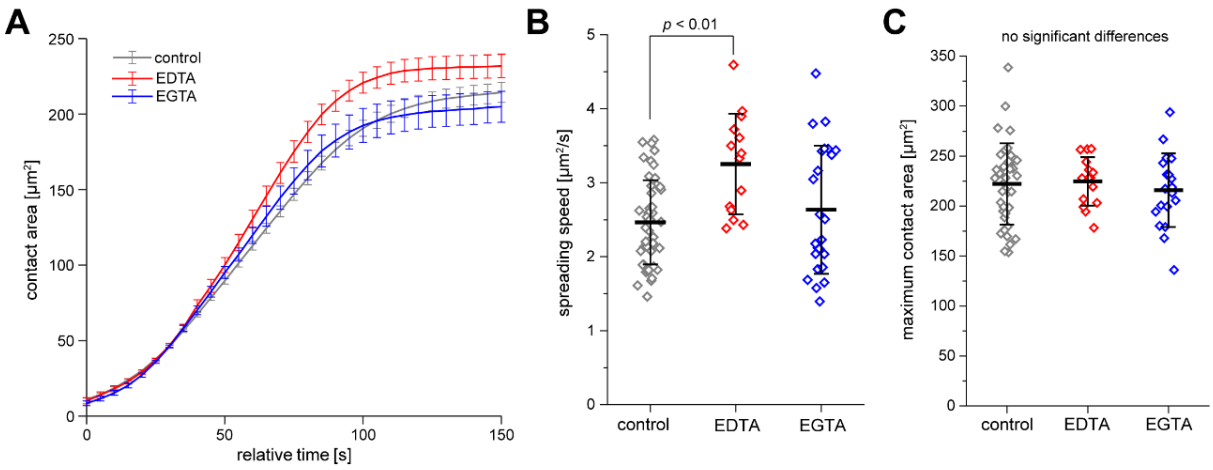

Fig 6.4: Frustrated phagocytosis experiments in the absence of extracellular Ca^{2+}. (A) Average contact area growth over time is very similar for EGTA and control cells, but in the absence of all divalent cations (EDTA), cells spread faster than control cells. **(B)** Spreading speed is significantly higher in the absence of all divalent cations (EDTA condition). **(C)** Maximum contact areas are similar across these three conditions. Error bars in (A) denote standard error of the mean, and error bars in (B) and (C) denote standard deviation.

Ca^{2+} treatments alter actin architecture during phagocytic spreading

We fixed cells during frustrated phagocytosis and stained with Alexa-Fluor-488-conjugated phalloidin to observe the F-actin architecture within spreading neutrophils. Under standard conditions, we observed that actin filaments formed intriguing punctate structures at the cell-substrate interface, indicating the formation of discrete adhesion structures on the surface, reminiscent of podosomes or focal adhesions (Fig 6.5A). Similar structures have been observed and characterized in macrophage frustrated phagocytosis on IgG or C3b-coated surfaces [46]. We automated detection of these structures using a machine-learning based classifier in the Weka ImageJ plugin, allowing us to discriminate between puncta, the remainder of the cell-substrate contact region, and the background (Fig 6.5B, Methods).

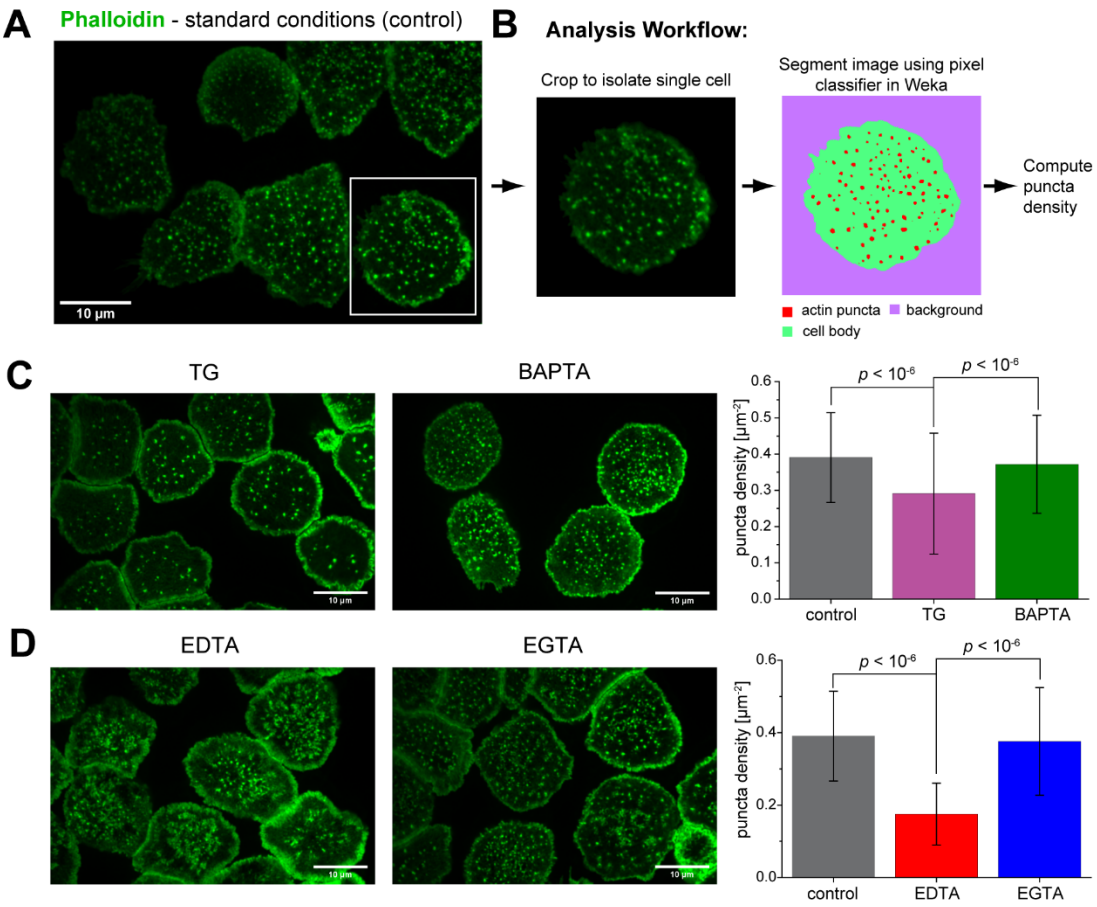

Fig 6.5: Phalloidin staining of neutrophils fixed during phagocytosis with altered intracellular or extracellular Ca^{2+} concentrations. (A) Under standard conditions, F-actin organizes into punctate structures during phagocytic spreading. **(B)** The number and density of these punctate F-actin structures was analyzed by cropping single cells and applying a machine learning classifier using the Weka plugin in ImageJ. The pixels were then sorted into three categories, as shown in the right-most image: actin puncta, cell body, and background. **(C)** Sample fluorescence images show the F-actin distribution in TG-treated cells and BAPTA-loaded cells during phagocytic spreading. TG-treated cells had a significantly lower density of actin puncta compared to both control cells and BAPTA-loaded cells. **(D)** Sample fluorescence images show the F-actin distribution in cells spreading in the absence of all extracellular divalent cations (EDTA) or with Ca^{2+} absent and Mg^{2+} present. Actin structure was significantly different when no divalent cations were present, as indicated by a much lower density of actin puncta, but inclusion of extracellular Mg^{2+} restores puncta density to the same level as control cells. Scale bars denote 10 µm. Error bars denote standard deviation.

We examined phalloidin stains for the four different conditions outlined above. Treatment protocols were identical to those in our frustrated phagocytosis assay, but in this case, cells were not pre-loaded with Fluo-4. TG-treated or BAPTA-loaded cells still formed actin puncta in the process of phagocytic spreading, but puncta density was significantly lower in TG-treated cells (Fig 6.5C).

Removal of all extracellular divalent cations resulted in significantly altered F-actin distributions (Fig 6.5D). Although puncta were still observed, they formed at much lower densities (Fig 6.5D). Furthermore, the periphery of cell-substrate contact regions exhibited denser bands of actin. In the presence of extracellular Mg^{2+}, these effects were eliminated (Fig 6.5D), in good agreement with the findings of our micropipette and frustrated phagocytic spreading experiments.

Discussion / Conclusions

Given the diverse roles of Ca^{2+} as a second messenger in the cell, Ca^{2+} bursts during phagocytosis are expected to have many implications for overall cell behavior. In this study, we found that Ca^{2+} bursts, although not strictly required for IgG-mediated phagocytosis, do regulate the efficiency of phagocytic spreading and the total amount of cell deformation.

In general, phagocytic spreading speed is determined by a balance between cytoskeletal protrusion and the cell's cortical tension. Incidentally, elevations in intracellular Ca^{2+} concentration can alter both protrusion stress and cortical tension. Increases in Ca^{2+} concentration lead to activation of integrins, which then form anchoring connections back to the cytoskeleton. This provides bracing support during phagocytic spreading, increasing the effective protrusion stress [14, 82]. Additionally, Ca^{2+}-dependent activation of calpain leads to cleavage of cytoskeleton-membrane linkages, lowering the local cortical tension and allowing for unfurling of folds in the plasma membrane [29, 81]. Cell surface area expansion is also supported by exocytosis, which is known to be Ca^{2+}-dependent [231]. Addition of membrane through

exocytosis is expected to lower the cortical tension and increase the maximum surface area available for spreading.

The above roles for Ca^{2+} bursts are consistent with our findings in experiments with TG-treated cells; these cells spread more slowly and reached smaller maximum contact areas compared to control cells. Following TG treatment, neutrophils formed actin puncta at lower densities than control cells, which likely indicates weaker coupling between the membrane and the cytoskeleton. Similar actin structures in macrophages were shown to be surrounded by β_2 integrin and integrin-binding proteins such as talin and vinculin [46], indicating they are normally sites of strong anchoring between the membrane and the cytoskeleton.

The results presented in this chapter are strictly limited to IgG-mediated phagocytosis, although some findings may carry over to other cases of phagocytosis. For instance, a significant correlation between Ca^{2+} burst magnitude and phagocytic spreading speed may also be present in complement-mediated phagocytosis. In fact, the effect may even be stronger, as in complement mediated phagocytosis, the main receptor involved, Mac-1, is an integrin whose activity is known to be modulated by intracellular Ca^{2+} [31, 229].

In addition to the putative role of Ca^{2+} bursts in regulating the mechanics of neutrophil phagocytic spreading, it should be noted that Ca^{2+} is known to play several significant roles in the late stages of phagocytosis. For instance, Ca^{2+} elevations trigger oxidase activity after phagosome closure [232] and are required for efficient granule fusion in phagosome maturation [226]. However, the Ca^{2+} elevations associated with these processes generally come after the initial burst we are focused on here.

Beyond the context of Ca^{2+} signaling, our findings have emphasized the key role of cytoskeleton-membrane linkages in the mechanics of phagocytosis. In the absence of extracellular divalent cations, we see clear evidence of weakened cytoskeleton-membrane connections, leading to altered cell morphology during phagocytosis. Neutrophils initially pushed IgG-coated beads outwards rather than simply spreading around them, a phenomenon that was previously explained by weakened cytoskeleton-membrane attachments at the region of cell-particle contact [11]. Indeed, we observe much lower densities of actin puncta forming in the absence of divalent cations, which may indicate weakened cytoskeleton-membrane coupling. These effects were not present in experiments conducted in the presence of extracellular Mg^{2+} only (EGTA condition), a condition that was previously shown to lead to higher constitutive activity of β_2-integrins when compared to experiments in media containing both Ca^{2+} and Mg^{2+} [233, 234]. In our case, this baseline activation of integrins did not result in any detectable changes from control cells, indicating that integrins are also activated during IgG-mediated phagocytosis in control cells, which agrees with other studies [17].

Interestingly, in the absence of divalent cations (EDTA condition), weakened cytoskeleton-membrane connections resulted in an increase in spreading speed during frustrated phagocytosis. This seems to contradict our claim that weakened cytoskeleton-membrane connections led to slower spreading in the case of TG-treated cells. However, because global Ca^{2+} bursts still occur in the EDTA treatment, this could still allow for sufficient calpain activation to facilitate rapid membrane unfolding. In this case, then, higher densities of actin-membrane linkages could slow spreading by acting as an effective friction, whereas weakening them could in fact speed up phagocytic spreading.

The above hypotheses regarding the effects of TG-treatment and extracellular divalent cation depletion on the mechanics of phagocytic spreading could be tested by inserting the relevant assumptions into our computational model developed in Chapter 3. In fact, once enough is known about how Ca^{2+} affects mechanics, we could couple our Ca^{2+} signaling model in Chapter 5 to the mechanical model in Chapter 3 to develop a full *in silico* model of the treatments tested here. Such attempts to quantitatively understand the complex coupling between cell mechanics and signaling are promising strategies for investigating not just neutrophil phagocytosis, but also many other cases of cell motility.

Acknowledgements:

Dr. Soichiro Yamada gave us key advice and assistance in the development of our fixation and phalloidin staining protocol, and provided the confocal microscope used to image phalloidin-stained neutrophils. We also thank Sahand Salari-Namin for assistance with some of the frustrated phagocytosis assays in the absence of extracellular Ca^{2+}, as shown in Fig 6.4.

Appendices

Opening note: Appendices A-F pertain to the modeling work presented in Chapter 3. Supplementary materials for Chapters 4 and 5 have been included as single appendices each (Appendix G and Appendix H, respectively).

Appendix A. Adhesion stress calculation

To compute the adhesion stress, we consider a potential acting between an adhesion molecule and a receptor in the cell membrane. Here, we use a 6-3 potential:

$$u_{adh}(D) = u_0\left[\left(\frac{D_0}{D}\right)^6 - 2\left(\frac{D_0}{D}\right)^3\right] \tag{A.1}$$

where D_0 is the distance associated with the energy minimum and u_0 sets the magnitude of the binding energy. The force due to this single interaction is

$$f_{adh}(D) = -\frac{du_{adh}(D)}{dD} = f_0\left[\left(\frac{D_0}{D}\right)^7 - \left(\frac{D_0}{D}\right)^4\right] \tag{A.2}$$

where $f_0 = 6u_0/D_0$. As D_0 is the location of the energy minimum, we also see that $f_{adh}(D_0) = 0$. We use $D_0 = 50$ nm in our simulations. Realistically, one might expect this distance to be much smaller (molecular scale), but the longer range here effectively includes membrane fluctuations and filopodia and serves as an upper limit. Adhesion potentials with a range of tens to hundreds of nanometers are common when modeling cells and vesicles at the mesoscopic scale [62, 109].

To solve for the overall adhesion stress, we integrate over the ligand-coated surface (surface coordinates $[r, \theta]$) and the region of membrane being considered (surface coordinates $[s, \psi]$) (Fig A.1A).

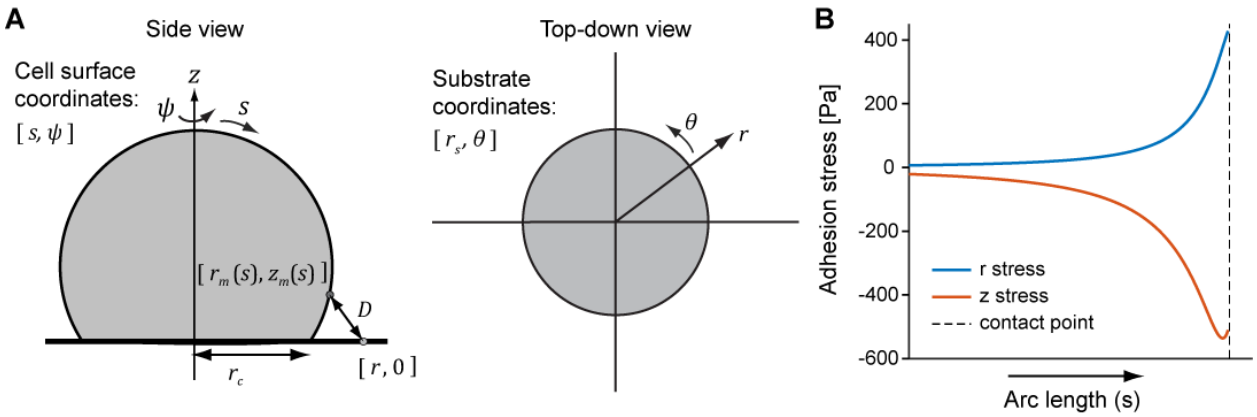

Fig A.1: Adhesion force calculation.
(A) The cell geometry is depicted from the side, as well as from the top, including definitions of coordinates used in the text. (B) Adhesion stress components are plotted as a function of arc length s for the cell shape shown in part A at a relative ligand density of 10%.

Individual interaction forces are specified as vectors, that is

$$\mathbf{f}_{single} = f_0 \left[\left(\frac{D_0}{D} \right)^7 - \left(\frac{D_0}{D} \right)^4 \right] \mathbf{f}_{unit} \tag{A.3}$$

The distance between a point on the membrane and a point on the surface is given by

$$D(r, \theta, s, \psi) = \sqrt{(r_m \cos\psi - r\cos\theta)^2 + (r_m \sin\psi - r\sin\theta)^2 + z_m{}^2} \tag{A.4}$$

The distance z_m is adjusted from the z coordinate used elsewhere so that the surface $z = 0$ corresponds to the zero-force distance D_0, i.e. $z_m = z + D_0$.

The direction of the force is expressed by a unit vector (we only calculate the r and z components, as the angular component cancels out due to symmetry)

$$\mathbf{f}_{unit} = \frac{1}{D} \begin{bmatrix} r_m \cos\psi - r\cos\theta \\ z_m \end{bmatrix} \tag{A.5}$$

Considering a region of the cell membrane extending from $s = s_{cur} - l/2$ to $s = s_{cur} + l/2$ along the arc length and from $\psi = -\Delta\psi/2$ to $\psi = \Delta\psi/2$ in the angular direction, we compute the pairwise force by the total integral

$$\mathbf{f}_{adh} = \int_{-\frac{\Delta\psi}{2}}^{\frac{\Delta\psi}{2}} \int_{s_{cur}-\frac{l}{2}}^{s_{cur}+\frac{l}{2}} \left(\int_0^{2\pi} \int_{r_c}^{\infty} \mathbf{f}_{single} \rho_l r dr d\theta \right) \rho_R r_m ds d\psi \tag{A.6}$$

where ρ_l is the ligand density on the substrate and ρ_R is the receptor density on the cell membrane. In practice, we lump f_0 and ρ_R into a single parameter $\sigma_0 = f_0 \rho_R$, which effectively serves as a force per unit area of cell membrane (see Table 3.1).

The stress per unit area of membrane is given by

$$\boldsymbol{\sigma}_{adh} = \frac{\mathbf{f}_{adh}}{\int_{-\frac{\Delta\psi}{2}}^{\frac{\Delta\psi}{2}} \int_{s_{cur}-\frac{l}{2}}^{s_{cur}+\frac{l}{2}} r_m ds d\psi} \tag{A.7}$$

In the limit $l\Delta\psi \to 0$, we obtain the final expression, as given in the main text

$$\boldsymbol{\sigma}_{adh} = \sigma_0 \rho_l \int_0^{2\pi} \int_{r_c}^{\infty} \mathbf{f}_{unit} \left[\left(\frac{D_0}{D} \right)^7 - \left(\frac{D_0}{D} \right)^4 \right] r dr d\theta \tag{A.8}$$

This integral is not readily carried out analytically. Therefore, we evaluate it numerically in MATLAB by performing trapezoidal integration in both dimensions, using log-spaced meshes for both r and θ. Results of this integration are essentially identical to those of integration with MATLAB built-in functions, but computation time is reduced well over 10-fold. An example of the adhesion stress components computed as a function of arc length s along the cell contour defined in Fig A.1A is shown in Fig A.1B for $\rho_l = 10\%$.

In practice, we modify the adhesion strength in simulations by varying the scaling factor $\sigma_0\rho_l$, but we cannot directly extract the ligand density ρ_l. Instead, we infer the adhesion energy per unit area γ from the equilibrium contact area A_c using simple geometry, conservation of volume, and the Young-Dupre equation, as explained in the main text. Using these estimated values of adhesion energy $\gamma(A_c)$ and the typical binding energy of a low affinity Fcγ receptor to IgG ($E_{bind} \approx 6 \times 10^{-20}$ J [112]), we estimate the IgG density $\rho_{IgG,est}$ as

$$\rho_{IgG,est} = \frac{\gamma(A_c)}{E_{bind}} \tag{A.9}$$

We perform a linear fit between $\rho_{IgG,est}$ and the relative adhesion strength $\rho_l / \rho_{l,max}$ to compute the effective IgG densities tested in our Brownian Zipper model (Fig A.2). From this fit, we find that ρ_l = 10% roughly corresponds to $\rho_{IgG,est}$ = 1,000 μm^{-2}.

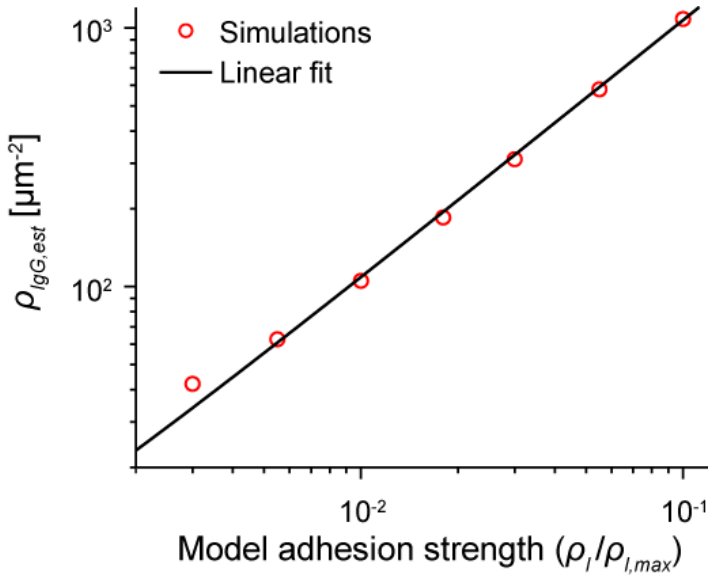

Fig A.2. Relationship between estimated IgG density and model adhesion strength.
A linear fit relates model adhesion strength to IgG density based on the equilibrium contact areas obtained from simulations.

Appendix B. Derivation of a power law for contact area growth in passive spreading

To develop an approximate analytical prediction of the functional dependence of the contact area on time, we start from the overall energy balance for our passive model cell spreading on a flat surface with adhesion energy density γ, analogous to the energy balance in the spreading of a viscous droplet [113]. After canceling a factor of 2π, this yields

$$\frac{\gamma}{2}\frac{\partial}{\partial t}(r_c^2) = 2\mu\iint e_{ij}e_{ij}rdrdz + \frac{\partial}{\partial t}\left(\tau\int rds\right) + \frac{\partial}{\partial t}\left(\iint prdrdz\right) \tag{B.1}$$

where r_c is the cell contact radius, μ is the effective cell viscosity, e_{ij} denotes the i,j component of the rate-of-strain tensor (repeated indices are summed over), τ is the cortical tension, and p is the pressure inside the cell. The left-hand side corresponds to energy gain due to cell-surface adhesion. The first term on the right-hand side is the viscous dissipation rate [235], the second term is the work required to deform the cortex, and the third is the change in energy due to changes in pressure and/or volume. In our simulations volume is kept constant, and any energy required for pressure changes is much lower than for changes of the surface area or tension; therefore, we neglect the last term of Eq (B.1) in the following analysis.

To estimate the remaining terms in the energy balance, we assume that the passively spreading cell adopts the shape of a spherical cap with contact radius r_c and radius of curvature R_{cell} (Fig B.1A). This geometry defines the contact angle as:

$$\sin\theta_c = \frac{r_c}{R_{cell}} \tag{B.2}$$

We focus this analysis on initial contact area growth, during which the contact angle is small and we can treat R_{cell} as a constant. Based on this geometry and features of the calculated flow

profile (Fig B.1A inset), we estimate the viscous dissipation rate and work required to deform the cortex as follows.

We first expand the dissipation term to include all non-zero components of the rate-of-strain tensor (all derivatives with respect to the polar angle are zero given axial symmetry):

$$\Pi = 2\mu \iint e_{ij} e_{ij} r dr dz = \mu \iint \left[2\left(\frac{\partial v_r}{\partial r} \right)^2 + 2\left(\frac{v_r}{r} \right)^2 + 2\left(\frac{\partial v_z}{\partial z} \right)^2 + \left(\frac{\partial v_r}{\partial z} + \frac{\partial v_z}{\partial r} \right)^2 \right] r dr dz \tag{B.3}$$

The main effect of the adhesion force is to "pull down" the membrane onto the flat surface; that is, the *z*-component of the adhesion stress generally dominates (Fig B.1B). Accordingly, we expect v_z to dominate over v_r in the portion of the cell closest to the substrate, which is confirmed by our calculations (Fig B.1A inset). Furthermore, due to incompressibility, we know

$$\frac{v_r}{r} + \frac{\partial v_r}{\partial r} + \frac{\partial v_z}{\partial z} = 0 \tag{B.4}$$

Therefore, if the contributions of v_r are small, $\partial v_z/\partial z$ must also be small, and we are left with:

$$\Pi \approx \mu \iint \left(\frac{\partial v_z}{\partial r} \right)^2 r dr dz \tag{B.5}$$

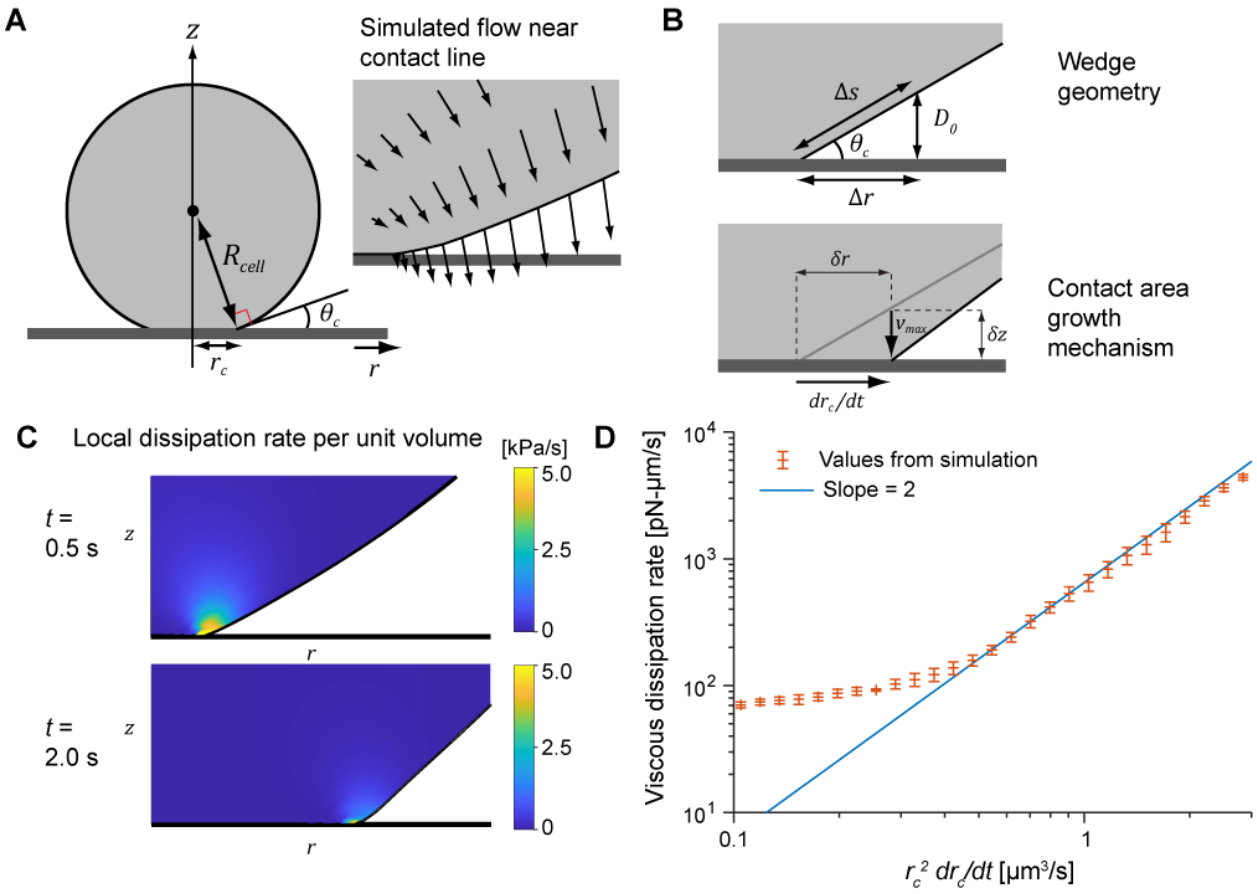

Fig B.1: Energy balance calculations.
(A) Geometry of a spreading droplet during early spreading. The inset illustrates fluid velocities (arrows) at the boundary near the contact line as predicted by a typical Brownian zipper simulation. (B) Simplified geometry of a wedge used to represent a spreading droplet. The top panel defines variable used in the text. The bottom panel illustrates the manner of contact area growth implemented in our model. (C) Local dissipation per unit volume at the contact line for two early time points as computed by a Brownian zipper simulation at a ligand density of 10%. The dissipation is tightly confined to the point of contact. (D) Total viscous dissipation rate was directly computed using linear shape functions and plotted against $r_c^2\ dr_c/dt$ on a log-log axis. Simulated values were binned and averaged for each interval on the x-axis. Error bars indicate standard deviation of binned data.

As a test geometry for points near the surface, we consider a wedge-like shape, as shown in Fig B.1B. The exact functional form of v_z within this wedge cannot be readily inferred *a priori*. Instead, we identify characteristic length scales to estimate the velocity gradient. We expect the *z*-velocity to be highest close to the surface, that is, within the length scale set by the adhesion potential (D_0). The associated distance in the *r*-direction Δr (Fig B.1B) is given by:

$$\Delta r = \frac{D_0}{\tan\theta_c} \approx \frac{D_0 R_{cell}}{r_c} \tag{B.6}$$

Before estimating the velocity gradient, we relate v_z to the rate of contact radius growth, dr_c/dt. Because there is no slip at the contact line itself, the only way for the contact area to increase is for nonadherent membrane to approach and touch the surface past the contact line. We consider a sample point close to the surface at which the membrane moves at maximum velocity v_{max} in the negative z direction (Fig B.1B). If this point moves down from a distance δz from the surface, then the contact line moves outward by a distance of δr in the r-direction (Fig B.1B), given by

$$\delta r = \frac{\delta z}{\tan\theta_c} \tag{B.7}$$

In terms of velocities, this yields

$$\frac{dr_c}{dt} = \frac{v_{max}}{\tan\theta_c} \approx \frac{v_{max} R_{cell}}{r_c} \tag{B.8}$$

Combining Eqs (B.6) and (B.8) and assuming the velocity gradient is highest in the direction tangent to the membrane, we approximate the sought velocity gradient:

$$\frac{\partial v_z}{\partial r} \approx \frac{v_{max}}{\Delta r} = \frac{{r_c}^2}{{R_{cell}}^2 D_0}\frac{dr_c}{dt} \tag{B.9}$$

We insert these estimates into the dissipation term (Eq (B.5)) and integrate over the wedge:

$$\begin{aligned}\Pi &\approx \mu\left(\frac{{r_c}^2}{{R_{cell}}^2 D_0}\frac{dr_c}{dt}\right)^2 \int_{D_0\frac{r-r_c}{\Delta r}}^{D_0}\left(\int_{r_c}^{r_c+\Delta r} r dr\right) dz \\ &= \mu\left(\frac{{r_c}^2}{{R_{cell}}^2 D_0}\frac{dr_c}{dt}\right)^2 \frac{D_0\Delta r}{6}\left(3r_c + \Delta r\right)\end{aligned} \tag{B.10}$$

Inserting the definition of Δr from Eq (B.6) and assuming $\Delta r << 3r_c$, we find

$$\Pi \approx \Pi_0 r_c^4 \left(\frac{dr_c}{dt} \right)^2 \tag{B.11}$$

where $\Pi_0 = \mu/(2R_{cell}^3)$. We verify this relationship by comparing it to numerically computed dissipation rates obtained in Brownian zipper simulations (Fig B.1C-D). The dissipation rate per unit volume is highest in a small region near the contact line (Fig B.1C). We integrate to compute the total dissipation rate at each time step, and then plot this as a function of $r_c^2(dr_c/dt)$ to compare it to our approximate analytical prediction from Eq (B.11) (Fig B.1D). When plotted on a log-log axis, this curve shows a linear region with a slope of 2, in agreement with the scaling in Eq (B.11).

We next estimate the work required to deform the cortex, as given by the second term on the right-hand side of Eq (B.1). For a spherical cap of contact radius r_c and height h:

$$\frac{\partial}{\partial t}\left(\tau \int r ds\right) = \frac{\partial}{\partial t}\left[\tau\left(r_c^2 + \frac{h^2}{2}\right)\right] \tag{B.12}$$

Early in spreading, h is approximately constant and tension changes slowly, therefore

$$\frac{\partial}{\partial t}\left[\tau\left(r_c^2 + \frac{h^2}{2}\right)\right] \approx 2\tau r_c \frac{dr_c}{dt} \tag{B.13}$$

Inserting the approximations from Eq (B.11) and Eq (B.13) into the energy balance (Eq (B.1)) and simplifying, we arrive at the following differential equation:

$$r_c^3 \left(\frac{dr_c}{dt} \right) = \frac{2(\gamma - \tau)}{\Pi_0} \tag{B.14}$$

In early spreading, tension changes more slowly than r_c; therefore, it can be treated as a constant. This leads to the spreading law observed in our model as well as in a previous computational model of passive cell spreading [62]:

$$r_c \propto t^{1/4} \rightarrow A_c \propto t^{1/2} \tag{B.15}$$

Appendix C. Development and testing of constitutive relations for cortical tension and protrusion stress

To best match the real-life behavior of cells, we developed versions of the piecewise relationships for tension (Eq (3.1)) and protrusion stress (Eq (3.11)) that have continuous first derivatives (C^1). We accomplished this by using polynomials to transition between each piecewise domain from the original C^0 relations. For tension, we use

$$\tau(A_{cell}) = \begin{cases} 0.01 + 0.16\left(\dfrac{A_{cell}}{A_{cell,0}} - 1\right) \ \dfrac{\text{mN}}{\text{m}} & \text{if} \quad \dfrac{A_{cell}}{A_{cell,0}} \le 1.13 \\ 0.7405\left(\dfrac{A_{cell}}{A_{cell,0}}\right)^2 - 1.5135\left(\dfrac{A_{cell}}{A_{cell,0}}\right) + 0.7955 \ \dfrac{\text{mN}}{\text{m}} & \text{if} \quad 1.13 < \dfrac{A_{cell}}{A_{cell,0}} \le 1.39 \\ 0.0516 + 0.545\left(\dfrac{A_{cell}}{A_{cell,0}} - 1.26\right) \ \dfrac{\text{mN}}{\text{m}} & \text{if} \quad \dfrac{A_{cell}}{A_{cell,0}} > 1.39 \end{cases} \tag{C.1}$$

The C^1 version of protrusion stress requires two separate transition regions, which we achieve using cubic polynomials:

$$\sigma_{prot} = \sigma_{prot,max} \begin{cases} 0.05 + 0.3\left(\dfrac{A_c}{A_{c,trans}}\right) & \text{if} \quad \dfrac{A_{cell}}{A_{cell,0}} \le 1.13 \\ c_3 A_c^{\,3} + c_2 A_c^{\,2} + c_1 A_c + c_0 & \text{if} \quad 1.13 < \dfrac{A_{cell}}{A_{cell,0}} \le 1.39 \\ 0.35 + 0.65\left(\dfrac{A_c - A_{c,trans}}{120\ \mu m^2}\right) & \text{if} \quad \dfrac{A_{cell}}{A_{cell,0}} > 1.39 \ \&\ A_c \le A_{c,trans} + 100\ \mu m^2 \\ d_3 A_c^{\,3} + d_2 A_c^{\,2} + d_1 A_c + d_0 & \text{if} \quad A_{c,trans} + 100\ \mu m^2 < A_c \le A_{c,trans} + 140\ \mu m^2 \\ 1 & \text{if} \quad A_c > A_{c,trans} + 140\ \mu m^2 \end{cases} \tag{C.2}$$

The c and d coefficients are found by solving the appropriate linear systems. Their values generally depend on the contact area A_c at different values of surface area deformation; namely, at $A_{cell} = 1.13\ A_{cell,0}$, $A_{cell} = 1.26\ A_{cell,0}$, and $A_{cell} = 1.39\ A_{cell,0}$. These are derived from sample runs of the simulation.

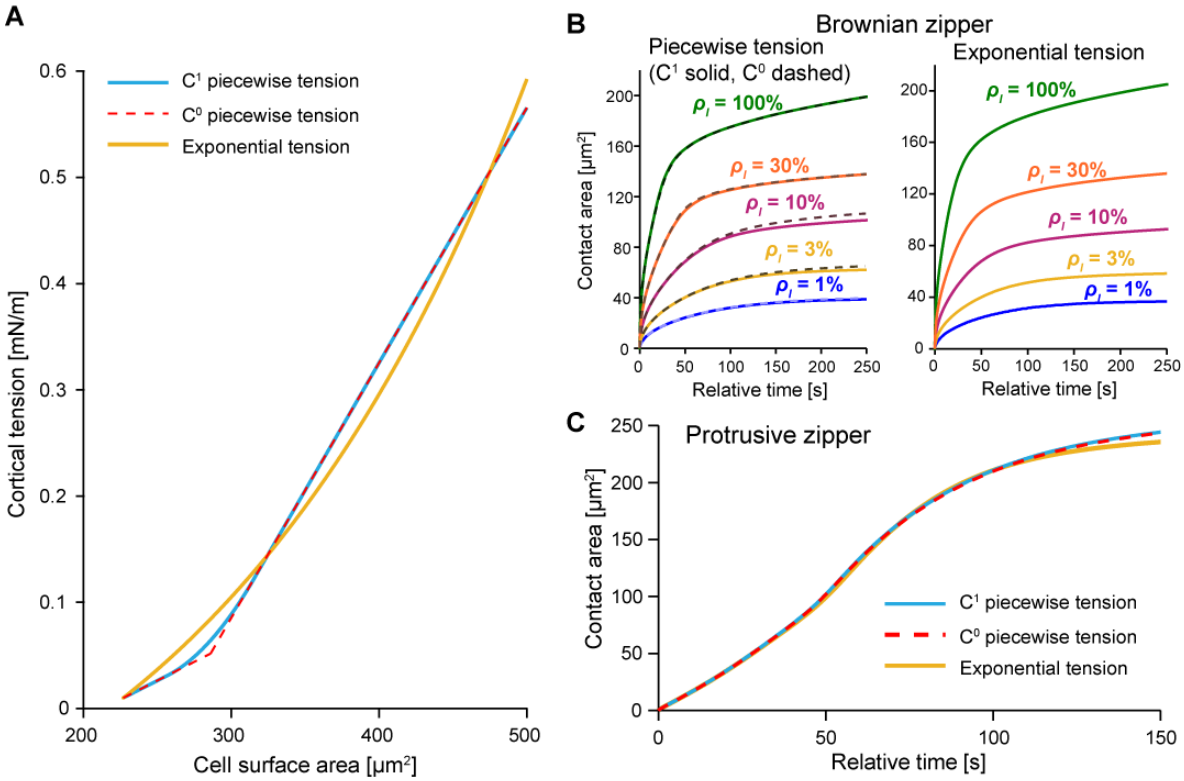

Fig C.1. Results of simulations using alternative cortical tension constitutive relations.
(A) Alternative relationships between cortical tension and cell surface area. (B) Brownian zipper results do not change qualitatively for different choices of cortical tension constitutive relations. (C) Contact area over time for the pure protrusive zipper varies only slightly between simulations using different relationships for cortical tension.

A comparison of the non-smooth (C^0) relationships with their smooth (C^1) counterparts reveals only minor differences in the respective graphs (Figs C.1A and C.2A). Furthermore, simulations performed with C^1 vs. C^0 relationships result only in slight changes in spreading dynamics that do not affect the main takeaways of this study (Figs C.1B-C and C.2B).

To confirm that our findings were not dependent on the relationships chosen for tension and protrusion stress, we also tested alternative expressions. For tension, a simpler relationship that has been used in previous numerical studies of cell deformations [236] is exponential:

$$\tau = \tau_0 + 0.15\left(e^{\frac{A_{cell} - A_{cell,0}}{A_{cell,0}}} - 1 \right) \tag{C.3}$$

As shown in Fig C.1B-C, this relationship does not qualitatively alter the Brownian Zipper or protrusive zipper contact area curves.

A simpler assumption for growth of the protrusion stress is that the stress grows linearly as a function of contact area:

$$\sigma_{prot} = \sigma_{prot,max} \begin{cases} 0.02 + 0.98\left(\dfrac{A_c}{250\ \mu\text{m}^2} \right) & \text{if} \quad A_c \le 250\ \mu\text{m}^2 \\ 1 & \text{if} \quad A_c > 250\ \mu\text{m}^2 \end{cases} \tag{C.4}$$

Remarkably, we find that even this simple relationship gives rise to the sigmoidal growth of contact area over time observed experimentally (Fig C.2C), indicating this is a general feature of our model that does not depend sensitively on the exact relationship chosen for protrusion stress.

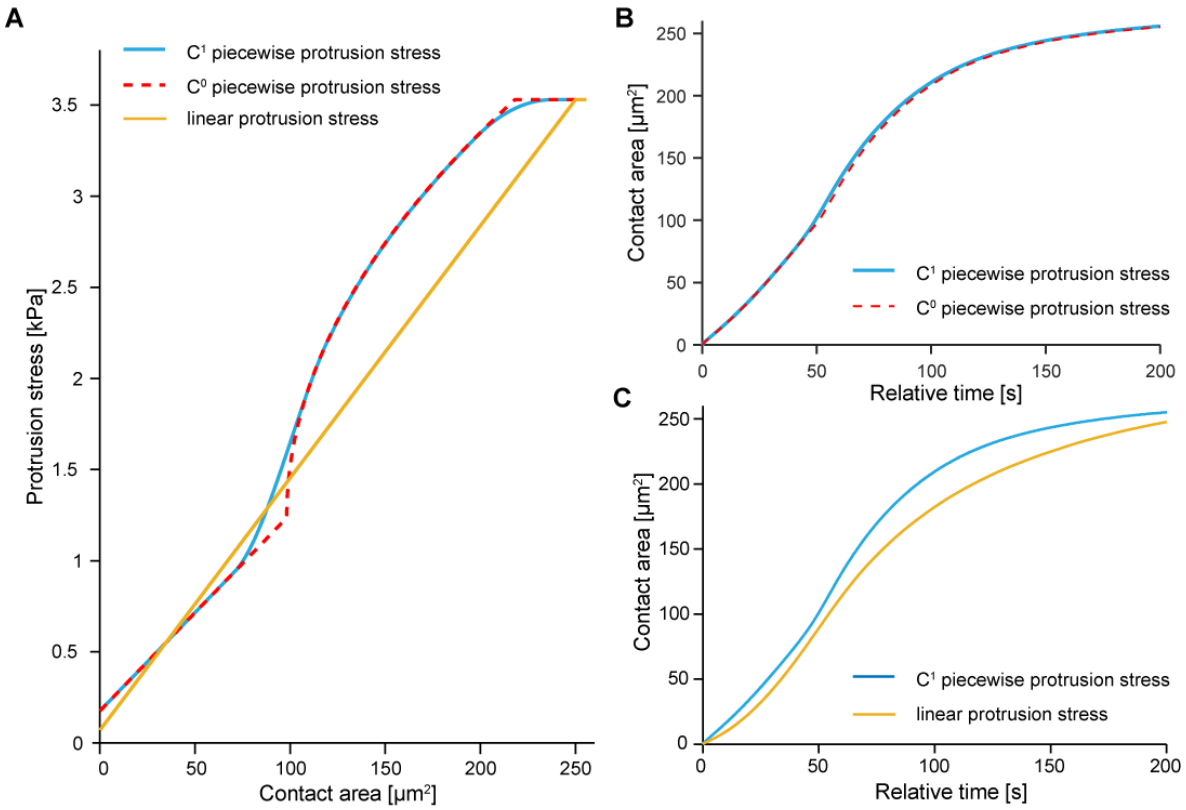

Fig C.2. Results of simulations using alternative protrusion stress constitutive relations.
(A) Alternative relationships between protrusion stress and cell-substrate contact area. (B) Results of the pure protrusive zipper simulation using the C^1 relationship only differ slightly from the C^0 version. (C) A linear relationship between protrusion stress and contact area gives rise to a sigmoidal contact area vs. time curve.

Appendix D. Details of finite element implementation

The governing equations are given in Methods, referred to as the "velocity equation" (Eq (3.17)) and the "pressure equation" (Eq (3.18)) below. Both equations are readily cast into a Galerkin form, which then is rewritten in matrix form as is conventional for finite element methods.

For reference, we give the elemental contributions to the stiffness matrices and load vectors for each finite element system, following the notation used by Hughes [131]. N_a is used to denote the finite element shape function associated with node a. We use bilinear quadrilateral shape functions and compute all integrals using two-by-two Gauss quadrature.

The velocity equation (Eq (3.17)) gives rise to the linear system

$$\mathbf{K}\mathbf{v}_{all} = \mathbf{F} \tag{D.1}$$

The vector $\mathbf{v}_{all}$ contains the velocity values $[v_r, v_z]$ at each node, and the global stiffness matrix **K** and global load vector **F** are assembled from elemental contributions. The contributions from nodes *a* and *b* belonging to element *e* are given as follows, where Ω_e denotes the element domain (note the factor of $2\pi r$ due to axial symmetry, as well as the term $(N_a N_b/r^2)$ which arises when computing $\nabla\mathbf{v}$ in cylindrical coordinates)

$$\begin{aligned}
\mathrm{K}_{arbr,e} &= \int\left(2\frac{\partial N_a}{\partial r}\frac{\partial N_b}{\partial r} + 2\frac{N_a N_b}{r^2} + \frac{\partial N_a}{\partial z}\frac{\partial N_b}{\partial z}\right)2\pi r d\Omega_e \\
\mathrm{K}_{arbz,e} &= \int\frac{\partial N_a}{\partial r}\frac{\partial N_b}{\partial z}2\pi r d\Omega_e \\
\mathrm{K}_{azbr,e} &= \int\frac{\partial N_a}{\partial z}\frac{\partial N_b}{\partial r}2\pi r d\Omega_e \\
\mathrm{K}_{arbr,e} &= \int\left(2\frac{\partial N_a}{\partial z}\frac{\partial N_b}{\partial z} + \frac{\partial N_a}{\partial r}\frac{\partial N_b}{\partial r}\right)2\pi r d\Omega_e
\end{aligned} \tag{D.2}$$

For the load vector

$$\begin{aligned}
\mathrm{F}_{ar,e} &= \int p_{est}\left(\frac{\partial N_a}{\partial r} + \frac{N_a}{r}\right)2\pi r d\Omega_e + \int N_a\sigma_r 2\pi r d\Gamma_e \\
\mathrm{F}_{az,e} &= \int p_{est}\left(\frac{\partial N_a}{\partial z}\right)2\pi r d\Omega_e + \int N_a\sigma_z 2\pi r d\Gamma_e
\end{aligned} \tag{D.3}$$

where the second term in the load vector arises from the Neumann boundary condition (stress balance) and Γ_e denotes the boundary of the element. The vector $[\sigma_r, \sigma_z]$ denotes the boundary stresses given by adding the adhesion stress, protrusion stress, and cortical stress, which are only non-zero for those elements which belong to the free boundary of the cell. For elements in

contact with the substrate, there is no contribution from the no-slip boundary condition because the enforced velocity is equal to zero.

The pressure equation (Eq (3.18)) gives rise to the linear system

$$\mathbf{Q}\,\mathbf{p}_{all} = \mathbf{G} \tag{D.4}$$

The vector $\mathbf{p}_{all}$ contains the pressure value p at each node. The global stiffness matrix **Q** and global load vector **G** are assembled from elemental contributions given by

$$\mathrm{Q}_{ab,e} = \int \left[N_a N_b - \epsilon \left(\frac{\partial N_a}{\partial r}\frac{\partial N_b}{\partial r} + \frac{\partial N_a}{\partial z}\frac{\partial N_b}{\partial z} \right) \right] 2\pi r d\Omega_e \tag{D.5}$$

$$\mathrm{G}_{a,e} = \int N_a \left[p_{est} - \frac{\partial v_r}{\partial r} - \frac{v_r}{r} - \frac{\partial v_z}{\partial z} \right] 2\pi r d\Omega_e \tag{D.6}$$

The expression for G_a incorporates the assumption that $\nabla p \cdot \mathbf{n}$ is zero along the cell boundary, as dictated by the boundary condition, and $\nabla^2 p = 0$ everywhere, which is satisfied exactly for an incompressible fluid. Derivatives of $[v_r, v_z]$ are computed using bilinear quadrilateral shape functions.

This system of equations is solved iteratively, as described in Chapter 3 Methods. Examples of the fluid velocities and pressures obtained by the Brownian zipper model (Fig D.1A) and the protrusive zipper model (Fig D.1B) are included for illustration.

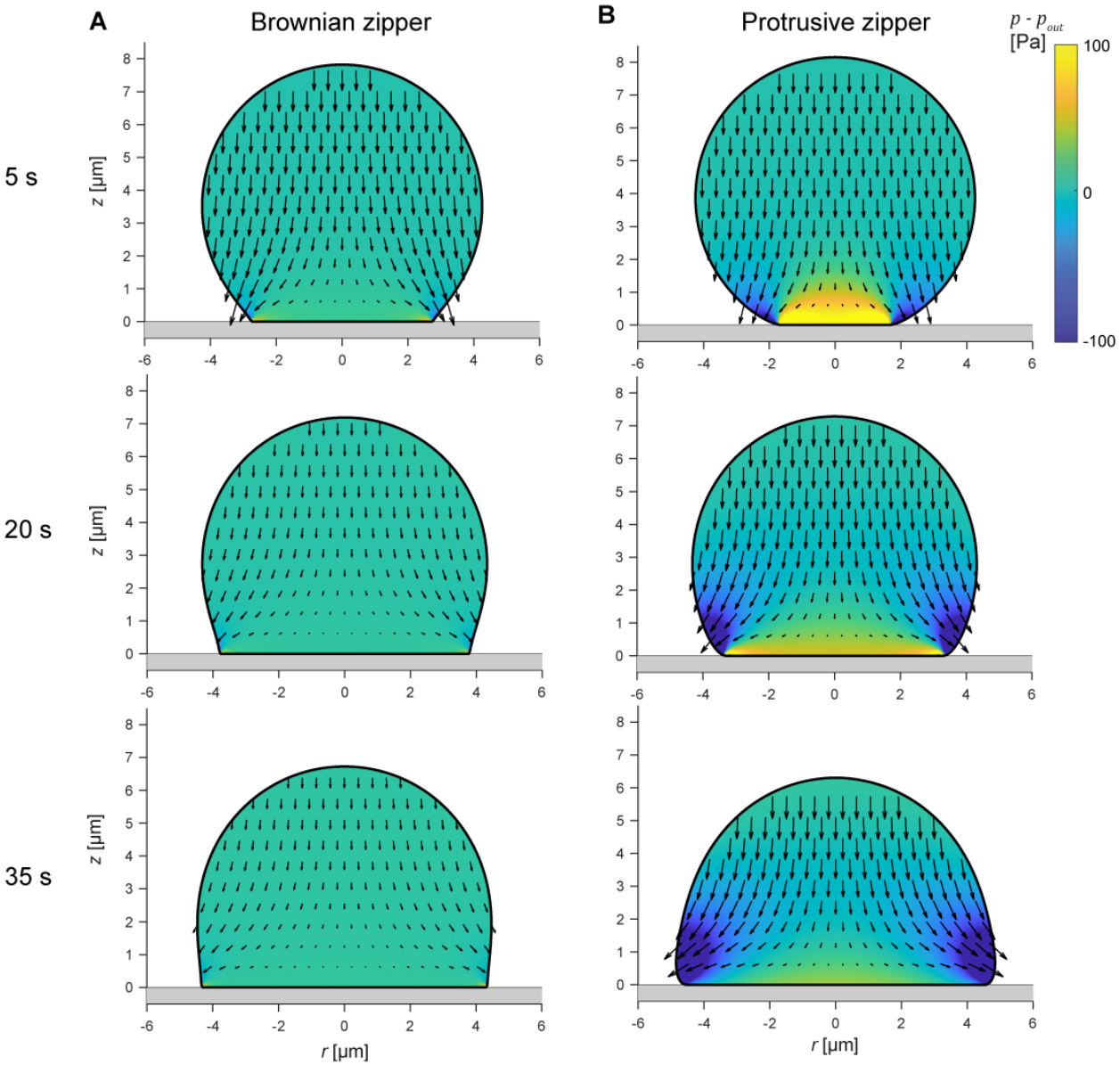

Fig D.1: Example velocity and pressure fields obtained by finite element computations.
(A) Fluid velocity vector fields and pressure scalar fields (heat maps) are shown for purely adhesion-driven spreading with a ligand density of 10%. The magnitude of fluid velocity decays relatively quickly over time. (B) Fluid velocity vector fields and pressure scalar fields (heat maps) are shown for purely protrusion-driven spreading. The velocities maintain a similar magnitude over time due to the time-dependent increase in protrusion stress.

Appendix E. Numerical testing and optimization

The accuracy of numerical computations such as used in this study can be affected by several factors. In this appendix, we document tests that we have carried out to verify the robustness of our numerical predictions. All tests of the Brownian zipper model are conducted for a ligand density (ρ_l) of 10%, and all tests of the protrusive zipper model are carried out in the absence of adhesion stress.

I. Test for incompressibility

Solving the governing equations for the perturbed Stokes equations given in Methods (Eqs (3.17) and (3.18)) yields an approximate satisfaction of incompressibility. The degree to which incompressibility is enforced depends on the magnitude of the perturbation parameter ϵ in Eq (3.18). Specifically, as ϵ goes to zero, the fluid becomes more incompressible. However, if ϵ is too small, there are numerical difficulties. Thus, it is worthwhile to evaluate how closely incompressibility is satisfied for different values of ϵ. In our model, ϵ scales with the characteristic radius of an individual element h_{mesh} and the effective viscosity μ [111]. As described in Eq 15 in Chapter 3, we generally require that $\epsilon \leq h_{mesh}^2/\mu$, but we can write more generally

$$\epsilon = \bar{\epsilon}\left(\frac{h_{mesh}^{\ 2}}{\mu}\right) \tag{E.1}$$

where $\bar{\epsilon}$ is a dimensionless scaling factor that should have a magnitude less than or equal to one to satisfy the above inequality. Here, we assess how this parameter affects the error in our model.

We quantify the degree of compressibility at different locations in the cell body in terms of the local rate of dilatation, obtained by integrating $\nabla \cdot \mathbf{v}$ over individual elements and dividing by the element volume V_{el}. That is,

$$\text{Dilatation rate} = \frac{\int (\nabla \cdot \mathbf{v})\, dV_{el}}{V_{el}} \tag{E.2}$$

This dilatation rate has units of inverse seconds and describes the rate of fluid expansion per unit volume. In general, we expect the largest departures from perfect incompressibility to occur in the immediate vicinity of the perimeter of the contact region, due to a well-known singularity that has been examined thoroughly for different cases of droplet spreading [113]. Focusing on this region, we have characterized how our choice of the value of ϵ affects the dilatation rate (Fig E.1A). We evaluate the overall error of the model in terms of the mean square error (MSE) for the incompressibility condition

$$\text{MSE} = \frac{\int (\nabla \cdot \mathbf{v})^2\, dV}{V_{tot}} \tag{E.3}$$

The MSE initially depends only weakly on the value of $\bar{\epsilon}$, but increases considerably at higher values, as expected (Fig E.1B-C). Generally, a value of $\bar{\epsilon} = 1$ results in sufficiently low error while also avoiding numerical difficulties associated with lower values of $\bar{\epsilon}$.

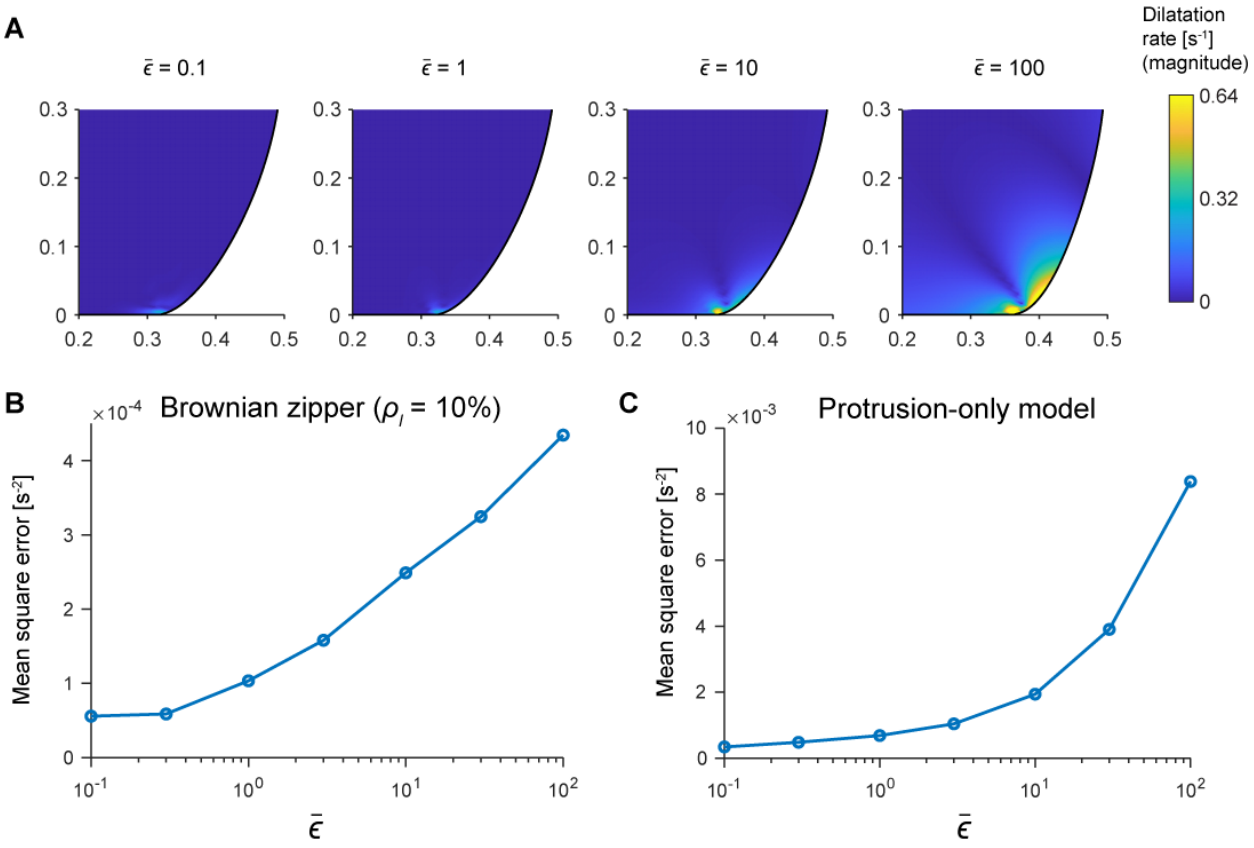

Fig E.1: Testing for incompressibility.
(A) Heat maps of the dilatation rate within the leading edge of the cell for purely protrusion-driven spreading at t = 15 s for different values of $\bar{\epsilon}$. (B) Volumetric mean square error is plotted as a function of $\bar{\epsilon}$ for Brownian Zipper simulations at t = 15 s. (C) Volumetric mean square error is plotted as a function of $\bar{\epsilon}$ for protrusion-only spreading at t = 15 s.

II. Time-step testing

The optimal time step Δt for fluid mechanics simulations depends on fluid velocity and the mesh resolution. A common reference for this is the Courant number, generally given by

$$C = \frac{v\Delta t}{l} \tag{E.4}$$

where l is a characteristic length and v is a characteristic velocity. For numerical stability, C should be much less than one.

We use Eq (E.4) to determine the appropriate time step for the minimum ratio of l/v across all elements; that is

$$\Delta t = C \min\left(\frac{l}{v}\right) = C \min_{\text{all el}}\left(\min\left[\frac{r_{span}}{v_{r,c}}, \frac{z_{span}}{v_{z,c}}\right]\right) \tag{E.5}$$

where r_{span} is the span of the element in the r direction, z_{span} is the span of the element in the z direction, $[v_{r,c}, v_{z,c}]$ is the velocity vector at the centroid of the element, and C is the desired Courant number. For instance, if $C = 0.1$, fluid flow crosses at most 10% of any individual element during a single time step. We performed a series of simulations using decreasing values of C to establish at which Courant number our computations converge satisfactorily. Figure E.2 shows examples of testing different time steps for the Brownian Zipper model (Fig E.2A) and the protrusive zipper model with no adhesion stress (Fig E.2B). For smaller time steps, the contact area curves become smoother and converge to a single solution. Generally, we find that $C \leq 0.1$ performs well in these cases, which is the value we choose for our simulations.

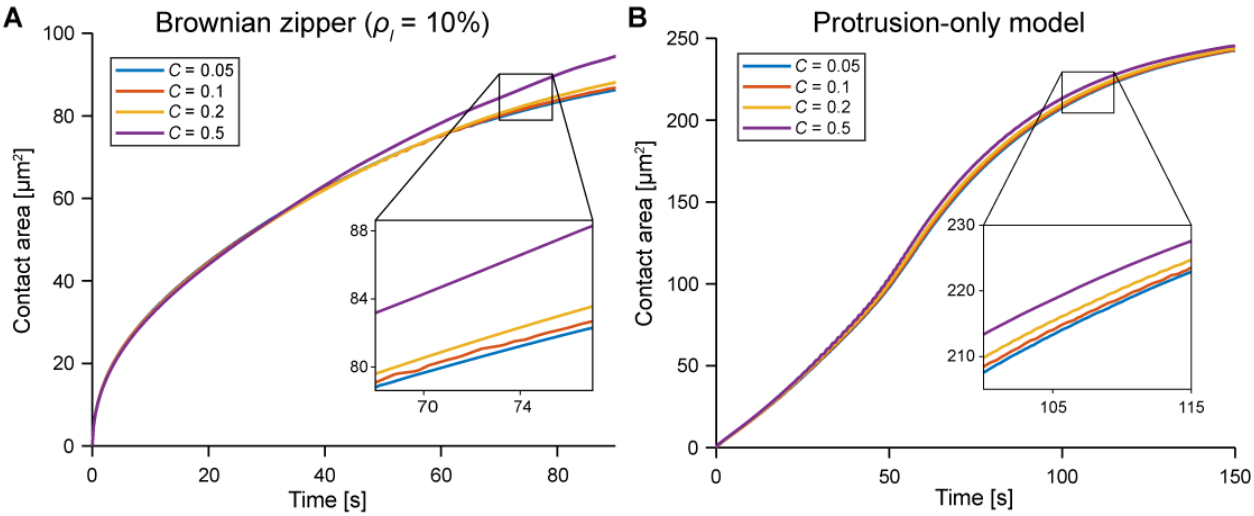

Fig E.2: Time-step testing.
Contact area versus time for different Courant numbers for (A) the Brownian zipper model and (B) purely protrusion-driven spreading.

III. Mesh refinement

We ensured that the results of our simulations do not depend significantly on the mesh resolution as follows. When constructing the mesh, we start by specifying the boundary nodes, choosing tight spacing near the substrate and gradually increasing spacing to 0.17 μm over the rest of the cell contour (Fig E.3A). After parameterizing the contour, we use transfinite interpolation to construct the interior mesh ([237], Fig E.3A). Using a global edge spacing of 0.17 μm generally results in about 2,000 elements. Here, we focus on refining the mesh spacing close to the surface where the stresses are most concentrated.

For both the Brownian zipper model and the protrusive zipper model, we tested minimum boundary point spacing values Δs_{min} of 25 nm, 10 nm, 5 nm, and 2.5 nm. In both cases, we find convergence for $\Delta s_{min} \leq 5$ nm (Fig E.3B-C). For our simulations in the main paper, we use $\Delta s_{min} = 2.5$ nm.

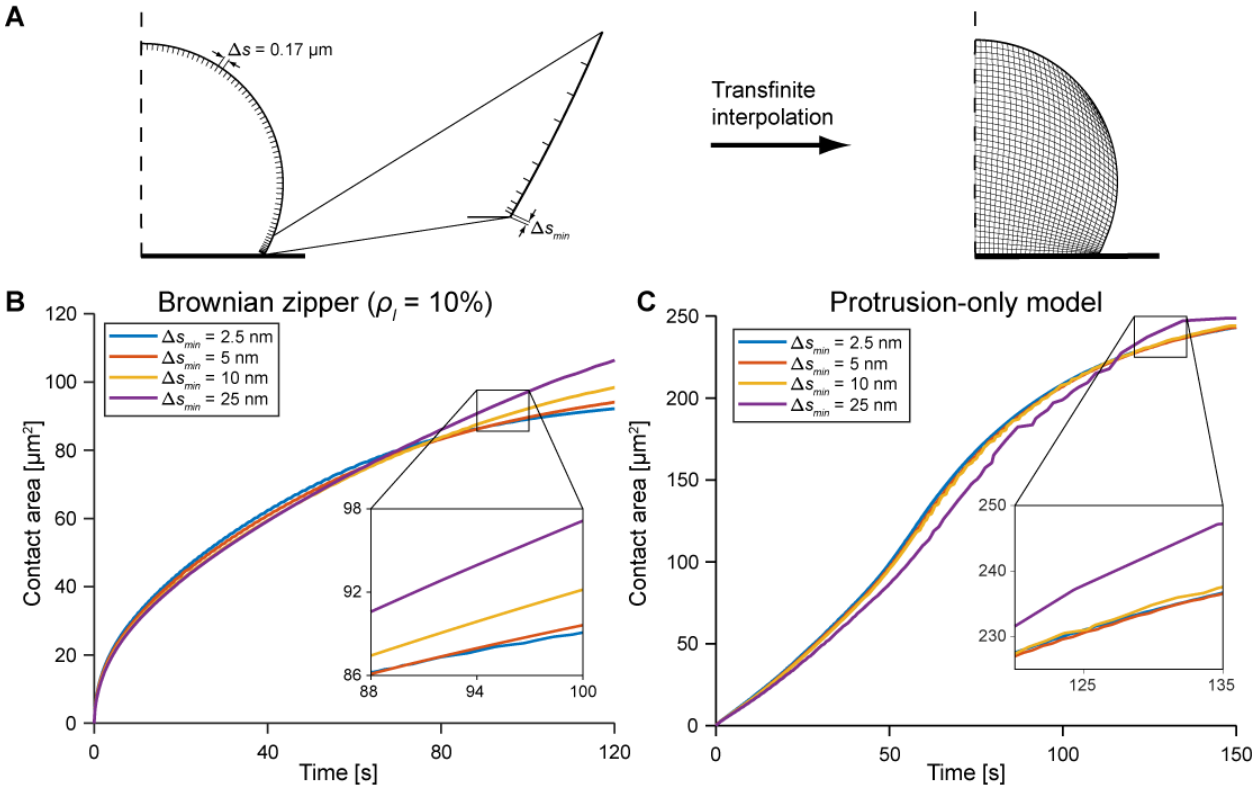

Fig E.3: Mesh refinement.
(A) Illustration of mesh construction including our choice of relevant boundary spacing intervals. Convergence of the simulations is evaluated by inspection of contact-area-versus-time curves obtained with different minimum mesh spacings close to the substrate (Δs_{min}) for (B) the Brownian zipper model and (C) purely protrusion-driven spreading.

Appendix F. Additional testing of the discrete adhesion model

As outlined in the main text, we introduced two main rules to implement a version of our protrusive zipper with discrete adhesion sites: 1) If the cell membrane is less than a threshold distance from a ligand (set by the magnitude of membrane fluctuations dictated by Eq (3.12)), the membrane is considered bound, and 2) the protrusion stress decays as a function of time since last binding a ligand (Eq (3.13)). The second rule contains a free parameter t_0, corresponding to a characteristic decay time for the protrusion stress. Because this parameter is not directly quantifiable from our data, we sought to determine how sensitive the outcomes of this version of the model were to our choice of t_0 (Fig F.1).

In the main text, we use t_0 = 66 s, and here we tested t_0 with either half this value (33 s, faster decay) or twice this value (132 s, slower decay). We also tested the model without any decay by setting $t_0 = \infty$. Regardless of the choice of t_0, we observe the same qualitative behavior of the model – spreading speeds remain similar across different ligand densities, but maximum contact area increases as a function of ligand density (Fig F.1A,B). However, the exact relationship between ligand density and maximum contact area depends on the choice of t_0. Faster decay rates (lower t_0) generally resulted in earlier termination of spreading, but with slow or absent decay, cells continue spreading longer (Fig F.1). This difference is most evident at lower ligand densities, where a more sustained protrusion stress is required to overcome larger gaps between ligands.

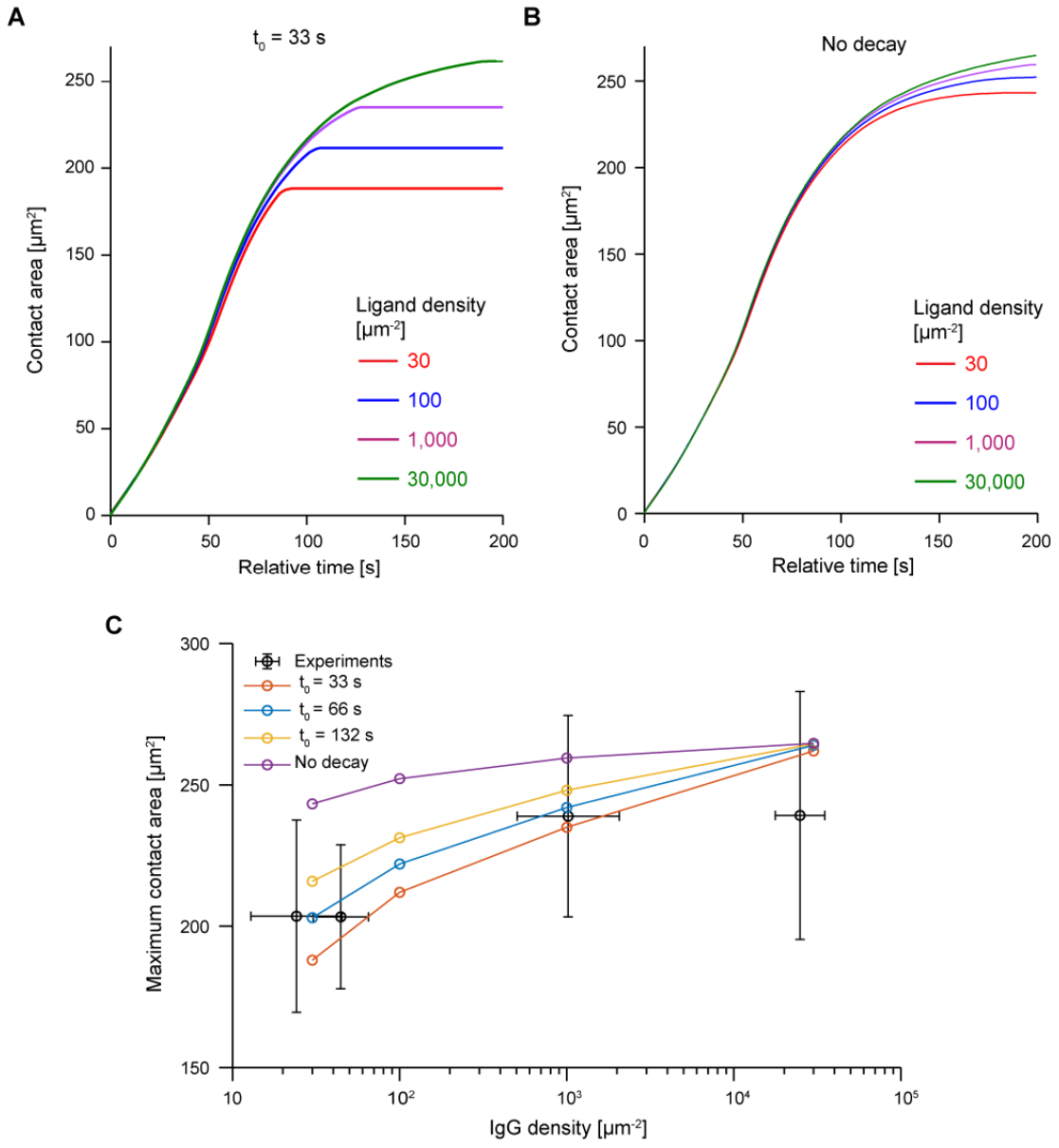

Fig F.1: Effect of varying t_0 on the protrusive zipper with discrete adhesion sites.
Contact-area-versus-time for spreading over different densities of discrete binding sites, plotted for t_0 = 33 s (faster decay) (A) and for no time-dependent decay of the protrusion stress (B). (C) The relationship between maximum contact area and IgG density depends on how quickly the protrusion stress decays.

We also noted that our experiments seemed to indicate a saturation in maximum contact area for IgG densities greater than about 1,000 μm^{-2}, but our model predicts a continued increase in maximum contact area up to the highest density tested (30,000 μm^{-2}). At these higher densities of IgG, receptors are the limiting factor of the maximum adhesion strength, which is not accounted

for in our model. Therefore, we conducted additional proof-of-principle simulations in which both ligands and receptors were treated as discrete.

On the order of 1×10^6 Fcγ receptors are present in the membrane of a passive neutrophil [238, 239]. The total membrane surface area includes not just the apparent surface area, but also membrane folds such as microvilli. Because neutrophils can expand their apparent surface area up to three times its resting value [7, 99], we conservatively estimated the total receptor density $\rho_{Fc\gamma R}$ as $1\times10^6 / 3SA_0$, or about 1,470 receptors per square micron.

Because these receptors are generally mobile, we assumed that any given receptor effectively occupied a length of membrane δl dictated by receptor mobility (effective diffusion coefficient D_{eff}) and the current time step Δt:

$$\delta l = \sqrt{4D_{eff}\Delta t} \tag{F.1}$$

If a given receptor is centered at a point on the membrane specified by arc length s_R, then the receptor can diffuse within a range bounded by $s_R - \delta l$ and $s_R + \delta l$ during a time interval of Δt (Fig F.2A inset). We here postulate that, for any given ligand, if the minimum distance to this receptor, d_{min}, is less than d_{thresh} (given by Eq 12 in the main text), then binding occurs.

Using the above approach to discretize receptors, we require the total region over which each receptor can diffuse ($2\delta l$ from Eq (F.1)) to be less than the receptor spacing; otherwise, the entire membrane would be available to bind free ligand, as in the original discrete adhesion model. This places an upper limit of about 4×10^{-4} $\mu m^2/s$ on D_{eff}, much lower than the values reported for Fcγ receptor diffusion coefficients (~0.01 to 0.1 $\mu m^2/s$) [240]. However, D_{eff} should be viewed as an effective parameter, capturing not only diffusion but also the effects of lateral confinement [211] and close contacts [241].

As a proof of concept, we performed simulations with $\rho_{FcγR}$ = 1,470 μm^{-2} and D_{eff} = 1×10^{-4} μm^2/s. (Fig F.2) These simulations indeed showed that spreading on lower densities of IgG was similar to our original simulations, but spreading on the highest density terminated earlier due to limited receptor availability (Fig F.2A,B). The results of this version of the model yielded an even better match to the experimentally measured relationship between IgG density and maximum contact area (Fig 3.8C).

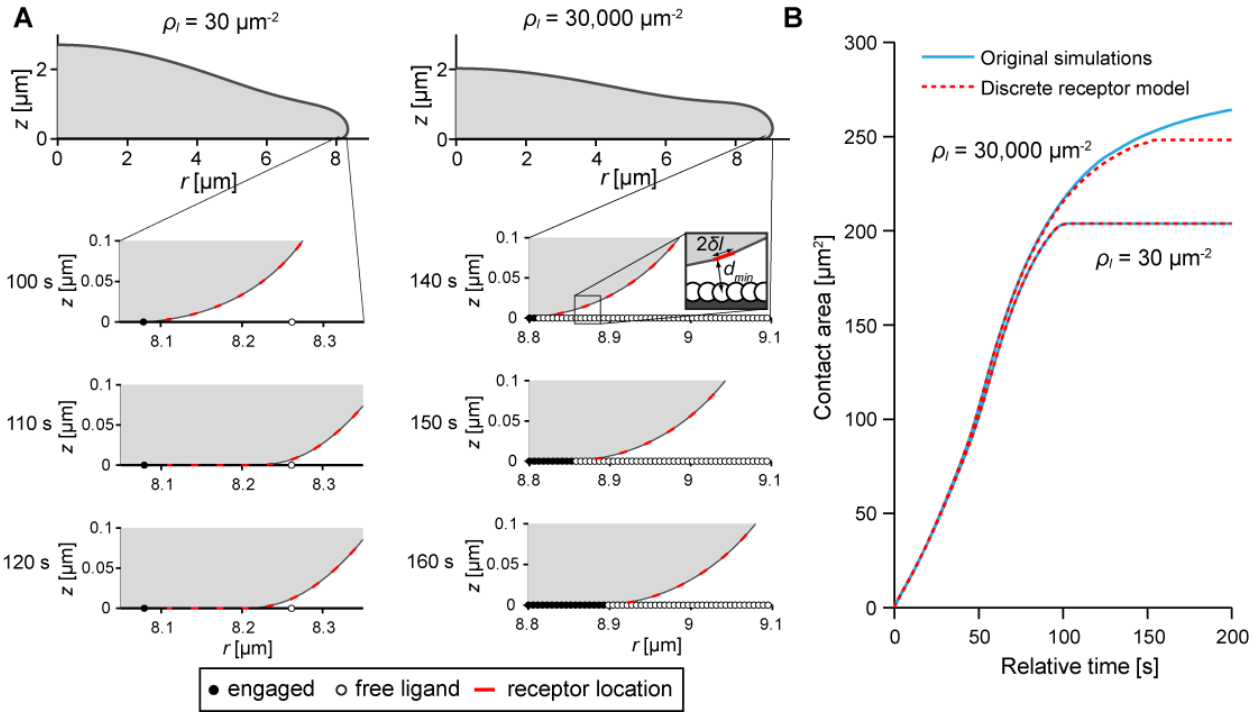

Fig F.2: Protrusive zipper with discrete ligands and discrete receptors.
(A) Sample cell profiles for spreading over different densities of binding sites with receptors only present in the membrane segments shown in red. The inset defines the variables used in the text. (B) Spreading over low densities of IgG (30 μm^{-2}) is unaffected by a discrete receptor model, whereas spreading is receptor-limited on high densities of IgG (30,000 μm^{-2}).

Appendix G. Chapter 4 supplementary materials

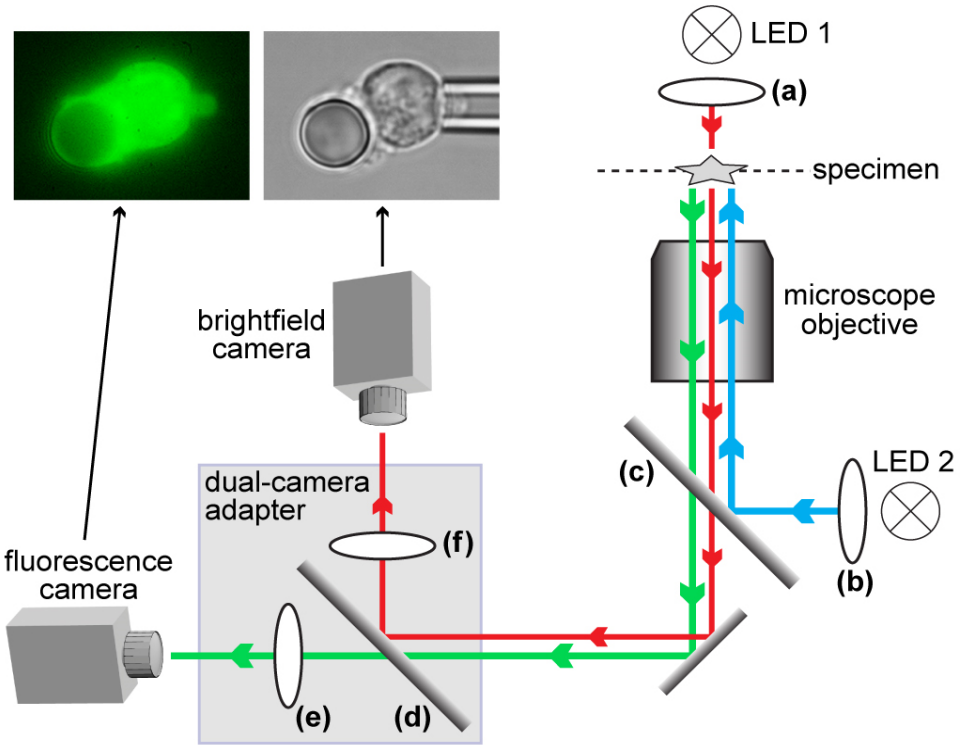

Fig G.1. Dual-camera setup for simultaneous recording of brightfield and fluorescence images. The LEDs emitted white (LED 1) or cyan (LED 2) light. The following filters and dichroic mirrors were used (all by Chroma Technology): (a) ET630/75m; (b) ET480/40x; (c) T510lpxrxt; (d) 59001bs; (e) ET535/50m; (f) ET610/20. (See Chapter 4 Materials and Methods for further details.)

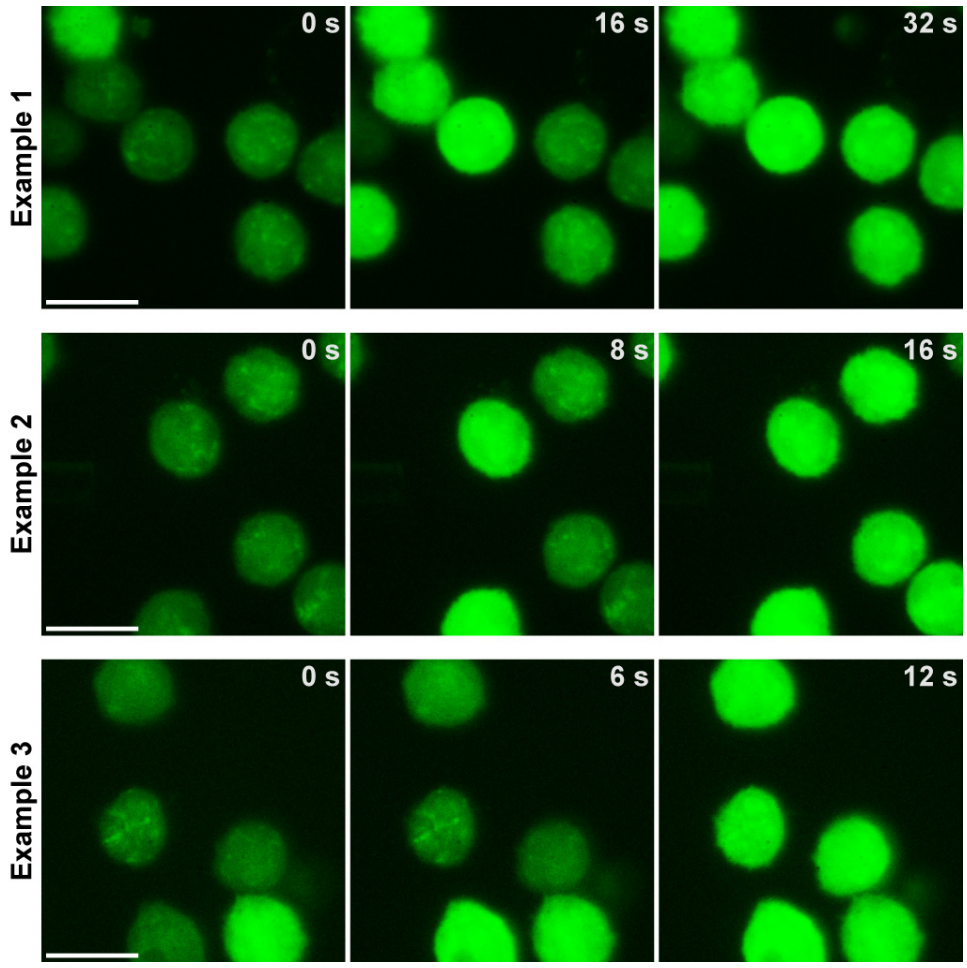

Fig G.2. Unphysiologically high concentrations of C5a trigger calcium bursts in resting human neutrophils without inducing chemotaxis. These examples (representing a total of $N = 67$ tested cells) illustrate the response of neutrophils pre-loaded with the calcium indicator Fluo-4 to jets of a 0.1 μM C5a solution applied from the left. The relative time at which each image was recorded is included. All scale bars denote 10 μm.

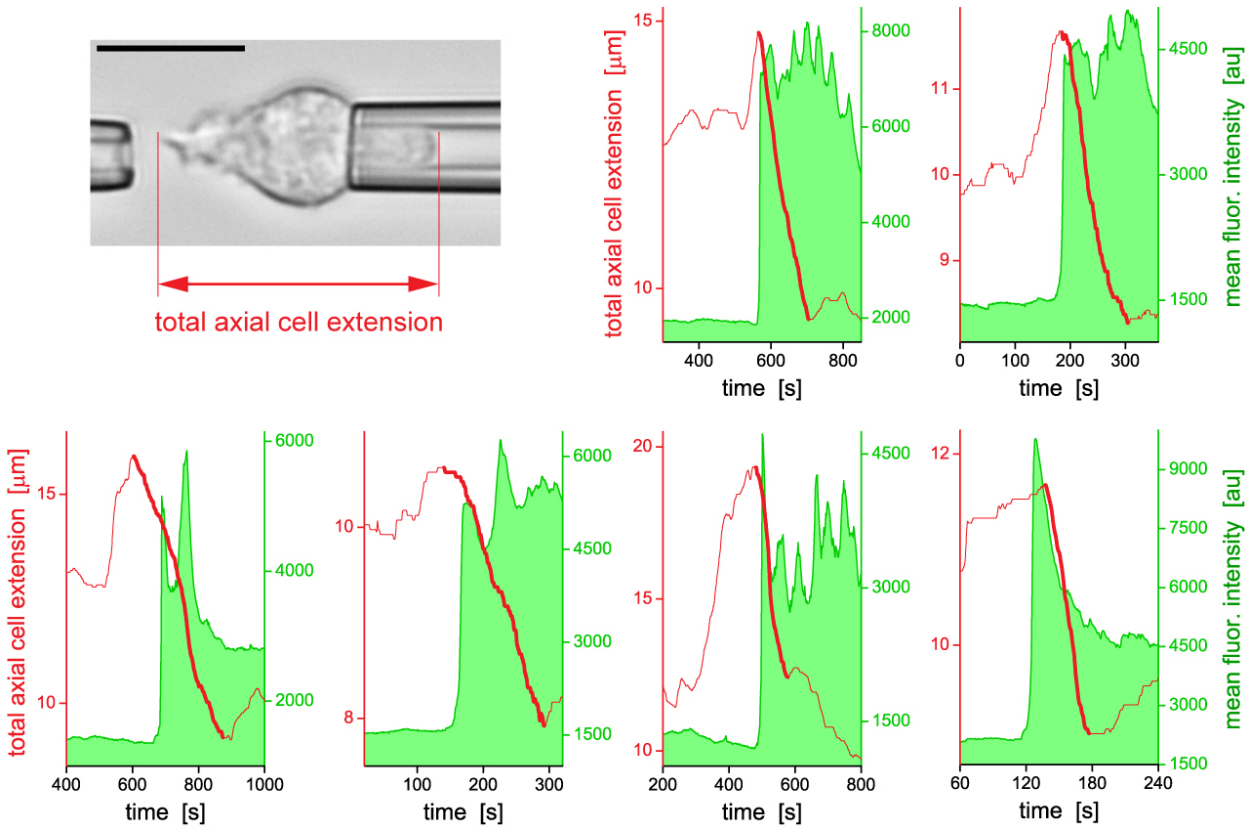

Fig G.3. Concurrence of calcium bursts and cellular contraction. Six example plots show the time course of the total axial cell extension (defined in the included videomicrograph) along with the mean fluorescence intensity of the calcium indicator Fluo-4. The aspiration pressure in the cell-holding pipette was kept constant during the depicted time windows. Monotonously decreasing segments of the cell-extension graphs (emphasized by thick red lines) expose periods of pronounced cellular contractions. Each contractile deformation coincides more or less with the onset and initial phase of a calcium burst. As mentioned in the main text, this coincidence reveals correlation, but not necessarily causation. We note that the pseudopod length and projection length can undergo spontaneous fluctuations, which can accelerate or delay the apparent onset of contractions such as shown here. It is also possible that in some cases, cell contractions are initiated first locally (e.g., by engaging a normal pulling force without triggering a calcium burst), followed by a global increase of the cortical tension. The scale bar denotes 10 µm.

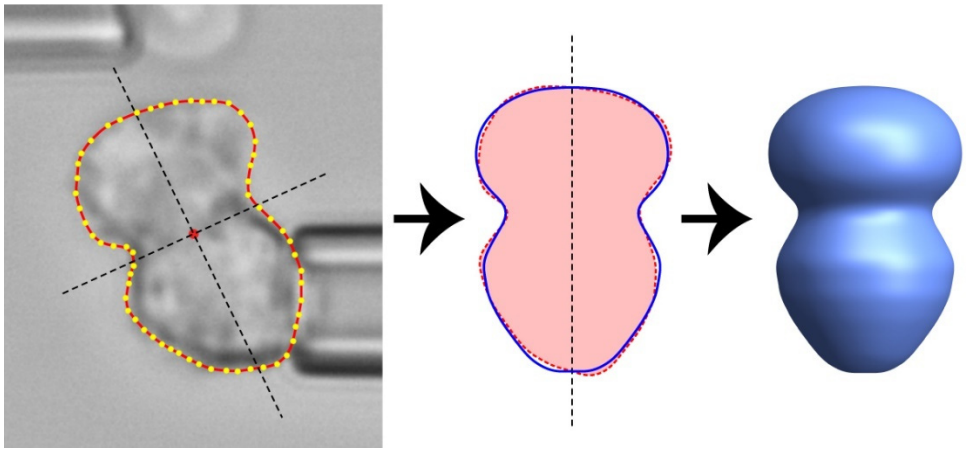

Fig G.4. Estimation of the cell-surface area. The figure illustrates the workflow of our calculation of the surface area of the cell body outside the pipette. It is based on the assumption that the video image of the cell body shows a 2D cross-section of an axisymmetric 3D body (see Materials and Methods for details). After finding a smooth and continuous mathematical representation of the cell contour (red line), we determine the most likely axis of rotation, and then reconstruct the 3D body using a symmetric version of the contour (blue line). Our calculation takes into account that the total cell volume remains constant during the deformations considered here.

Movie 4.1. Close-up view of a calcium burst in a human neutrophil. The video starts with a composite brightfield/fluorescence view of a calcium burst during phagocytosis of an antibody-coated bead by a human neutrophil that had been pre-loaded with the calcium indicator Fluo-4. The second part presents a plot of the fluorescence intensity versus time for the same experiment. The video illustrates that calcium bursts are rapid, global, and dramatic surges of the free intracellular calcium concentration.

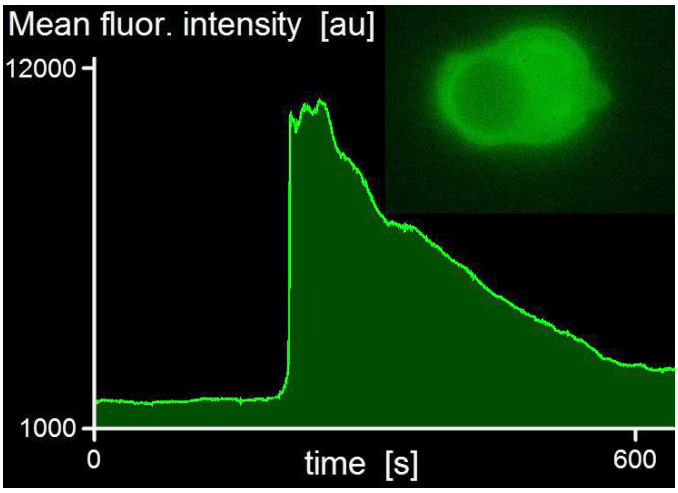

Movie 4.2. Absence of calcium bursts during complement-mediated, pure chemotaxis of a human neutrophil toward a zymosan particle. A zymosan particle (made from cell walls of yeast) is maneuvered to different sides of a pipette-held, nonadherent human neutrophil. The neutrophil responds vigorously by extending chemotactic pseudopods toward the target particle. Eventually, the particle is handed over to the cell, resulting in its phagocytosis. The simultaneously recorded fluorescence intensity of the calcium indicator Fluo-4 reveals that a calcium burst occurs during the phagocytic stage of this experiment, but not during pure chemotaxis.

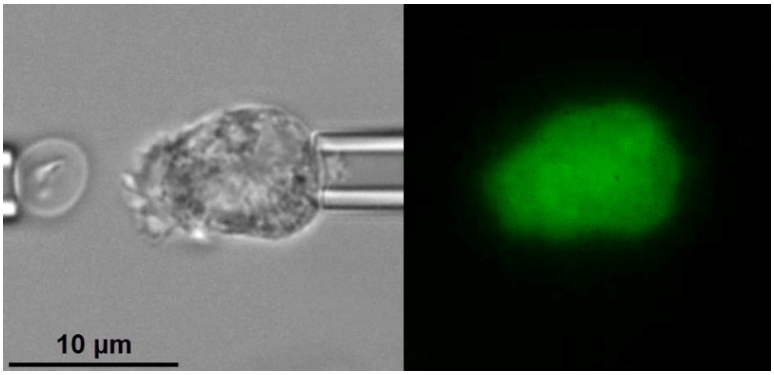

Movie 4.3. Absence of calcium bursts during complement-mediated, pure chemotaxis of a human neutrophil toward a cluster of β-glucan particles. A cluster of β-glucan particles is maneuvered to different sides of a pipette-held, nonadherent human neutrophil. The neutrophil responds vigorously by extending chemotactic pseudopods toward the target cluster. Eventually, the cluster is handed over to the cell, resulting in its phagocytosis. The simultaneously recorded fluorescence intensity of the calcium indicator Fluo-4 reveals that a calcium burst occurs during the phagocytic stage of this experiment, but not during pure chemotaxis.

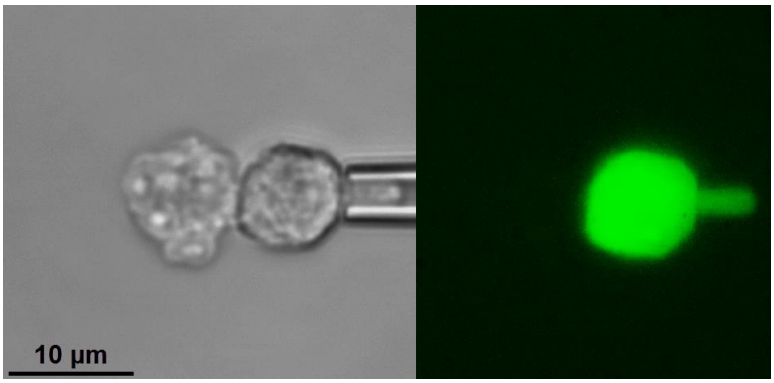

Movie 4.4. Unphysiological concentrations of C5a or co-stimulation by shear flow can induce calcium bursts in nonadherent human neutrophils. This video showcases three example experiments in which pipette-held neutrophils are subjected to jets of different C5a solutions. The lowest C5a concentration (0.1 nM) elicits a clear chemotactic response but does not trigger a calcium burst. In the second example (using 10 nM C5a), the chemotaxing neutrophil twice exhibits calcium bursts after the jet pressure in the left pipette is increased 5-fold. In the last example, the neutrophil almost immediately reacts to a low-pressure, 0.1 µM C5a jet with a calcium burst, without prior chemotaxis. The calcium bursts coincide with a contractile cell-morphology change that momentarily stalls, reverses, or even prevents chemotaxis. For more details, see Figs. 4.3 and 4.4 and Fig G.3.

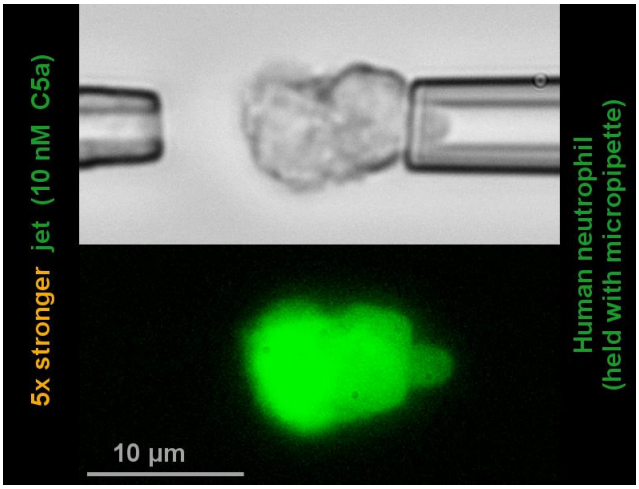

Appendix H: Full model description and sensitivity analysis from Chapter 5

Table H.1: Summary of parameter values with associated notes and references.

	Parameter	Meaning	Value	Fold variation[#]	Notes/Sources
1	D_{cell}	Diameter of passive neutrophil	8.75 μm	1.1	Determines vol_{tot} and the resting apparent surface area A_0
2	A_{tot} / A_0	Total microscopic cell surface area (including folds)	2.1	1.1	Determines the total number of receptors in the membrane and the maximum deformation. Set by the deformation required to form a spherical cap with contact area 240 μm^2 (Eq (2.5) in Chapter 2)
3	vol_i / vol_{tot}	Cytosolic volume fraction	0.63	1.1	Measured in human neutrophils [242]
4	vol_{ER} / vol_{tot}	ER volume fraction	0.05	1.5	Agrees with values used for RAW macrophages [218] and smooth muscle cells [243]
5	ρ_{IgG}	Varies for different simulations	20-20,000 μm^{-2}	1.5	Densities measured for our surfaces in Chapter 2
6	$N_{FcγR,tot}$	Total number of FcγRs in the neutrophil membrane	4.09×10^5	2	Varies from donor to donor, average total number in healthy donors was 8.5×10^5 in [239]
7	$\rho_{ITAM,0} / \rho_{R,0}$	Fraction of Fc gamma receptors with ITAM domains	0.06	2	Varies from donor to donor, average ratio was .06 over three healthy donors in [239]
8	$D_R / l_{diffusion}$	Receptor diffusion coefficient divided by a characteristic length of receptor diffusion in membrane	0.01 μm/s	1.5	For diffusion occurring over a characteristic length of 1 μm, this corresponds to a typical receptor diffusion coefficient of 0.01 μm^2/s, in good agreement with measurements of FcγR diffusion [240]
9	Δt_{signal}	Time over which freshly bound membrane actively signals	10 s	2	Proposed for this model specifically

10	$K_{a,RL}$	2D receptor-ligand binding affinity	30 μm^{-2}	1.5	Matches measured binding affinity of 1μM for low-affinity FcγRs [112] *
11	v_{Src}	Reaction rate for Src on bound receptors at leading edge	0.5 s^{-1}	2	Agrees with the on-rate of Src family kinases determined for B cells [244]**
12	K_{Src}	Michaelis constant for Src-ITAM	10 μm^{-2}	2	Corresponds to ~0.3μM *, estimated based on threshold from our experiments
13	k_{dephos}	Dephophorylation rate for phosphorylated ITAM	0.1 s^{-1}	2	Matches the catalytic rate for ITAM dephosphorylation used for B cells in [244]
14	α_{PLC}	Reaction rate for PLC converting PIP_2 to IP_3	2.5×10^{-4} s^{-1}	2	Chosen to match the order of magnitude of PLC activity from GPCR activity in RAW macrophage model [218] and in other cell types [245, 246]
15	K_{PLC}	Michaelis constant for Ca^{2+} binding to PLC	0.4 μM	2	Values from paper which originally developed the equations for this part of the model [245]
16	r_r	Rate of PIP_2 recycling	.015 s^{-1}	2	
17	$k_{deg,IP3}$	IP_3 degradation rate	1.25 s^{-1}	2	
18	$N_{PIP2,tot}$	Total number of PIP_2 molecules in membrane	2×10^{7}	2	Corresponds to ~150 μM (over the whole cell body volume), in the range specified for RAW macrophages [218]
19	P_{IP3R}	Maximum total permeability of IP_3R	2880 μM/s	1.5	Values adopted from smooth muscle cell models [246, 247]
20	$K_{i,IP3R}$	IP_3 dissociation constant for IP_3R	0.1 μM	1.5	
21	$K_{a,IP3R}$	Ca^{2+} dissociation constant for IP_3R activating site	0.17 μM	1.5	

22	$K_{d,h}$	Ca^{2+} dissociation constant for IP_3R deactivating site	0.12 μM	1.5	
23	A_h	Time scale for IP_3R deactivation	1.4 s	2	
24	v_{SERCA}	SERCA pump permeability	51.8 μM/s	1.5	Converted from max uptake current value given for smooth muscle cells in [243] ***, in between values previously used for neutrophils [155] and RAW macrophages [218]
25	K_{SERCA}	Ca^{2+} dissociation constant for SERCA	0.5 μM	1.5	In between values previously used for neutrophils [155] and RAW macrophages [218]
26	$v_{leak,ER}$	ER leak permeability	0.01 s^{-1}	1.5	Determined by steady state considerations
27	g_{SOCE}	SOCE channel conductance	0.005 nS	2	Under standard conditions, this leads to a maximum 1 pA influx, on the same order of magnitude as SOCE fluxes in Jurkat T cells [248]
28	c_{ref}	Store concentration for half SOCE activation	70 μM	1.5	Corresponds to about 1/3 the resting ER Ca^{2+} concentration, as in [248]
29	v_{PMCA}	PMCA permeability	0.839 μM/s	1.5	Determined by steady state considerations
30	$K_{m,PMCA}$	Michaelis constant for PMCA activation	0.17 μM	2	Value measured in smooth muscle cells [249]
31	$B_{i,tot}$	Total concentration of Ca^{2+} buffer in the cytosol	300 μM	2	In between value measured in human neutrophils [250] and lower values more commonly used in literature
32	$K_{i,B}$	Average dissociation constant for cytosolic Ca^{2+} buffers	0.5 μM	1.5	Measured in human neutrophils [250]
33	$B_{ER,tot}$	Total concentration of Ca^{2+} buffer in ER	60 mM	2	Chosen to match values used for RAW macrophages [218]

34	$K_{ER,B}$	Equilibrium constant for Ca^{2+} binding to buffers in the ER	500 μM	1.5	Chosen to match values used for RAW macrophages [218]
35	V_i	Membrane voltage	-60 mV	1.5	Typical resting membrane voltage for a human neutrophil measured in [251] and estimated in [252]
36	$A_{c,max}$	Maximum contact area during spreading	200-240 μm^2	1.2	Value is determined by IgG density according to the relationship between ρ_{IgG} and maximum contact area measured in Chapter 2.
37	t_{shift}	Time shift factor (defines $t = 0$)	100 s	1.2	Corresponds to the time from the start of the simulation to the maximum speed of spreading (given Eq (H.5))
38	t_0	Characteristic time for sigmoidal contact area growth	17-20 s	1.2	Sets the speed of spreading, chosen to match 3 $\mu m^2/s$ regardless of ligand density, as measured in Chapter 2. For a sigmoidal relationship (Eq (H.5)), the max. slope is $A_{c,max} / 4t_0$

[#] "Fold-variation" indicates the factor by which the parameter is allowed to vary in sensitivity analysis (see "Sensitivity analysis" section below).

* To relate 2D densities to 3D concentrations, we need to consider a relevant height over which the interactions can occur (e.g. height of membrane fluctuations in region with uniform mixing). We chose to use 50 nm (.05 μm).

** To convert from on-rate in the B cell model [244] (given in units of $\mu M^{-1}s^{-1}$) to our on-rate (given in s^{-1}), we multiplied by the concentration of Src in their model (~1.5 μM).

*** To convert from current in picoamperes to total flux by concentration (μM/s), we divided by $2 F vol_{ref}$, where F is Faraday's constant and vol_{ref} is the volume of the cell in the paper being referenced.

Full description of computational model

Although many detailed computational models of intracellular Ca^{2+} dynamics have been developed, most have focused on excitable cells such as neurons or muscle cells. However, non-excitable cells such as fibroblasts or immune cells also show dramatic patterns of Ca^{2+} transients which remain poorly understood. Here, we develop a model for Ca^{2+} dynamics during neutrophil phagocytosis based on existing ODE-based models of Ca^{2+} signaling. Many relationships we used in this model are outlined nicely in [253].

In this model, we examine global changes in Ca^{2+} concentration; that is, we neglect intracellular gradients in Ca^{2+}. While detailed spatial models may prove valuable in the future, our experimental observations show that Ca^{2+} is relatively uniform when examined over the time scale of seconds. Therefore, this model can be formulated as a system of ODEs that can be readily solved using an ODE solver in MATLAB.

We consider fluxes between 3 compartments in our model: the extracellular space, the cytosol, and the endoplasmic reticulum (ER) (Fig 5.8). Assuming the extracellular Ca^{2+} level remains constant, this gives us two flux balance equations:

$$\frac{dc_i}{dt} = B_i \left(j_{IP_3R} + j_{ER,leak} - j_{SERCA} + j_{SOCE} - j_{PMCA} \right) \tag{H.1}$$

$$\frac{dc_{ER}}{dt} = B_{ER} \frac{vol_i}{vol_{ER}} \left(j_{SERCA} - j_{IP_3R} - j_{ER,leak} \right) \tag{H.2}$$

The fluxes (j terms) are expressed in terms of concentration per unit time (μM/s) and are defined as the molecular flux divided by the cytosolic volume. The terms B_i and B_{ER} arise from the rapid buffering approximation [214]. This involves assuming a separation of timescales; namely,

Ca^{2+} buffering occurs much faster than changes in overall free Ca^{2+}. Under standard conditions, we assume a total concentration c_B for Ca^{2+} buffers in the cytosol such as calmodulin, with an average dissociation constant $K_{d,B}$. Additional buffers can also be included in this term as indicated:

$$B_i = \left(1 + \frac{K_{d,B} c_B}{\left(K_{d,B} + c_i \right)^2} + \frac{K_{d,other} c_{other}}{\left(K_{d,other} + c_i \right)^2} + \ldots \right)^{-1} \tag{H.3}$$

The ER generally contains a high concentration ($c_{B,ER}$) of low-affinity buffer (dissociation constant $K_{d,ER}$), which dictates B_{ER} :

$$B_{ER} = \left(1 + \frac{K_{d,CS} c_{CS}}{\left(K_{d,CS} + c_i \right)^2} \right)^{-1} \tag{H.4}$$

To solve for intracellular Ca^{2+} concentration from Eqs (H.1) and (H.2) we must compute all the fluxes, which introduces an additional five differential equations through the following sequence of events:

1. Ligand-receptor binding: The input for this model is the cell-target contact area over time, given by:

$$A_c(t) = \frac{A_{c,max}}{1 + \exp\left(-\frac{t - t_{shift}}{t_0} \right)} \tag{H.5}$$

This relationship was chosen to be sigmoidal to match our measurements of contact area from our frustrated phagocytosis experiments. $A_{c,max}$ sets the maximum contact area the cell reaches in spreading, t_{shift} determines when our simulation begins (sets $t = 0$), and t_0 sets the speed of spreading. We chose the values of these parameters to match those from

our measurements of frustrated phagocytosis (maximum contact area depends on the IgG density and spreading speed = 3.0 $\mu m^2/s$), but their values (and the overall relationship itself) can be readily adjusted to model other cases of phagocytosis.

Given $A_c(t)$ and its rate of change $dA_c(t)/dt$, we can solve for the number of FcγRs bound to IgG at each time step.

$$\frac{dN_{Fc\gamma R,cup}}{dt} = D_{Fc\gamma R}(2\pi r_c)\nabla\rho_{Fc\gamma R,unbound} + \frac{dA_c}{dt}\rho_{Fc\gamma R,body} \tag{H.6}$$

Eq (H.6) includes receptor diffusion (first term on the right-hand-side) and increased binding purely due to contact area growth (second term on the right-hand-side). The equation can be expressed in terms of a single unknown, $N_{Fc\gamma R,bound}$, by assuming rapid binding to a known density of IgG ρ_{IgG} with binding affinity K_{IgG}. Similar to the rapid buffering approximation above, assuming separation of timescales, the relationship between the total number of the receptors in the contact region ($N_{Fc\gamma R,cup}$) and the number of bound receptors ($N_{Fc\gamma R,cup}$) is:

$$N_{Fc\gamma R,cup} = N_{Fc\gamma R,bound}\left(1 + \frac{K_{IgG}A_c}{\rho_{IgG}A_c - N_{Fc\gamma R,bound}}\right) \tag{H.7}$$

The time derivative is given by:

$$\frac{dN_{Fc\gamma R,cup}}{dt} = \frac{dN_{Fc\gamma R,bound}}{dt}\left(1 + \frac{K_{IgG}\rho_{IgG}A_c^{\,2}}{\left(\rho_{IgG}A_c - N_{Fc\gamma R,bound}\right)^2}\right) + \frac{dA_c}{dt}\frac{K_{IgG}}{\left(\rho_{IgG}A_c - N_{Fc\gamma R,bound}\right)^2} \tag{H.8}$$

Using these expressions, all terms in Eq (H.6) can be written with $N_{Fc\gamma R,bound}$ as the only unknown. In particular, we can write:

$$\nabla \rho_{Fc\gamma R,unbound} = \frac{\rho_{Fc\gamma R,body} A_c - (N_{Fc\gamma R,cup} - N_{Fc\gamma R,bound})}{l_{diff} A_c} \tag{H.9}$$

where l_{diff} is a characteristic membrane length over which diffusion occurs, and:

$$\rho_{Fc\gamma R,body} = \frac{N_{Fc\gamma R,tot} - N_{Fc\gamma R,cup}}{A_{tot} - A_c} \tag{H.10}$$

where $N_{Fc\gamma R,tot}$ is the total number of FcγRs in the membrane and A_{tot} is the total microscopic membrane surface area (including folds such as microvilli). Note that we assume that both A_{tot} and $N_{Fc\gamma R,tot}$ remain constant over the time course of phagocytosis. Both could increase due to exocytosis, but for the short time scales modeled here, treating them as constants provides a good initial estimate.

2. Phosphorylation events: Binding and clustering of FcγRs leads to Src-family kinase (SFK)-mediated phosphorylation of immunoreceptor tyrosine activation motifs (ITAMs), which are cytosolic domains present on some subtypes of FcγRs on neutrophils (mainly FcγRIIa). Experimental measurements from our lab indicate that about 5-10% of FcγRs present in resting neutrophil membranes are FcγRIIa [239]. Therefore if we denote the number of unphosphorylated ITAM domains in the contact region as N_{ITAM} and the number of phosphorylated ITAM domains in the contact region as N_{pITAM}, we approximate:

$$N_{ITAM} + N_{pITAM} = \left(\frac{\rho_{ITAM,0}}{\rho_{R,0}} \right) N_{Fc\gamma R,bound} \tag{H.11}$$

To then calculate the overall change in phosphorylated ITAMs, we assume that only the ITAM domains of receptors which were bound in the last 10 s ($N_{ITAM,10\,s}$) are available for phosphorylation. This value of 10 s can be adjusted, but the overall phenomenon agrees

well with experiments that show enhanced signaling at the leading edge of pseudopods during phagocytosis [70]. We furthermore assume that SFKs bind in a manner dependent on the local ITAM density, with a binding constant K_{Src} specified in units of μm^{-2}. Finally, assuming a dephosphorylation rate of k_{dephos}, this yields:

$$\frac{dN_{pITAM}}{dt} = N_{ITAM,10s}\nu_{Src}\left(\frac{N_{ITAM}}{K_{Src}A_c + N_{ITAM}}\right) - k_{dephos}N_{pITAM} \tag{H.12}$$

Spleen tyrosine kinase (Syk) then binds to phosphorylated ITAM domains and proceeds to phosphorylate many other enzymes downstream. FcγRIIa-mediated Ca^{2+} signals are primarily mediated by phospholipase C (PLC) [221], which cleaves PIP_2 in the membrane, producing diacylglycerol (DAG) and inositol triphosphate (IP_3). We simplify this series of steps to the following set of differential equations originally given in [245]:

$$\frac{dN_{PIP_2}}{dt} = -\left(\alpha_{PLC}N_{pITAM}\frac{c_i}{K_{a,PLC}+c_i} + r_r\right)N_{PIP_2} - r_r vol_i N_A[IP_3] + r_r N_{PIP_2,tot} \tag{H.13}$$

$$\frac{d[IP_3]}{dt} = \alpha_{PLC}N_{pITAM}\frac{c_i}{K_{a,PLC}+c_i}\left(\frac{N_{PIP_2}}{vol_i N_A}\right) - k_{deg,IP_3}[IP_3] \tag{H.14}$$

N_A is Avogadro's number, which together with the cytosolic volume vol_i is used to convert between numbers of molecules and concentrations. All other terms and parameters are defined in Table H.1.

3. IP_3 receptor (IP_3R)-mediated Ca^{2+} release: IP_3 binds to its receptor in the ER membrane, which also acts as a Ca^{2+} channel. The conductance of the IP_3R is also Ca^{2+}-dependent, obeying the well-known relationship [212, 213]:

$$j_{IP_3R} = \frac{P_{IP_3R}[IP_3]^3 c_i^3 h^3}{([IP_3]+K_{i,IP_3R})^3(c_i+K_{a,IP_3R})^3}\left(\frac{c_{ER}-c_i}{c_{ER,0}}\right) \tag{H.15}$$

This flux is enhanced by elevated intracellular Ca^{2+} with an activation constant $K_{a,IP3R}$. However, it is also deactivated by Ca^{2+} on a slower timescale, dictated by the variable h, which obeys the dynamical relationship:

$$\frac{dh}{dt} = A_h \left(K_{d,h} - (c_i + K_{d,h})h \right) \tag{H.16}$$

Ca^{2+} is also pumped back into the ER by SERCA pumps:

$$j_{SERCA} = \frac{v_{SERCA} c_i^{\,2}}{K_{SERCA}^{\,2} + c_i^{\,2}} \tag{H.17}$$

and leaks out of the ER gradually:

$$j_{ER,leak} = v_{ER,leak} \left(c_{ER} - c_i \right) \tag{H.18}$$

At steady state, the leak and SERCA fluxes perfectly balance each other, assuming the baseline IP_3 concentration is negligible.

4. Store-operated calcium entry: Following Ca^{2+} release from the ER, STIM molecules oligimerize in the ER membrane and associate with Orai channels in the plasma membrane, leading to Ca^{2+} influx. This process, known as store-operated calcium entry (SOCE), has been extensively characterized over the past two decades. Here, we use an empirical model for a flux which depends on store emptying, based on measurements in T cells [248]:

$$j_{SOCE} = \frac{g_{SOCE}}{2F\bar{V}_i \left(1 + \left(\frac{c_{ER}}{c_{ref}} \right)^4 \right)} \left(V_m - E_{Ca^{2+}} \right) \tag{H.19}$$

where E_{Ca2+} is the Nernst potential, calculated given the gas constant R, temperature T (room temperature to match our experiments), and Faraday's constant F:

$$E_{Ca^{2+}} = \frac{RT}{2F} \ln\left(\frac{c_{EC}}{c_i}\right) \tag{H.20}$$

In conjunction with this influx, Ca^{2+} is also pumped out of the cytosol by PMCA pumps:

$$j_{PMCA} = v_{PMCA}\left(\frac{c_i}{c_i + K_{m,PMCA}}\right) \tag{H.21}$$

At steady state, PMCA efflux balances a slow leak of Ca^{2+} into the cell due to Eq (H.19).

The system of ODEs was solved using ode15s in MATLAB. The 7 state variables and their initial conditions are summarized in Table H.2.

Table H.2: State variables and initial conditions

Variable	Description	Initial value	Notes/Sources
c_i	cytosolic Ca^{2+} concentration	0.1 μM	Chosen to match our measurements in Chapter 5, agrees with previous measurements in human neutrophils [198]
c_{ER}	ER Ca^{2+} concentration	200 μM	Chosen to match values previously used for human neutrophils [155] and RAW macrophages [218]
$N_{FcγR,bound}$	number of bound FcγRs	Variable, approaches $\rho_{IgG}A_{c,0}$ for complete binding	Determined by starting contact area, IgG density, and other parameters in Eq (H.7)
N_{pITAM}	number of phosphorylated ITAM domains	0	Assuming no baseline activation
N_{PIP2}	number of PIP_2 molecules in the membrane	2×10^7	Corresponds to ~150 μM (over the whole cell body volume), in the range specified for RAW macrophages [218]
$[IP_3]$	cytosolic IP_3 concentration	0 μM	Limiting case in which IP_3 levels in resting neutrophils are negligible
h	fraction of IP_3 channels not deactivated by Ca^{2+}	0.545	Set by the values for $K_{d,h}$ and c_i at equilibrium (see Eq (H.16))

Sensitivity analysis

Our goal in conducting this sensitivity analysis was to compute the first-order Sobol indices and total-order Sobol indices for a set of chosen model outputs as an indicator of the model's sensitivity to different parameters [216, 254]. The first-order indices capture the effects of varying a single parameter at a time, whereas the total-order index for a given parameter captures interactions between parameters (including all higher-order effects). By assessing the difference between the first-order and the total-order indices, we can evaluate the importance of interactions between parameters. Our chosen outputs for this analysis were:

1. Steady-state Ca^{2+} concentration $[Ca^{2+}]_{SS}$
2. Total area under the ($[Ca^{2+}]$ - $[Ca^{2+}]_{SS}$) curve (Total AUC)
3. Contact area at the time of the Ca^{2+} burst onset ($A_c(t_{burst})$)
4. Area under the ($[Ca^{2+}]$ - $[Ca^{2+}]_{SS}$) curve from $t = t_{burst}$ to $t = t_{burst} + 100$
5. Number of peaks in the $[Ca^{2+}]$ curve

All computations below were done using the SALib library in Python [209, 210].

The first-order Sobol index associated with the i^{th} parameter (i goes from 1 to 38 as listed in Table H.1) and a given output (for example, Total AUC) corresponds to that parameter's first order contribution $V_{AUC,i}$ to the total variance V_{AUC} :

$$S_{AUC,i}^{first} = \frac{V_{AUC,i}}{V_{AUC}} \tag{H.22}$$

This index includes all higher-order effects (interactions between parameters). However, we can also compute the total Sobol index, which includes all higher-order terms:

$$S_{AUC,i}^{tot} = \frac{V_{AUC,i} + \sum_{j \neq i} V_{AUC,ij} + \ldots}{V_{AUC}} \tag{H.23}$$

To compute these indices, we first generated a population of models in which each parameter was sampled from a log-normal distribution with geometric standard deviation equal to the fold-variation indicated in Table H.1. For example, if the fold-variation is 1.5, the parameter generally varies from 2/3 to 1.5 times its baseline value. We used Saltelli's sampling scheme [255] to generate the population of models, with 2,048 samples per parameter. We then ran the model in MATLAB for each parameter set, storing as outputs the five outputs defined above. For each set of 38 parameters, we computed the steady-state values for all 7 state variables and specified these as the initial conditions.

The Sobol sensitivity indices defined in Eqs (H.22) and (H.23) were computed using variance estimators developed by Sobol and Saltelli [216, 256]. Confidence intervals were estimated using a bootstrap approach with 1,000 resamples. For each output, we focused our subsequent analysis on the parameters with the five highest total sensitivity indices.

First, we examined the sensitivity of the steady-state Ca^{2+} concentration, which does not depend on IgG density or any IP_3R-related variables in our model, as we set the initial IP_3 concentration to zero (Table H.2). We find that parameters with the highest Sobol index are associated with the SERCA pumps (Fig H.1), which emphasizes their key role in intracellular Ca^{2+} homeostasis. The first-order and total-order Sobol indices are similar for the parameters with the highest overall Sobol indices (Fig H.1A), indicating that first-order effects dominate in this case.

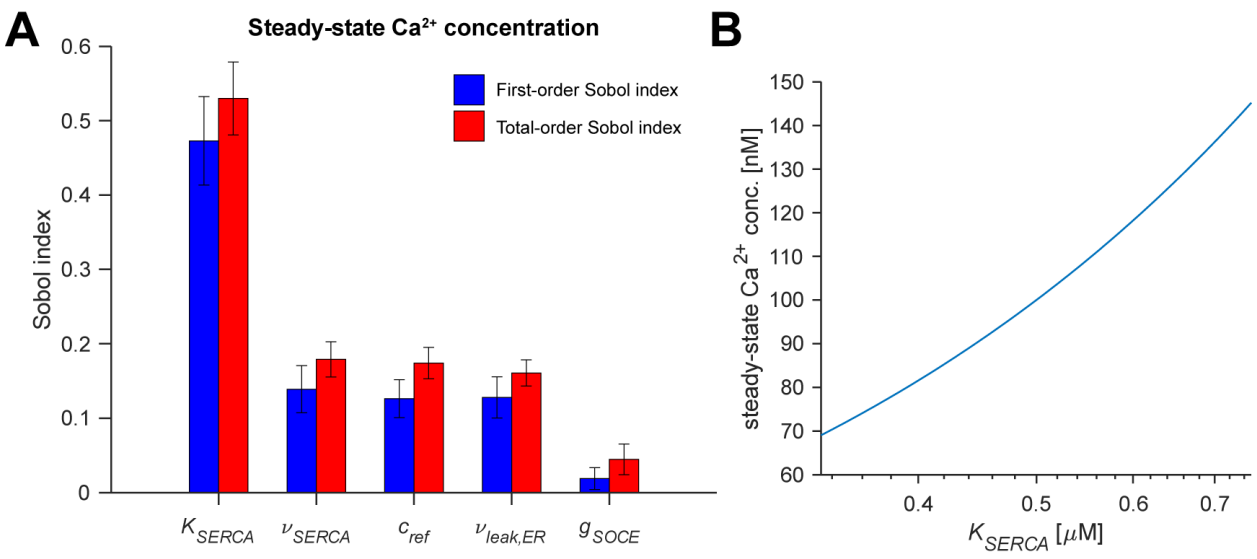

Fig H.1: Sensitivity of steady-state Ca^{2+} concentration to changes in parameters. (A) The five parameters with the highest Sobol indices for steady-state Ca^{2+} concentration, with first- and total-order Sobol indices indicated in blue and red, respectively. Error bars denote 95% confidence intervals. **(B)** This graph shows the steady-state Ca^{2+} concentration for different values of K_{SERCA} while keeping all other parameters fixed.

We then determined the Sobol indices for the four other outputs on different densities of IgG. Results of the sensitivity analysis on low (24.1 μm^{-2}), moderate (1,020 μm^{-2}), and high (24,900 μm^{-2}) densities of IgG are summarized in Figs H.2 to H.4 below. These values of IgG density were chosen to match measurements of density on our 0.1%, 10%, and 100% coated surfaces in Chapter 2.

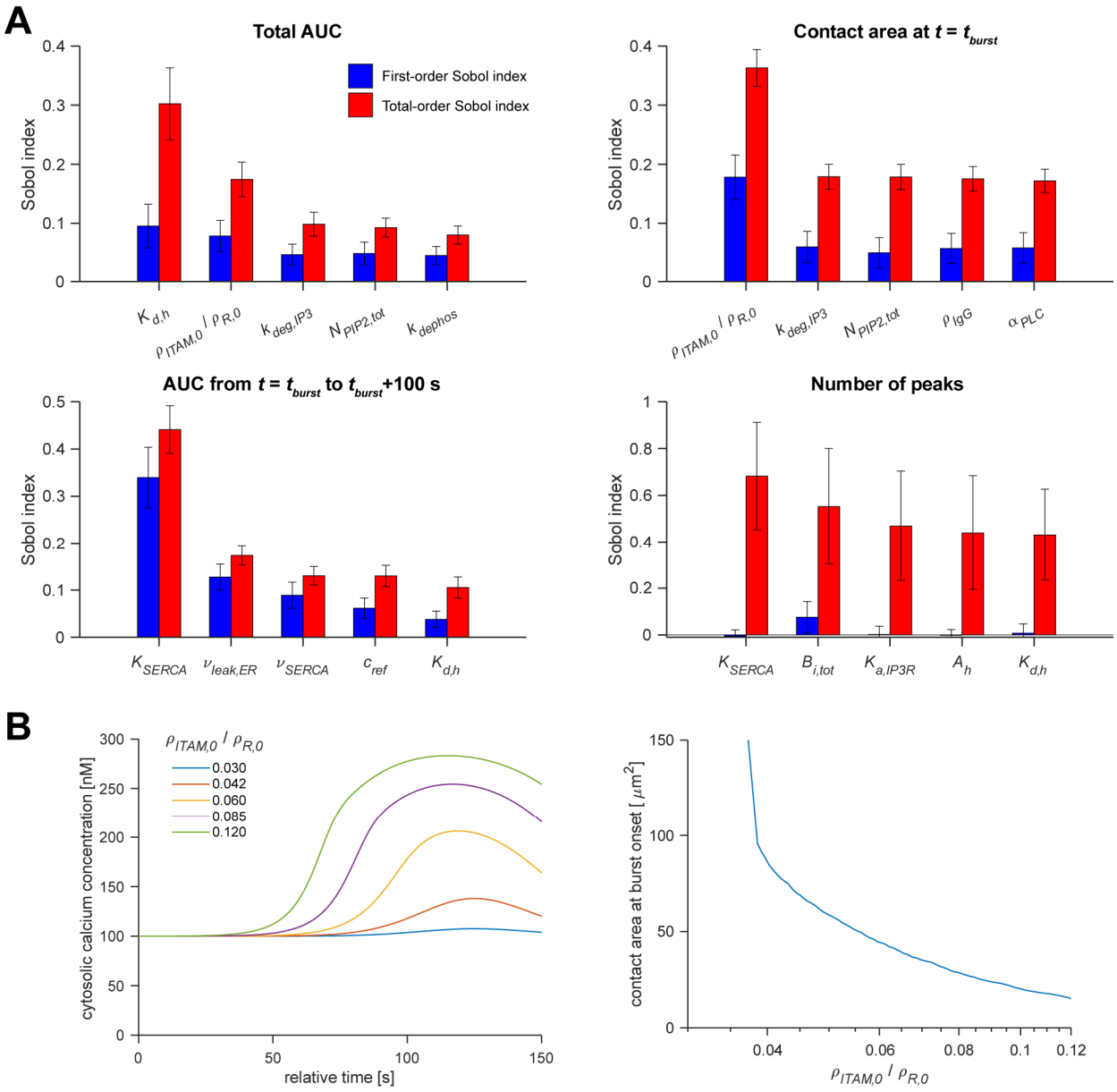

Fig H.2: Model sensitivity for low IgG density (ρ_{IgG} = 24.1 μm^{-2}). (A) First-order (blue) and total-order (red) Sobol indices for outputs defined in the text. Error bars denote 95% confidence intervals. **(B)** Simulations showing the effect of varying the fraction of FcγRs with ITAM domains. The graph on the left shows the results of five simulations with different values of this parameter (all other parameters are kept equal), and the right graph shows the overall relationship between contact area at the time of the burst and this parameter.

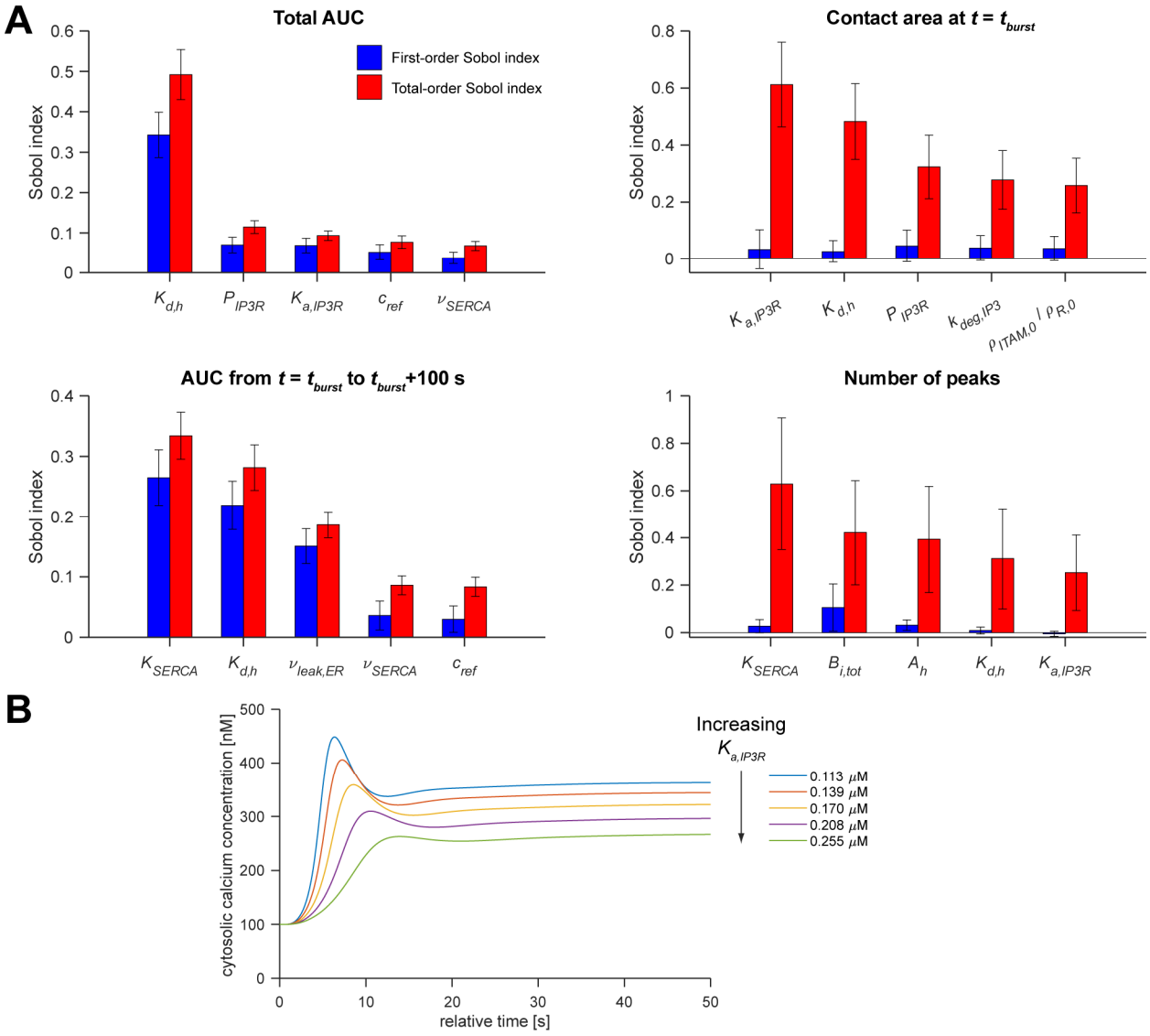

Fig H.3: Model sensitivity for moderate IgG density (ρ_{IgG} = 1,020 μm^{-2}). (A) First-order (blue) and total-order (red) Sobol order indices for outputs defined in the text. Error bars denote 95% confidence intervals. **(B)** Simulations showing the effect of changing the Ca^{2+} dissociation constant for the IP_3R activating site while keeping other parameters constant. Increasing the value of this parameter effectively increases the activation threshold and slows the onset of Ca^{2+} bursts.

For all three analyses, we see that the overall area under the curve (total AUC) is most sensitive to changes in $K_{d,h}$ (Ca^{2+} dissociation constant for IP_3R deactivating site), whereas the AUC from $t = t_{burst}$ to $t = t_{burst} + 100$ is most sensitive to K_{SERCA} (Ca^{2+} dissociation constant for SERCA pumps). Both of these findings make sense from an intuitive standpoint. $K_{d,h}$

dictates how high the Ca^{2+} concentration can get before the IP_3Rs begin to get deactivated (channel closing), thus limiting the overall increase in intracellular Ca^{2+}. K_{SERCA} also limits the increase in Ca^{2+}, but in this case by limiting how high the Ca^{2+} concentration reaches before it gets rapidly pumped back into the ER. K_{SERCA} acts on a fast time scale, whereas $K_{d,h}$ acts on a slower time scale, explaining why they have the largest impacts on the initial AUC and the total AUC, respectively.

Also common to all three analyses is the observation that higher-order effects dominate in determining how many peaks occur in the $[Ca^{2+}]$-versus-time curve. This indicates that multiple parameters need to be varied simultaneously to permit sustained Ca^{2+} oscillations. With different choices of baseline parameters, Ca^{2+} oscillations occur much more commonly, as documented in the literature [212, 213]. In all three cases, K_{SERCA} has the largest overall contribution, showing that the action of SERCA pumps is key to driving Ca^{2+} oscillations. The total amount of intracellular buffer, $B_{i,tot}$, also makes a substantial contribution, in agreement with a seminal study indicating that intracellular buffers can impact the amplitude, frequency, and existence of Ca^{2+} oscillations [214].

On low densities of IgG, the fraction of FcγRs with ITAM domains is the most important factor in determining the signaling threshold for the Ca^{2+} burst (Fig H.2). If this fraction is too low, Ca^{2+} bursts do not occur, and if the fraction is higher, then Ca^{2+} bursts are induced earlier in spreading (Fig H.2B). On moderate or high densities of IgG, the timing of bursts is dominated by higher order effects. $K_{a,IP3R}$ and $K_{d,h}$ (Ca^{2+} dissociation constants for the IP_3R activating site and deactivating site, respectively) are two of the parameters with the highest total-order Sobol indices for this output. Increasing $K_{a,IP3R}$ (Fig H.3B) or decreasing $K_{d,h}$ (Fig H.4B) have similar effects of slowing the onset of Ca^{2+} bursts. Notably, the timing of Ca^{2+} bursts is sensitive

to the total number of FcγRs ($N_{FcγR,tot}$) only on the highest density of IgG (Fig H.4A), reflecting the fact that on high densities of IgG, the receptor density rather than the IgG density is the limiting factor.

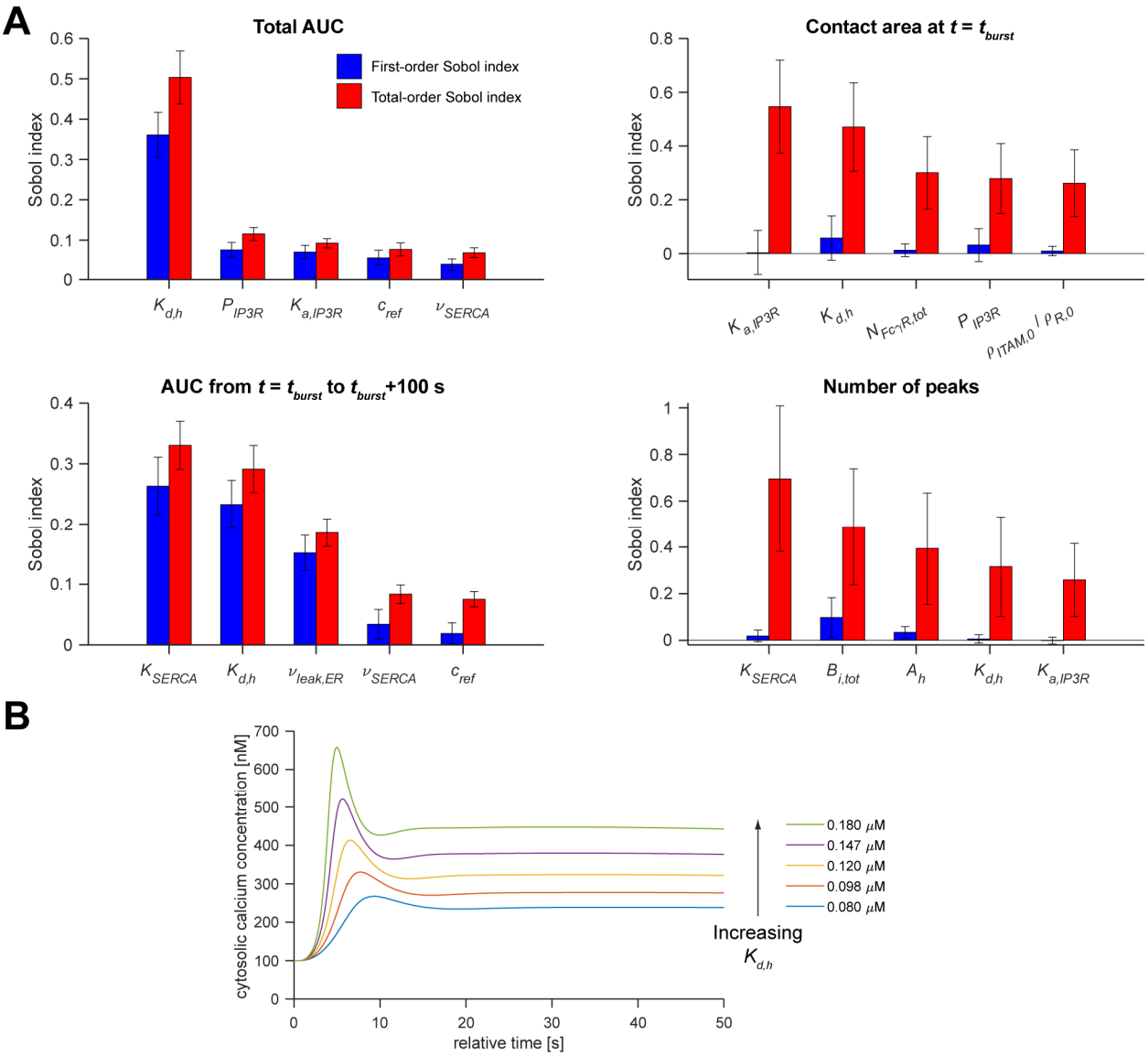

Fig H.4: Model sensitivity for high IgG density (ρ_{IgG} = 24,900 μm^{-2}). (A) First-order (blue) and total-order (red) Sobol order indices for outputs defined in the text. Error bars denote 95% confidence intervals. **(B)** Simulations showing the effect of changing the Ca^{2+} dissociation constant for the IP_3R deactivating site while keeping other parameters constant. Increasing the value of this parameter effectively decreases the binding affinity for Ca^{2+} to the deactivating site, increasing the overall magnitude of Ca^{2+} bursts.

References

1. Bournazos S, Wang TT, Ravetch JV. The Role and Function of Fcgamma Receptors on Myeloid Cells. Microbiol Spectr. 2016;4(6). Epub 2017/01/15. doi: 10.1128/microbiolspec.MCHD-0045-2016. PubMed PMID: 28087938; PubMed Central PMCID: PMCPMC5240797.
2. Dustin ML. Complement Receptors in Myeloid Cell Adhesion and Phagocytosis. Microbiol Spectr. 2016;4(6). Epub 2016/11/05. doi: 10.1128/microbiolspec.MCHD-0034-2016. PubMed PMID: 27809953; PubMed Central PMCID: PMCPMC5580235.
3. Swanson JA, Baer SC. Phagocytosis by zippers and triggers. Trends Cell Biol. 1995;5(3):89-93. Epub 1995/03/01. doi: 10.1016/s0962-8924(00)88956-4. PubMed PMID: 14732161.
4. Griffin FM, Jr., Griffin JA, Leider JE, Silverstein SC. Studies on the mechanism of phagocytosis. I. Requirements for circumferential attachment of particle-bound ligands to specific receptors on the macrophage plasma membrane. J Exp Med. 1975;142(5):1263-82. Epub 1975/11/11. doi: 10.1084/jem.142.5.1263. PubMed PMID: 1194852; PubMed Central PMCID: PMCPMC2189973.
5. Allen LA, Aderem A. Molecular definition of distinct cytoskeletal structures involved in complement- and Fc receptor-mediated phagocytosis in macrophages. J Exp Med. 1996;184(2):627-37. Epub 1996/08/01. doi: 10.1084/jem.184.2.627. PubMed PMID: 8760816; PubMed Central PMCID: PMCPMC2192718.
6. Aderem A, Underhill DM. Mechanisms of phagocytosis in macrophages. Annual review of immunology. 1999;17:593-623. Epub 1999/06/08. doi: 10.1146/annurev.immunol.17.1.593. PubMed PMID: 10358769.
7. Simon SI, Schmid-Schonbein GW. Biophysical aspects of microsphere engulfment by human neutrophils. Biophys J. 1988;53(2):163-73. Epub 1988/02/01. doi: 10.1016/S0006-3495(88)83078-9. PubMed PMID: 3345329; PubMed Central PMCID: PMCPMC1330137.
8. Cannon GJ, Swanson JA. The macrophage capacity for phagocytosis. J Cell Sci. 1992;101 (Pt 4):907-13. Epub 1992/04/01. PubMed PMID: 1527185.
9. Herant M, Heinrich V, Dembo M. Mechanics of neutrophil phagocytosis: behavior of the cortical tension. J Cell Sci. 2005;118(Pt 9):1789-97. Epub 2005/04/14. doi: 10.1242/jcs.02275. PubMed PMID: 15827090.
10. Herant M, Heinrich V, Dembo M. Mechanics of neutrophil phagocytosis: experiments and quantitative models. J Cell Sci. 2006;119(Pt 9):1903-13. Epub 2006/04/26. doi: 10.1242/jcs.02876. PubMed PMID: 16636075.
11. Herant M, Lee CY, Dembo M, Heinrich V. Protrusive push versus enveloping embrace: computational model of phagocytosis predicts key regulatory role of cytoskeletal membrane anchors. PLoS Comput Biol. 2011;7(1):e1001068. doi: 10.1371/journal.pcbi.1001068. PubMed PMID: 21298079; PubMed Central PMCID: PMCPMC3029235.
12. Lee C-Y, Herant M, Heinrich V. Target-specific mechanics of phagocytosis: protrusive neutrophil response to zymosan differs from the uptake of antibody-tagged pathogens. J Cell Sci. 2011;124(7):1106-14. doi: 10.1242/jcs.078592. PubMed Central PMCID: PMCPMC3056606
13. Heinrich V. Controlled One-on-One Encounters between Immune Cells and Microbes Reveal Mechanisms of Phagocytosis. Biophys J. 2015;109(3):469-76. Epub 2015/08/06. doi: 10.1016/j.bpj.2015.06.042. PubMed PMID: 26244729; PubMed Central PMCID: PMCPMC4572503.
14. Jaumouille V, Cartagena-Rivera AX, Waterman CM. Coupling of beta2 integrins to actin by a mechanosensitive molecular clutch drives complement receptor-mediated phagocytosis. Nat Cell Biol. 2019;21(11):1357-69. Epub 2019/10/30. doi: 10.1038/s41556-019-0414-2. PubMed PMID: 31659275; PubMed Central PMCID: PMCPMC6858589.
15. Yao M, Goult BT, Chen H, Cong P, Sheetz MP, Yan J. Mechanical activation of vinculin binding to talin locks talin in an unfolded conformation. Sci Rep. 2014;4:4610. Epub 2014/04/10. doi: 10.1038/srep04610. PubMed PMID: 24714394; PubMed Central PMCID: PMCPMC3980218.

16. Freeman SA, Goyette J, Furuya W, Woods EC, Bertozzi CR, Bergmeier W, et al. Integrins Form an Expanding Diffusional Barrier that Coordinates Phagocytosis. Cell. 2016;164(1-2):128-40. Epub 2016/01/16. doi: 10.1016/j.cell.2015.11.048. PubMed PMID: 26771488; PubMed Central PMCID: PMCPMC4715264.
17. Jongstra-Bilen J, Harrison R, Grinstein S. Fcgamma-receptors induce Mac-1 (CD11b/CD18) mobilization and accumulation in the phagocytic cup for optimal phagocytosis. J Biol Chem. 2003;278(46):45720-9. Epub 2003/08/28. doi: 10.1074/jbc.M303704200. PubMed PMID: 12941957.
18. Barger SR, Gauthier NC, Krendel M. Squeezing in a Meal: Myosin Functions in Phagocytosis. Trends Cell Biol. 2020;30(2):157-67. Epub 2019/12/15. doi: 10.1016/j.tcb.2019.11.002. PubMed PMID: 31836280; PubMed Central PMCID: PMCPMC7244380.
19. Barger SR, Reilly NS, Shutova MS, Li Q, Maiuri P, Heddleston JM, et al. Membrane-cytoskeletal crosstalk mediated by myosin-I regulates adhesion turnover during phagocytosis. Nat Commun. 2019;10(1):1249. Epub 2019/03/21. doi: 10.1038/s41467-019-09104-1. PubMed PMID: 30890704; PubMed Central PMCID: PMCPMC6425032.
20. Flannagan RS, Jaumouille V, Grinstein S. The cell biology of phagocytosis. Annu Rev Pathol. 2012;7:61-98. Epub 2011/09/14. doi: 10.1146/annurev-pathol-011811-132445. PubMed PMID: 21910624.
21. Marks PW, Maxfield FR. Local and global changes in cytosolic free calcium in neutrophils during chemotaxis and phagocytosis. Cell Calcium. 1990;11(2-3):181-90. Epub 1990/02/01. PubMed PMID: 2354498.
22. Davies EV, Campbell AK, Hallett MB. Ca2+ oscillations in neutrophils triggered by immune complexes result from Ca2+ influx. Immunology. 1994;82(1):57-62. Epub 1994/05/01. PubMed PMID: 8045594; PubMed Central PMCID: PMCPMC1414847.
23. Kruskal BA, Maxfield FR. Cytosolic Free Calcium Increases before and Oscillates during Frustrated Phagocytosis in Macrophages. Journal of Cell Biology. 1987;105(6):2685-93. doi: DOI 10.1083/jcb.105.6.2685. PubMed PMID: WOS:A1987L414400026.
24. Lew DP, Andersson T, Hed J, Di Virgilio F, Pozzan T, Stendahl O. Ca2+-dependent and Ca2+-independent phagocytosis in human neutrophils. Nature. 1985;315(6019):509-11. Epub 1985/06/06. doi: 10.1038/315509a0. PubMed PMID: 3158824.
25. Theler JM, Lew DP, Jaconi ME, Krause KH, Wollheim CB, Schlegel W. Intracellular pattern of cytosolic Ca2+ changes during adhesion and multiple phagocytosis in human neutrophils. Dynamics of intracellular Ca2+ stores. Blood. 1995;85(8):2194-201. Epub 1995/04/15. PubMed PMID: 7718891.
26. Kummerow C, Junker C, Kruse K, Rieger H, Quintana A, Hoth M. The immunological synapse controls local and global calcium signals in T lymphocytes. Immunol Rev. 2009;231(1):132-47. Epub 2009/09/17. doi: 10.1111/j.1600-065X.2009.00811.x. PubMed PMID: 19754894.
27. Laffafian I, Hallett MB. Does cytosolic free Ca2+ signal neutrophil chemotaxis in response to formylated chemotactic peptide? J Cell Sci. 1995;108 (Pt 10):3199-205. Epub 1995/10/01. PubMed PMID: 7593281.
28. Meshulam T, Proto P, Diamond RD, Melnick DA. Calcium modulation and chemotactic response: divergent stimulation of neutrophil chemotaxis and cytosolic calcium response by the chemotactic peptide receptor. J Immunol. 1986;137(6):1954-60. PubMed PMID: 3745918.
29. Dewitt S, Francis RJ, Hallett MB. Ca(2)(+) and calpain control membrane expansion during the rapid cell spreading of neutrophils. J Cell Sci. 2013;126(Pt 20):4627-35. Epub 2013/08/15. doi: 10.1242/jcs.124917. PubMed PMID: 23943875; PubMed Central PMCID: PMCPMC3795336.
30. Dewitt S, Hallett MB. Cytosolic free Ca(2+) changes and calpain activation are required for beta integrin-accelerated phagocytosis by human neutrophils. J Cell Biol. 2002;159(1):181-9. doi: 10.1083/jcb.200206089. PubMed PMID: 12379807; PubMed Central PMCID: PMCPMC2173489.
31. Morikis VA, Simon SI. Neutrophil Mechanosignaling Promotes Integrin Engagement With Endothelial Cells and Motility Within Inflamed Vessels. Frontiers in Immunology. 2018;9. doi: ARTN 2774

10.3389/fimmu.2018.02774. PubMed PMID: WOS:000451662700001.
32. Francis EA, Xiao H, Teng LH, Heinrich V. Mechanisms of frustrated phagocytic spreading of human neutrophils on antibody-coated surfaces. BioRxiv [Preprint]. 2022. Epub February 22, 2022. doi: 10.1101/2022.02.18.481104.
33. Lim JJ, Grinstein S, Roth Z. Diversity and Versatility of Phagocytosis: Roles in Innate Immunity, Tissue Remodeling, and Homeostasis. Front Cell Infect Microbiol. 2017;7:191. Epub 2017/06/08. doi: 10.3389/fcimb.2017.00191. PubMed PMID: 28589095; PubMed Central PMCID: PMCPMC5440456.
34. Cougoule C, Wiedemann A, Lim J, Caron E. Phagocytosis, an alternative model system for the study of cell adhesion. Semin Cell Dev Biol. 2004;15(6):679-89. Epub 2004/11/25. doi: 10.1016/j.semcdb.2004.09.001. PubMed PMID: 15561587.
35. Futosi K, Fodor S, Mocsai A. Neutrophil cell surface receptors and their intracellular signal transduction pathways. Int Immunopharmacol. 2013;17(3):638-50. Epub 2013/09/03. doi: 10.1016/j.intimp.2013.06.034. PubMed PMID: 23994464; PubMed Central PMCID: PMCPMC3827506.
36. Rosales C, Uribe-Querol E. Phagocytosis: A Fundamental Process in Immunity. Biomed Res Int. 2017;2017:9042851. Epub 2017/07/12. doi: 10.1155/2017/9042851. PubMed PMID: 28691037; PubMed Central PMCID: PMCPMC5485277.
37. Uribe-Querol E, Rosales C. Phagocytosis: Our Current Understanding of a Universal Biological Process. Front Immunol. 2020;11:1066. Epub 2020/06/26. doi: 10.3389/fimmu.2020.01066. PubMed PMID: 32582172; PubMed Central PMCID: PMCPMC7280488.
38. Lee CY, Thompson GR, 3rd, Hastey CJ, Hodge GC, Lunetta JM, Pappagianis D, et al. Coccidioides Endospores and Spherules Draw Strong Chemotactic, Adhesive, and Phagocytic Responses by Individual Human Neutrophils. PLoS One. 2015;10(6):e0129522. doi: 10.1371/journal.pone.0129522. PubMed PMID: 26070210; PubMed Central PMCID: PMCPMC4466529.
39. Hallett MB, Dewitt S. Ironing out the wrinkles of neutrophil phagocytosis. Trends Cell Biol. 2007;17(5):209-14. Epub 2007/03/14. doi: 10.1016/j.tcb.2007.03.002. PubMed PMID: 17350842.
40. Lam J, Herant M, Dembo M, Heinrich V. Baseline mechanical characterization of J774 macrophages. Biophys J. 2009;96(1):248-54. Epub 2008/10/07. doi: 10.1529/biophysj.108.139154. PubMed PMID: 18835898; PubMed Central PMCID: PMCPMC2710052.
41. Champion JA, Mitragotri S. Role of target geometry in phagocytosis. Proc Natl Acad Sci U S A. 2006;103(13):4930-4. Epub 2006/03/22. doi: 10.1073/pnas.0600997103. PubMed PMID: 16549762; PubMed Central PMCID: PMCPMC1458772.
42. Pacheco P, White D, Sulchek T. Effects of microparticle size and Fc density on macrophage phagocytosis. PLoS One. 2013;8(4):e60989. Epub 2013/05/01. doi: 10.1371/journal.pone.0060989. PubMed PMID: 23630577; PubMed Central PMCID: PMCPMC3632606.
43. Paul D, Achouri S, Yoon YZ, Herre J, Bryant CE, Cicuta P. Phagocytosis dynamics depends on target shape. Biophys J. 2013;105(5):1143-50. Epub 2013/09/10. doi: 10.1016/j.bpj.2013.07.036. PubMed PMID: 24010657; PubMed Central PMCID: PMCPMC3762343.
44. van Zon JS, Tzircotis G, Caron E, Howard M. A mechanical bottleneck explains the variation in cup growth during FcgammaR phagocytosis. Mol Syst Biol. 2009;5:298. Epub 2009/08/20. doi: 10.1038/msb.2009.59. PubMed PMID: 19690567; PubMed Central PMCID: PMCPMC2736656.
45. Kovari DT, Wei W, Chang P, Toro JS, Beach RF, Chambers D, et al. Frustrated Phagocytic Spreading of J774A-1 Macrophages Ends in Myosin II-Dependent Contraction. Biophys J. 2016;111(12):2698-710. Epub 2016/12/22. doi: 10.1016/j.bpj.2016.11.009. PubMed PMID: 28002746; PubMed Central PMCID: PMCPMC5194617.
46. Ostrowski PP, Freeman SA, Fairn G, Grinstein S. Dynamic Podosome-Like Structures in Nascent Phagosomes Are Coordinated by Phosphoinositides. Dev Cell. 2019;50(4):397-410 e3. Epub 2019/06/25. doi: 10.1016/j.devcel.2019.05.028. PubMed PMID: 31231039.
47. Warrier R. max_inscribed_circle. MATLAB Central File Exchange: Rahul Warrier; 2017.
48. D'Errico J. A suite of minimal bounding objects. MATLAB Central File Exchange: John D'Errico; 2017.

49. Gorelik R, Gautreau A. Quantitative and unbiased analysis of directional persistence in cell migration. Nat Protoc. 2014;9(8):1931-43. Epub 2014/07/18. doi: 10.1038/nprot.2014.131. PubMed PMID: 25033209.
50. Warmerdam PA, van de Winkel JG, Gosselin EJ, Capel PJ. Molecular basis for a polymorphism of human Fc gamma receptor II (CD32). J Exp Med. 1990;172(1):19-25. Epub 1990/07/01. doi: 10.1084/jem.172.1.19. PubMed PMID: 2141627; PubMed Central PMCID: PMCPMC2188138.
51. Shashidharamurthy RB, E.; Patel, J.; Kaur, R.; Meganathan, J.; Selvaraj, P. Analysis of cross-species IgG binding to human and mouse Fcgamma receptors (FcγRs). The Journal of Immunology. 2010;184.
52. Lubeck MD, Steplewski Z, Baglia F, Klein MH, Dorrington KJ, Koprowski H. The interaction of murine IgG subclass proteins with human monocyte Fc receptors. J Immunol. 1985;135(2):1299-304. Epub 1985/08/01. PubMed PMID: 3159790.
53. Tran-Son-Tay R, Needham D, Yeung A, Hochmuth RM. Time-dependent recovery of passive neutrophils after large deformation. Biophys J. 1991;60(4):856-66. Epub 1991/10/01. doi: 10.1016/S0006-3495(91)82119-1. PubMed PMID: 1742456; PubMed Central PMCID: PMCPMC1260136.
54. Yeung A, Evans E. Cortical shell-liquid core model for passive flow of liquid-like spherical cells into micropipets. Biophys J. 1989;56(1):139-49. Epub 1989/07/01. doi: 10.1016/S0006-3495(89)82659-1. PubMed PMID: 2752083; PubMed Central PMCID: PMCPMC1280459.
55. Dobereiner HG, Dubin-Thaler B, Giannone G, Xenias HS, Sheetz MP. Dynamic phase transitions in cell spreading. Phys Rev Lett. 2004;93(10):108105. Epub 2004/09/28. doi: 10.1103/PhysRevLett.93.108105. PubMed PMID: 15447457.
56. Dubin-Thaler BJ, Giannone G, Dobereiner HG, Sheetz MP. Nanometer analysis of cell spreading on matrix-coated surfaces reveals two distinct cell states and STEPs. Biophys J. 2004;86(3):1794-806. Epub 2004/03/03. doi: 10.1016/S0006-3495(04)74246-0. PubMed PMID: 14990505; PubMed Central PMCID: PMCPMC1304013.
57. Dubin-Thaler BJ, Hofman JM, Cai Y, Xenias H, Spielman I, Shneidman AV, et al. Quantification of cell edge velocities and traction forces reveals distinct motility modules during cell spreading. PLoS One. 2008;3(11):e3735. Epub 2008/11/18. doi: 10.1371/journal.pone.0003735. PubMed PMID: 19011687; PubMed Central PMCID: PMCPMC2581916.
58. Reinhart-King CA, Dembo M, Hammer DA. The dynamics and mechanics of endothelial cell spreading. Biophys J. 2005;89(1):676-89. Epub 2005/04/26. doi: 10.1529/biophysj.104.054320. PubMed PMID: 15849250; PubMed Central PMCID: PMCPMC1366566.
59. Hategan A, Sengupta K, Kahn S, Sackmann E, Discher DE. Topographical pattern dynamics in passive adhesion of cell membranes. Biophys J. 2004;87(5):3547-60. Epub 2004/09/02. doi: 10.1529/biophysj.104.041475. PubMed PMID: 15339814; PubMed Central PMCID: PMCPMC1304820.
60. Wolfenson H, Iskratsch T, Sheetz MP. Early events in cell spreading as a model for quantitative analysis of biomechanical events. Biophys J. 2014;107(11):2508-14. Epub 2014/12/04. doi: 10.1016/j.bpj.2014.10.041. PubMed PMID: 25468330; PubMed Central PMCID: PMCPMC4255173.
61. Janmey PA, Hinz B, McCulloch CA. Physics and Physiology of Cell Spreading in Two and Three Dimensions. Physiology (Bethesda). 2021;36(6):382-91. Epub 2021/10/28. doi: 10.1152/physiol.00020.2021. PubMed PMID: 34704856; PubMed Central PMCID: PMCPMC8560373.
62. Etienne J, Duperray A. Initial dynamics of cell spreading are governed by dissipation in the actin cortex. Biophys J. 2011;101(3):611-21. Epub 2011/08/03. doi: 10.1016/j.bpj.2011.06.030. PubMed PMID: 21806929; PubMed Central PMCID: PMCPMC3145312.
63. Cuvelier D, Thery M, Chu YS, Dufour S, Thiery JP, Bornens M, et al. The universal dynamics of cell spreading. Curr Biol. 2007;17(8):694-9. Epub 2007/03/24. doi: 10.1016/j.cub.2007.02.058. PubMed PMID: 17379524.
64. Chamaraux F, Fache S, Bruckert F, Fourcade B. Kinetics of cell spreading. Phys Rev Lett. 2005;94(15):158102. Epub 2005/05/21. doi: 10.1103/PhysRevLett.94.158102. PubMed PMID: 15904192.

65. Frisch T, Thoumine O. Predicting the kinetics of cell spreading. J Biomech. 2002;35(8):1137-41. Epub 2002/07/20. doi: 10.1016/s0021-9290(02)00075-1. PubMed PMID: 12126672.
66. Fardin MA, Rossier OM, Rangamani P, Avigan PD, Gauthier NC, Vonnegut W, et al. Cell spreading as a hydrodynamic process. Soft Matter. 2010;6(19):4788-99. doi: 10.1039/c0sm00252f. PubMed PMID: WOS:000282008300022.
67. Xiong Y, Rangamani P, Fardin MA, Lipshtat A, Dubin-Thaler B, Rossier O, et al. Mechanisms controlling cell size and shape during isotropic cell spreading. Biophys J. 2010;98(10):2136-46. Epub 2010/05/21. doi: 10.1016/j.bpj.2010.01.059. PubMed PMID: 20483321; PubMed Central PMCID: PMCPMC2872297.
68. Odenthal T, Smeets B, Van Liedekerke P, Tijskens E, Van Oosterwyck H, Ramon H. Analysis of initial cell spreading using mechanistic contact formulations for a deformable cell model. PLoS Comput Biol. 2013;9(10):e1003267. Epub 2013/10/23. doi: 10.1371/journal.pcbi.1003267. PubMed PMID: 24146605; PubMed Central PMCID: PMCPMC3798278.
69. DiNapoli KT, Robinson DN, Iglesias PA. A mesoscale mechanical model of cellular interactions. Biophys J. 2021;120(22):4905-17. Epub 2021/10/24. doi: 10.1016/j.bpj.2021.10.021. PubMed PMID: 34687718; PubMed Central PMCID: PMCPMC8633826.
70. Zhang Y, Hoppe AD, Swanson JA. Coordination of Fc receptor signaling regulates cellular commitment to phagocytosis. Proc Natl Acad Sci U S A. 2010;107(45):19332-7. Epub 2010/10/27. doi: 10.1073/pnas.1008248107. PubMed PMID: 20974965; PubMed Central PMCID: PMCPMC2984174.
71. Ben M'Barek K, Molino D, Quignard S, Plamont MA, Chen Y, Chavrier P, et al. Phagocytosis of immunoglobulin-coated emulsion droplets. Biomaterials. 2015;51:270-7. Epub 2015/03/17. doi: 10.1016/j.biomaterials.2015.02.030. PubMed PMID: 25771017.
72. Richards DM, Endres RG. The mechanism of phagocytosis: two stages of engulfment. Biophys J. 2014;107(7):1542-53. Epub 2014/10/09. doi: 10.1016/j.bpj.2014.07.070. PubMed PMID: 25296306; PubMed Central PMCID: PMCPMC4190621.
73. Footer MJ, Kerssemakers JWJ, Theriot JA, Dogterom M. Direct measurement of force generation by actin filament polymerization using an optical trap. P Natl Acad Sci USA. 2007;104(7):2181-6. doi: 10.1073/pnas.0607052104. PubMed PMID: WOS:000244438500028.
74. Kovar DR, Pollard TD. Insertional assembly of actin filament barbed ends in association with formins produces piconewton forces. Proc Natl Acad Sci U S A. 2004;101(41):14725-30. Epub 2004/09/21. doi: 10.1073/pnas.0405902101. PubMed PMID: 15377785; PubMed Central PMCID: PMCPMC522035.
75. Parekh SH, Chaudhuri O, Theriot JA, Fletcher DA. Loading history determines the velocity of actin-network growth. Nat Cell Biol. 2005;7(12):1219-23. Epub 2005/11/22. doi: 10.1038/ncb1336. PubMed PMID: 16299496.
76. Freeman SA, Grinstein S. Phagocytosis: receptors, signal integration, and the cytoskeleton. Immunol Rev. 2014;262(1):193-215. Epub 2014/10/17. doi: 10.1111/imr.12212. PubMed PMID: 25319336.
77. Nelsen E, Hobson CM, Kern ME, Hsiao JP, O'Brien Iii ET, Watanabe T, et al. Combined Atomic Force Microscope and Volumetric Light Sheet System for Correlative Force and Fluorescence Mechanobiology Studies. Sci Rep. 2020;10(1):8133. Epub 2020/05/20. doi: 10.1038/s41598-020-65205-8. PubMed PMID: 32424215; PubMed Central PMCID: PMCPMC7234992.
78. Vorselen D, Wang Y, de Jesus MM, Shah PK, Footer MJ, Huse M, et al. Microparticle traction force microscopy reveals subcellular force exertion patterns in immune cell-target interactions. Nat Commun. 2020;11(1):20. Epub 2020/01/09. doi: 10.1038/s41467-019-13804-z. PubMed PMID: 31911639; PubMed Central PMCID: PMCPMC6946705.
79. Vorselen D, Barger SR, Wang Y, Cai W, Theriot JA, Gauthier NC, et al. Phagocytic 'teeth' and myosin-II 'jaw' power target constriction during phagocytosis. Elife. 2021;10. Epub 2021/10/29. doi: 10.7554/eLife.68627. PubMed PMID: 34708690; PubMed Central PMCID: PMCPMC8585483.
80. Roberts RE, Hallett MB. Neutrophil Cell Shape Change: Mechanism and Signalling during Cell Spreading and Phagocytosis. Int J Mol Sci. 2019;20(6). Epub 2019/03/22. doi: 10.3390/ijms20061383. PubMed PMID: 30893856; PubMed Central PMCID: PMCPMC6471475.

81. Dewitt S, Hallett MB. Calpain Activation by Ca(2+) and Its Role in Phagocytosis. Adv Exp Med Biol. 2020;1246:129-51. Epub 2020/05/14. doi: 10.1007/978-3-030-40406-2_8. PubMed PMID: 32399829.
82. Jaumouille V, Waterman CM. Physical Constraints and Forces Involved in Phagocytosis. Front Immunol. 2020;11:1097. Epub 2020/07/01. doi: 10.3389/fimmu.2020.01097. PubMed PMID: 32595635; PubMed Central PMCID: PMCPMC7304309.
83. Roberts RE, Martin M, Marion S, Elumalai GL, Lewis K, Hallett MB. Ca(2+)-activated cleavage of ezrin visualised dynamically in living myeloid cells during cell surface area expansion. J Cell Sci. 2020;133(5). Epub 2020/01/15. doi: 10.1242/jcs.236968. PubMed PMID: 31932511.
84. Henry SJ, Crocker JC, Hammer DA. Ligand density elicits a phenotypic switch in human neutrophils. Integr Biol (Camb). 2014;6(3):348-56. doi: 10.1039/c3ib40225h. PubMed PMID: 24480897.
85. Roberts RE, Dewitt S, Hallett MB. Membrane Tension and the Role of Ezrin During Phagocytosis. Adv Exp Med Biol. 2020;1246:83-102. Epub 2020/05/14. doi: 10.1007/978-3-030-40406-2_6. PubMed PMID: 32399827.
86. Lee CY, Herant M, Heinrich V. Target-specific mechanics of phagocytosis: protrusive neutrophil response to zymosan differs from the uptake of antibody-tagged pathogens. J Cell Sci. 2011;124(Pt 7):1106-14. Epub 2011/03/10. doi: 10.1242/jcs.078592. PubMed PMID: 21385838; PubMed Central PMCID: PMCPMC3056606.
87. Francis EA, Heinrich V. Integrative experimental/computational approach establishes active cellular protrusion as the primary driving force of phagocytic spreading by immune cells. BioRxiv. 2022. doi: 10.1101/2022.03.01.482589.
88. Hoang AN, Jones CN, Dimisko L, Hamza B, Martel J, Kojic N, et al. Measuring neutrophil speed and directionality during chemotaxis, directly from a droplet of whole blood. Technology (Singap World Sci). 2013;1(1):49. Epub 2014/05/09. doi: 10.1142/S2339547813500040. PubMed PMID: 24809064; PubMed Central PMCID: PMCPMC4010229.
89. Ascione F, Vasaturo A, Caserta S, D'Esposito V, Formisano P, Guido S. Comparison between fibroblast wound healing and cell random migration assays in vitro. Exp Cell Res. 2016;347(1):123-32. doi: 10.1016/j.yexcr.2016.07.015. PubMed PMID: WOS:000383217500013.
90. Czirok A. Endothelial cell motility, coordination and pattern formation during vasculogenesis. Wiley Interdiscip Rev Syst Biol Med. 2013;5(5):587-602. Epub 2013/07/17. doi: 10.1002/wsbm.1233. PubMed PMID: 23857825; PubMed Central PMCID: PMCPMC3737767.
91. Schneider L, Cammer M, Lehman J, Nielsen SK, Guerra CF, Veland IR, et al. Directional cell migration and chemotaxis in wound healing response to PDGF-AA are coordinated by the primary cilium in fibroblasts. Cell Physiol Biochem. 2010;25(2-3):279-92. Epub 2010/01/30. doi: 10.1159/000276562. PubMed PMID: 20110689; PubMed Central PMCID: PMCPMC2924811.
92. Morrissey MA, Williamson AP, Steinbach AM, Roberts EW, Kern N, Headley MB, et al. Chimeric antigen receptors that trigger phagocytosis. Elife. 2018;7. doi: ARTN e36688

10.7554/eLife.36688. PubMed PMID: WOS:000435593500001.
93. Feng MY, Jiang W, Kim BYS, Zhang CC, Fu YX, Weissman IL. Phagocytosis checkpoints as new targets for cancer immunotherapy. Nat Rev Cancer. 2019;19(10):568-86. doi: 10.1038/s41568-019-0183-z. PubMed PMID: WOS:000492743400012.
94. Carter SB. Haptotaxis and the mechanism of cell motility. Nature. 1967;213(5073):256-60. Epub 1967/01/21. doi: 10.1038/213256a0. PubMed PMID: 6030602.
95. Herant M, Dembo M. An integrative toy model of cell flattening, spreading, and ruffling. Biorheology. 2015;52(5-6):405-14. Epub 2015/11/26. doi: 10.3233/BIR-14042. PubMed PMID: 26600264.
96. Callens SJP, Uyttendaele RJC, Fratila-Apachitei LE, Zadpoor AA. Substrate curvature as a cue to guide spatiotemporal cell and tissue organization. Biomaterials. 2020;232:119739. Epub 2020/01/09. doi: 10.1016/j.biomaterials.2019.119739. PubMed PMID: 31911284.

97. van der Putten C, Buskermolen ABC, Werner M, Brouwer HFM, Bartels PAA, Dankers PYW, et al. Protein Micropatterning in 2.5D: An Approach to Investigate Cellular Responses in Multi-Cue Environments. ACS Appl Mater Interfaces. 2021;13(22):25589-98. Epub 2021/05/26. doi: 10.1021/acsami.1c01984. PubMed PMID: 34032413; PubMed Central PMCID: PMCPMC8193632.
98. Richards DM, Endres RG. Target shape dependence in a simple model of receptor-mediated endocytosis and phagocytosis. Proc Natl Acad Sci U S A. 2016;113(22):6113-8. Epub 2016/05/18. doi: 10.1073/pnas.1521974113. PubMed PMID: 27185939; PubMed Central PMCID: PMCPMC4896703.
99. Lee C-Y, Thompson III GR, Hastey CJ, Hodge GC, Lunetta JM, Pappagianis D, et al. *Coccidioides* Endospores and Spherules Draw Strong Chemotactic, Adhesive, and Phagocytic Responses by Individual Human Neutrophils. PLoS ONE. 2015;10(6):e0129522. doi: 10.1371/journal.pone.0129522.
100. Tollis S, Dart AE, Tzircotis G, Endres RG. The zipper mechanism in phagocytosis: energetic requirements and variability in phagocytic cup shape. BMC Syst Biol. 2010;4:149. Epub 2010/11/10. doi: 10.1186/1752-0509-4-149. PubMed PMID: 21059234; PubMed Central PMCID: PMCPMC2991294.
101. Manley HR, Keightley MC, Lieschke GJ. The Neutrophil Nucleus: An Important Influence on Neutrophil Migration and Function. Front Immunol. 2018;9:2867. Epub 2018/12/20. doi: 10.3389/fimmu.2018.02867. PubMed PMID: 30564248; PubMed Central PMCID: PMCPMC6288403.
102. Murphy K, Weaver C. Janeway's immunobiology. 9th edition. ed. New York, NY: Garland Science/Taylor & Francis Group, LLC; 2016. xx, 904 pages p.
103. Herant M, Marganski WA, Dembo M. The mechanics of neutrophils: synthetic modeling of three experiments. Biophys J. 2003;84(5):3389-413. Epub 2003/04/30. doi: 10.1016/s0006-3495(03)70062-9. PubMed PMID: 12719267; PubMed Central PMCID: PMCPMC1302898.
104. Zak A, Merino-Cortes SV, Sadoun A, Mustapha F, Babataheri A, Dogniaux S, et al. Rapid viscoelastic changes are a hallmark of early leukocyte activation. Biophys J. 2021. Epub 2021/03/18. doi: 10.1016/j.bpj.2021.02.042. PubMed PMID: 33730552.
105. Needham D, Hochmuth RM. A sensitive measure of surface stress in the resting neutrophil. Biophys J. 1992;61(6):1664-70. Epub 1992/06/01. doi: 10.1016/S0006-3495(92)81970-7. PubMed PMID: 1617145; PubMed Central PMCID: PMCPMC1260460.
106. Herant M, Heinrich V, Dembo M. Mechanics of neutrophil phagocytosis: behavior of the cortical tension. J Cell Sci. 2005;118(Pt 9):1789-97. doi: 10.1242/jcs.02275. PubMed PMID: 15827090.
107. Evans E, Yeung A. Apparent viscosity and cortical tension of blood granulocytes determined by micropipet aspiration. Biophys J. 1989;56(1):151-60. Epub 1989/07/01. doi: 10.1016/S0006-3495(89)82660-8. PubMed PMID: 2752085; PubMed Central PMCID: PMCPMC1280460.
108. Zhelev DV, Needham D, Hochmuth RM. Role of the membrane cortex in neutrophil deformation in small pipets. Biophys J. 1994;67(2):696-705. Epub 1994/08/01. doi: 10.1016/S0006-3495(94)80529-6. PubMed PMID: 7948682; PubMed Central PMCID: PMCPMC1225412.
109. Sukumaran S, Seifert U. Influence of shear flow on vesicles near a wall: A numerical study. Phys Rev E. 2001;64(1). doi: ARTN 011916

DOI 10.1103/PhysRevE.64.011916. PubMed PMID: WOS:000169907100090.
110. Marcy Y, Prost J, Carlier MF, Sykes C. Forces generated during actin-based propulsion: a direct measurement by micromanipulation. Proc Natl Acad Sci U S A. 2004;101(16):5992-7. Epub 2004/04/14. doi: 10.1073/pnas.0307704101. PubMed PMID: 15079054; PubMed Central PMCID: PMCPMC395911.
111. Drury JL, Dembo M. Hydrodynamics of micropipette aspiration. Biophys J. 1999;76(1 Pt 1):110-28. Epub 1999/01/06. doi: 10.1016/S0006-3495(99)77183-3. PubMed PMID: 9876128; PubMed Central PMCID: PMCPMC1302505.
112. Maenaka K, van der Merwe PA, Stuart DI, Jones EY, Sondermann P. The human low affinity Fcgamma receptors IIa, IIb, and III bind IgG with fast kinetics and distinct thermodynamic properties. J Biol Chem. 2001;276(48):44898-904. Epub 2001/09/07. doi: 10.1074/jbc.M106819200. PubMed PMID: 11544262.
113. Bonn D, Eggers J, Indekeu J, Meunier J, Rolley E. Wetting and spreading. Rev Mod Phys. 2009;81(2):739-805. doi: 10.1103/RevModPhys.81.739. PubMed PMID: WOS:000267197500008.

114. Evans EA. Detailed mechanics of membrane-membrane adhesion and separation. II. Discrete kinetically trapped molecular cross-bridges. Biophys J. 1985;48(1):185-92. Epub 1985/07/01. doi: 10.1016/S0006-3495(85)83771-1. PubMed PMID: 4016208; PubMed Central PMCID: PMCPMC1329388.
115. Helfrich W, Servuss RM. Undulations, Steric Interaction and Cohesion of Fluid Membranes. Nuovo Cimento D. 1984;3(1):137-51. doi: Doi 10.1007/Bf02452208. PubMed PMID: WOS:A1984SF44800012.
116. Biswas A, Alex A, Sinha B. Mapping Cell Membrane Fluctuations Reveals Their Active Regulation and Transient Heterogeneities. Biophys J. 2017;113(8):1768-81. Epub 2017/10/19. doi: 10.1016/j.bpj.2017.08.041. PubMed PMID: 29045871; PubMed Central PMCID: PMCPMC5647594.
117. Turlier H, Betz T. Fluctuations in Active Membranes. In: Bassereau P, Sens P, editors. Physics of Biological Membranes. Cham: Springer International Publishing; 2018. p. 581-619.
118. Francis EA, Heinrich V. Mechanistic Understanding of Single-Cell Behavior is Essential for Transformative Advances in Biomedicine. Yale J Biol Med. 2018;91(3):279-89. Epub 2018/09/28. PubMed PMID: 30258315; PubMed Central PMCID: PMCPMC6153630.
119. McGrath JL. Cell spreading: the power to simplify. Curr Biol. 2007;17(10):R357-8. Epub 2007/05/16. doi: 10.1016/j.cub.2007.03.057. PubMed PMID: 17502086.
120. Cao Y, Karmakar R, Ghabache E, Gutierrez E, Zhao Y, Groisman A, et al. Cell motility dependence on adhesive wetting. Soft Matter. 2019;15(9):2043-50. Epub 2019/02/07. doi: 10.1039/c8sm01832d. PubMed PMID: 30724956.
121. Fritz-Laylin LK, Riel-Mehan M, Chen BC, Lord SJ, Goddard TD, Ferrin TE, et al. Actin-based protrusions of migrating neutrophils are intrinsically lamellar and facilitate direction changes. Elife. 2017;6. Epub 2017/09/28. doi: 10.7554/eLife.26990. PubMed PMID: 28948912; PubMed Central PMCID: PMCPMC5614560.
122. Heinrich V, Lee C-Y. Blurred line between chemotactic chase and phagocytic consumption: an immunophysical single-cell perspective. Journal of Cell Science. 2011;124(18):3041-51. doi: 10.1242/jcs.086413.
123. Sadhu RK, Penic S, Iglic A, Gov NS. Modelling cellular spreading and emergence of motility in the presence of curved membrane proteins and active cytoskeleton forces. Eur Phys J Plus. 2021;136(5). doi: ARTN 495

10.1140/epjp/s13360-021-01433-9. PubMed PMID: WOS:000651515200002.
124. Mogilner A, Oster G. Cell motility driven by actin polymerization. Biophys J. 1996;71(6):3030-45. Epub 1996/12/01. doi: 10.1016/S0006-3495(96)79496-1. PubMed PMID: 8968574; PubMed Central PMCID: PMCPMC1233792.
125. Dickinson RB, Caro L, Purich DL. Force generation by cytoskeletal filament end-tracking proteins. Biophys J. 2004;87(4):2838-54. Epub 2004/09/30. doi: 10.1529/biophysj.104.045211. PubMed PMID: 15454475; PubMed Central PMCID: PMCPMC1304702.
126. Barnhart EL, Lee KC, Keren K, Mogilner A, Theriot JA. An adhesion-dependent switch between mechanisms that determine motile cell shape. PLoS Biol. 2011;9(5):e1001059. Epub 2011/05/12. doi: 10.1371/journal.pbio.1001059. PubMed PMID: 21559321; PubMed Central PMCID: PMCPMC3086868.
127. Ziebert F, Aranson IS. Effects of adhesion dynamics and substrate compliance on the shape and motility of crawling cells. PLoS One. 2013;8(5):e64511. Epub 2013/06/07. doi: 10.1371/journal.pone.0064511. PubMed PMID: 23741334; PubMed Central PMCID: PMCPMC3669322.
128. Copos CA, Walcott S, Del Alamo JC, Bastounis E, Mogilner A, Guy RD. Mechanosensitive Adhesion Explains Stepping Motility in Amoeboid Cells. Biophys J. 2017;112(12):2672-82. Epub 2017/06/22. doi: 10.1016/j.bpj.2017.04.033. PubMed PMID: 28636923; PubMed Central PMCID: PMCPMC5478966.
129. Shao D, Levine H, Rappel WJ. Coupling actin flow, adhesion, and morphology in a computational cell motility model. Proc Natl Acad Sci U S A. 2012;109(18):6851-6. Epub 2012/04/12.

doi: 10.1073/pnas.1203252109. PubMed PMID: 22493219; PubMed Central PMCID: PMCPMC3344950.
130. Kuusela E, Alt W. Continuum model of cell adhesion and migration. J Math Biol. 2009;58(1-2):135-61. Epub 2008/05/20. doi: 10.1007/s00285-008-0179-x. PubMed PMID: 18488227.
131. Hughes TJR. The Finite Element Method: Linear Static and Dynamic Finite Element Analysis: Dover; 2000.
132. Francis EA, Heinrich V. Extension of chemotactic pseudopods by nonadherent human neutrophils does not require or cause calcium bursts. Sci Signal. 2018;11(521). Epub 2018/03/15. doi: 10.1126/scisignal.aal4289. PubMed PMID: 29535263; PubMed Central PMCID: PMCPMC7053518.
133. White JR, Naccache PH, Molski TF, Borgeat P, Sha'afi RI. Direct demonstration of increased intracellular concentration of free calcium in rabbit and human neutrophils following stimulation by chemotactic factor. Biochem Biophys Res Commun. 1983;113(1):44-50. PubMed PMID: 6305358.
134. Lew DP. Receptor signalling and intracellular calcium in neutrophil activation. Eur J Clin Invest. 1989;19(4):338-46. Epub 1989/08/01. PubMed PMID: 2550240.
135. Norgauer J, Dobos G, Kownatzki E, Dahinden C, Burger R, Kupper R, et al. Complement fragment C3a stimulates Ca2+ influx in neutrophils via a pertussis-toxin-sensitive G protein. Eur J Biochem. 1993;217(1):289-94. Epub 1993/10/01. PubMed PMID: 8223566.
136. Schorr W, Swandulla D, Zeilhofer HU. Mechanisms of IL-8-induced Ca2+ signaling in human neutrophil granulocytes. Eur J Immunol. 1999;29(3):897-904. doi: 10.1002/(SICI)1521-4141(199903)29:03<897::AID-IMMU897>3.0.CO;2-5. PubMed PMID: 10092093.
137. Ibrahim FB, Pang SJ, Melendez AJ. Anaphylatoxin signaling in human neutrophils. A key role for sphingosine kinase. J Biol Chem. 2004;279(43):44802-11. doi: 10.1074/jbc.M403977200. PubMed PMID: 15302883.
138. Partida-Sanchez S, Iribarren P, Moreno-Garcia ME, Gao JL, Murphy PM, Oppenheimer N, et al. Chemotaxis and calcium responses of phagocytes to formyl peptide receptor ligands is differentially regulated by cyclic ADP ribose. J Immunol. 2004;172(3):1896-906. PubMed PMID: 14734775.
139. Schaff UY, Yamayoshi I, Tse T, Griffin D, Kibathi L, Simon SI. Calcium flux in neutrophils synchronizes beta2 integrin adhesive and signaling events that guide inflammatory recruitment. Ann Biomed Eng. 2008;36(4):632-46. Epub 2008/02/19. doi: 10.1007/s10439-008-9453-8. PubMed PMID: 18278555; PubMed Central PMCID: PMC2668576.
140. Schaff UY, Dixit N, Procyk E, Yamayoshi I, Tse T, Simon SI. Orai1 regulates intracellular calcium, arrest, and shape polarization during neutrophil recruitment in shear flow. Blood. 2010;115(3):657-66. Epub 2009/12/08. doi: 10.1182/blood-2009-05-224659. PubMed PMID: 19965684; PubMed Central PMCID: PMCPMC2810981.
141. Dixit N, Yamayoshi I, Nazarian A, Simon SI. Migrational guidance of neutrophils is mechanotransduced via high-affinity LFA-1 and calcium flux. J Immunol. 2011;187(1):472-81. Epub 2011/06/03. doi: 10.4049/jimmunol.1004197. PubMed PMID: 21632714; PubMed Central PMCID: PMCPMC3414252.
142. Huang B, Ling Y, Lin J, Du X, Fang Y, Wu J. Force-dependent calcium signaling and its pathway of human neutrophils on P-selectin in flow. Protein Cell. 2017;8(2):103-13. Epub 2017/01/18. doi: 10.1007/s13238-016-0364-4. PubMed PMID: 28097631; PubMed Central PMCID: PMCPMC5291781.
143. Jaconi ME, Theler JM, Schlegel W, Appel RD, Wright SD, Lew PD. Multiple elevations of cytosolic-free Ca2+ in human neutrophils: initiation by adherence receptors of the integrin family. J Cell Biol. 1991;112(6):1249-57. Epub 1991/03/01. PubMed PMID: 1900302; PubMed Central PMCID: PMCPMC2288892.
144. Clapham DE. Calcium signaling. Cell. 1995;80(2):259-68. PubMed PMID: 7834745.
145. Feske S. ORAI1 and STIM1 deficiency in human and mice: roles of store-operated Ca2+ entry in the immune system and beyond. Immunol Rev. 2009;231(1):189-209. doi: 10.1111/j.1600-065X.2009.00818.x. PubMed PMID: 19754898.

146. Bogeski I, Kummerow C, Al-Ansary D, Schwarz EC, Koehler R, Kozai D, et al. Differential redox regulation of ORAI ion channels: a mechanism to tune cellular calcium signaling. Sci Signal. 2010;3(115):ra24. doi: 10.1126/scisignal.2000672. PubMed PMID: 20354224.
147. Clemens RA, Lowell CA. Store-operated calcium signaling in neutrophils. J Leukoc Biol. 2015;98(4):497-502. doi: 10.1189/jlb.2MR1114-573R. PubMed PMID: 25714804; PubMed Central PMCID: PMCPMC4763866.
148. Sogkas G, Vogtle T, Rau E, Gewecke B, Stegner D, Schmidt RE, et al. Orai1 controls C5a-induced neutrophil recruitment in inflammation. Eur J Immunol. 2015;45(7):2143-53. Epub 2015/04/29. doi: 10.1002/eji.201445337. PubMed PMID: 25912155.
149. Saul S, Gibhardt CS, Schmidt B, Lis A, Pasieka B, Conrad D, et al. A calcium-redox feedback loop controls human monocyte immune responses: The role of ORAI Ca2+ channels. Sci Signal. 2016;9(418):ra26. doi: 10.1126/scisignal.aaf1639. PubMed PMID: 26956485.
150. Demaurex N, Nunes P. The role of STIM and ORAI proteins in phagocytic immune cells. Am J Physiol Cell Physiol. 2016;310(7):C496-508. Epub 2016/01/15. doi: 10.1152/ajpcell.00360.2015. PubMed PMID: 26764049; PubMed Central PMCID: PMCPMC4824159.
151. Zimmerli W, Reber AM, Dahinden CA. The role of formylpeptide receptors, C5a receptors, and cytosolic-free calcium in neutrophil priming. J Infect Dis. 1990;161(2):242-9. Epub 1990/02/01. PubMed PMID: 2153739.
152. Elsner J, Kaever V, Emmendorffer A, Breidenbach T, Lohmann-Matthes ML, Roesler J. Heterogeneity in the mobilization of cytoplasmic calcium by human polymorphonuclear leukocytes in response to fMLP, C5a and IL-8/NAP-1. J Leukoc Biol. 1992;51(1):77-83. PubMed PMID: 1740648.
153. Partida-Sanchez S, Cockayne DA, Monard S, Jacobson EL, Oppenheimer N, Garvy B, et al. Cyclic ADP-ribose production by CD38 regulates intracellular calcium release, extracellular calcium influx and chemotaxis in neutrophils and is required for bacterial clearance in vivo. Nat Med. 2001;7(11):1209-16. Epub 2001/11/02. doi: 10.1038/nm1101-1209. PubMed PMID: 11689885.
154. Itagaki K, Kannan KB, Livingston DH, Deitch EA, Fekete Z, Hauser CJ. Store-operated calcium entry in human neutrophils reflects multiple contributions from independently regulated pathways. J Immunol. 2002;168(8):4063-9. PubMed PMID: 11937565.
155. Beste MT, Lomakina EB, Hammer DA, Waugh RE. Immobilized IL-8 triggers phagocytosis and dynamic changes in membrane microtopology in human neutrophils. Ann Biomed Eng. 2015;43(9):2207-19. Epub 2015/01/15. doi: 10.1007/s10439-014-1242-y. PubMed PMID: 25582838; PubMed Central PMCID: PMCPMC4500759.
156. Jaconi ME, Lew DP, Carpentier JL, Magnusson KE, Sjogren M, Stendahl O. Cytosolic free calcium elevation mediates the phagosome-lysosome fusion during phagocytosis in human neutrophils. J Cell Biol. 1990;110(5):1555-64. Epub 1990/05/01. PubMed PMID: 2110568; PubMed Central PMCID: PMCPMC2200167.
157. Pettit EJ, Hallett MB. Pulsatile Ca2+ influx in human neutrophils undergoing CD11b/CD18 integrin engagement. Biochem Biophys Res Commun. 1997;230(2):258-61. Epub 1997/01/13. doi: 10.1006/bbrc.1996.5931. PubMed PMID: 9016761.
158. Löfgren R, Serrander L, Forsberg M, Wilsson Å, Wasteson Å, Stendahl O. CR3, FcγRIIA and FcγRIIIB induce activation of the respiratory burst in human neutrophils: the role of intracellular Ca2+, phospholipase D and tyrosine phosphorylation. Biochimica et Biophysica Acta (BBA) - Molecular Cell Research. 1999;1452(1):46-59. doi: 10.1016/s0167-4889(99)00112-3.
159. Dewitt S, Hallett MB. Cytosolic free Ca(2+) changes and calpain activation are required for beta integrin-accelerated phagocytosis by human neutrophils. J Cell Biol. 2002;159(1):181-9. doi: 10.1083/jcb.200206089. PubMed PMID: 12379807; PubMed Central PMCID: PMCPMC2173489.
160. Nunes P, Demaurex N. The role of calcium signaling in phagocytosis. J Leukoc Biol. 2010;88(1):57-68. doi: 10.1189/jlb.0110028. PubMed PMID: 20400677.
161. Marks PW, Maxfield FR. Transient increases in cytosolic free calcium appear to be required for the migration of adherent human neutrophils. J Cell Biol. 1990;110(1):43-52. PubMed PMID: 2295684; PubMed Central PMCID: PMCPMC2115989.

162. Mankovich AR, Lee CY, Heinrich V. Differential effects of serum heat treatment on chemotaxis and phagocytosis by human neutrophils. PLoS One. 2013;8(1):e54735. doi: 10.1371/journal.pone.0054735. PubMed PMID: 23349959; PubMed Central PMCID: PMCPMC3551912.
163. Heinrich V, Simpson WD, 3rd, Francis EA. Analytical prediction of the spatiotemporal distribution of chemoattractants around their source: theory and application to complement-mediated chemotaxis. Front Immunol. 2017;8(578):578. Epub 2017/06/13. doi: 10.3389/fimmu.2017.00578. PubMed PMID: 28603522; PubMed Central PMCID: PMCPMC5445147.
164. Merle NS, Church SE, Fremeaux-Bacchi V, Roumenina LT. Complement System Part I - Molecular Mechanisms of Activation and Regulation. Front Immunol. 2015;6:262. Epub 2015/06/18. doi: 10.3389/fimmu.2015.00262. PubMed PMID: 26082779; PubMed Central PMCID: PMCPMC4451739.
165. Guo RF, Ward PA. Role of C5a in inflammatory responses. Annual review of immunology. 2005;23:821-52. Epub 2005/03/18. doi: 10.1146/annurev.immunol.23.021704.115835. PubMed PMID: 15771587.
166. Huber-Lang MS, Younkin EM, Sarma JV, McGuire SR, Lu KT, Guo RF, et al. Complement-induced impairment of innate immunity during sepsis. J Immunol. 2002;169(6):3223-31. Epub 2002/09/10. doi: 10.4049/jimmunol.169.6.3223. PubMed PMID: 12218141.
167. Ward PA. The dark side of C5a in sepsis. Nat Rev Immunol. 2004;4(2):133-42.
168. Zhang F, Liu AL, Gao S, Ma S, Guo SB. Neutrophil dysfunction in sepsis. Chin Med J (Engl). 2016;129(22):2741-4. Epub 2016/11/09. doi: 10.4103/0366-6999.193447. PubMed PMID: 27824008; PubMed Central PMCID: PMCPMC5126167.
169. Bhan C, Dipankar P, Chakraborty P, Sarangi PP. Role of cellular events in the pathophysiology of sepsis. Inflamm Res. 2016;65(11):853-68. Epub 2016/07/10. doi: 10.1007/s00011-016-0970-x. PubMed PMID: 27392441.
170. Shen XF, Cao K, Jiang JP, Guan WX, Du JF. Neutrophil dysregulation during sepsis: an overview and update. J Cell Mol Med. 2017;21(9):1687-97. Epub 2017/03/01. doi: 10.1111/jcmm.13112. PubMed PMID: 28244690; PubMed Central PMCID: PMCPMC5571534.
171. Marc MM, Kristan SS, Rozman A, Kern I, Flezar M, Kosnik M, et al. Complement factor C5a in acute exacerbation of Chronic Obstructive Pulmonary Disease. Scand J Immunol. 2010;71(5):386-91. Epub 2010/05/27. doi: 10.1111/j.1365-3083.2010.02385.x. PubMed PMID: 20500690.
172. Stove S, Welte T, Wagner TO, Kola A, Klos A, Bautsch W, et al. Circulating complement proteins in patients with sepsis or systemic inflammatory response syndrome. Clin Diagn Lab Immunol. 1996;3(2):175-83. Epub 1996/03/01. PubMed PMID: 8991632; PubMed Central PMCID: PMCPMC170271.
173. Lechner J, Chen M, Hogg RE, Toth L, Silvestri G, Chakravarthy U, et al. Higher plasma levels of complement C3a, C4a and C5a increase the risk of subretinal fibrosis in neovascular age-related macular degeneration: Complement activation in AMD. Immun Ageing. 2016;13(1):4. Epub 2016/02/18. doi: 10.1186/s12979-016-0060-5. PubMed PMID: 26884800; PubMed Central PMCID: PMCPMC4754842.
174. Francis EA, Heinrich V. Quantifying the Sensitivity of Human Immune Cells to Chemoattractant. Biophys J. 2017;112(5):834-7. doi: 10.1016/j.bpj.2017.01.009. PubMed PMID: 28185642; PubMed Central PMCID: PMCPMC5355482.
175. Heit B, Tavener S, Raharjo E, Kubes P. An intracellular signaling hierarchy determines direction of migration in opposing chemotactic gradients. J Cell Biol. 2002;159(1):91-102. Epub 2002/10/09. doi: 10.1083/jcb.200202114. PubMed PMID: 12370241; PubMed Central PMCID: PMCPMC2173486.
176. Heit B, Robbins SM, Downey CM, Guan ZW, Colarusso P, Miller BJ, et al. PTEN functions to 'prioritize' chemotactic cues and prevent 'distraction' in migrating neutrophils. Nat Immunol. 2008;9(7):743-52. doi: 10.1038/ni.1623. PubMed PMID: WOS:000256904900011.
177. Wangdi T, Lee CY, Spees AM, Yu C, Kingsbury DD, Winter SE, et al. The Vi capsular polysaccharide enables Salmonella enterica serovar typhi to evade microbe-guided neutrophil chemotaxis. PLoS Pathog. 2014;10(8):e1004306. doi: 10.1371/journal.ppat.1004306. PubMed PMID: 25101794; PubMed Central PMCID: PMCPMC4125291.

178. Chodniewicz D, Alteraifi AM, Zhelev DV. Experimental Evidence for the Limiting Role of Enzymatic Reactions in Chemoattractant-induced Pseudopod Extension in Human Neutrophils. Journal of Biological Chemistry. 2004;279(23):24460-6. doi: 10.1074/jbc.M312764200.
179. Zhelev DV, Alteraifi AM, Chodniewicz D. Controlled pseudopod extension of human neutrophils stimulated with different chemoattractants. Biophys J. 2004;87(1):688-95. Epub 2004/07/09. doi: 10.1529/biophysj.103.036699

S0006-3495(04)73554-7 [pii]. PubMed PMID: 15240502; PubMed Central PMCID: PMC1304392.
180. Ting-Beall HP, Needham D, Hochmuth RM. Volume and osmotic properties of human neutrophils. Blood. 1993;81(10):2774-80. PubMed PMID: 8490184.
181. Herant M, Heinrich V, Dembo M. Mechanics of neutrophil phagocytosis: experiments and quantitative models. J Cell Sci. 2006;119:1903 - 13.
182. Herant M, Heinrich V, Dembo M. Mechanics of neutrophil phagocytosis: behavior of the cortical tension. J Cell Sci. 2005;118:1789 - 97.
183. Makino A, Prossnitz ER, Bünemann M, Wang JM, Yao W, Schmid-Schönbein GW. G protein-coupled receptors serve as mechanosensors for fluid shear stress in neutrophils. American Journal of Physiology - Cell Physiology. 2006;290(6):C1633-C9. doi: 10.1152/ajpcell.00576.2005.
184. Mitchell MJ, King MR. Shear-induced resistance to neutrophil activation via the formyl peptide receptor. Biophys J. 2012;102(8):1804-14. Epub 2012/07/10. doi: 10.1016/j.bpj.2012.03.053. PubMed PMID: 22768936; PubMed Central PMCID: PMCPMC3328724.
185. Mitchell MJ, Lin KS, King MR. Fluid shear stress increases neutrophil activation via platelet-activating factor. Biophys J. 2014;106(10):2243-53. Epub 2014/05/24. doi: 10.1016/j.bpj.2014.04.001. PubMed PMID: 24853753; PubMed Central PMCID: PMCPMC4052238.
186. Nathan CF. Neutrophil activation on biological surfaces. Massive secretion of hydrogen peroxide in response to products of macrophages and lymphocytes. J Clin Invest. 1987;80(6):1550-60. Epub 1987/12/01. doi: 10.1172/JCI113241. PubMed PMID: 2445780; PubMed Central PMCID: PMCPMC442423.
187. Reis ES, Chen H, Sfyroera G, Monk PN, Kohl J, Ricklin D, et al. C5a receptor-dependent cell activation by physiological concentrations of desarginated C5a: insights from a novel label-free cellular assay. J Immunol. 2012;189(10):4797-805. Epub 2012/10/09. doi: 10.4049/jimmunol.1200834. PubMed PMID: 23041570; PubMed Central PMCID: PMCPMC3521166.
188. Franco S, Perrin B, Huttenlocher A. Isoform specific function of calpain 2 in regulating membrane protrusion. Exp Cell Res. 2004;299(1):179-87. doi: http://dx.doi.org/10.1016/j.yexcr.2004.05.021.
189. Franco SJ, Rodgers MA, Perrin BJ, Han J, Bennin DA, Critchley DR, et al. Calpain-mediated proteolysis of talin regulates adhesion dynamics. Nat Cell Biol. 2004;6(10):977-83. doi: http://www.nature.com/ncb/journal/v6/n10/suppinfo/ncb1175_S1.html.
190. Cortesio CL, Boateng LR, Piazza TM, Bennin DA, Huttenlocher A. Calpain-mediated proteolysis of paxillin negatively regulates focal adhesion dynamics and cell migration. J Biol Chem. 2011;286(12):9998-10006. Epub 2011/01/29. doi: 10.1074/jbc.M110.187294. PubMed PMID: 21270128; PubMed Central PMCID: PMCPMC3060554.
191. Diamond MS, Garcia-Aguilar J, Bickford JK, Corbi AL, Springer TA. The I domain is a major recognition site on the leukocyte integrin Mac-1 (CD11b/CD18) for four distinct adhesion ligands. The Journal of Cell Biology. 1993;120(4):1031-43. doi: 10.1083/jcb.120.4.1031.
192. Podolnikova NP, Podolnikov AV, Haas TA, Lishko VK, Ugarova TP. Ligand recognition specificity of leukocyte integrin alphaMbeta2 (Mac-1, CD11b/CD18) and its functional consequences. Biochemistry. 2015;54(6):1408-20. Epub 2015/01/24. doi: 10.1021/bi5013782. PubMed PMID: 25613106; PubMed Central PMCID: PMCPMC4532391.
193. Jongstra-Bilen J, Harrison R, Grinstein S. Fcγ-receptors induce Mac-1 (CD11b/CD18) mobilization and accumulation in the phagocytic cup for optimal phagocytosis. Journal of Biological Chemistry. 2003;278(46):45720-9. doi: 10.1074/jbc.M303704200.

194. Lomakina E, Knauf PA, Schultz JB, Law FY, McGraw MD, Waugh RE. Activation of human neutrophil Mac-1 by anion substitution. Blood Cells Mol Dis. 2009;42(3):177-84. Epub 2009/02/28. doi: 10.1016/j.bcmd.2009.01.006. PubMed PMID: 19246218; PubMed Central PMCID: PMCPMC2671573.
195. Hunniger K, Bieber K, Martin R, Lehnert T, Figge MT, Loffler J, et al. A second stimulus required for enhanced antifungal activity of human neutrophils in blood is provided by anaphylatoxin C5a. J Immunol. 2015;194(3):1199-210. Epub 2014/12/30. doi: 10.4049/jimmunol.1401845. PubMed PMID: 25539819.
196. Graham IL, Gresham HD, Brown EJ. An immobile subset of plasma-membrane Cd11b/Cd18 (Mac-1) is involved in phagocytosis of targets recognized by multiple receptors. J Immunol. 1989;142(7):2352-8. PubMed PMID: WOS:A1989T802000026.
197. Heinrich V, Rawicz W. Automated, high-resolution micropipet aspiration reveals new insight into the physical properties of fluid membranes. Langmuir. 2005;21(5):1962-71. PubMed PMID: 15723496; PubMed Central PMCID: PMCPMID: 15723496
198. Dianzani C, Lombardi G, Collino M, Ferrara C, Cassone MC, Fantozzi R. Priming effects of substance P on calcium changes evoked by interleukin-8 in human neutrophils. J Leukoc Biol. 2001;69(6):1013-8. Epub 2001/06/19. PubMed PMID: 11404389.
199. Morikis VA, Masadeh E, Simon SI. Tensile force transmitted through LFA-1 bonds mechanoregulate neutrophil inflammatory response. J Leukoc Biol. 2020;108(6):1815-28. Epub 2020/06/13. doi: 10.1002/JLB.3A0520-100RR. PubMed PMID: 32531836.
200. Dusi S, Donini M, Della Bianca V, Rossi F. Tyrosine phosphorylation of phospholipase C-gamma 2 is involved in the activation of phosphoinositide hydrolysis by Fc receptors in human neutrophils. Biochem Biophys Res Commun. 1994;201(3):1100-8. Epub 1994/06/30. doi: 10.1006/bbrc.1994.1819. PubMed PMID: 7517665.
201. Fallman M, Andersson R, Andersson T. Signaling properties of CR3 (CD11b/CD18) and CR1 (CD35) in relation to phagocytosis of complement-opsonized particles. J Immunol. 1993;151(1):330-8. Epub 1993/07/01. PubMed PMID: 8326130.
202. Pettit EJ, Hallett MB. Localised and global cytosolic Ca2+ changes in neutrophils during engagement of Cd11b/CD18 integrin visualised using confocal laser scanning reconstruction. J Cell Sci. 1996;109 (Pt 7):1689-94. Epub 1996/07/01. doi: 10.1242/jcs.109.7.1689. PubMed PMID: 8832391.
203. Rosales C, Brown EJ. Signal transduction by neutrophil immunoglobulin G Fc receptors. Dissociation of intracytoplasmic calcium concentration rise from inositol 1,4,5-trisphosphate. J Biol Chem. 1992;267(8):5265-71. Epub 1992/03/15. PubMed PMID: 1531982.
204. Rosales C, Brown EJ. Two mechanisms for IgG Fc-receptor-mediated phagocytosis by human neutrophils. J Immunol. 1991;146(11):3937-44. Epub 1991/06/01. PubMed PMID: 2033263.
205. Helmchen F. Calibration of fluorescent calcium indicators. Cold Spring Harb Protoc. 2011;2011(8):923-30. Epub 2011/08/03. doi: 10.1101/pdb.top120. PubMed PMID: 21807862.
206. Helmchen F. Calibration protocols for fluorescent calcium indicators. Cold Spring Harb Protoc. 2011;2011(8):980-4. Epub 2011/08/03. doi: 10.1101/pdb.prot5649. PubMed PMID: 21807855.
207. Nordstrom T, Stahls A, Pessa-Morikawa T, Mustelin T, Andersson LC. Phorbol 12-myristate 13-acetate (TPA) blocks CD3-mediated Ca2+ mobilization in Jurkat T cells independently of protein kinase C activation. Biochem Biophys Res Commun. 1990;173(1):396-400. Epub 1990/11/30. doi: 10.1016/s0006-291x(05)81071-x. PubMed PMID: 2147852.
208. Millius A, Weiner OD. Manipulation of neutrophil-like HL-60 cells for the study of directed cell migration. Methods Mol Biol. 2010;591:147-58. Epub 2009/12/04. doi: 10.1007/978-1-60761-404-3_9. PubMed PMID: 19957129; PubMed Central PMCID: PMCPMC3128798.
209. Iwanaga TU, W.; Herman, J. Toward SALib 2.0: Advancing the accessibility and interpretability of global sensitivity analyses. Socio-Environmental Systems Modelling. 2022;4:18155. doi: 10.18174/sesmo.18155.
210. Herman JU, W. . SALib: An open-source Python library for sensitivity analysis. Journal of Open Source Software. 2017;2. doi: 10.21105/joss.00097.

211. Jaqaman K, Kuwata H, Touret N, Collins R, Trimble WS, Danuser G, et al. Cytoskeletal control of CD36 diffusion promotes its receptor and signaling function. Cell. 2011;146(4):593-606. Epub 2011/08/23. doi: 10.1016/j.cell.2011.06.049. PubMed PMID: 21854984; PubMed Central PMCID: PMCPMC3160624.
212. Li YX, Rinzel J. Equations for InsP3 receptor-mediated [Ca2+]i oscillations derived from a detailed kinetic model: a Hodgkin-Huxley like formalism. J Theor Biol. 1994;166(4):461-73. Epub 1994/02/21. doi: 10.1006/jtbi.1994.1041. PubMed PMID: 8176949.
213. De Young GW, Keizer J. A single-pool inositol 1,4,5-trisphosphate-receptor-based model for agonist-stimulated oscillations in Ca2+ concentration. Proc Natl Acad Sci U S A. 1992;89(20):9895-9. Epub 1992/10/15. doi: 10.1073/pnas.89.20.9895. PubMed PMID: 1329108; PubMed Central PMCID: PMCPMC50240.
214. Wagner J, Keizer J. Effects of rapid buffers on Ca2+ diffusion and Ca2+ oscillations. Biophys J. 1994;67(1):447-56. Epub 1994/07/01. doi: 10.1016/S0006-3495(94)80500-4. PubMed PMID: 7919018; PubMed Central PMCID: PMCPMC1225377.
215. Link KG, Stobb MT, Di Paola J, Neeves KB, Fogelson AL, Sindi SS, et al. A local and global sensitivity analysis of a mathematical model of coagulation and platelet deposition under flow. PLoS One. 2018;13(7):e0200917. Epub 2018/07/27. doi: 10.1371/journal.pone.0200917. PubMed PMID: 30048479; PubMed Central PMCID: PMCPMC6062055.
216. Saltelli A, Annoni P, Azzini I, Campolongo F, Ratto M, Tarantola S. Variance based sensitivity analysis of model output. Design and estimator for the total sensitivity index. Comput Phys Commun. 2010;181(2):259-70. doi: 10.1016/j.cpc.2009.09.018. PubMed PMID: WOS:000273192100002.
217. Zheng S, Zhou L, Ma G, Zhang T, Liu J, Li J, et al. Calcium store refilling and STIM activation in STIM- and Orai-deficient cell lines. Pflugers Arch. 2018;470(10):1555-67. Epub 2018/06/24. doi: 10.1007/s00424-018-2165-5. PubMed PMID: 29934936; PubMed Central PMCID: PMCPMC6153602.
218. Maurya MR, Subramaniam S. A kinetic model for calcium dynamics in RAW 264.7 cells: 1. Mechanisms, parameters, and subpopulational variability. Biophys J. 2007;93(3):709-28. Epub 2007/05/08. doi: 10.1529/biophysj.106.097469. PubMed PMID: 17483174; PubMed Central PMCID: PMCPMC1913151.
219. Davies EV, Hallett MB. A novel pathway for Ca2+ signalling in neutrophils by immune complexes. Immunology. 1995;85(4):538-43. Epub 1995/08/01. PubMed PMID: 7558146; PubMed Central PMCID: PMCPMC1383780.
220. Jakus Z, Simon E, Frommhold D, Sperandio M, Mocsai A. Critical role of phospholipase Cgamma2 in integrin and Fc receptor-mediated neutrophil functions and the effector phase of autoimmune arthritis. J Exp Med. 2009;206(3):577-93. Epub 2009/03/11. doi: 10.1084/jem.20081859. PubMed PMID: 19273622; PubMed Central PMCID: PMCPMC2699137.
221. Shen ZH, Lin CT, Unkeless JC. Correlations among Tyrosine Phosphorylation of Shc, P72(Syk), Plc-Gamma-1, and [Ca2+](I) Flux in Fc-Gamma-Riia Signaling. Journal of Immunology. 1994;152(6):3017-23. PubMed PMID: WOS:A1994NC77300043.
222. Gewirtz AT, Simons ER. Phospholipase D mediates Fc gamma receptor activation of neutrophils and provides specificity between high-valency immune complexes and fMLP signaling pathways. J Leukocyte Biol. 1997;61(4):522-8. doi: DOI 10.1002/jlb.61.4.522. PubMed PMID: WOS:A1997WU02500019.
223. Hinkovska-Galcheva V, Kjeldsen L, Mansfield PJ, Boxer LA, Shayman JA, Suchard SJ. Activation of a plasma membrane-associated neutral sphingomyelinase and concomitant ceramide accumulation during IgG-dependent phagocytosis in human polymorphonuclear leukocytes. Blood. 1998;91(12):4761-9. Epub 1998/06/17. PubMed PMID: 9616175.
224. Dixit N, Kim MH, Rossaint J, Yamayoshi I, Zarbock A, Simon SI. Leukocyte function antigen-1, kindlin-3, and calcium flux orchestrate neutrophil recruitment during inflammation. J Immunol. 2012;189(12):5954-64. Epub 2012/11/13. doi: 10.4049/jimmunol.1201638. PubMed PMID: 23144497; PubMed Central PMCID: PMCPMC3723394.

225. Ma VP, Hu Y, Kellner AV, Brockman JM, Velusamy A, Blanchard AT, et al. The magnitude of LFA-1/ICAM-1 forces fine-tune TCR-triggered T cell activation. Sci Adv. 2022;8(8):eabg4485. Epub 2022/02/26. doi: 10.1126/sciadv.abg4485. PubMed PMID: 35213231; PubMed Central PMCID: PMCPMC8880789.
226. Tapper H, Furuya W, Grinstein S. Localized exocytosis of primary (lysosomal) granules during phagocytosis: role of Ca2+-dependent tyrosine phosphorylation and microtubules. J Immunol. 2002;168(10):5287-96. Epub 2002/05/08. doi: 10.4049/jimmunol.168.10.5287. PubMed PMID: 11994486.
227. Baylor SM, Hollingworth S. Calcium indicators and calcium signalling in skeletal muscle fibres during excitation-contraction coupling. Prog Biophys Mol Biol. 2011;105(3):162-79. Epub 2010/07/06. doi: 10.1016/j.pbiomolbio.2010.06.001. PubMed PMID: 20599552; PubMed Central PMCID: PMCPMC2974769.
228. Bengtsson T, Jaconi ME, Gustafson M, Magnusson KE, Theler JM, Lew DP, et al. Actin dynamics in human neutrophils during adhesion and phagocytosis is controlled by changes in intracellular free calcium. Eur J Cell Biol. 1993;62(1):49-58. Epub 1993/10/01. PubMed PMID: 8269978.
229. Lomakina EB, Waugh RE. Signaling and Dynamics of Activation of LFA-1 and Mac-1 by Immobilized IL-8. Cell Mol Bioeng. 2010;3(2):106-16. Epub 2011/05/03. doi: 10.1007/s12195-009-0099-x. PubMed PMID: 21532911; PubMed Central PMCID: PMCPMC3084010.
230. Arganda-Carreras I, Kaynig V, Rueden C, Eliceiri KW, Schindelin J, Cardona A, et al. Trainable Weka Segmentation: a machine learning tool for microscopy pixel classification. Bioinformatics. 2017;33(15):2424-6. Epub 2017/04/04. doi: 10.1093/bioinformatics/btx180. PubMed PMID: 28369169.
231. Nusse O, Serrander L, Lew DP, Krause KH. Ca2+-induced exocytosis in individual human neutrophils: high- and low-affinity granule populations and submaximal responses. EMBO J. 1998;17(5):1279-88. Epub 1998/04/18. doi: 10.1093/emboj/17.5.1279. PubMed PMID: 9482725; PubMed Central PMCID: PMCPMC1170476.
232. Dewitt S, Laffafian I, Hallett MB. Phagosomal oxidative activity during beta2 integrin (CR3)-mediated phagocytosis by neutrophils is triggered by a non-restricted Ca2+ signal: Ca2+ controls time not space. J Cell Sci. 2003;116(Pt 14):2857-65. Epub 2003/05/29. doi: 10.1242/jcs.00499. PubMed PMID: 12771186.
233. Ma Q, Shimaoka M, Lu C, Jing H, Carman CV, Springer TA. Activation-induced conformational changes in the I domain region of lymphocyte function-associated antigen 1. J Biol Chem. 2002;277(12):10638-41. Epub 2002/01/17. doi: 10.1074/jbc.M112417200. PubMed PMID: 11792712.
234. Dransfield I, Cabanas C, Craig A, Hogg N. Divalent cation regulation of the function of the leukocyte integrin LFA-1. J Cell Biol. 1992;116(1):219-26. Epub 1992/01/01. doi: 10.1083/jcb.116.1.219. PubMed PMID: 1346139; PubMed Central PMCID: PMCPMC2289255.
235. Aris R. Vectors, Tensors, and the Basic Equations of Fluid Mechanics: Dover Publications, Inc.; 1962.
236. Sens P, Safran SA. Pore formation and area exchange in tense membranes. Europhys Lett. 1998;43(1):95-100. doi: DOI 10.1209/epl/i1998-00325-6. PubMed PMID: WOS:000074819100017.
237. Knupp PS, S.L. The Fundamentals of Grid Generation. 1st ed: CRC Press; 1993.
238. Wang Y, Jonsson F. Expression, Role, and Regulation of Neutrophil Fcgamma Receptors. Front Immunol. 2019;10:1958. Epub 2019/09/12. doi: 10.3389/fimmu.2019.01958. PubMed PMID: 31507592; PubMed Central PMCID: PMCPMC6718464.
239. Lee CY. Quantifying the Mechanics of Phagocytosis by Human Neutrophils: UC Davis; 2011.
240. Freeman SA, Vega A, Riedl M, Collins RF, Ostrowski PP, Woods EC, et al. Transmembrane Pickets Connect Cyto- and Pericellular Skeletons Forming Barriers to Receptor Engagement. Cell. 2018;172(1-2):305-17 e10. Epub 2018/01/13. doi: 10.1016/j.cell.2017.12.023. PubMed PMID: 29328918; PubMed Central PMCID: PMCPMC5929997.
241. Taylor R, Allard J, Read EL. Simulation of receptor triggering by kinetic segregation shows role of oligomers and close contacts. Biophys J. 2022;121(9):1660-74. Epub 2022/04/04. doi: 10.1016/j.bpj.2022.03.033. PubMed PMID: 35367423.

242. Schmid-Schonbein GW, Shih YY, Chien S. Morphometry of human leukocytes. Blood. 1980;56(5):866-75. Epub 1980/11/01. PubMed PMID: 6775712.
243. Kapela A, Bezerianos A, Tsoukias NM. A mathematical model of Ca2+ dynamics in rat mesenteric smooth muscle cell: agonist and NO stimulation. J Theor Biol. 2008;253(2):238-60. Epub 2008/04/22. doi: 10.1016/j.jtbi.2008.03.004. PubMed PMID: 18423672.
244. Mukherjee S, Zhu J, Zikherman J, Parameswaran R, Kadlecek TA, Wang Q, et al. Monovalent and Multivalent Ligation of the B Cell Receptor Exhibit Differential Dependence upon Syk and Src Family Kinases. Science Signaling. 2013;6(256). doi: ARTN ra1

10.1126/scisignal.2003220. PubMed PMID: WOS:000312958300002.
245. Lemon G, Gibson WG, Bennett MR. Metabotropic receptor activation, desensitization and sequestration-I: modelling calcium and inositol 1,4,5-trisphosphate dynamics following receptor activation. J Theor Biol. 2003;223(1):93-111. Epub 2003/06/05. doi: 10.1016/s0022-5193(03)00079-1. PubMed PMID: 12782119.
246. Bennett MR, Farnell L, Gibson WG. A quantitative description of the contraction of blood vessels following the release of noradrenaline from sympathetic varicosities. J Theor Biol. 2005;234(1):107-22. Epub 2005/02/22. doi: 10.1016/j.jtbi.2004.11.013. PubMed PMID: 15721040.
247. Fink CC, Slepchenko B, Loew LM. Determination of time-dependent inositol-1,4,5-trisphosphate concentrations during calcium release in a smooth muscle cell. Biophys J. 1999;77(1):617-28. Epub 1999/07/02. doi: 10.1016/S0006-3495(99)76918-3. PubMed PMID: 10388786; PubMed Central PMCID: PMCPMC1300358.
248. Luik RM, Wang B, Prakriya M, Wu MM, Lewis RS. Oligomerization of STIM1 couples ER calcium depletion to CRAC channel activation. Nature. 2008;454(7203):538-42. Epub 2008/07/04. doi: 10.1038/nature07065. PubMed PMID: 18596693; PubMed Central PMCID: PMCPMC2712442.
249. O'Donnell ME, Owen NE. Regulation of ion pumps and carriers in vascular smooth muscle. Physiol Rev. 1994;74(3):683-721. Epub 1994/07/01. doi: 10.1152/physrev.1994.74.3.683. PubMed PMID: 8036250.
250. von Tscharner V, Deranleau DA, Baggiolini M. Calcium fluxes and calcium buffering in human neutrophils. J Biol Chem. 1986;261(22):10163-8. Epub 1986/08/05. PubMed PMID: 3090032.
251. Krause KH, Welsh MJ. Voltage-dependent and Ca2(+)-activated ion channels in human neutrophils. J Clin Invest. 1990;85(2):491-8. Epub 1990/02/01. doi: 10.1172/JCI114464. PubMed PMID: 2153708; PubMed Central PMCID: PMCPMC296450.
252. Messerer DAC, Denk S, Fohr KJ, Halbgebauer R, Braun CK, Hones F, et al. Complement C5a Alters the Membrane Potential of Neutrophils during Hemorrhagic Shock. Mediators Inflamm. 2018;2018:2052356. Epub 2018/07/14. doi: 10.1155/2018/2052356. PubMed PMID: 30002598; PubMed Central PMCID: PMCPMC5996468.
253. Fall CPM, E. S.; Wagner, J. M.; Tyson, J. J. Computational Cell Biology: Springer; 2002.
254. Sobol IM. Sensitivity estimates for nonlinear mathematical models. Mathematical Modelling and Computational Experiments. 1993.
255. Campolongo F, Saltelli A, Cariboni J. From screening to quantitative sensitivity analysis. A unified approach. Comput Phys Commun. 2011;182(4):978-88. doi: 10.1016/j.cpc.2010.12.039. PubMed PMID: WOS:000288404300012.
256. Sobol IM. Global sensitivity indices for nonlinear mathematical models and their Monte Carlo estimates. Math Comput Simulat. 2001;55(1-3):271-80. doi: Doi 10.1016/S0378-4754(00)00270-6. PubMed PMID: WOS:000167385700029.